

Study of Neutrino-Induced Neutral Current Neutral Pion Production in the T2K Near Detector

Samantha Short

High Energy Physics
Blackett Laboratory
Imperial College London

A thesis submitted to Imperial College London
for the degree of Doctor of Philosophy

March 2013

*Dedicated to the residents of Tokai.
I am eternally grateful for everything you
did in the aftermath of the
Great East Japan Earthquake.*

Abstract

The T2K experiment is a long baseline neutrino oscillation experiment. The most intense accelerator muon neutrino beam ever built is produced at the J-PARC facility in Tokai, located on the east coast of Japan, and directed (2.5° off-axis) toward the Super-Kamiokande water Cherenkov detector, located 295 km away in the mountains of western Japan.

For the current T2K ν_e appearance analysis, 23% of the background at Super-Kamiokande is from neutral current interactions that produce one π^0 in the final state (NC $1\pi^0$). This study uses ND280 Run 2 data totalling 7.832×10^{19} POT and selects neutrino-induced NC $1\pi^0$ interactions in FGD1 and FGD2 where both π^0 decay photons convert in the barrel and downstream ECAL.

Overall, neglecting photon reconstruction efficiency, an efficiency of 22% and purity of 16% is obtained. For the case where both π^0 decay photons convert in the downstream (barrel) ECAL an efficiency of 33% (12%) and purity of 43% (9%) is achieved. When one photon converts in the barrel ECAL and the other in the downstream ECAL the efficiency (purity) is 29% (16%).

Systematic uncertainties arising from cross-section model parameters and final state interactions, the neutrino flux prediction and the shape discrepancy between ECAL variables in data and MC are evaluated. The predicted total number of events when both photons convert in the downstream and barrel ECAL is 7.1 ± 2.3 (syst) ± 0.5 (stat) and 31.6 ± 8.9 (syst) ± 1.2 (stat), respectively. Whereas when one decay photon is reconstructed in the barrel ECAL and the other in the downstream ECAL the expected number of events is 38.1 ± 8.7 (syst) ± 1.3 (stat). The selected number of events in data is 5, 22 and 31, respectively, which agrees with the prediction within errors.

The calibration of the time offsets for the barrel and downstream ECAL is also presented in this thesis. The application of this calibration reduces the timing resolution from 9 ns to approximately 2.5 ns, for high charge hits.

Declaration

This thesis is the result of my own work, except where explicit reference is made to the work of others.

Chapter 2 introduces neutrino physics and discusses the motivation for studying NC $1\pi^0$ interactions. This chapter is an amalgamation of a large number of published articles that are appropriately referenced.

A brief summary of the T2K experiment can be found in Chapter 3. The sources used for this chapter are predominantly those published by the T2K collaboration and a referenced where necessary.

Chapter 4 describes the offline ND280 software. The tracker and global reconstruction algorithms are the work of many T2K collaborators. Additionally, the ECAL calibration and reconstruction algorithms are the combined work of many members of the T2KUK group. The ECAL performance plots were made by the author.

The calibration of the barrel and downstream ECAL time offsets presented in Chapter 5 is the sole work of the author. It should be noted that, as a result of regular updates presented to the ND280 calibration group, the study benefited from the knowledge and expertise of other T2K collaborators. Furthermore, the simple track fitting reconstruction algorithm used in the study was developed by the T2KUK group.

Chapter 6 presents a study of NC $1\pi^0$ interactions in the T2K near detector ND280. The selection was developed by the author, but uses the TMVA package in ROOT and reconstructed quantities developed by other T2K collaborators. The systematic uncertainties associated with this measurement were able to be considered as a result of the hard work of the Neutrino Interactions Working Group and the T2K Beam Group and are referenced were possible.

The final chapter of this thesis, Chapter 7, provides a conclusion of the thesis as a whole.

The copyright of this thesis rests with the author and is made available under a Creative Commons Attribution Non-Commercial No Derivatives licence. Researchers are free to copy, distribute or transmit the thesis on the condition that they attribute it, that they do not use it for commercial purposes and that they do not alter, transform or build upon it. For any reuse or redistribution, researchers must make clear to others the licence terms of this work

Samantha Short

Acknowledgements

I would like to begin by expressing my gratitude to my supervisor Dr. Morgan Wascko for his support, guidance and encouragement throughout my PhD. I am especially grateful for the detailed and helpful feedback I received prior to submitting my thesis, in addition to being taught how to use semicolons!

I would also like to thank the staff at Imperial: Dr. Yoshi Uchida for his useful comments and feedback during weekly group meetings; Dr. Asher Kaboth for the extremely beneficial physics and coding discussions in the office and Dr. Per Jonsson for all his expert advice.

I wish to also acknowledge the ND280 π^0 working group, in addition to other T2K collaborators: Dr. Jon Perkin for all his help with the π^0 analysis tools package; Dr. Phill Litchfield for answering any and all of my calibration questions and Dr. Helen O'Keeffe for being my Northern partner in crime.

I could not have asked for better Imperial and T2KUK students to work, and in Japan live, with. The atmosphere in the T2K office was the perfect balance of distraction and physics; it was a really great place to work. Solving coding issues would have taken a significant amount of time longer were it not for the help of T2K students Jim Dobson, Mark Scott and Ben Smith. Additionally, I would have found understanding NEUT and neutrino interactions in general a lot more difficult were it not for Peter Sinclair. I would also like to thank Sarah Ives and, my coffee buddy, Nick Wardle for keeping me sane. I have fond memories of both the physics and non-physics chats we had during numerous breaks.

Finally, I would like to thank my family and friends for their continued support and encouragement. I would not have successfully completed my PhD were it not for some of the best people in the world: Anne Lawler, Olie Dearie and Tom Wyss. I am eternally grateful to Anne and Olie for letting me live with them upon my abrupt return from Japan and specifically to Anne for proofreading every single page of this thesis, despite having no interest in physics whatsoever! Tom, without your unwavering support and belief I would never have been able to complete my PhD and for that I am truly thankful.

Contents

Glossary	15
List of Figures	19
List of Tables	25
1. Introduction	27
2. Motivation	29
2.1. A brief history of neutrino physics	29
2.2. Neutrino physics at T2K	30
2.3. Current state of neutrino physics	32
2.4. Neutrino-nucleon interactions at T2K	36
2.5. Neutrino-induced NC $1\pi^0$ interactions	37
2.5.1. Production mechanisms	39
2.5.2. Current and future measurements	39
3. The T2K experiment	43
3.1. Physics goals and current status	44
3.2. Accelerator and off-axis neutrino beam	46
3.2.1. Off-axis neutrino beam	46
3.2.2. J-PARC accelerator	46
3.2.3. Neutrino beamline	47
3.2.4. Neutrino flux prediction	50
3.3. The T2K near detector suite	51
3.3.1. Scintillator-based readout	51
3.3.2. The on-axis INGRID detector	53
3.3.3. The off-axis ND280 detector	54
3.4. The T2K far detector Super-Kamiokande	64

4. ND280 offline software	67
4.1. General overview	67
4.2. ECAL geometries	68
4.3. Calibration	69
4.4. Tracker and global reconstruction	70
4.5. ECAL reconstruction and performance	76
4.5.1. Hits and clustering	76
4.5.2. Photon reconstruction efficiency	78
4.5.3. Energy estimation	78
4.5.4. Particle identification	83
4.5.5. Direction reconstruction	84
5. Calibration of the barrel and downstream ECAL time offsets	87
5.1. Data samples	87
5.2. Method for calculating TFB offsets	89
5.3. Method for calculating RMM offsets	93
5.4. Method validation	94
5.5. Offset stability over time	95
5.6. Timing resolution	96
5.7. Impact of improved timing	104
6. Selecting NC $1\pi^0$ interactions in the FGD	107
6.1. Signal definition	107
6.2. Data and Monte Carlo samples	111
6.3. ECAL preselection and vetoes	113
6.4. Selecting proton-like tracks	116
6.4.1. TPC particle identification	117
6.4.2. FGD particle identification	119
6.4.3. ECAL particle identification	123
6.4.4. Effectiveness of proton cuts	123
6.5. Using the ECAL to select photons	125
6.5.1. ECAL variables used in TMVA	127
6.5.2. Pre-TMVA cuts made to ECAL variables	129
6.5.3. Distribution of ECAL variables used in TMVA	131
6.5.4. TMVA response	131

6.6. Determining an interaction vertex	141
6.6.1. Reconstructed tracks in the TPC and FGD	141
6.6.2. Unused FGD hits not associated with a reconstructed tracker object	141
6.6.3. Information from ECAL clusters only	142
6.6.4. Performance of vertexing methods	142
6.7. Efficiency and purity for selecting NC $1\pi^0$ interactions	143
6.8. Systematic uncertainties	149
6.8.1. Cross-section model parameter systematic errors	149
6.8.2. Cross-section final state interaction systematic errors	157
6.8.3. Neutrino flux prediction systematic errors	162
6.8.4. Multi-variate analysis systematic errors	168
6.8.5. Combined systematic error	170
6.8.6. Discussion of detector systematics	174
6.9. Summary	176
7. Conclusions	177
Bibliography	181
A. Supplementary information for NC $1\pi^0$ selection	189
B. Supplementary information for the analysis of systematic uncertainties	223

Glossary

BLM beam loss monitor. 48

BrECAL barrel ECAL; six ECAL modules surrounding the TPCs and FGDs. 60

Category one two isolated reconstructed clusters in the downstream ECAL. 127

Category two two isolated reconstructed clusters in the barrel ECAL. 127

Category three one isolated reconstructed cluster in the downstream ECAL and one in the barrel ECAL. 127

Cherry picked MC a stripped down version of the magnet MC; events are “cherry picked” to contain only one NC $1\pi^0$ neutrino interaction per spill. This MC sample is used only to train the multi-variate analysis and evaluate the performance of the vertexing methods. 113

CT current transformer; monitors the intensity of the proton beam. 48

CTM cosmic trigger module; used when deciding if there was a cosmic event in the ND280 detector. There are two CTMs: one takes signals from Trip-t based detectors and the other is connected to the FGDs. 64

DsECAL downstream ECAL; one ECAL module acting as an ND280 endcap. 60

ECAL (sampling) electromagnetic calorimeter; active layers of plastic scintillator bars and lead sheets surrounding the P0D, TPCs and FGDs providing almost hermetic coverage for particles exiting the inner detector. 59

ESM electrostatic monitor; monitors the proton beam position. 48

FGD fine grained detector. The ND280 detector contains two FGDs: FGD1 and FGD2. The FGDs provide the target mass (1.1 tons) for neutrino interactions and also have tracking capabilities. 59

INGRID Interactive Neutrino GRID; on-axis neutrino detector, located 280 m from the target, used to measure the on-axis neutrino beam profile. 53

J-PARC Japan Proton Accelerator Research Complex; a facility located in Tokai, on the east coast of Japan. 43

JNUBEAM the simulation package used predict kinematic information for particles emerging from the target. 50

LINAC linear accelerator; designed to accelerate an H^- beam to an energy of 400 MeV. 46

Magnet MC Monte Carlo simulating neutrino-induced interactions over the whole ND280 geometry, including the UA1 magnet, produced using the NEUT neutrino interaction generator. 113

MCM master clock module; receives signals from the accelerator and GPS-based clock and sends signals to SCMs. 63

MEU MIP equivalent units; the most probable value of charge deposited by a minimum-ionising particle (MIP), where 1 MEU is approximately 25 PEU. 76

MPPC multi-pixel photon counter; a photosensor composed of an array of independent avalanche photodiodes operated in Geiger mode. 52

MR main ring synchrotron; receives the proton beam from the RCS and accelerates the protons to 30 GeV every 2 – 3 seconds. 46

MUMON muon monitor; measures the profile of muons with momenta greater than 5 GeV. 50

NA61/SHINE an experiment providing hadron production measurements spanning the whole kinematic region of interest for T2K. 50

ND280 off-axis neutrino detector located 280 m from the target; used to characterise the beam before oscillations occur and make neutrino cross-section measurements.

54

OTR optical transition radiation monitor; monitors proton beam profile. 49

p.e. unit photon equivalent unit; obtained by converting the charge from each MPPC into a number of photons incident on the MPPC, taking into account the likelihood of more than one photon impinging on the same pixel. 174

P0D π^0 detector; designed and built to measure neutral current processes on a water target. 55

P0DECAL P0D ECAL; six ECAL modules surrounding the P0D. 60

PEU pixel-equivalent units; obtained by converting the charge from each MPPC into a number of pixels fired. Not to be confused with the photon equivalent (p.e.) unit, which takes into account the likelihood of more than one photon impinging on the same pixel. 76

PMT photomultiplier tube; used in the Super-Kamiokande detector. 64

POT protons on target. 44

RCS rapid-cycling synchrotron; converts the H^- beam from the LINAC into a proton beam that is then accelerated to 3 GeV with a cycle frequency of 25 Hz. 46

RMM readout merger module; controls TFBs by distributing clock and trigger signals. There is one RMM per ECAL module. 63

RMM offset the time offset arising as a result of the differing cable lengths between the MCM and RMMs. 87

Sand MC Monte Carlo simulating neutrino-induced interactions in the sand and cavern walls surrounding the ND280 detector, produced using the NEUT neutrino interaction generator. 113

SCM slave clock module; connected to both the MCM and individual subdetector RMMs. There is one SCM per ND280 subdetector, allowing independent electronics configuration and operation. 64

SK Super-Kamiokande; the cylindrical water Cherenkov T2K far detector located 295 km west of the T2K near detector suite. 64

SMRD side muon range detector; system of 440 scintillator modules inserted into the innermost air gaps between steel plates in the magnet yoke elements and performs a number of functions: measures the momentum of muons escaping the ND280; cosmic ray trigger and can be used to veto neutrino-induced interactions in the cavern walls and magnet. 62

SSEM segmented secondary emission monitor; monitors the proton beam profile. 48

T2K Tokai to Kamioka; a long baseline neutrino oscillation experiment. 43

TFB Trip-t front end board; houses four Trip-t chips, each of which can be connected to up to 16 MPPCs. 63

TFB offset the time offset arising as a result of differing cable lengths between each RMM and the TFBs connected. 87

TPC time projection chamber. The ND280 detector houses three TPCs (TPC1, TPC2 and TPC3) containing an argon-based drift gas. The TPCs are used to track charged particles emerging from the FGDs; make momentum measurements and, using energy loss measurements, distinguish between different particle species. 57

WLS fibre wavelength shifting fibre; used in scintillator bars to increase the wavelength of scintillation light (blue) to an optimum wavelength for the MPPC (green). 52

List of Figures

2.1. Allowed and excluded regions of the neutrino oscillation parameters Δm^2 and θ	33
2.2. Latest T2K ν_μ disappearance results for θ_{23} and Δm^2_{32}	34
2.3. Inverted and normal neutrino mass hierarchies	36
2.4. Charged current neutrino cross-sections as a function of neutrino energy in GeV	38
2.5. Feynman diagrams for NC $1\pi^0$ interactions	40
2.6. NC $1\pi^0$ cross-section measurements	42
3.1. Schematic of the T2K experiment	43
3.2. Delivered number of protons on target at T2K	45
3.3. Latest T2K ν_e appearance results for θ_{13}	45
3.4. Muon neutrino survival probability at 295 km and neutrino fluxes for different off-axis angles	47
3.5. Overview of the T2K neutrino beamline and the side view of the secondary beamline	48
3.6. ND280 near detector complex	52
3.7. Magnified face view and ceramic package of an MPPC	52
3.8. Schematic of the INGRID on-axis detector	54
3.9. Exploded view of the ND280 off-axis detector	55
3.10. Schematic of the π^0 subdetector in ND280	56

3.11. Simplified cut-away drawing of a TPC in ND280	58
3.12. External view of an ECAL module	60
3.13. View of SMRD scintillator counter components prior to assembly	62
3.14. General layout of the ND280 electronics	63
3.15. Super-Kamiokande detector schematic	65
3.16. Reconstructed muon- and electron-like interactions at SK	66
4.1. Schematic of the ND280 software suite	68
4.2. ECAL local and global geometry	69
4.3. Event display showing a globally reconstructed track	72
4.4. Particle energy loss as a function of momentum in the TPC	74
4.5. Particle energy loss as a function of track range in the FGD	75
4.6. True energy and ECAL entry angle for photons in NC $1\pi^0$ interactions .	79
4.7. Photon reconstruction efficiency as a function of true energy and ECAL entry angle	80
4.8. ECAL photon reconstruction efficiency as a function of opening angle between photons	81
4.9. Comparison of true and reconstructed energy in the ECAL	82
4.10. Comparison of true and reconstructed angle in the ECAL	86
5.1. Illustration of Prim's algorithm	91
5.2. Time difference between hits on different TFBs	92
5.3. Hit time distribution for an RMM after the application of TFB offsets .	95
5.4. Mean TFB time before and after TFB and RMM offsets are applied . . .	96
5.5. Residual ECAL TFB offsets for the 6000 ND280 data runs	97
5.6. Residual ECAL TFB offsets for the 7000 ND280 data runs	98

5.7. Time difference between the highest charge hit and all other hits in an ECAL track	99
5.8. Timing resolution for one ND280 data run	100
5.9. Timing resolution before time offsets are applied as a function of charge and ND280 run number	102
5.10. Timing resolution after time offsets are applied as a function of charge and ND280 run number	103
5.11. Time difference between ECAL clusters with and without TFB and RMM offsets applied	104
5.12. Purity for selecting NC $1\pi^0$ interactions with varying timing cuts between ECAL clusters	106
6.1. Photon subdetector conversion location	108
6.2. True π^0 momentum and angle for NC $1\pi^0$ interactions in the FGD	109
6.3. Flowchart outlining selection of NC $1\pi^0$ interactions	110
6.4. Event display showing golden signal interactions	112
6.5. Run 2 data and Monte Carlo bunch timing structure	114
6.6. Time difference between ECAL clusters in a π^0 candidate	115
6.7. TPC pull distributions	118
6.8. Proton selection efficiency and purity curves for TPC pulls	120
6.9. FGD pull distributions	121
6.10. Proton selection efficiency and purity curves for FGD pulls	122
6.11. ECAL PID variable distribution and efficiency and purity curves	124
6.12. Signal and background distributions for category two TMVA input variables after pre-TMVA cuts	132
6.13. Area normalised data and MC distributions for category two TMVA input variables after pre-TMVA cuts	135

6.14. Correlation matrices for TMVA input variables	138
6.15. Transformed likelihood response from TMVA	139
6.16. Significance of different cut values of the transformed likelihood	140
6.17. Difference between true and reconstructed interaction vertex position . .	144
6.18. Final π^0 invariant mass distribution	147
6.19. Input and Cholesky decomposed cross-section parameter covariance matrix	151
6.20. Invariant mass distribution with and without cross-section parameter errors	155
6.21. Covariance and correlation matrices for application of cross-section pa- rameter errors (category one)	156
6.22. Probability of final state interactions as a function of momentum	158
6.23. Invariant mass with and without FSI errors (category one)	160
6.24. Covariance and correlation matrices for application of cross-section FSI errors (category one)	161
6.25. Fractional neutrino flux error for muon neutrinos at ND280	165
6.26. Input and Cholesky decomposed flux covariance matrix	166
6.27. Covariance and correlation matrices for application of flux uncertainties (category one)	167
6.28. Shifted and nominal MC transformed likelihood response	168
6.29. χ^2 comparison of data and MC for the transformed likelihood response .	169
6.30. Effect of the TMVA shape systematic for category one	170
6.31. Covariance and correlation matrices for application of TMVA shape dis- crepancy error (category two)	171
6.32. Total fractional covariance matrix	172
A.1. Signal and background distributions for category one TMVA input vari- ables before pre-TMVA cuts	190

A.2. Signal and background distributions for category two TMVA input variables before pre-TMVA cuts	193
A.3. Signal and background distributions for category three TMVA input variables before pre-TMVA cuts	196
A.4. Signal and background distributions for category one TMVA input variables after pre-TMVA cuts	199
A.5. Signal and background distributions for category three TMVA input variables after pre-TMVA cuts	202
A.6. Area normalised data and MC distributions for category one TMVA input variables after pre-TMVA cuts	205
A.7. Area normalised data and MC distributions for category three TMVA input variables after pre-TMVA cuts	208
A.8. POT normalised data and MC distributions for category one TMVA input variables after pre-TMVA cuts	211
A.9. POT normalised data and MC distributions for category two TMVA input variables after pre-TMVA cuts	214
A.10. POT normalised data and MC distributions for category three TMVA input variables after pre-TMVA cuts	217
B.1. Covariance and correlation matrices for application of cross-section model parameter errors (categories two and three)	224
B.2. Invariant mass with and without FSI errors (categories two and three) . .	225
B.3. Covariance and correlation matrices for application of FSI errors (categories two and three)	226
B.4. Covariance and correlation matrices for application of flux errors (categories two and three)	227
B.5. Effect of TMVA shape systematic (categories one and three)	228
B.6. Covariance and correlation matrices for application of TMVA shape discrepancy error (categories two and three)	228

List of Tables

2.1. The current best fit values and 3σ allowed ranges for the three neutrino oscillation parameters	32
2.2. Typical neutrino interactions at T2K	38
5.1. Location and number of TFBs connected to each ECAL RMM	89
5.2. Cosmic trigger masks used when calculating RMM offsets	93
6.1. Global coordinates of the FGD fiducial volume	111
6.2. Percentage of isolated ECAL objects per bunch	114
6.3. True particle associated with reconstructed tracks in the tracker	116
6.4. PID information available for reconstructed tracks originating from the tracker	117
6.5. Proton selection efficiency and purity for TPC pulls	119
6.6. Proton selection efficiency and purity for FGD pulls	123
6.7. Selection efficiency and purity after proton-like cut	125
6.8. ECAL variables used in TMVA	128
6.9. Cuts made to ECAL variables prior to using TMVA	130
6.10. Optimum TMVA cut values	134
6.11. Information available to reconstruct the neutrino interaction vertex	141
6.12. Final selection efficiency and purity for category one	145

6.13. Final selection efficiency and purity for category two	146
6.14. Final selection efficiency and purity for category three	146
6.15. Official T2K NEUT cross-section parameters and errors	150
6.16. Official T2K NEUT final state interaction parameters and errors	159
6.17. Systematic errors to account for the data and MC shape discrepancy . . .	169
A.1. Breakdown of backgrounds by interaction type for ECAL cluster position category one.	220
A.2. Breakdown of backgrounds by interaction type for ECAL cluster position category two.	221
A.3. Breakdown of backgrounds by interaction type for ECAL cluster position category three.	222

Chapter 1.

Introduction

This thesis presents a study of neutrino-induced neutral current interactions that produce one π^0 in the final state (NC $1\pi^0$) in the T2K off-axis near detector ND280. The selection focuses on interactions occurring in FGD1 and FGD2, which collectively contain both carbon and water targets, where both photons from the π^0 decay convert in the barrel or downstream ECAL.

Chapter 2 presents a brief history of neutrino physics, outlines the method used to obtain the neutrino oscillation probability formula for T2K and the current state of neutrino physics with regards to recent results and remaining unanswered questions. Next, the motivation for studying NC $1\pi^0$ interactions is discussed with an emphasis on current and future cross-section measurements and the backgrounds to the T2K ν_e appearance analysis.

Chapter 3 is a brief summary of the T2K experiment including the physics goals and current status. Information on the T2K accelerator, neutrino beamline and neutrino flux prediction is presented, in addition to detailed information on the T2K near detector suite. The ND280 ECAL is discussed in more detail, as it is used extensively in the analysis presented. Finally, the T2K far detector Super-Kamiokande is discussed.

The software used to reconstruct neutrino-induced interactions in the ND280 detector is detailed in Chapter 4. The calibration applied to data collected by the ECAL is briefly presented, followed by a discussion of the tracker and global reconstruction algorithms. Furthermore, the particle identification techniques used on FGD and TPC tracks is reviewed. Finally, the ECAL reconstruction algorithms are presented and the performance of the ECAL to reconstruct photons from NC $1\pi^0$ interactions in the FGD is shown.

Chapter 5 details work conducted by the author to calibrate the barrel and downstream ECAL time offsets. The algorithms used to calculate the size of the offsets are discussed in addition to the timing resolution of the ECAL before and after the offsets were applied.

A thorough definition of the NC $1\pi^0$ signal can be found in Chapter 6. This chapter also describes the ND280 data and Monte Carlo used in the study, as well as giving a step-by-step account of the selection cuts made and the motivation behind them. The selection uses a likelihood estimator to select photons in the ECAL, in addition to using particle identification variables to ensure the event is neutral current. After all selection cuts are made, the π^0 invariant mass distribution is plotted for both data and Monte Carlo and the final efficiency and purity for selecting NC $1\pi^0$ interactions is presented. Furthermore, the systematic uncertainties associated with this measurement are presented in the form of covariance matrices. The sources of uncertainty considered are cross-section model parameter and final state interaction errors; neutrino flux prediction errors and an estimate of the systematic uncertainty associated with the multi-variate analysis resulting from the shape discrepancy between data and MC.

The final chapter of this thesis, Chapter 7, provides a conclusion of the thesis as a whole.

Chapter 2.

Motivation

This chapter discusses the importance of studying neutrino-induced neutral current interactions that produce one π^0 in the final nuclear state. First a brief history of neutrino physics is presented, followed by an outline of the method used to obtain the neutrino oscillation formula applicable to T2K. Section 2.3 discusses the current state of neutrino physics, including the most recent results and remaining unanswered questions. The types of neutrino-nucleon interactions observed at T2K are briefly mentioned in Section 2.4 before focussing on NC $1\pi^0$ interactions in Section 2.5. The importance of studying the NC $1\pi^0$ channel is discussed and the current absolute and ratio cross-section measurements are presented.

2.1. A brief history of neutrino physics

In 1998, forty one years after Bruno Pontecorvo postulated neutrino oscillations [1], the Super-Kamiokande (SK) collaboration announced the first unambiguous and statistically significant evidence in support of the theory [2]. The SK data showed that the deficit in the flux of atmospheric muon neutrinos, when compared with expectations, was dependent on the neutrino path length (baseline), L , and energy, E .

This issue of oscillating neutrinos had been prominent throughout the previous two decades in solar neutrino experiments. In 1967, Raymond Davis created the first solar neutrino detector and found there was a deficit in the solar neutrino flux [3]. In 2002, the Sudbury Neutrino Observatory (SNO) collaboration published strong evidence for the flavour transformation of electron neutrinos into muon and tau neutrinos [4]. With the efforts of many other groups, such as Homestake [5], GALLEX [6], SAGE [7],

Kamiokande [8] and SK [9], SNO were able to confirm the Mikheyev Smirnov Wolfenstein (MSW) effect [10], an effect that enhances the neutrino oscillation in the presence of large matter densities in the sun, whilst providing a solution to the problem of the solar neutrino deficit.

In January 2003, The KamLAND (Kamioka Liquid-scintillator AntiNeutrino Detector) experiment demonstrated reactor $\bar{\nu}_e$ disappearance at long baselines (typically 180 km) with a high confidence of 99.95% for the first time [11]. Then, in 2004, they obtained data which supported the conclusion that the observation of reactor $\bar{\nu}_e$ disappearance was due to neutrino oscillation [12].

This evidence for neutrino oscillations and hence, non-zero neutrino mass, is an extension to the current standard model of particle physics.

2.2. Neutrino physics at T2K

Neutrinos interact via charged current (CC) and neutral current (NC) weak interactions and are therefore weak, or flavour, eigenstates ν_α , where α corresponds to the flavour of the neutrino e, μ, τ . These flavour eigenstates are a linear combination of mass eigenstates ν_i , where $i = 1, 2, 3$, and are related by a unitary transformation $U_{\alpha i}$, given by

$$| \nu_\alpha \rangle = U_{\alpha i} | \nu_i \rangle, \quad (2.1)$$

where $U_{\alpha i}$ is the Pontecorvo-Maki-Nakagawa-Sakata (PMNS) matrix,

$$U_{\alpha i} \equiv \begin{pmatrix} 1 & 0 & 0 \\ 0 & c_{23} & s_{23} \\ 0 & -s_{23} & c_{23} \end{pmatrix} \begin{pmatrix} c_{13} & 0 & -s_{13}e^{i\delta} \\ 0 & 1 & 0 \\ s_{13}e^{-i\delta} & 0 & c_{13} \end{pmatrix} \begin{pmatrix} c_{12} & s_{12} & 0 \\ -s_{12} & c_{12} & 0 \\ 0 & 0 & 1 \end{pmatrix}, \quad (2.2)$$

with $c_{ij} = \cos \theta_{ij}$, $s_{ij} = \sin \theta_{ij}$ and δ is a CP violating phase. The angles θ_{12} , θ_{23} and θ_{13} are often referred to as the solar, atmospheric and reactor/accelerator parameters, respectively. The particular parametrisation of the PMNS matrix in Equation 2.2 is

useful as it clearly shows the contribution from atmospheric, reactor/accelerator and solar experiments.

In 1957, when Bruno Pontecorvo first postulated neutrino oscillations he considered them to be a two-level quantum mechanical system described by a simple time evolution equation. If the system is prepared in one of the eigenstates of the Hamiltonian (a mass eigenstate) it will remain in this state and no oscillations will occur. However, if the system is not in an eigenstate of the Hamiltonian (such as a flavour eigenstate) the probability to find the system in a given state will oscillate with time.

Consider a flavour eigenstate produced at a time $t = 0$ given by $|\nu(0)\rangle = |\nu_\alpha\rangle = U_{\alpha i} |\nu_i\rangle$. After a time t the neutrino will be in the state

$$|\nu(t)\rangle = e^{-iE_i t} U_{\alpha i} |\nu_i\rangle, \quad (2.3)$$

where $e^{-iE_i t}$ is the phase factor which describes the neutrino mass eigenstate as it propagates in time. As the neutrino travels it develops a relative phase with frequency given by $E_2 - E_1$ where $E_{1,2}$ denotes the eigenenergies of the system. This is a direct result from the fact that the mass eigenstates have a non-zero mass difference.

The oscillation probability for the neutrinos can be obtained using

$$P(\nu_\alpha \rightarrow \nu_\beta; t) = |\langle \nu_\beta | \nu(t) \rangle|^2 = |U_{\beta i} e^{-iE_i t} U_{\alpha i}^*|^2, \quad (2.4)$$

which yields

$$P(\nu_\mu \rightarrow \nu_\mu) \simeq 1 - \cos^4 \theta_{13} \sin^2 2\theta_{23} \sin^2 \left[1.27 \frac{\Delta m_{32}^2 L}{E} \right], \quad (2.5)$$

$$P(\nu_\mu \rightarrow \nu_e) \simeq \sin^2 2\theta_{13} \sin^2 \theta_{23} \sin^2 \left[1.27 \frac{\Delta m_{13}^2 L}{E} \right], \quad (2.6)$$

where E is the neutrino energy in GeV, L is the baseline in km and Δm_{ij}^2 is the mass squared difference $m_i^2 - m_j^2$ in eV². Equations 2.5 and 2.6 describe the muon neutrino survival probability and the probability of a muon neutrino oscillating into an electron neutrino, respectively, neglecting matter effects for the T2K experiment. The oscillation amplitude for Equation 2.6 is proportional to $\sin^2 2\theta_{13}$ and hence a measurement of this

Parameter	Best fit $\pm 1\sigma$	3σ
$\Delta m_{21}^2 [\times 10^{-5} \text{ eV}^2]$	$7.58^{+0.22}_{-0.26}$	$6.99 - 8.18$
$ \Delta m_{31}^2 [\times 10^{-3} \text{ eV}^2]$	$2.35^{+0.12}_{-0.09}$	$2.06 - 2.67$
$\sin^2 \theta_{12}$	$0.312^{+0.018}_{-0.015}$	$0.265 - 0.364$
$\sin^2 \theta_{23}$	$0.42^{+0.08}_{-0.03}$	$0.34 - 0.64$
$\sin^2 \theta_{13}$	$0.025^{+0.007}_{-0.008}$	$0.005 - 0.050$
$\sin^2 \theta_{13}$	$0.0251^{+0.0034}_{-0.0034}$	$0.015 - 0.036$

Table 2.1.: The current best fit values and 3σ allowed ranges for the three neutrino oscillation parameters. The first set of results is from global analyses of existing neutrino oscillation data [17] including T2K [14] and MINOS [18], but excluding the Daya Bay and RENO results. Thus, the second/lower section of the table is a PDG average of the results from Daya Bay [15], RENO [16] and Double CHOOZ [19]. Table taken from [20].

channel will lead to a direct measurement of θ_{13} , provided θ_{23} , Δm_{12}^2 and Δm_{32}^2 are known.

2.3. Current state of neutrino physics

The current best fit values and allowed regions for neutrino oscillation parameters can be found in Table 2.1 and Figure 2.1, respectively. Solar neutrino experiments and KamLAND are responsible for the excellent measurements of θ_{12} and Δm_{21}^2 . Initially, experiments such as Super-Kamiokande and MINOS constrained the angle θ_{23} and the magnitude of the mass squared difference Δm_{32}^2 . However, a recent result from T2K, which is not displayed in Figure 2.1, further reduces the uncertainty associated with θ_{23} and is shown in Figure 2.2. When Figure 2.1 was produced, there was little knowledge of the size of the mixing angle θ_{13} and thus only the limit that $\sin^2 2\theta_{13} < 0.17$, set by the CHOOZ reactor $\bar{\nu}_e$ disappearance experiment [13], features. In June 2011, the T2K experiment reported an indication that θ_{13} was non-zero [14]; this was later confirmed by reactor neutrino experiments Daya Bay (5.2σ) [15] and RENO (4.9σ) [16], making θ_{13} the best measured mixing angle. Nevertheless, there still remain unanswered questions in neutrino physics.

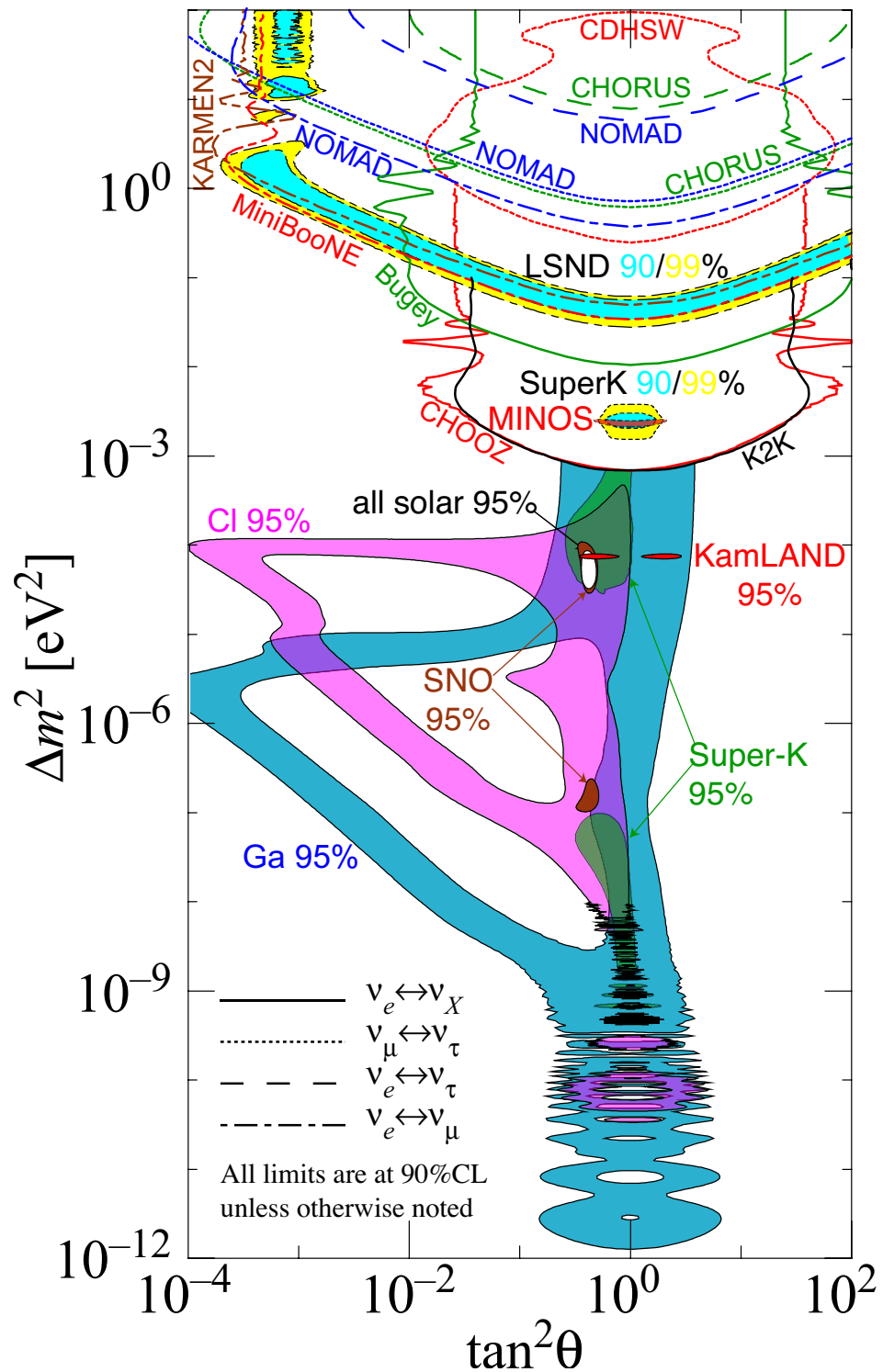


Figure 2.1.: Allowed and excluded regions of the neutrino oscillation parameters Δm^2 and θ . Allowed parameter spaces are block colour, whereas the lines represent limits. Results are from various experiments and are based on two flavour neutrino oscillation analyses. The recent θ_{13} results from T2K [14], Daya Bay [15] and RENO [16] are not included. Figure taken from [20, 21].

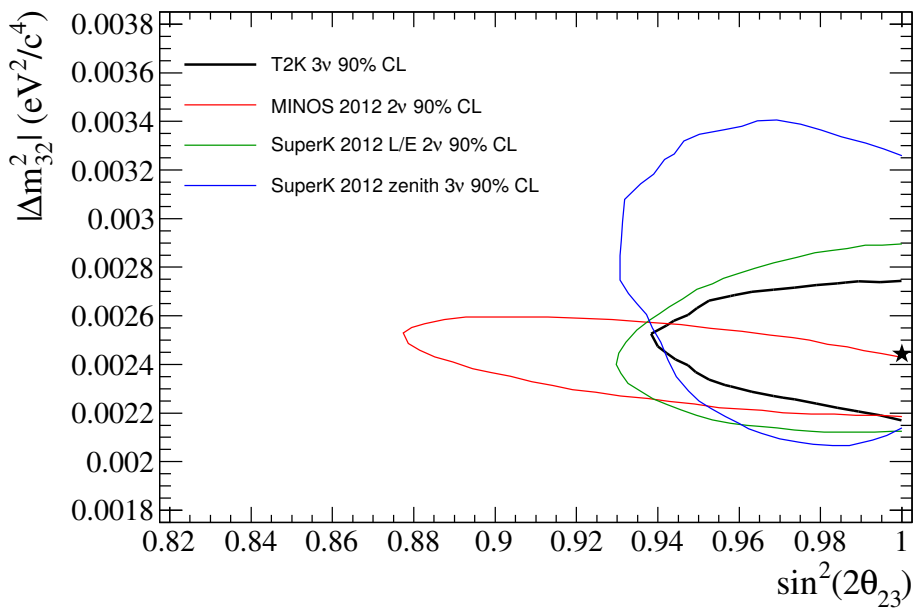


Figure 2.2.: Latest T2K ν_μ disappearance results for θ_{23} and Δm_{32}^2 . Comparison between 90% confidence level (CL) allowed regions from MINOS (from Neutrino 2012) and Super-Kamiokande atmospheric data (from Neutrino 2012), and the 90% CL region obtained using the T2K Run 1 + 2 + 3 dataset totalling 3.010×10^{20} POT [22] (paper in progress).

Experiments such as SNO+ [23] and SuperNEMO [24] will determine if neutrinos are Majorana ($\nu = \bar{\nu}$) or Dirac ($\nu \neq \bar{\nu}$) particles by looking for neutrinoless double beta decay ($0\nu\beta\beta$), a lepton number violating process that is only possible if neutrinos are Majorana particles¹,

The absolute mass of neutrinos is also unknown. Experiments such as KATRIN [26] will probe the electron neutrino mass to $m(\nu_e) = 0.2$ eV by measuring the distortion in the electron energy spectrum for beta decay, which corresponds to the presence of a neutrino with non-zero mass.

The discovery that θ_{13} is non-zero, in addition to the measurement of the other oscillation parameters, means that the next generation of neutrino oscillation experiments have moved one step closer to discovering CP violation in the lepton sector and determining the neutrino mass hierarchy. The normal hierarchy contains one large and two smaller masses i.e. $m_1 \approx m_2 \ll m_3$, where m_i corresponds to the mass eigenvalue of the neutrino, whereas the inverted hierarchy is given by $m_3 \ll m_1 \approx m_2$, as illustrated in Figure 2.3. The inverted hierarchy of neutrino masses is disfavoured by supernova 1987A [27], but laboratory results are yet to confirm this. Determining the sign of the neutrino mass squared difference $\Delta m_{32}^2 = m_3^2 - m_2^2$ will provide a solution to the hierarchy problem and can be done using long baseline experiments. The presence of matter has a cumulative effect on the neutrino oscillation probability; the greater the distance the neutrino travels in matter, the greater the effect the matter has on the probability of oscillation. The NO ν A experiment [28] has a baseline of 810 km and, as a result, the oscillation probability in matter can differ by up to 30% from that of the vacuum oscillation case. The T2K experiment has a shorter baseline of 295 km, meaning matter has only a 10% effect on the neutrino oscillation. If Δm_{32}^2 is positive (negative), the probability of oscillation for $\nu_\mu \rightarrow \nu_e$ is enhanced (decreases). Combining T2K and NO ν A data will increase the sensitivity to the sign of Δm_{32}^2 further and could also be used to confirm or refute the existence of a complex phase, δ , in the PMNS matrix, which makes CP violation in the lepton sector possible. However, the significance of the measurement is highly dependent on the amount of data collected when running in either neutrino or antineutrino mode.

In 1996, the LSND short baseline experiment saw evidence of neutrino oscillations of $\bar{\nu}_\mu \rightarrow \bar{\nu}_e$, indicating $\Delta m^2 \sim 1$ eV² [30]. This large value of Δm^2 suggests the existence of at least one sterile neutrino in addition to the three weakly interacting neutrinos

¹ See [25], or similar, for a brief theoretical description of neutrinoless double beta decay and details of experimental techniques.

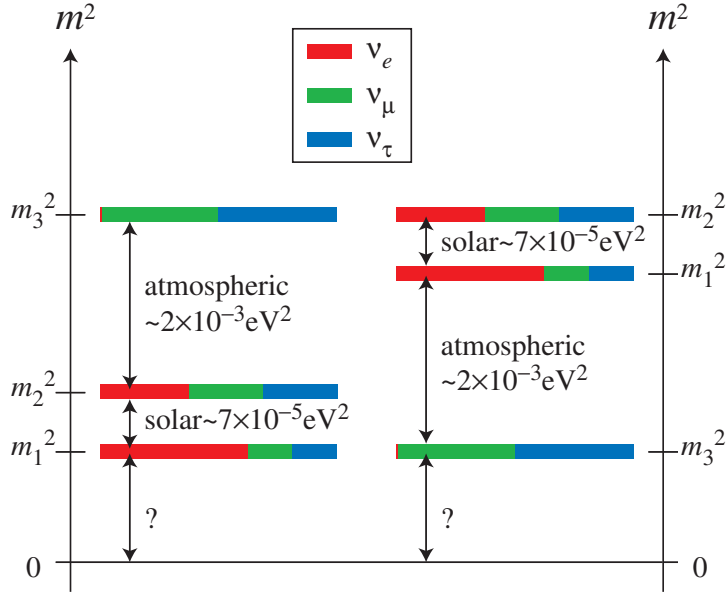


Figure 2.3.: The neutrino mass hierarchy on the left (right) is called the normal (inverted) hierarchy. The coloured bands represent the probability of finding a particular weak eigenstate ν_e , ν_μ and ν_τ in a particular mass eigenstate. The absolute scale of neutrino masses is not fixed by oscillation data and the lightest neutrino mass may vary from 0.0 eV – 0.3 eV. Figure and caption taken from [29].

ν_e , ν_μ and ν_τ . Thus, the MiniBooNE experiment [31] was commissioned to confirm or refute the existence of sterile neutrinos. To maximise the sensitivity to oscillations at $\Delta m^2 \sim 1 \text{ eV}^2$ MiniBooNE has $L[\text{m}]/E[\text{MeV}] \sim 1$, similar to that of LSND. In 2010, MiniBooNE announced an excess of $\bar{\nu}_e$ events in the energy range $475 \text{ MeV} < E_\nu < 1250 \text{ MeV}$, which is consistent with the allowed region for Δm^2 published by LSND at 1.5σ [32]. However, MiniBooNE has seen no indication of oscillation in the channel $\nu_\mu \rightarrow \nu_e$ for the same energy range, but does see an unexplained excess in electron-like events in the reconstructed neutrino energy range from 200 MeV to 475 MeV [33]. Results published in 2012 using combined data from MiniBooNE and SciBooNE further improves the ν_μ disappearance limit [34].

2.4. Neutrino-nucleon interactions at T2K

As the neutrino is a lepton with no electric charge, and thus only interacts via the weak force, details of the interaction must be inferred from the observable particles produced. Table 2.2 gives a summary of some neutrino interactions expected at T2K.

The cross-section for charged current interactions as a function of neutrino energy can be found in Figure 2.4. In the region of interest to T2K (the peak neutrino energy at T2K is 0.6 GeV) the cross-section is dominated by quasi-elastic interactions and those that produce a pion. At larger neutrino energies deep inelastic scattering (DIS) is the dominant neutrino-induced interaction.

In charged current quasi-elastic interactions the neutrino interacts with a neutron in the nucleus to produce a charged lepton and proton in the final state. Whereas for neutral current interactions, the neutrino interacts with a nucleon in the nucleus to produce a neutrino and a nucleon (with the same isospin as the original nucleon) in the final state.

There are two main mechanisms that produce a single pion in the final state at T2K. Resonant production is the dominant mechanism for single pion production in low energy neutrino interactions. The neutrino interacts with a nucleon in the nucleus producing a baryon resonance that decays to a nucleon and pion. In coherent pion production the neutrino interacts with, and transfers little energy to, the whole nucleus, as the neutrino scatters leaving the original nucleus intact and produces a distinctly forward-going pion. In both cases of pion production, if the vector boson transfers sufficient momentum, it is possible for more massive mesons (e.g. kaons) to be produced. However, the peak and average neutrino energy of the T2K beam means that such events will be rare.

At energies above a few GeV, such as those found in the high energy tail of the neutrino energy distribution at T2K, deep inelastic scattering (DIS) interactions are dominant. In DIS interactions the neutrino interacts with quarks, comprising the nucleon, transferring a large amount of momentum to the nucleus, which is enough to break it apart producing hadronic showers.

2.5. Neutrino-induced NC $1\pi^0$ interactions

For the current T2K ν_e appearance analysis, 23% of the background at Super-Kamiokande is from neutral current interactions that produce one π^0 in the final state (NC $1\pi^0$)². The π^0 has a mean lifetime of 8.52×10^{-17} s and decays to produce two photons, which are back to back in the π^0 rest frame, with a branching ratio of 98.9% [36]. If the opening

² The largest background, accounting for 53% of background events, is from the intrinsic ν_e contamination of the beam.

Neutrino process	Abbreviation	Interaction
Charged current quasi-elastic	CCQE	$\nu_\alpha + n \rightarrow \alpha^- + p$
Charged current single π^0	CC $1\pi^0$	$\nu_\alpha + n \rightarrow \alpha^- + p + \pi^0$
Charged current single π^+	CC $1\pi^+$	$\nu_\alpha + n \rightarrow \alpha^- + n + \pi^+$
Neutral current quasi-elastic	NCQE	$\nu_\alpha + n(p) \rightarrow \nu_\alpha + n(p)$
Neutral current single π^0	NC $1\pi^0$	$\nu_\alpha + n(p) \rightarrow \nu_\alpha + n(p) + \pi^0$
Neutral current single π^\pm	NC $1\pi^\pm$	$\nu_\alpha + n(p) \rightarrow \nu_\alpha + p(n) + \pi^-(\pi^+)$

Table 2.2.: Typical neutrino interactions at T2K where α corresponds to e , μ ; p and n correspond to protons and neutrons, respectively, and all other symbols have their usual meanings.

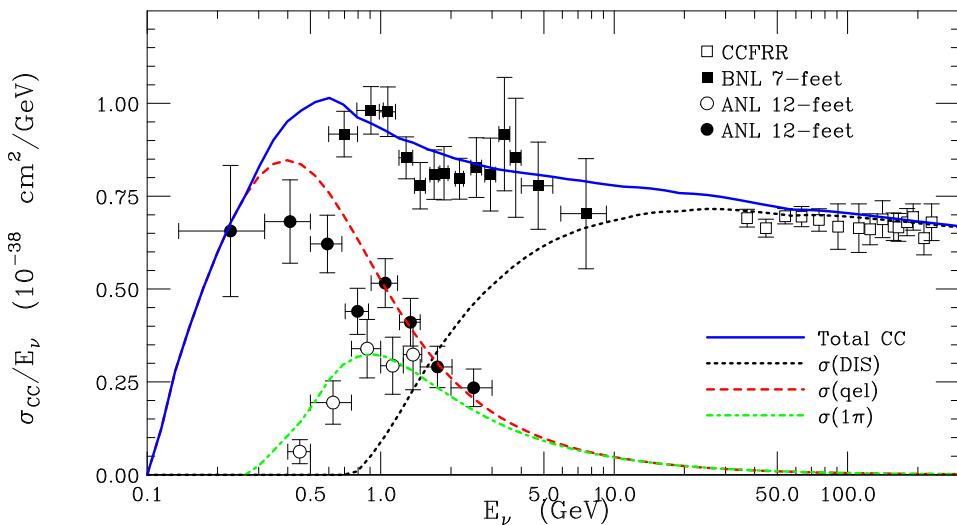


Figure 2.4.: Charged current neutrino cross-sections as a function of neutrino energy in GeV. Shown are the contributions from quasi-elastic (dashed), single pion (dot-dash) and deep inelastic scattering (dotted) processes. Figure and caption taken from [35].

angle, in the laboratory frame, between these two photons is small or if one photon is not reconstructed, the NC $1\pi^0$ interaction can mimic a ν_e interaction at Super-Kamiokande, as the Cherenkov ring produced by a photon is similar to that produced by an electron.

The T2K off-axis detector ND280 (see Section 3.3.3 for a description of this detector) receives a large flux of neutrinos, meaning high statistics cross-section measurements can be made. The P0D and ECAL subdetectors in the ND280 were designed to measure NC $1\pi^0$ interactions. The analysis performed using the P0D is complimentary to the study presented in this thesis and is documented in [37, 38]. This analysis proves that the ECAL can be used to select photons from neutrino-induced NC $1\pi^0$ interactions in FGD1 and FGD2 and is the first step toward a cross-section measurement.

There many reasons to study NC $1\pi^0$ interactions in the T2K near detector ND280. Measuring an absolute cross-section will improve Monte Carlo simulations and reduce the systematic error assigned to the cross-section in the ν_e appearance analysis (currently 43%). Additionally, by making a ratio measurement of NC $1\pi^0$ and CC inclusive interactions a comparison can be made with other experiments, whereas the ratio of NC $1\pi^0$ and CC 1π interactions is useful for model testing. Furthermore, the T2K flux and cross-section models can be constrained using the number of NC $1\pi^0$ interactions at the ND280 in conjunction with other channels (e.g. charged current inclusive, charged current single π^0). The best fit values of cross-section and flux parameters obtained as a result of a likelihood fit performed on ND280 data can then be used in the T2K oscillation analyses.

2.5.1. Production mechanisms

As mentioned in Section 2.4, there are two main production mechanisms for an NC $1\pi^0$ interaction at T2K: resonant and coherent. The resonant interaction involves the decay of a baryon resonance to a neutral pion and nucleon, whereas in the coherent interaction the neutrino interacts with the nucleus as a whole (coherently) and produces a forward going pion, as shown in the tree level Feynman diagrams in Figure 2.5.

2.5.2. Current and future measurements

Neutral current interactions are notoriously difficult to measure. In addition to the fact that the reconstructed neutrino vertex could be anywhere in the detector (c.f. a

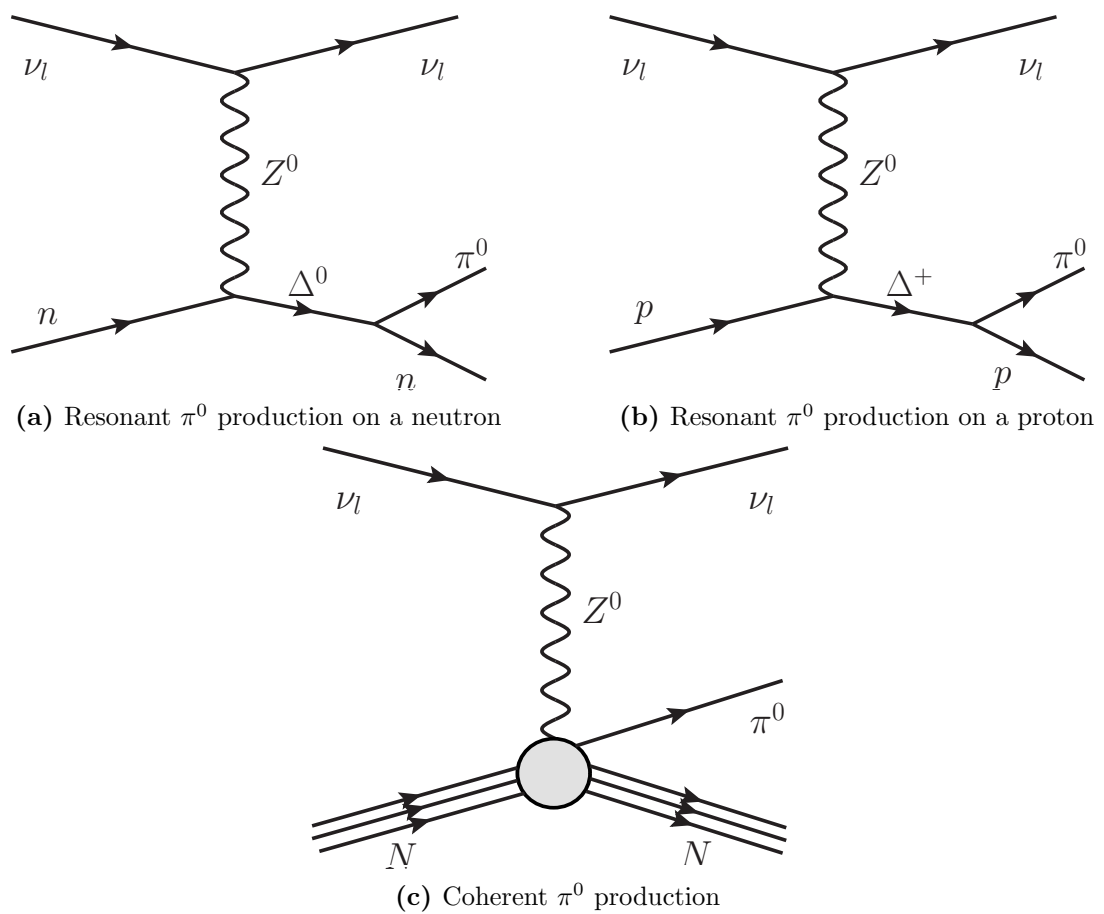
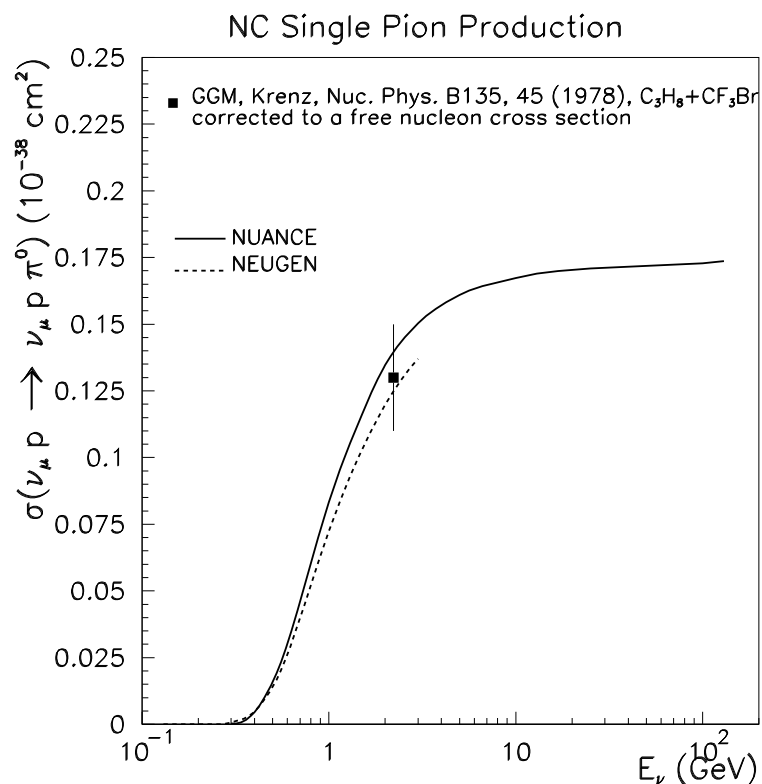
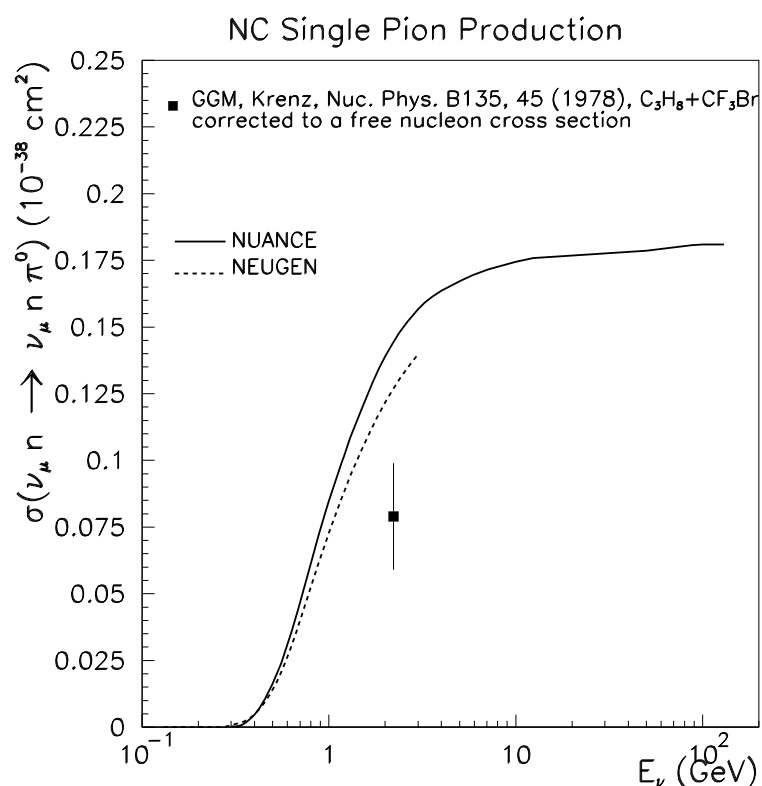


Figure 2.5.: Feynman diagrams for neutrino-induced NC $1\pi^0$ interactions. Made using Jaxo-Draw [39].

collider experiment where the approximate vertex position is always known, as it is where the protons collide), these interactions do not produce a charged lepton. The NC $1\pi^0$ interaction is especially difficult to select as the only charged particles produced in the interaction are protons, which might not exit the nuclear environment as a result of final state interactions, or may be too low in energy to be reconstructed in the detector. This is not the case for the inclusive measurement, as charged pions are produced in, for example, NC deep inelastic scattering.

As a result of this difficulty, there are very few measurements of the absolute NC $1\pi^0$ cross-section, as shown in Figure 2.6. Most measurements of this channel are presented as a ratio of NC/CC, many of which were determined using bubble chamber experiments, with the exception of the K2K result in 2004 [40]. The K2K collaboration measured the NC $1\pi^0$ cross-section relative to the total charged current cross-section for neutrinos with a mean energy of 1.3 GeV to be 0.064 ± 0.001 (stat) ± 0.007 (syst) using a 1000 ton water Cherenkov detector. A more recent measurement of the absolute cross-section, not shown in Figure 2.6, was made by the MiniBooNE collaboration in 2009 [41]. They found the absolute neutrino cross-section on CH_2 to be $(4.76 \pm 0.05$ (stat) ± 0.76 (syst)) $\times 10^{-40}$ $\text{cm}^2/\text{nucleon}$ at a mean neutrino energy of 808 MeV. This lack of measurements of the NC $1\pi^0$ cross-section manifests itself in the uncertainty of 43% assigned in the current T2K ν_e appearance analysis.

In addition to future T2K results, measurements of the NC $1\pi^0$ cross-section are expected from the MINER ν A collaboration [42], having developed the necessary tools to select photons from π^0 in their CC $1\pi^0$ analysis. MINER ν A will run with low (~ 3 GeV) and medium (~ 6 GeV) energy neutrino beams and has several targets for neutrino interactions, namely carbon, iron, lead, liquid helium and water.

(a) $\sigma(\nu_\mu p \rightarrow \nu_\mu p \pi^0)$ (b) $\sigma(\nu_\mu n \rightarrow \nu_\mu n \pi^0)$ **Figure 2.6.:** NC $1\pi^0$ cross-section measurements. Taken from [35].

Chapter 3.

The T2K experiment

The T2K (Tokai-to-Kamioka) experiment is a long baseline neutrino oscillation experiment. The most intense accelerator muon neutrino beam ever built is produced at the J-PARC facility in Tokai, located on the east coast of Japan, and directed (2.5° off-axis) toward the Super-Kamiokande (SK) detector, located 295 km away in the mountains of western Japan, as shown in Figure 3.1.

This chapter summarises the various components of the T2K experiment; for further information see [43] and references therein.

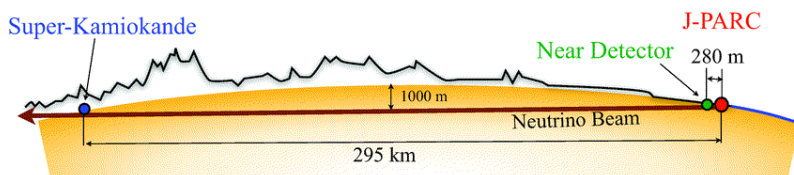


Figure 3.1.: A schematic of a neutrino's journey from the neutrino beamline at J-PARC, through the near detectors (green dot), which are used to determine the properties of the neutrino beam, and then 295 km underneath the main island of Japan to Super-Kamiokande. Figure and caption taken from [43].

3.1. Physics goals and current status

One of the main physics goals of the T2K experiment is the discovery of the oscillation $\nu_\mu \rightarrow \nu_e$. By exploring this channel T2K were the first experiment to report an indication of non-zero θ_{13} in June 2011, which was later confirmed by Daya Bay [15] and RENO [16] in March and April 2012, respectively. Measuring θ_{13} is the first step in the search for CP violation in the neutrino sector and toward determining the neutrino mass hierarchy, as discussed in Section 2. Furthermore, T2K will achieve precision measurements of oscillation parameters in ν_μ disappearance i.e. the atmospheric mixing parameters. The current limits on Δm_{32}^2 and $\sin^2 2\theta_{23}$ are set by MINOS, K2K and SK. T2K will achieve sensitivities of $\delta(\Delta m_{32}^2) = 10^{-4}$ and $\delta(\sin^2 2\theta_{23}) = 0.01$.

Based on the NEUT neutrino interaction simulator for T2K Run 1 (50 kW beam power, 3.7×10^{13} protons on target (POT) per spill), Run 2 (120 kW beam power, 8.0×10^{13} POT per spill) and Run 3 (178 kW beam power, 9.5×10^{13} POT per spill), the expected number of neutrino interactions per beam spill at ND280 is 4.0, 9.2 and 10.9, respectively. This large neutrino flux at the near detector suite enables the collaboration to make measurements of charged current (CC) and neutral current (NC), inclusive and exclusive, neutrino-induced interaction cross-sections on carbon, water and lead.

At the time of writing T2K is running stably and, as of 31 January 2013, has accumulated a total of 4.544×10^{20} POT, as shown in Figure 3.2. T2K expect to accumulate a total of 4.9073×10^{20} POT by the summer shutdown at the end of July 2013 and will be running with a beam power greater than or equal to 228 kW. Furthermore, all detectors (INGRID, ND280 and Super-Kamiokande) are running stably, taking data and are fully commissioned as described in later sections.

The latest ν_μ disappearance and ν_e appearance results from the T2K collaboration, obtained using data totalling 3.010×10^{20} POT, can be found in Figures 2.2 and 3.3, respectively. The disappearance analysis produces competitive measurements of the atmospheric oscillation parameters θ_{23} and Δm_{32}^2 . The appearance analysis, with eleven ν_e candidates, shows direct evidence of $\nu_\mu \rightarrow \nu_e$ oscillations at 3.2σ , which further reduces the uncertainty on the mixing angle θ_{13} .

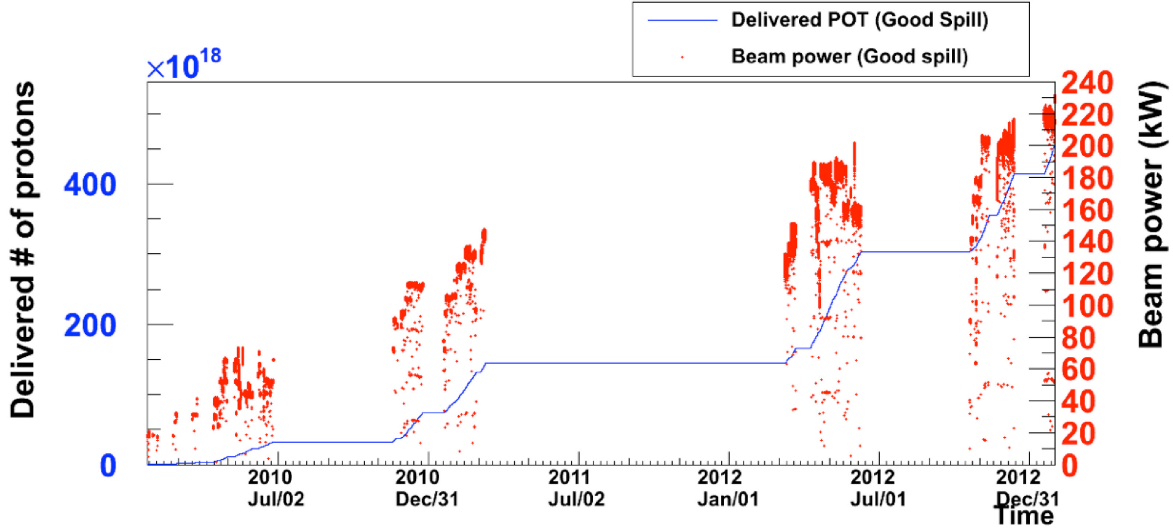


Figure 3.2.: Delivered number of protons on target and proton beam power as a function of date (up to 31 January 2013) [22].

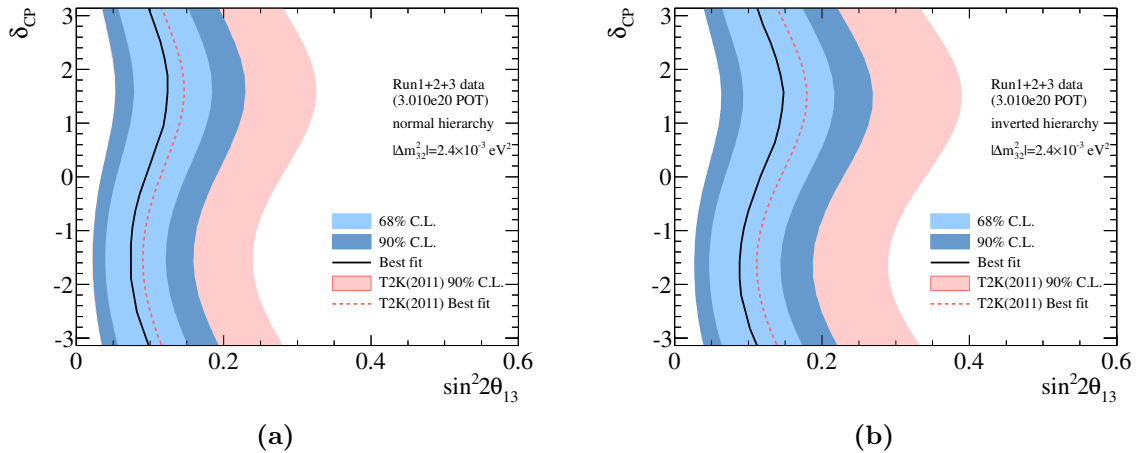


Figure 3.3.: T2K ν_e appearance result obtained using 3.010×10^{20} protons on target [22]. (a) and (b) show the best fit value for $\sin^2 2\theta_{13}$ as a function of the CP violating parameter δ for the normal and inverted neutrino mass hierarchy, respectively. The 68% and 90% confidence limits and the 2011 T2K result presented in [14] are also shown.

3.2. Accelerator and off-axis neutrino beam

3.2.1. Off-axis neutrino beam

The neutrino beam produced in the T2K experiment employs the off-axis method. As shown in Figure 3.4, the peak neutrino energy and spread of energies can be tuned by changing the off-axis angle. This tuning ability arises from the kinematics of the two body decay of charged pions that produce the beam neutrinos ($\pi^+ \rightarrow \mu^+ \nu_\mu$).

By directing a (narrow-band) neutrino beam toward Super-Kamiokande deliberately at an off-axis angle of 2.5° T2K achieve a peak neutrino energy of 0.6 GeV and subsequently maximise the effect of neutrino oscillations at a distance of 295 km from the production point. Furthermore, the flux of neutrinos at the oscillation maximum (0.6 GeV) is higher for an off-axis beam than it is for the conventional, on-axis neutrino beam. By producing a narrow-band beam, the number of high energy neutrinos, which do not contribute to the appearance signal but do enrich the background for the search of $\nu_\mu \rightarrow \nu_e$ oscillations, is reduced. Additionally, the NC $1\pi^0$ background and the intrinsic ν_e contamination in the ν_μ beam are reduced using this off-axis method.

The T2K neutrino beam is composed of 99% of ν_μ , with kaons being the dominant source of ν_μ production at energies above the peak energy. The 1% contamination from ν_e comes from muon and kaon decay.

3.2.2. J-PARC accelerator

There are three accelerators found in the newly constructed J-PARC site in Tokai-mura, on the east coast of Japan: a linear accelerator (LINAC); a rapid-cycling synchrotron (RCS) and the main ring (MR) synchrotron. The LINAC was designed to accelerate an H^- beam to an energy of 400 MeV. Upon injection into the RCS, this beam of H^- anions is converted to a proton beam (H^+) by charge-stripping foils. The RCS then accelerates this proton beam to 3 GeV with a cycle frequency of 25 Hz. The RCS supplies protons to the MR (5%) and to the Material and Life Science Facility at J-PARC. Upon injection into the MR, eight (six prior to June 2010) bunches of protons are accelerated to 30 GeV every 2 – 3 seconds. These bunches are then extracted for the neutrino beamline using a single-turn fast-extraction method that takes approximately $5 \mu s$. This beam spill structure of eight proton bunches, with an inter-bunch separation of 582 ns, is extremely

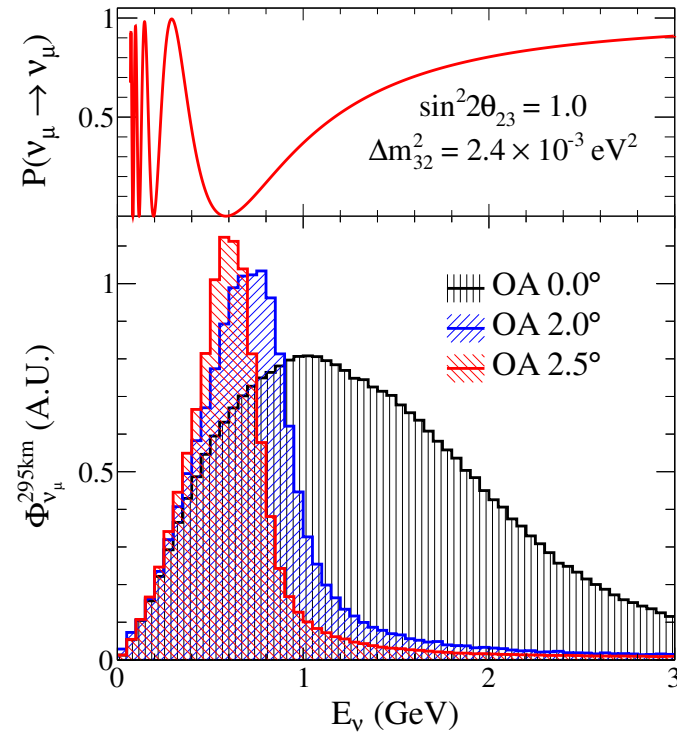


Figure 3.4.: Muon neutrino survival probability at 295 km and neutrino fluxes for different off-axis angles. Taken from [44].

important for background rejection of cosmic ray interactions. The bunch structure can be seen in Figure 6.5.

3.2.3. Neutrino beamline

The T2K neutrino beamline receives eight proton bunches per spill from the MR and is composed of a primary and secondary beamline, as shown in the schematic in Figure 3.5a. The primary beamline serves to ensure the proton beam is pointed in the direction of Kamioka, the location of the Super-Kamiokande detector, whereas in the secondary beamline the proton beam impinges on a carbon (graphite) target, producing secondary pions. It is these secondary pions that are focussed by magnetic horns and decay to produce the neutrinos that form the T2K neutrino beam.

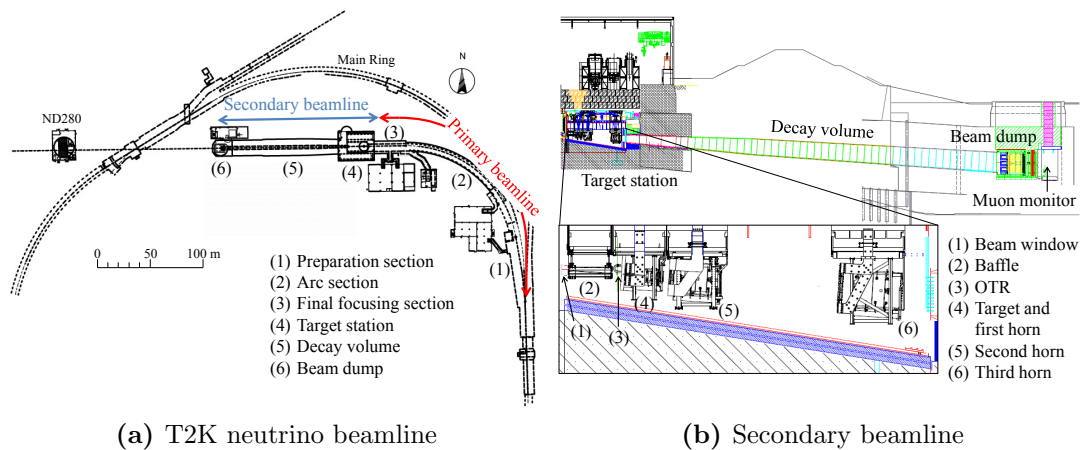


Figure 3.5.: (a) shows an overview of the T2K neutrino beamline and (b) shows the side view of the secondary beamline. The length of the decay volume is ~ 96 m. Figures taken from [43].

Primary beamline

The primary beamline is composed of a 54 m long preparation section and an arc section (147 m), which is then followed by a 37 m long final focussing section. In the preparation section, eleven normal conducting magnets tune the extracted proton beam to prepare it for the arc section. The arc section has a radius of curvature of 104 m and it is here that superconducting combined function magnets [45] bend the beam by 80.7° so that it points toward Kamioka. In addition, horizontal and vertical superconducting steering magnets correct the beam orbit. As the beam passes into the final focussing section, it is guided by ten normal conducting magnets toward the graphite target. The magnets also direct the beam downward at an angle of 3.637° (with respect to the horizontal axis) to ensure the desired 2.5° off-axis angle is achieved.

The proton beam must be well-tuned to minimise beam loss, produce a high-power beam and ensure stable neutrino beam production. Thus, the T2K experiment monitors the intensity of the beam using five current transformers (CTs), beam position with 21 electrostatic monitors (ESMs), profile of the proton beam using 19 segmented secondary emission monitors (SSEM) and any beam losses using 5 beam loss monitors (BLMs), in the primary section of the beamline. (For further details of the monitoring devices see [43].)

As a result of excellent monitoring, the absolute proton beam intensity is known with a 2% uncertainty; the measurement precision of the beam position is less than 450 μm ;

the beam width is known to within $200\ \mu\text{m}$ and the beam loss monitors have sensitivity down to a 16 mW beam loss.

Secondary beamline

Once the proton beam is pointing toward Kamioka, it approaches the secondary beamline, as shown in Figure 3.5b. The secondary beamline is comprised of a target station (expanded in the bottom half of the previously referenced figure), decay volume, beam dump and finally a muon monitor (MUMON).

The target station contains a baffle (1.7 m long, 0.3 m wide, 0.4 m high and composed of graphite with a 30 mm beam hole) to collimate the proton beam thus protecting the magnetic horns. Additionally, an optical transition radiation monitor (OTR) monitors the beam profile by collecting transition radiation that is produced as the beam passes through a thin piece of titanium-alloy foil as it approaches the target. Next, the proton beam impinges on the target generating secondary pions. The target is a graphite rod that is 91.4 cm long (1.9 interaction lengths), 2.6 cm in diameter and has a density of $1.8\ \text{g}/\text{cm}^3$. When running at the design power of 750 kW, interactions of the proton beam with the target are likely to result in temperatures of $\sim 700\ ^\circ\text{C}$; for this reason the target is cooled with helium gas. Also, to maximise the number of pions that are focussed by the horns, the target is housed within the first magnetic horn. The pions emerging from the target are focussed by three magnetic horns. Each horn consists of two coaxial aluminium alloy conductors housed within a closed volume. A toroidal magnetic field that varies as a reciprocal of the distance from the horn axis is generated in the closed volume. The purpose of the first horn is to collect the charged pions that are produced in the target, whereas the second and third horns focus the pions. The neutrino flux at 0.6 GeV at Super-Kamiokande increases by a factor of ~ 16 when the horns are operated with a (design) current of 320 kA (which produces a magnetic field of 2.1 T), when compared to operation with 0 kA. At the time of writing, the horn current is 250 kA with a measurement uncertainty less than 2%.

The pions produced when the proton beam impacts with the target enter the decay volume that is $\sim 96\ \text{m}$ in length and has an upstream (downstream) cross-section of $1.4\ \text{m} \times 1.7\ \text{m}$ ($3.0\ \text{m} \times 5.0\ \text{m}$). Whilst in the decay volume most pions decay to μ^+ and ν_μ (99.99% [36]). In addition to pions, a non-negligible amount of positively charged kaons are produced when the proton beam impinges on the target. These kaons decay to

produce ν_μ (higher in energy than those from π^+) and ν_e . The ν_e from kaons make a significant contribution to the total 1% contamination of the ν_μ beam. All hadrons and muons with momenta less than ~ 5 GeV leaving the decay volume are stopped by the graphite beam dump ($3.2\text{ m} \times 1.9\text{ m} \times 4.7\text{ m}$). Muons with momenta above 5 GeV pass through the beam dump to the MUMON for monitoring. The neutrinos are unaffected by the beam dump and proceed to the near detector suite.

The MUMON is composed to two types of detector arrays; the most upstream array is of ionisation chambers, followed by silicon PIN photodiodes. By measuring the profile of muons entering the MUMON, it is capable of monitoring the neutrino beam intensity and direction on a bunch-by-bunch basis, with a precision of 0.25 mrad and 3%, respectively.

3.2.4. Neutrino flux prediction

Measurements made at both the near detector suite and Super-Kamiokande rely heavily on the neutrino flux prediction. For T2K to achieve the goals outlined at the beginning of this chapter the ratio of fluxes at ND280 and Super-Kamiokande as a function of energy must be known to better than 3%. Furthermore, to make neutrino cross-section measurements at ND280 a small absolute flux uncertainty is necessary.

It is difficult to accurately predict the neutrino flux due to uncertainties in the hadron production processes in proton-nucleus scattering. The neutrino flux simulation at T2K begins upstream of the baffle (in the secondary beamline) and ends with the decay of particles producing neutrinos. The simulation is driven using results from the NA61/SHINE [46] experiment, a dedicated experiment that covers the whole kinematic region of interest for T2K, proton beam profile measurements and studies of the horn magnetic field.

FLUKA2008 [47] is used to simulate hadronic interactions inside the target and baffle (this is where most secondary pions are created) as it is found to have the best agreement with external hadron production data. The kinematic information for particles emerging from the target is predicted using the JNUBEAM simulation package. The Monte Carlo tools in JNUBEAM are based on GEANT3 [48] and model the baffle, target, horns, beam dump and muon monitor. JNUBEAM also uses GCALOR [49] to model hadronic interactions. Particles are tracked until they interact, decay or fall below a kinematic cut-off. Additionally, the produced neutrinos are required to point toward Super-Kamiokande or a randomly chosen point near the detector plane.

3.3. The T2K near detector suite

The T2K near detector suite is situated 280 m away from the neutrino production location (in the direction of Super-Kamiokande) and is comprised of two detectors: INGRID, the on axis detector, and ND280, the 2.5° off-axis, magnetised detector. Both detectors are housed in a pit that is 37 m deep and has a diameter of 17.5 m, as shown in Figure 3.6.

The Interactive Neutrino GRID (INGRID) is an array of detectors made from iron and plastic scintillator and measures the on-axis neutrino beam profile.

The subdetectors that make up the ND280 are contained within the recycled UA1 magnet. At the most upstream end of the ND280 (i.e. nearest the beam production point) is the π^0 detector (P0D), a scintillator based detector containing water and carbon targets. The tracker is located downstream of the P0D and is composed of three time projection chambers (TPCs) and two fine grained detectors (FGDs). An electromagnetic calorimeter (ECAL) surrounds the P0D and tracker and plays a large role in detecting photons from π^0 produced in neutral current interactions¹. Additionally, the yoke of the magnet is instrumented with plastic scintillator, which allows it measure the range of muons exiting the off-axis detector.

All detectors use the same right-handed global coordinate system where the positive z direction is along the nominal neutrino beam axis, x is the horizontal direction and y is the vertical.

3.3.1. Scintillator-based readout

The T2K near detector suite has many scintillator-based detectors, namely INGRID and several subdetectors that make up the off-axis detector ND280 (P0D, FGD, ECAL and SMRD). The operation and readout principle for these detectors is the same: a 1 mm diameter Y11 Kuraray wavelength shifting (WLS) fibre runs down the length of the scintillator bar and collects scintillation light; this light is then transported to a photosensor, which converts the light into an electrical signal.

The scintillation light emission peak is at a wavelength of 420 nm (blue). This is well matched to the absorption spectrum of the WLS fibre, which is centred at a wavelength of 420 nm (blue). Furthermore, the re-emitted light from the WLS fibres peaks at 476 nm

¹ Using the ECAL to select NC $1\pi^0$ interactions is discussed in more detail in Chapter 6.

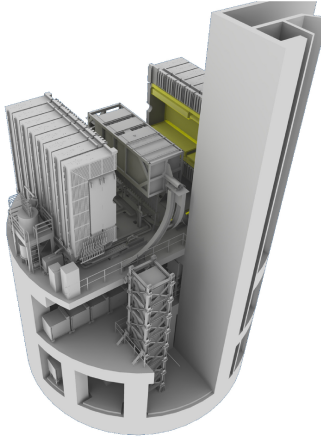


Figure 3.6.: ND280 near detector complex. The off-axis detector is located on the upper level; horizontal INGRID modules are located on the level below; and the vertical INGRID modules span the bottom two levels. Figure and caption taken from [43].

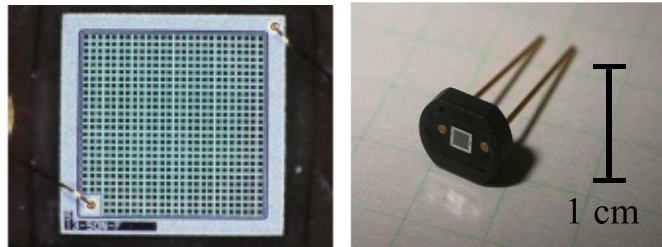


Figure 3.7.: Photographs of an MPPC with a sensitive area of $1.3 \text{ mm} \times 1.3 \text{ mm}$: magnified face view (left) with 667 pixels in a 26×26 array (a 9-pixel square in the corner is occupied by an electrode); the ceramic package of this MPPC (right). Figure and caption taken from [43].

(green). This small overlap in absorption and emission spectra of the WLS fibre ensures self-absorption effects are small.

The photosensor in question is the novel Hamamatsu Multi-Pixel Photon Counter (MPPC), which was chosen as it is compact, well matched to the emission spectra of the WLS fibres and functions within a 0.2 T magnetic field environment without degradation. A photograph of an MPPC can be found in Figure 3.7.

The MPPC is an array of 667 independent avalanche photodiodes. These photodiodes operate in Geiger mode, held at a reverse bias voltage greater than the breakdown voltage. Thus a photoelectron is capable of producing an ionisation cascade (“avalanche”), which in turn generates a large reverse current. The MPPC gain is determined using the charge produced in a single pixel avalanche, Q_{pixel} defined as: $Q_{\text{pixel}} = C_{\text{pixel}}(V - V_{\text{BD}})$, where

the capacitance of a single pixel, C_{pixel} , is 90 fF, V is the operating voltage, which is approximately 70 Volts for MPPCs; this is $(0.8 - 1.5)$ Volts above the breakdown voltage of the photodiode V_{BD} . The MPPC gain is in the range $(0.5 - 1.5) \times 10^6$. As each pixel on the photodiode operates as a binary device, the photodiode signal is the sum of fired pixels on the MPPC. For further information regarding the response of MPPCs to scintillation light see [50].

3.3.2. The on-axis INGRID detector

The on-axis detector in the T2K near detector suite, known as the Interactive Neutrino GRID (INGRID), is located beneath, and also slightly further downstream of, the off-axis detector ND280. The INGRID design ensures there are sufficient neutrino interactions with iron each day to monitor the neutrino beam direction and intensity. Using neutrino interactions in each module, the beam centre is measured to a precision better than 0.4 mrad.

The detector comprises seven vertically stacked, seven horizontally stacked and two off diagonal modules, as shown in Figure 3.8. Each module is installed with a position accuracy of 2 mm in directions perpendicular to the neutrino beam. The centre of the INGRID cross, where there are two overlapping modules, corresponds to the neutrino beam centre; this is 0° with respect to the direction of the primary proton beamline. Furthermore, the two off-axis modules enable monitoring of the axial symmetry of the neutrino beam.

Each INGRID module is identical and consists of nine iron plates ($124 \text{ cm} \times 124 \text{ cm} \times 6.5 \text{ cm}$ in x , y and along the beam direction, respectively) sandwiched between 11 tracking scintillator planes². Each tracking scintillator plane is composed of 24 scintillator bars in the horizontal direction with 24 bars perpendicular, in the vertical direction. The dimensions of each scintillator bar are $1.0 \text{ cm} \times 5.0 \text{ cm} \times 120.3 \text{ cm}$. This structure is then surrounded by veto scintillator planes to help reject interactions occurring outside the module. Each veto plate is composed of 22 scintillator bars ($1.0 \text{ cm} \times 5.0 \text{ cm} \times 111.9 \text{ cm}$ (bottom) and $1.0 \text{ cm} \times 5.0 \text{ cm} \times 129.9 \text{ cm}$ (top, right and left sides)) that are segmented in the beam direction. Scintillator bars used in the tracking and veto planes are made of polystyrene doped with PPI (1%) and POPOP (0.03%) scintillator

² Due to weight restrictions, there is no iron plate between the 10th and 11th tracking planes, however this has been shown to have no effect on the tracking performance.

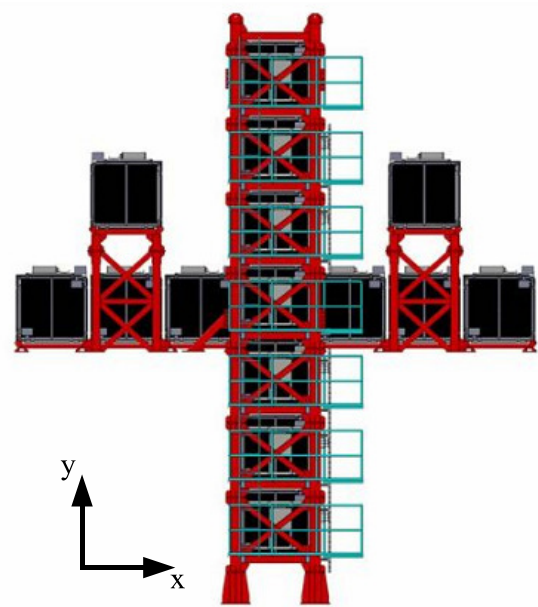


Figure 3.8.: Schematic of the INGRID on-axis detector. Figure taken from [43]

flours. In addition, each scintillator bar is coated with a thin, white layer of titanium oxide to improve the light collection efficiency, as light escaping the bar is reflected back in. Furthermore, a wavelength shifting fibre runs down the length of the bar and is connected to an MPPC, as described in Section 3.3.1.

An additional module, called the Proton Module, consisting of scintillator planes without iron plates surrounded by veto planes, was added to enable the detection of muons and protons from neutrino-induced CCQE interactions in INGRID for comparison with Monte Carlo simulations of beamline and neutrino interactions. This module is positioned in the centre of the INGRID cross, between the vertical and horizontal modules.

3.3.3. The off-axis ND280 detector

The primary purpose of the ND280 detector is to characterise the neutrino beam prior to oscillation. The detector provides measurements of neutrino flux, energy spectrum and the ν_e contamination of the beam as a function of neutrino energy. Due to the high neutrino flux, the ND280 is also capable of rate measurements for both inclusive and exclusive interactions; this characterises both signal and background interactions in Super-Kamiokande.

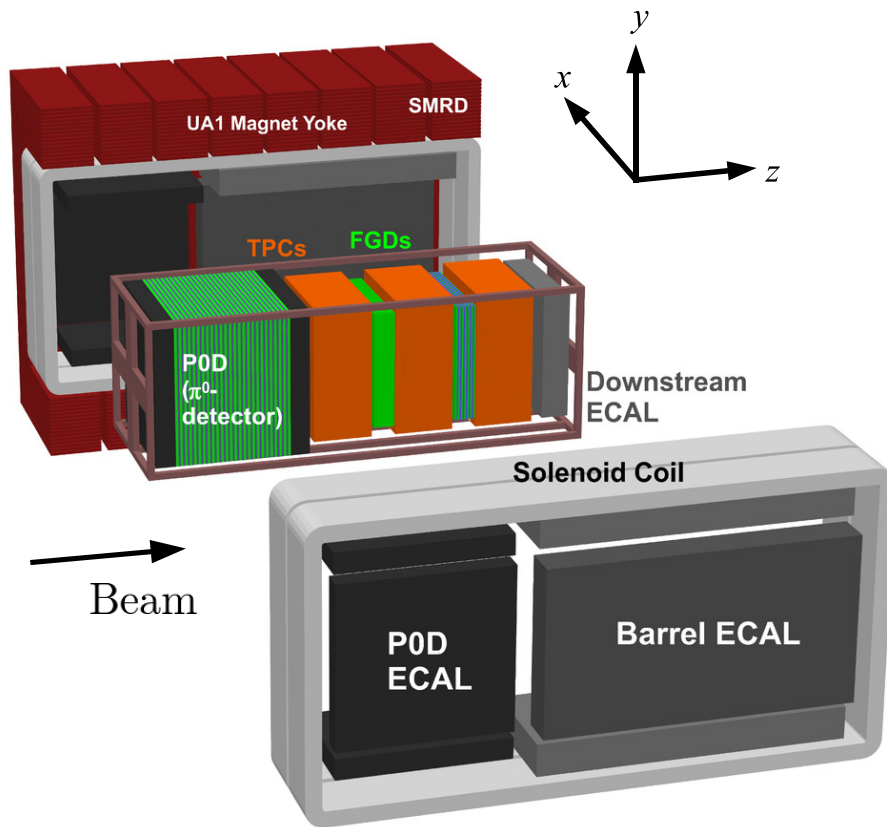


Figure 3.9.: Exploded view of the ND280 off-axis detector and the global coordinate system. Figure taken from [43].

As shown in Figure 3.9, the ND280 detector is composed of several subdetectors contained within the UA1 magnet/SMRD. The most upstream subdetector is the P0D, which is followed by the tracker (three TPCs interleaved with FGDs). The tracker is placed inside a metal “basket” frame, which has dimensions $6.5\text{ m} \times 2.6\text{ m} \times 2.5\text{ m}$, and is surrounded by the ECAL.

π^0 Detector (P0D)

The P0D was designed and built to measure the neutral current processes on a water target that produce one π^0 in the final nuclear state³, as this is one of the main backgrounds to the ν_e appearance measurement at Super-Kamiokande.

The schematic found in Figure 3.10 shows the defining features of the P0D; it comprises scintillator bars in the x and y planes, interleaved with fillable water target bags and

³ The analysis performed using the P0D is complimentary to that described in detail in Chapter 6.

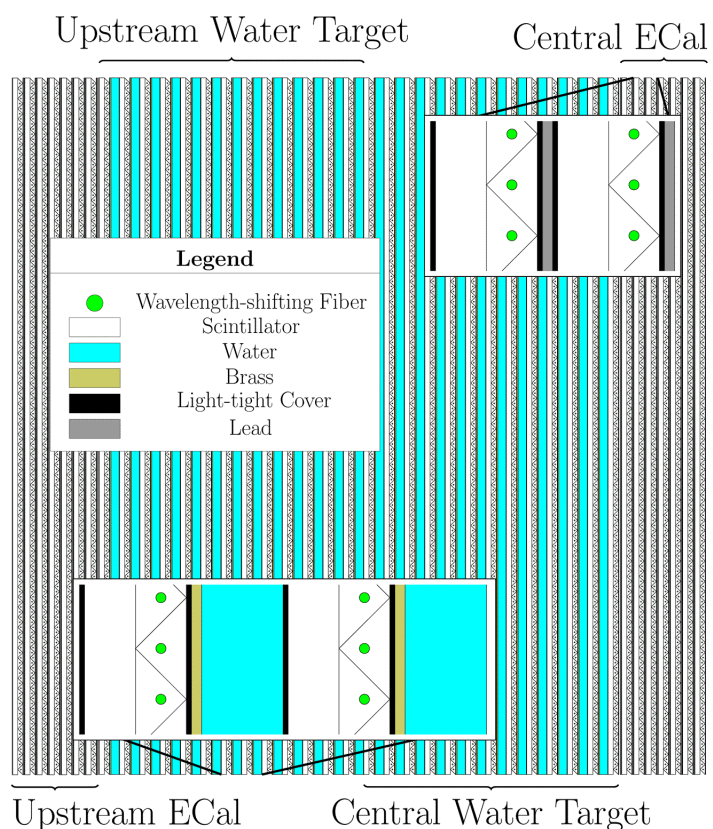


Figure 3.10.: Schematic of the π^0 detector. The beam direction is from left to right. Figure taken from [43].

sheets of brass and lead. Conveniently, data can be taken with full or empty water target bags, meaning a subtraction method can be used to determine the NC $1\pi^0$ cross-section on water.

There are 40 P0D scintillator modules (P0Dules) in the P0D. Each P0Dule has 134 vertical bars (2200 mm in length) mounted perpendicular to 126 horizontal bars (2340 mm in length), where the bars in question are doped (1% PPO, 0.03% POPOP) polystyrene, triangular (isosceles), scintillator bars (33 mm base, 17 mm height). The bars are also coated with TiO_2 , to reflect light escaping back into the bar, and contain a WLS fibre that spans the length of the bar. This WLS fibre is mirrored at one end and has an MPPC at the other.

The central section of the P0D comprises an “upstream water target” and a “central water target”; each of these targets is composed of 13 P0Dules. The upstream water target has 13 (28 mm thick) water bag layers and 13 (1.5 mm thick) brass sheets sandwiched between P0Dules, whereas the central water target contains only 12 water bags and 12 additional brass sheets. The total active target region of the P0D has dimensions 2103 mm \times 2239 mm \times 2400 mm. Additionally, the mass of the detector with and without water in the bags is 16.1 tons and 13.3 tons, respectively.

The most upstream and downstream sections of the P0D are made up of electromagnetic calorimeters (ECals) (these are not to be confused with the P0DECAL, which is part of the ECAL). Both the “upstream ECal” and “central ECal” consist of seven P0Dules each alternating with (seven) stainless steel clad lead sheets, which are 4 mm thick. In addition to improving the containment of electromagnetic showers, the ECals provide a veto region around the water targets and allow effective rejection of particles entering the P0D from neutrino-induced interactions occurring elsewhere in the ND280.

Time Projection Chambers (TPCs)

The ND280 detector contains three TPCs located on each side of the FGDs called TPC1, TPC2 and TPC3, where TPC1 is upstream and TPC3 has the most downstream global z coordinate. As TPCs have excellent imaging capabilities in three dimensions, they enable the ND280 to track charged particles emerging from neutrino-induced interactions in the FGDs. Furthermore, as the ND280 operates in a magnetic field, the TPCs can make momentum measurements using the curvature of the tracks created by charged particles. By comparing the amount of energy lost by particles as a result of ionisation

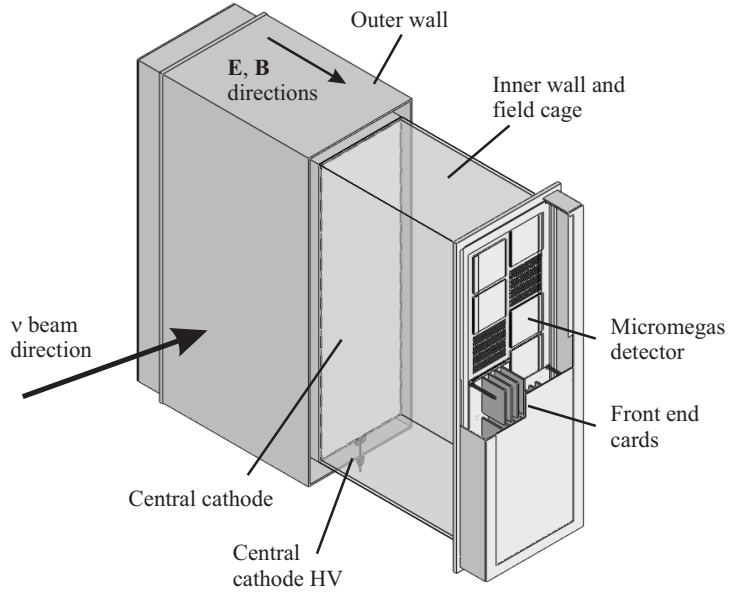


Figure 3.11.: Simplified cut-away drawing showing the main aspects of the TPC design. The outer dimensions of the TPC are approximately $2.3\text{ m} \times 2.4\text{ m} \times 1.0\text{ m}$. Figure and caption taken from [43].

with the same quantity for known particles, as a function of momentum, the TPCs can be used to distinguish between different particle species.

Each TPC is composed of two boxes, as shown in the simplified drawing in Figure 3.11. The outer box is filled with CO_2 gas for insulation, whereas the inner box contains an argon-based drift gas⁴ and is divided into two sections by a central cathode panel. This cathode panel, in conjunction with (11.5 mm) copper strips that line the inside of the box, produces a uniform electric field along the x axis, i.e. aligned with the field produced by the UA1 magnet. As charged particles pass through the TPC, their interactions with the gas molecules produce ionisation electrons. These electrons drift away from the central cathode and toward one of the readout planes. Each readout plane contains twelve micromegas modules [51] organised into two, slightly offset⁵, vertical columns. Each of these modules is $342\text{ mm} \times 359\text{ mm}$ in size and is made of 1728 7.0 mm \times 9.8 mm anode pads. In total there are 72 micromegas modules in the ND280 detector; this provides an active surface that is approximately 9 m^2 in area.

⁴ Ar:CF₄:iC₄H₁₀ (ratio 95:3:2) chosen for its high speed, low diffusion and good performance with micromegas chambers.

⁵ The micromegas modules are slightly offset to ensure there is no alignment between the small inactive regions in the modules.

Fine Grained Detectors (FGDs)

There are two Fine Grained Detectors in ND280, named FGD1 and FGD2, as shown in Figure 3.9. The FGDs provide the target mass (1.1 tons) for neutrino interactions in addition to tracking charged particles emerging from the interaction vertex.

Each FGD is made from bars of extruded polystyrene scintillator (9.61 mm \times 9.61 mm \times 1864.3 mm) that are coated in a reflective substance containing TiO_2 and are structured into layers, with each layer oriented perpendicular to the beam in either the x or y direction. These scintillator bars provide the neutrino target mass and their orientation makes full three dimensional reconstruction possible. Each bar contains a WLS fibre that runs the whole length of the bar; one end of the fibre has a mirrored aluminium surface, whilst the alternate end is attached to an MPPC.

The total outer dimensions of each FGD are 2300 mm \times 2400 mm \times 365 mm (c.f. width \times height \times depth in beam direction). The most upstream FGD, FGD1, has 30 layers of scintillator, with each layer containing 192 bars. However, FGD2 is made from seven “XY modules” (where a module is one layer of scintillator bars oriented in the x direction, glued to one layer of bars in the y direction) of scintillator alternating with six 2.5 cm thick layers of (sub-atmospheric pressure) water, giving a total water thickness of 15 cm. The addition of a water target allows interaction rates on both carbon and water to be studied.

Electromagnetic Calorimeter (ECAL)

The ND280 ECAL is a sampling calorimeter comprised of active layers of plastic scintillator bars and lead sheets. As shown in Figure 3.9, it surrounds the P0D and tracker (TPCs and FGDs), providing almost hermetic coverage for particles exiting the inner detector. The addition of ECAL information complements that provided by the inner detectors and provides electromagnetic energy estimates, directional information for charged particles and the information relevant to perform particle identification. As discussed in Chapter 6, the barrel and downstream ECAL, surrounding the tracker, perform a crucial role in the reconstruction of π^0 produced in neutrino-induced interactions in the FGDs. Furthermore, the ECAL enclosing the P0D (P0DECAL) complements the P0D reconstruction, as it provides information regarding particles escaping the P0D.

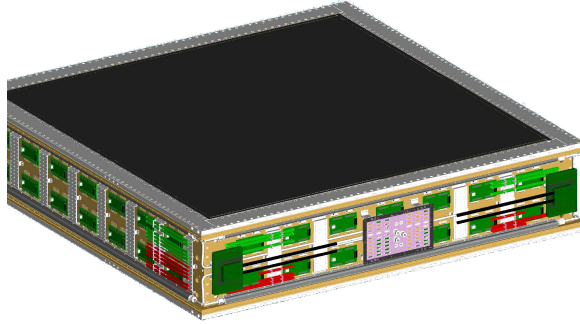


Figure 3.12.: External view of one ECAL module. The scintillator bars run horizontally inside the module as shown. The readout electronics, signal and power cables, and cooling pipes can be seen mounted on the aluminium plates on the sides of the module. The grey surface at the top is the carbon fibre sandwich front plate, which in the final module position is facing towards the inner subdetectors (P0D, FGDs and TPCs). Figure and caption taken from [43].

The ECAL is made of 13 independent modules, arranged as in Figure 3.9. There are six barrel ECAL (BrECAL) modules surrounding the tracker; one downstream module (DsECAL) that acts as an endcap and six P0DECAL modules that surround the P0D. A schematic of the external view of an ECAL module can be found in Figure 3.12. The barrel ECAL modules are mounted on the UA1 magnet and are configured such that there is one module on each side and then two separate modules on both the top and bottom; this is necessary for magnet opening and closing.

Regardless of the module, all ECAL scintillator bars are made of doped polystyrene (1% PPO and 0.03% POPOP), are coated with a 0.24 mm layer of TiO_2 , to provide light reflection and isolation, and have a cross-section of 4.0 cm \times 1.0 cm. Also, each bar has an elliptical hole running along the length that contains a WLS fibre. Depending on the ECAL module in question, some WLS fibres are double ended readout (i.e. they have an MPPC connected to both ends), whereas those that are single ended readout are mirrored at one end and have an MPPC attached to the other. Additionally, all modules are sealed with thin aluminium covers for structural protection and to prevent light both escaping and entering the module.

Each layer in the DsECAL module is made of 50 scintillator bars (2.04 m in length), all of which have double ended readout. A total of 34 layers make up the DsECAL, with each layer rotated at 90° to its predecessor (e.g. if a layer has bars oriented along x , the

bars of the subsequent layer are along y), allowing three-dimensional reconstruction, and is sandwiched between 1.75 mm thick lead sheets (giving a total lead thickness of 10.6 radiation lengths).

As the BrECAL is located inside the UA1 magnet, its design required many spatial considerations. Each BrECAL module has a similar structure to the DsECAL: there are 31 layers of scintillator bars interleaved with 1.75 mm thick lead sheets (totalling 9.7 radiation lengths). Bars aligned along the z direction are 3.84 m long and have double ended MPPC read out. Bars in the top/bottom (side) ECAL modules, which are aligned along the x (y) axis, are 1.52 m (2.36 m) in length and have single ended readout.

The primary aim of the P0DECAL module is to aid the reconstruction of neutrino-induced interactions that produce π^0 particles in the P0D. As well as detecting photons that only partially enter the P0D and those that do not convert in the active P0D volume, the P0DECAL is also capable of identifying charged particles and thus acts as a veto for incoming backgrounds. With these aims in mind, the P0DECAL has a simpler construction; each module is made of six active scintillator layers separated by five 4 mm thick lead sheets, giving a total of 3.6 radiation lengths. All bars have single ended readout, run along the z direction and are 2.34 m in length.

Magnet and Side Muon Range Detector (SMRD)

The magnet used in the ND280 detector has been recycled from the UA1 [52] and NOMAD [53] experiments. It produces a 0.2 T dipole magnetic field (with an uncertainty of 0.0002 T for each field component) and enables subdetectors enclosed in the magnet to measure the momenta and sign of charged particles produced in neutrino-induced interactions.

The magnet is comprised of aluminium coils, which are water cooled and create the horizontally oriented dipole field, and a flux return yoke. The inner (external) dimensions of the structure are 7.0 m \times 3.5 m \times 3.6 m (7.6 m \times 5.6 m \times 6.1 m). The yoke has a total weight of 850 tons. To ensure access to the subdetectors contained within the magnet, the magnet is halved (symmetrically). Each half of the yoke consists of eight individual C-shaped elements that are fitted onto rails operated by hydraulic movers. These elements are made up of 16 steel plates with 15 air gaps, which are 4.8 cm and 1.7 cm thick, respectively.

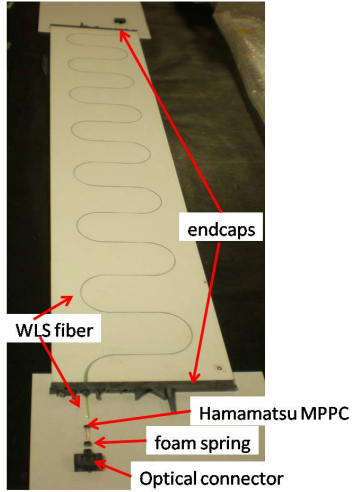


Figure 3.13.: View of SMRD scintillator counter components prior to assembly. Figure taken from [43].

The SMRD is a system of 440 scintillator modules that are inserted into the innermost air gaps (i.e. those nearest the centre of the ND280) between steel plates in the magnet yoke elements and performs a number of functions. The SMRD is able to record the momenta of muons escaping the ND280 at high angles, with respect to the beam direction. Also, the SMRD is used as a cosmic ray trigger for cosmic muons entering the ND280 and can also be used to veto neutrino-induced interactions in the cavern walls and in the magnet itself.

The SMRD has three layers of scintillator modules on the top and bottom for all yokes. Counting the yokes from upstream → downstream, the five most upstream yokes have three layers of scintillator modules on both sides, whereas the sixth yoke has four layers and the seventh and eighth yokes have six layers of modules. To maximise the active area in each magnet air space, horizontal (vertical) modules are composed of four (five) scintillation counters with dimensions 875 mm × 167 mm × 7 mm (875 mm × 175 mm × 7 mm).

A scintillation counter, prior to assembly, can be found in Figure 3.13. The scintillator counters are made of extruded polystyrene and dimethylacetamide with admixtures of POPOP and para-terphenyl. Each counter is coated in a white diffuse layer that acts as a reflector and contains an S-shaped channel housing a WLS fibre, which is connected to an MPPC for readout.

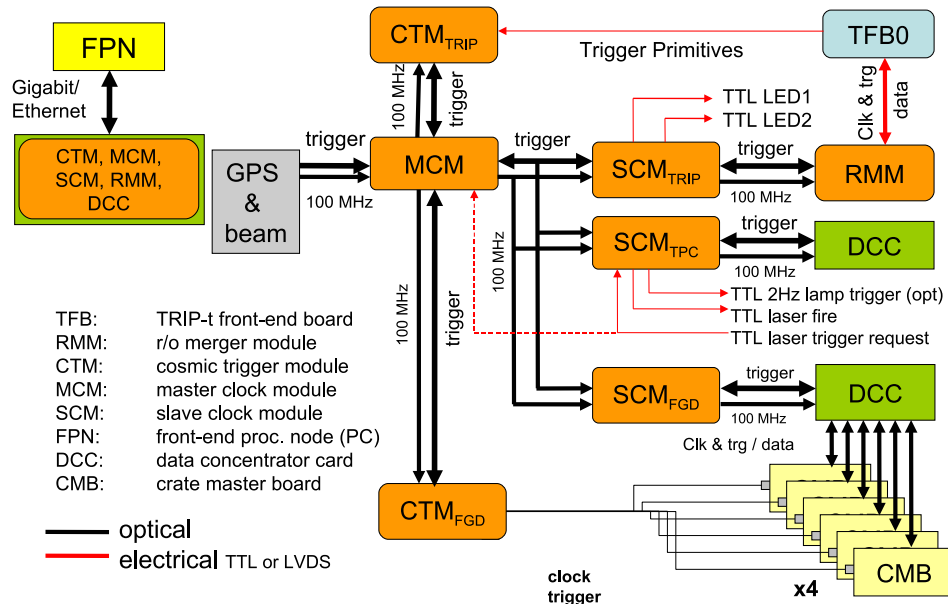


Figure 3.14.: General layout of the ND280 electronics. Figure taken from [43].

Trip-t readout electronics

Both INGRID and many ND280 subdetectors (ECAL, P0D and SMRD) make use of Trip-t electronics to read out information from the MPPCs (as discussed in Section 3.3.1). A Trip-t front end board (TFB) houses four Trip-t chips [54], each of which can be connected to up to 16 MPPCs. To increase the dynamic range of the electronics, each MPPC has a high and low gain channel, saturating at 50 and 500 photoelectrons, respectively. The Trip-t chips integrate charge in programmable integration windows of 480 ns, separated by a reset period of 100 ns. These integration windows, of which there are 23, are synchronised with the bunches of the neutrino beam spill. The output of the high gain channel is routed to a discriminator that produces a timestamp when the integrated charge exceeds 2.5 – 3.5 photoelectrons, depending on the subdetector, with an accuracy of 2.5 ns.

Figure 3.14 shows the general overview of the Trip-t electronics in the ND280 detector⁶. TFBs are connected to readout merger modules (RMMs) by electrical cables. The role of the RMMs is to control the TFBs by distributing clock and trigger signals. When the master clock module (MCM) receives signals from the accelerator and a GPS-based clock informing it of a neutrino beam spill, it sends a signal, via an optical Rocket I/O

⁶ The INGRID detector operates independently of the ND280 detector and has one MCM and a single CTM.

cable, to the slave clock modules (SCMs)⁷ for electronics readout to begin. These SCMs are connected to RMMs⁸ via optical cables, which in turn are connected to the TFBs⁹ by electrical cables. Additionally, the MCM is connected to a cosmic trigger module (CTM)¹⁰, which decides if there was a cosmic event in the detector based on a selection criteria and triggers electronics readout.

3.4. The T2K far detector Super-Kamiokande

Super-Kamiokande (SK, Super-K) is a cylindrical water Cherenkov detector located 295 km west of the T2K near detector suite, 1000 m deep inside the Ikenoyama mountain. SK contains approximately 13,000 photomultiplier tubes (PMTs) and is filled with 50 kton of pure water, allowing it to image neutrino interactions. The SK detector has been running since 1996 and, as a result, is very stable and well understood. The energy scale is known to the percent level and the agreement between calibration data samples and Monte Carlo (MC) also agrees to the percent level.

Super-Kamiokande comprises an inner detector (ID), which has a diameter of 33.8 m and is 36.2 m high, and an outer detector (OD), which is approximately 2 m thick, as shown in the schematic in Figure 3.15. Both ID and OD are lined with PMTs to collect light produced by relativistic charged particles. The ID houses 11,129 inward-facing, 50 cm diameter PMTs (40% surface coverage), which is sufficient, with regards to spatial resolution, to effectively imagine neutrino interactions occurring in the ID. The OD is only sparsely instrumented and contains 1,885 outward-facing, 20 cm diameter PMTs. Despite this instrumentation, the OD is capable of almost 100% rejection of cosmic ray muon backgrounds. There is a 50 cm wide boundary between the ID and OD; this barrier is a stainless steel scaffold covered in plastic sheets, to optically separate the ID and OD. The wall facing into the ID is lined with black plastic to absorb light and minimise the number of photons re-entering the ID by scattering off the ID wall. The wall also reduces the number of photons passing through to the OD from the ID. The walls facing the OD are lined with a highly reflective material to increase the likelihood of a photon being detected by a PMT in the OD.

⁷ There is one SCM for each subdetector in ND280 (SMRD, ECAL, P0D, FGD and TPC); this enables the electronics to be configured and operated independently.

⁸ The P0D, ECAL and SMRD have 22 RMMs in total.

⁹ Each RMM is connected to a maximum of 48 TFBs.

¹⁰ There are two cosmic trigger modules: one takes signals from Trip-t based detectors (P0D, SMRD and the downstream ECAL) and the other is connected to the FGDs.

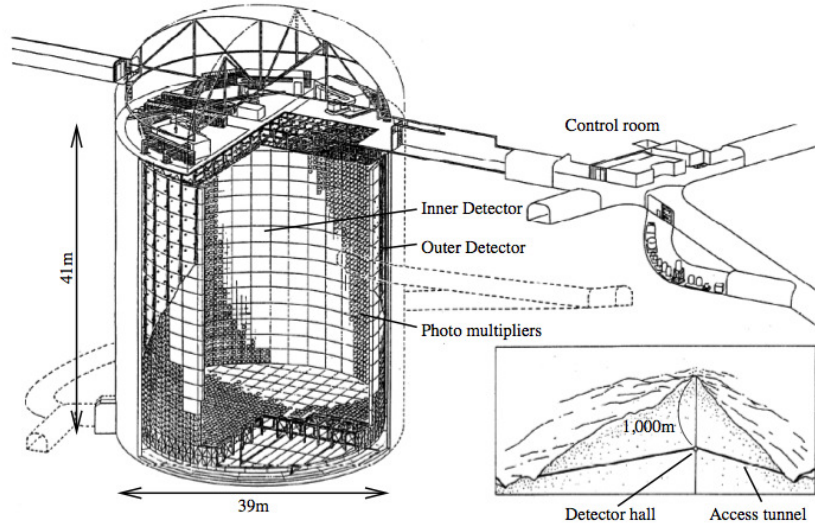
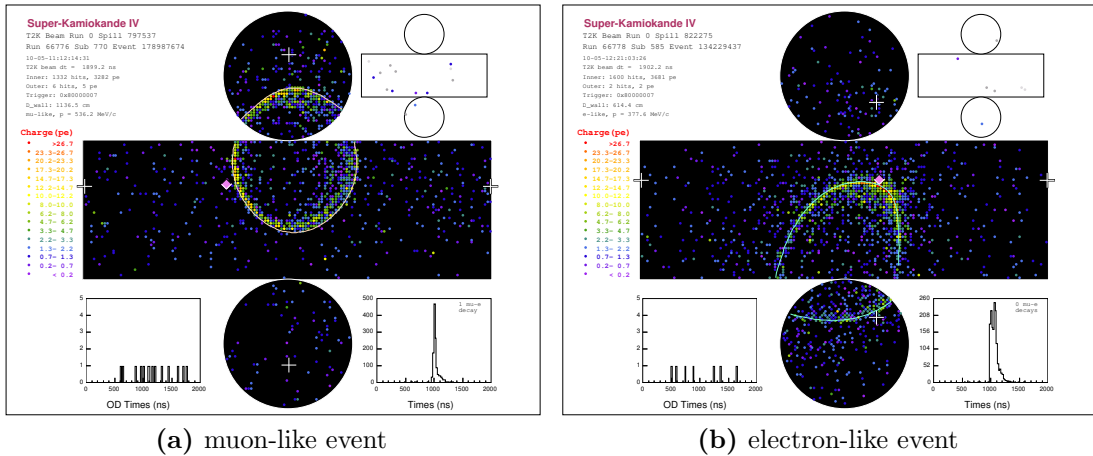


Figure 3.15.: Super-Kamiokande detector schematic. Figure taken from [55]

Provided that the charged particles produced by neutrino-induced interactions in the SK ID are above an energy threshold, a cone of Cherenkov light is seen as the particles traverse the water. Reconstruction of photons reaching the PMTs on the walls of the ID provides information regarding the interaction vertex position and momenta of particles. By studying the ring shape produced by the Cherenkov light, it is possible to infer the type of neutrino that induced the interaction. For the T2K ν_e appearance (ν_μ disappearance) analysis the relevant charged current quasi-elastic (CCQE) interaction in SK is ν_e (ν_μ) + neutron \rightarrow electron (muon) + proton. Hence, T2K looks to count the number of electrons (muons) produced in CCQE interactions in SK to extract neutrino oscillation parameters for ν_e appearance (ν_μ disappearance). The typical electron-like and muon-like Cherenkov rings seen in the SK detector can be found in Figure 3.16. Electron and muon-like events are easily distinguished; an electron undergoes multiple scattering making its ring “fuzzy”, whereas a muon is highly penetrating and produces a much sharper, well-defined ring.



(a) muon-like event

(b) electron-like event

Figure 3.16.: Example of reconstructed T2K events in Super-Kamiokande for (a) a muon-like ring and (b) an electron-like ring. Both figures show the cylindrical detector, unrolled onto a plane. Each coloured point represents a PMT, with the colour corresponding to the amount of charge, and the reconstructed cone is shown as a white line. The second figure in the upper right corner shows the same hit map for the OD. The white crosses indicate the location of the reconstructed vertex. The diamond marks the location where a ray starting from the event vertex and heading in the direction of the beam would intersect the detector wall. Figure and caption taken from [43].

Chapter 4.

ND280 offline software

This chapter discusses the software relevant to the analysis presented in this thesis. For information beyond the scope of the analysis see [56] and [57] for calibration and reconstruction details, respectively.

4.1. General overview

The ND280 offline software is used for both data and Monte Carlo (MC). The underlying framework of the software is based on ROOT [58]; GEANT4 [59] is used as the basic simulation library. The purpose of the software is to take raw data, or produce MC events, apply any relevant calibration chains and reconstruction algorithms and then save the output in a format suitable for the user, as can be seen in Figure 4.1.

For data, the raw events are unpacked into a C++ based “oaEvent” format. This oaEvent format is used throughout the ND280 software chain until events are saved into purely ROOT-based objects (in “oaAnalysis”), which are then used by the analyser. Next, the data is calibrated using both time-dependent and time independent routines. The time-dependent calibration applies parameters calculated based on detector and environmental conditions that are stored in a MYSQL database, whereas time-independent calibration parameters are hard-coded, as they are valid for any period in time. The events are then reconstructed, first on a sub-detector basis and then using a global reconstruction package. Finally, events are processed through the oaAnalysis package; this package saves ROOT-based objects and significantly reduces the output file size.

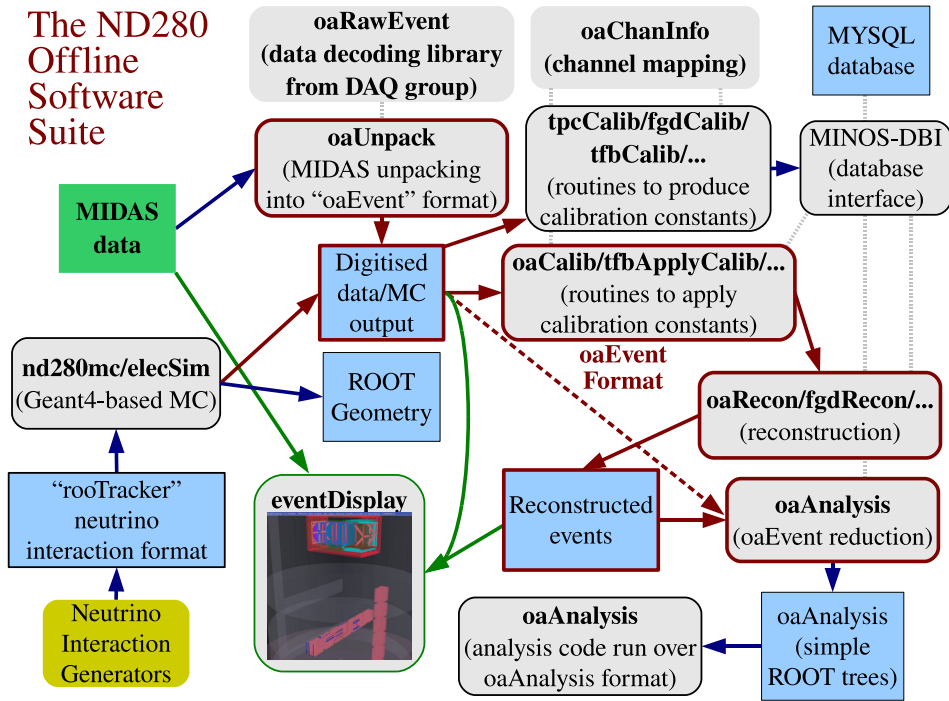


Figure 4.1.: Schematic of the package structure of the ND280 software suite. Only the most representative packages are included. Figure taken from [43].

For MC, the neutrino beam is simulated using JNUBEAM, as described in Section 3.2.4. The interaction of neutrinos with different nuclei in the ND280 detector is simulated using both GENIE [60] and NEUT [61] event generators. These events are then supplied to detector simulation packages called “nd280mc” and “elecSim”. The nd280mc package uses GEANT4 libraries to simulate the trajectories and energy deposits of final state particles, i.e. those escaping the nuclear environment, produced in the neutrino-induced interaction. The elecSim package is custom-written and is responsible for simulating the response of the electronics in the ND280 detector. At this stage, the MC is in the same format as the unpacked raw data. The MC then has the relevant calibration and reconstruction algorithms applied before finally being simplified by the oaAnalysis package.

4.2. ECAL geometries

The ND280 software defines both local and global ECAL geometries, as shown in Figure 4.2. The global geometry uses the same coordinate system as the whole ND280,

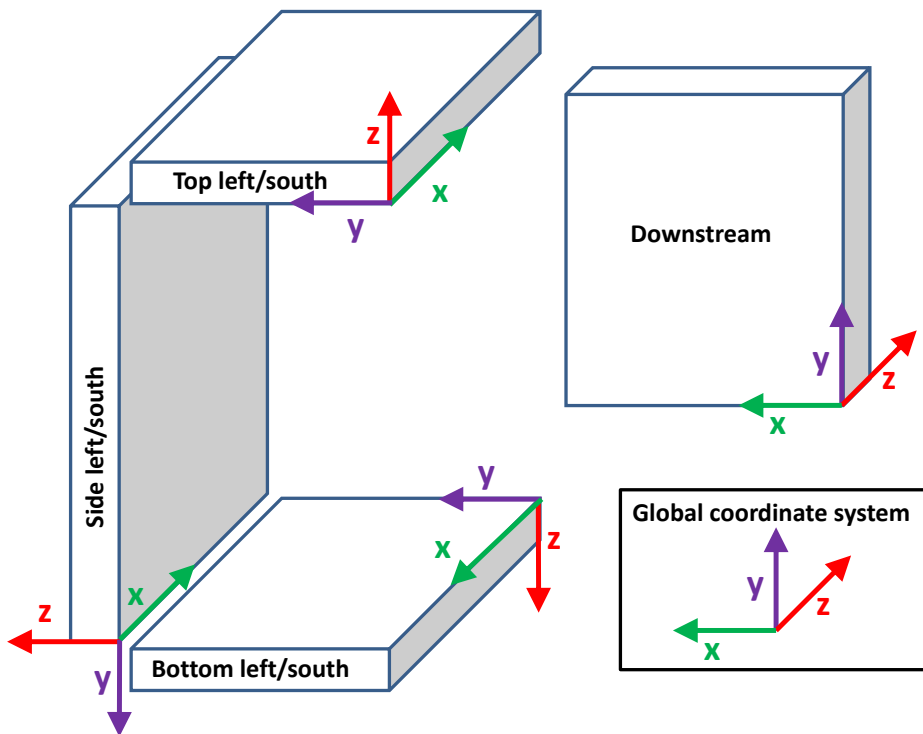


Figure 4.2.: The local ECAL geometry for the left/south side barrel ECAL modules and the downstream ECAL module. The right/north side barrel ECAL is simply a reflection of the left/south side. The downstream ECAL module has the same geometry as the global ND280 geometry. Additionally, the neutrino beam is travelling along the global z coordinate.

as shown in Figure 3.9. The local ECAL geometry is defined such that the z -axis is always pointing out of the ND280. This local geometry means that all ECAL modules can be treated in a similar manner when studying particles produced by neutrino-induced interactions in the ND280.

4.3. Calibration

This section focuses predominantly on the energy and time calibration applied to data collected using the ECAL in the ND280 off-axis detector. Details of the FGD, P0D

and SMRD (i.e. Trip-t based subdetectors) calibration can be found in [56], whereas an in-depth account of the TPC calibration is presented in [62] and [63].

To achieve good agreement between data and MC for the energy response several calibrations are performed. The pedestal¹ is subtracted and a correction is made to account for the non-linear response of the Trip-t to input charges. As the breakdown voltage of an MPPC varies linearly with temperature (approximately 50 mV per $^{\circ}\text{C}$), the gain must be calculated and stored for each channel individually. A correction is also made to account for the MPPC photon detection efficiency.

Good time calibration is important for effective clustering of hits, noise rejection and direction determination. There are several reasons the hit time of one MPPC may differ from that of another. Time offsets that arise due to different cable lengths between RMMs and TFBs (TFB offsets) and the SCM and RMMs (RMM offsets) are discussed in Chapter 5. Additionally, when a signal is received a timestamp is produced when the integrated charge exceeds a certain threshold. However, large signals (i.e. large charge) take less time to exceed the threshold than small signals, thus low charge signals have a delayed timestamp; this effect is called an electronics time-walk and is corrected for. A correction is also made to take into account the fibre time-walk that arises because the scintillation fluors in the Y11 wavelength shifting fibre emit light according to an exponential decay function; this means there is a time delay in the detection of the charge, which is integrated to make a timestamp. The length of the delay depends on the fibre time constant, the discriminator threshold and the total number of photoelectrons. The effect is statistical, meaning the magnitude of the time-walk will vary between identical events.

4.4. Tracker and global reconstruction

The tracker (two FGDs and three TPCs) and global reconstruction utilise routines provided by an external reconstruction toolkit called RecPack [64]. RecPack provides a series of functions for track fitting, propagation and matching whilst taking into

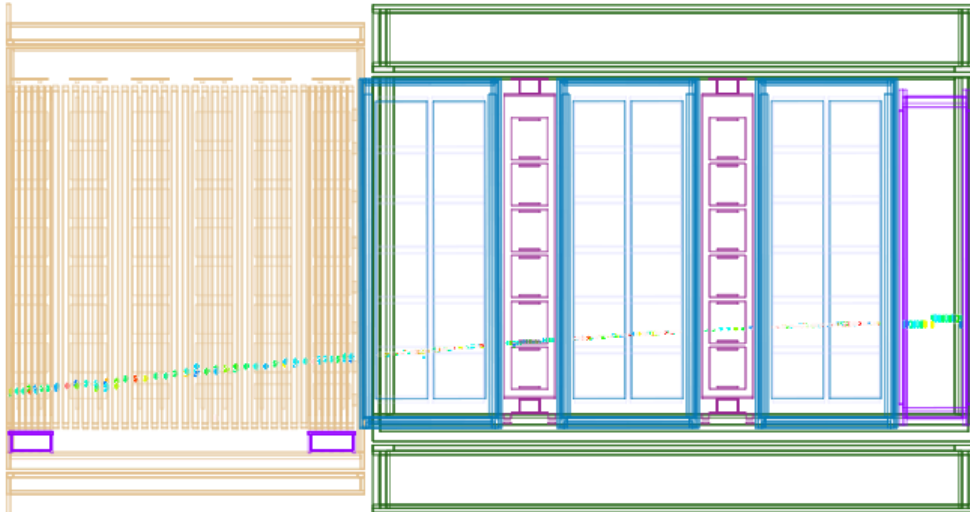
¹ The electronics output when there is no signal is referred to as the pedestal. The pedestal is due to electronics noise and a bias that is deliberately introduced to avoid very low charge in each integration cycle being supplied to the analogue-to-digital (ADC) converters, as there is a non-linear response at low charges.

consideration the ND280 geometry, magnetic field and multiple scattering and energy losses of particles.

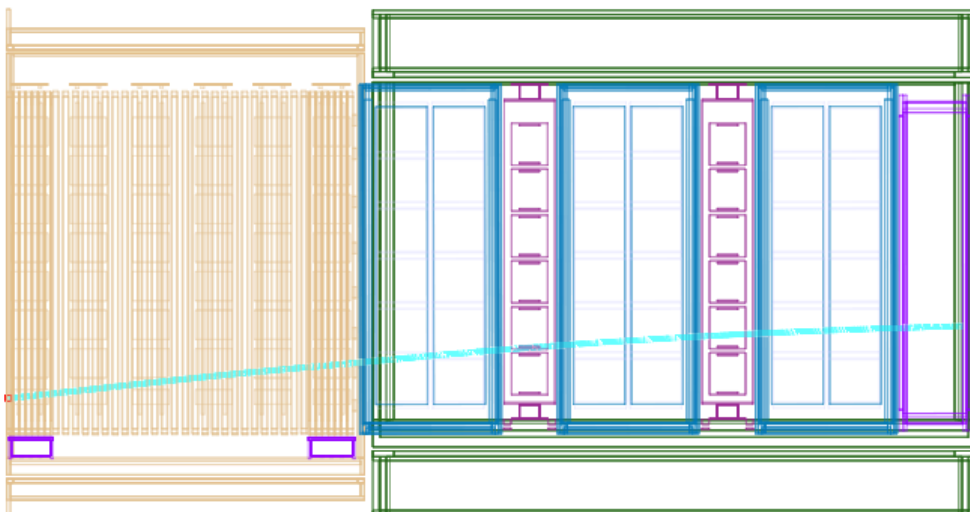
The tracker reconstruction has several stages. First, the TPC reconstruction algorithms are applied to the calibrated data and MC for each individual TPC in turn. The TPC reconstruction first groups TPC hits together if they are near in time and space and then uses pattern recognition algorithms to join the groups of hits together. A likelihood fit is performed to the fitted track to determine the track coordinates, angle and curvature. Additionally, the ionisation energy released in the TPC gas as function of the track length is calculated; this is for particle identification. Next, the TPC tracks are used to seed FGD reconstruction; a Kalman filter is used to incrementally match tracks from the TPC to hits in the FGD. Any hits remaining in the FGD after this incremental matching (assumed to be from tracks that are confined to the FGD) are reconstructed using algorithms that focus on the FGD only. Initially, in the isolated FGD reconstruction, hits are grouped together in the two views, XZ and YZ, using pattern recognition algorithms. These two dimensional views are then matched to form a three dimensional track. The charge weighted position of any remaining hits or unmatched two dimensional tracks is saved². Finally, the tracker reconstruction algorithms use a Kalman filter to join all TPC and FGD tracks together. The track direction is also determined using timing information from the FGDs.

The purpose of the global reconstruction is to combine results from all subdetector reconstruction packages. An event that was reconstructed using the global reconstruction package can be found in Figure 4.3. Initially attempts are made to match reconstructed objects in the tracker to neighbouring subdetectors i.e. the ECAL and P0D. This matching is done by extrapolating the tracker track into the subdetector in question and searching for reconstructed objects near the entry position of the track. Objects are matched together if the resultant χ^2 , from a fit performed based on the position and direction of the object, is less than 100 (or 200 for the case of matching to objects in the P0D and SMRD). A very loose time cut requiring reconstructed objects to be within 300 ns is also made. Finally, the track is refit using a Kalman filter and, taking into account expected energy losses and the individual reconstructed momentum for the objects, the position, direction and momentum are recalculated. The global reconstruction repeats this procedure until no more objects can be matched together. Attempts are also made

² These remaining FGD hits are used to try to locate an NC $1\pi^0$ vertex, as discussed in Section 6.6.



(a) Calibrated ND280 hits



(b) Reconstructed global track

Figure 4.3.: An ND280 data event showing (a) calibrated hits and (b) the globally reconstructed track. The event (number 146768) is from a beam spill trigger in ND280 run 6829, sub-run 34. The beam direction is from left to right. The track traverses the P0D, TPC1, FGD1, TPC2, FGD2, TPC3 and the DsECAL.

to combine ND280 objects that do not have a tracker component, for example tracks traversing the P0D and SMRD.

TPC particle identification

TPC particle identification (PID) relies on the energy loss of charged particles per unit length and features in the analysis presented in Chapter 6 (for an in depth description of the TPC PID see [62] and [65]).

As previously stated, the TPC reconstruction first clusters hits close in position and time and then joins clusters together to form a track. For the PID calculation, a truncated mean, which was optimised using both test beam studies and Monte Carlo simulations and is defined as the lowest 70% of cluster charges, is calculated for each TPC track in turn. This truncated mean represents the energy loss of the particle in the gas. Figure 4.4 shows the measured energy loss as a function of the reconstructed particle momentum and the expected curves for different particle hypotheses (muon, electron, proton and pion).

For the PID, a pull, which is a measure of the number of standard deviations a measured energy loss $(dE/dx)^{\text{measured}}$ is away from the expected value $(dE/dx)_{\alpha}^{\text{expected}}$ for a given particle hypothesis, is defined as

$$\text{pull}_{\alpha} = \frac{(dE/dx)^{\text{measured}} - (dE/dx)_{\alpha}^{\text{expected}}}{\sigma((dE/dx)^{\text{measured}} - (dE/dx)_{\alpha}^{\text{expected}})}, \quad (4.1)$$

where α represents the particle species (electron, muon, proton or pion). The resolution is $\sim 7.8\%$ for minimum ionising particles.

FGD particle identification

The particle identification in the FGD was initially developed for tracks created by protons, charged pions and muons that are contained within the FGD (studies found that less than 1% of kaons and electrons stop in the FGD), i.e. the particles deposit all their kinetic energy in the FGD and do not enter a TPC.

A pull variable, constructed using the observed and expected energy loss, is used to distinguish between different particle species. For each particle type, $i = \text{muon, pion, proton}$, the pull hypothesis is defined as

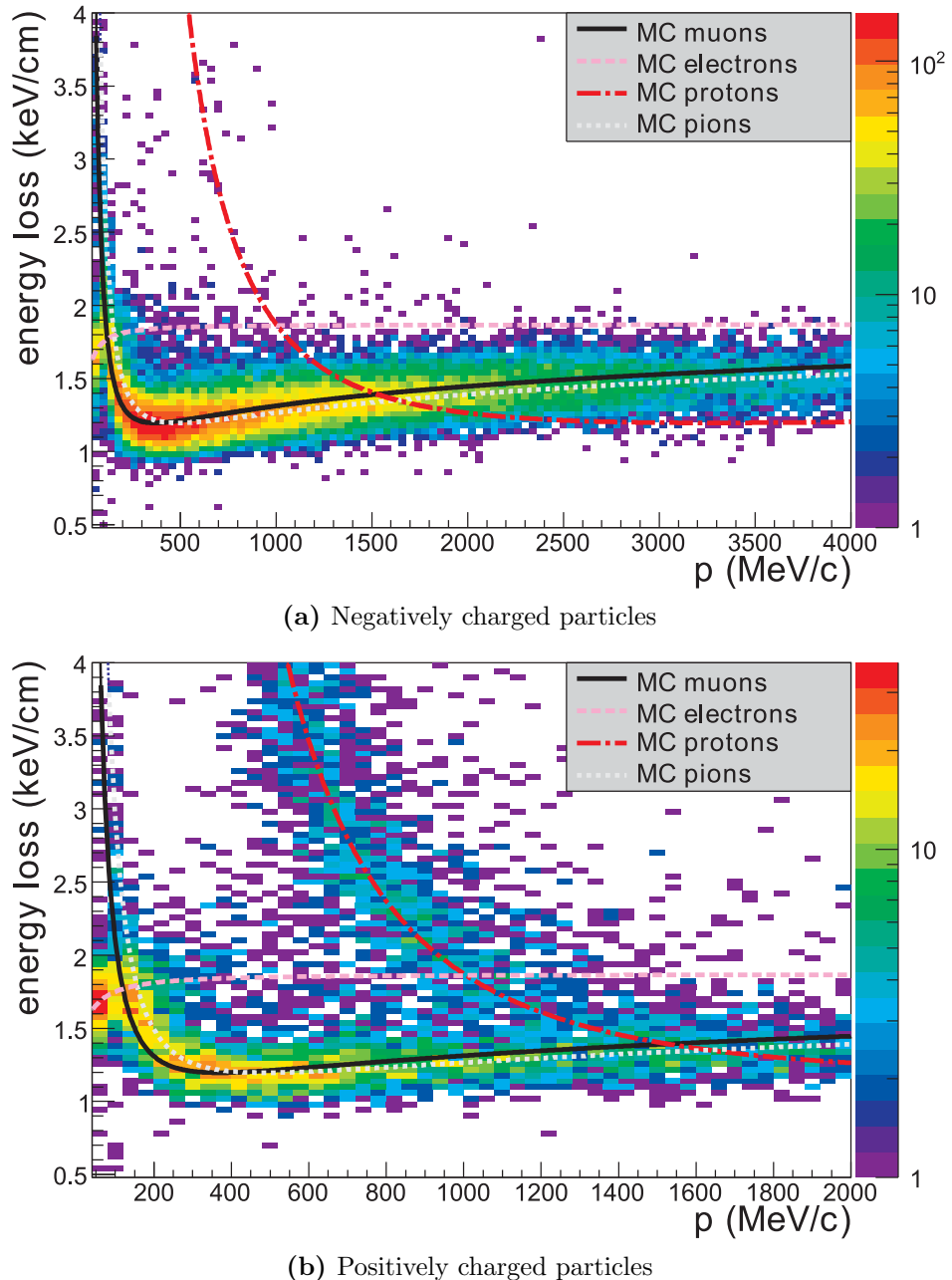


Figure 4.4.: Distribution of the energy loss as a function of the momentum for negatively and positively charged particles produced in neutrino interactions in the Run 1 ND280 data set, compared to the expected (MC) curves for muons, electrons, protons, and pions. Figure and (edited) caption taken from [62].

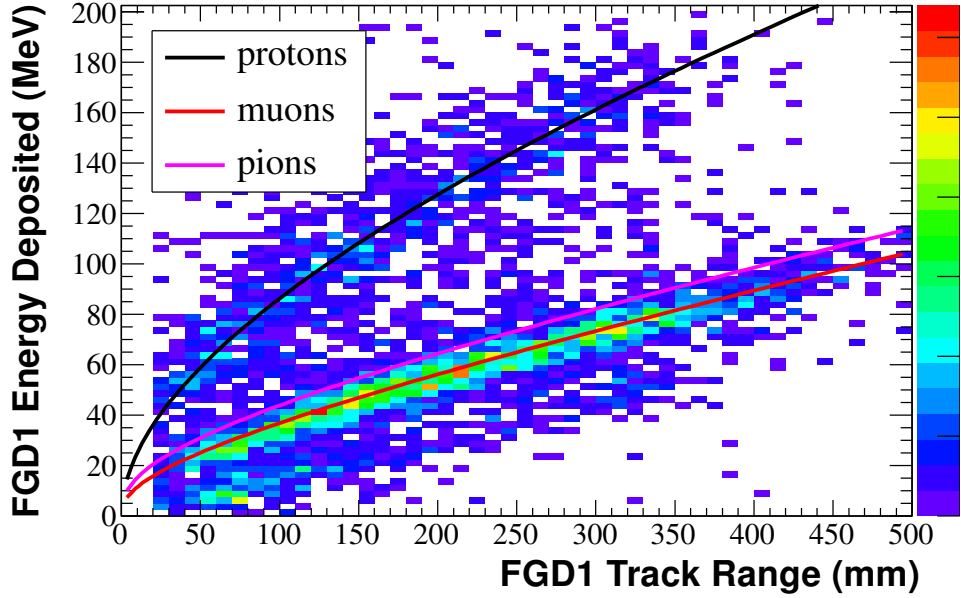


Figure 4.5.: Reconstructed track range and energy deposited for tracks that stop in FGD1, having traversed more than three FGD1 layers. Tracks that have a TPC1 component are used if they have more than 60 hits and meet the following PID requirements. For the proton hypothesis, the absolute muon and pion pull are required to be greater than 2.5, whereas the absolute proton pull must be less than 2.5. To select muons and pions, the absolute pull of the proton must be greater than 2.5 with an absolute muon and pion pull less than 2.5. The data plotted is Run 1 and Run 2 ND280 data; the expected energy loss curves based on Monte Carlo studies for muons, pions and protons are overlaid

[22].

$$\text{pull}_i = \frac{E - E_i(x)}{\sigma_i(x)}, \quad (4.2)$$

where E is the measured energy deposited and $E_i(x)$ and $\sigma_i(x)$ are the expected energy deposited and resolution for a measured track length x , respectively. Figure 4.5 shows the track range and energy deposited for tracks in FGD1 for Run 1 (March 2010 – June 2010, 2.888×10^{19} POT) and Run 2 (November 2010 – March 2011, 7.832×10^{19} POT) data.

Whilst the PID method is not suitable for separating muons and pions, it provides a good discriminator for protons that stop in the FGD. The PID study is ongoing and current work includes the addition of an electron identification for stopping tracks, this should be especially useful for identifying electrons produced by pions that stop in the

FGD and Michel electrons from cosmic muons that stop in the FGD. Work is also being done to expand the method to include tracks exiting the FGD using additional TPC information.

4.5. ECAL reconstruction and performance

This section details the barrel and downstream ECAL reconstruction and performance, as they play a large role in the analysis presented in Chapter 6. The P0DECAL, due to its simple structure, uses different reconstruction algorithms and is not described here. Reconstruction in the ECAL is performed by a dedicated package called “ecalRecon,” which takes calibrated hits and outputs three dimensional reconstructed objects.

4.5.1. Hits and clustering

Hit preparation

Each calibrated hit has a time and a position in two dimensions based on the layer and bar location of the hit. At this stage in the reconstruction the position of the hit down the bar is not known. Thus, hits are considered in two views, (local) XZ and (local) YZ. After a charge cut of 0.3 PEU, where PEU stands for pixel-equivalent units and is obtained by converting the charge from each MPPC sensor into a number of pixels fired, the reconstruction considers groups of hits in windows of 50 ns separately.

The “recombination” of the charge and time associated with a hit may be necessary if the bar containing the hit has double ended readout. For double ended bars, each hit may correspond to two calibrated hits, as a hit represents information read out from a sensor. All DsECAL bars and the longer BrECAL bars have double ended readout, as discussed in Section 3.3.3. Thus, the charge and time of these hits are “recombined” and an estimate of the unknown coordinate is made.

Next, a correction is applied to account for the light attenuation in the WLS fibre and to equalise all the channels connected to a TFB. All charges are now in MIP equivalent units (MEU), this is the most probable value of charge deposited by a minimum-ionising particle (MIP), where 1 MEU is approximately 25 PEU.

Two dimensional clustering

The algorithms in the two dimensional clustering consider clusters in the (local) XZ and (local) YZ views separately. By selecting the hit in the 50 ns group with the highest charge as a seed, the clustering algorithms search for hits to cluster together. If a hit is within ± 15 ns of the seed, is in the neighbouring or next to neighbouring bar and is in the neighbouring or next to neighbouring layer, it is clustered with the seed hit. This process is then repeated using every hit in the cluster as a seed.

The second stage of clustering is to combine any of the clusters formed in the first step, provided there are three or more hits in the cluster. The cluster with the most hits is used as a seed and is combined with another cluster if the average time of the candidate cluster is within 40 ns of the seed. A discriminator, based on the width of the clusters and a charge weighted axis output from a principal component analysis (PCA), is also used. Finally, attempts are made to match any unclustered hits with the two dimensional clusters.

Three dimensional clustering

A likelihood based on the ratio of cluster charges and the difference in starting layer (the layer with the smallest local z coordinate) between clusters is used to decide if two dimensional clusters should be matched to make one three dimensional cluster. The matching also considers any clusters produced from the tracker reconstruction as a seed. By forming the likelihood variable for all possible combinations of clusters the best possible match is selected.

There is also a re-matching step that tries to associate unclustered hits with any two dimensional clusters that have not successfully been matched to form three dimensional clusters. This step is especially important for reconstruction of low energy particles, namely photons, where there is perhaps only a single hit in one view and a cluster in the other. Any single hits are required to be within 10 ns of the mean cluster time and the layer containing the hit, L_{hit} is required to be within $L_{\text{min}} - 1 \geq L_{\text{hit}} \leq L_{\text{max}} + 1$, where $L_{\text{min(max)}}$ is the minimum (maximum) layer of the (two dimensional) cluster.

The three dimensional clusters make it possible to (re)calculate the unknown hit coordinate for hits in (double) single ended bars using hits in the other view. Subsequently,

the attenuation correction and the MIP equalisation are reapplied based on the new reconstructed position.

4.5.2. Photon reconstruction efficiency

The photon reconstruction efficiency as a function of energy and angle for the top north, side north and the downstream ECAL is presented. To avoid repetition, these ECAL modules were chosen as they are an accurate representation of all other modules. The plots for the top north module have the same results as the top south, bottom north and bottom south ECAL modules. Similarly, the results for the side north module is representative of the side south ECAL module.

The plots were made by selecting photons that convert in the ECAL from NC $1\pi^0$ interactions in FGD1 and FGD2. Figure 4.6 shows the true energy of the high and low energy photons and ECAL entry angle (with respect to the local z axis in that module) for photons produced in NC $1\pi^0$ interactions. The comparisons suggest, and are confirmed by Figure 4.7, that the reconstruction efficiency of photons from NC $1\pi^0$ interactions is poor at low energies; this is not unexpected. The reconstruction efficiency as a function of entry angle is flat, but becomes poor at high angles. The reconstruction efficiency as a function of the opening angle between photons is also plotted in Figure 4.8 for the case where both photons convert in the downstream ECAL, the barrel ECAL and where one photon converts in the DsECAL and one in the BrECAL. All ECAL modules perform well at small opening angles and have a smaller reconstruction efficiency at large angles.

4.5.3. Energy estimation

The energy of the three dimensional reconstructed clusters is estimated using an energy fitting algorithm. The algorithm uses a likelihood function with three parameters: the total charge; the rms of the charge divided by the mean charge and the skew of charge in the cluster. The fitting procedure was tuned using Monte Carlo particle gun photons with energies ranging from 75 MeV to 25 GeV, with the coverage focussed toward the region below 2 GeV.

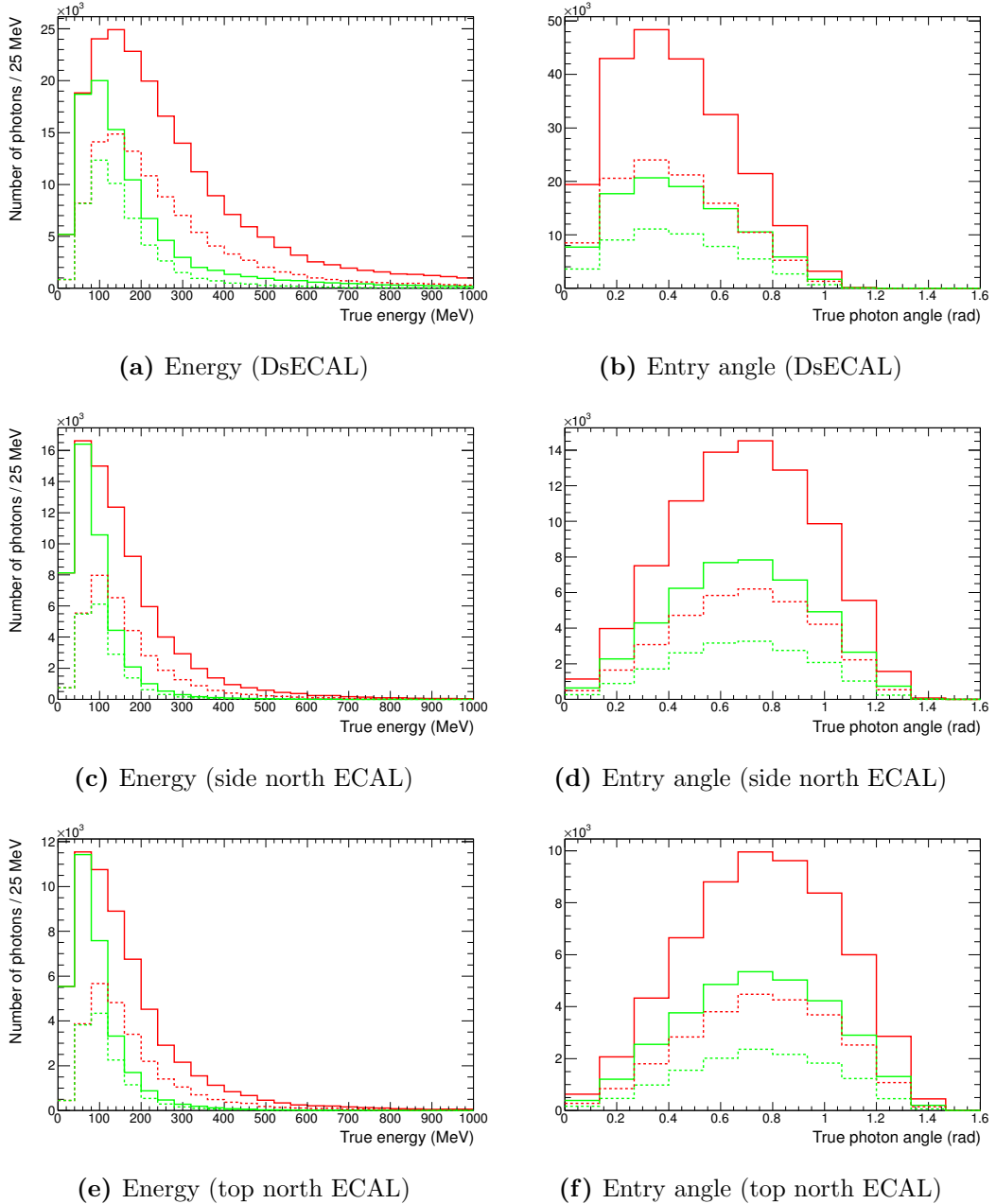


Figure 4.6.: True energy and true ECAL entry angle (with respect to the local z axis) for photons produced in NC $1\pi^0$ interactions in FGD 1 and FGD 2. The solid lines represent photons that convert in the ECAL in truth, whereas the dashed lines are for the photons that convert in the ECAL in truth *and* are reconstructed in the ECAL. The red and green lines represent the high and low energy photons, respectively. The plots were made using cherry picked Monte Carlo.

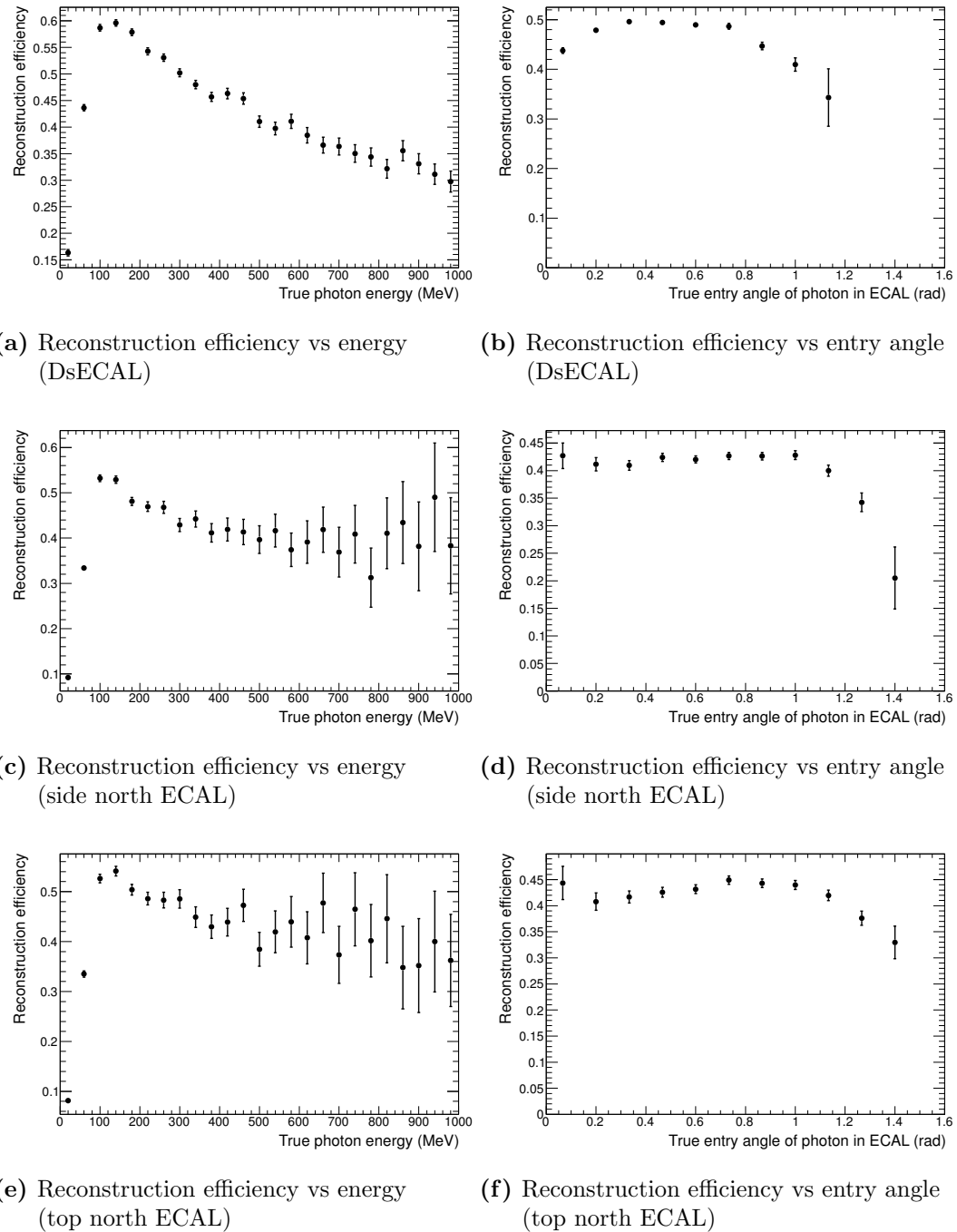


Figure 4.7.: Reconstruction efficiency as a function of true photon energy and true ECAL entry angle for photons from NC $1\pi^0$ interactions in FGD 1 and FGD 2. The plots were made using cherry picked Monte Carlo.

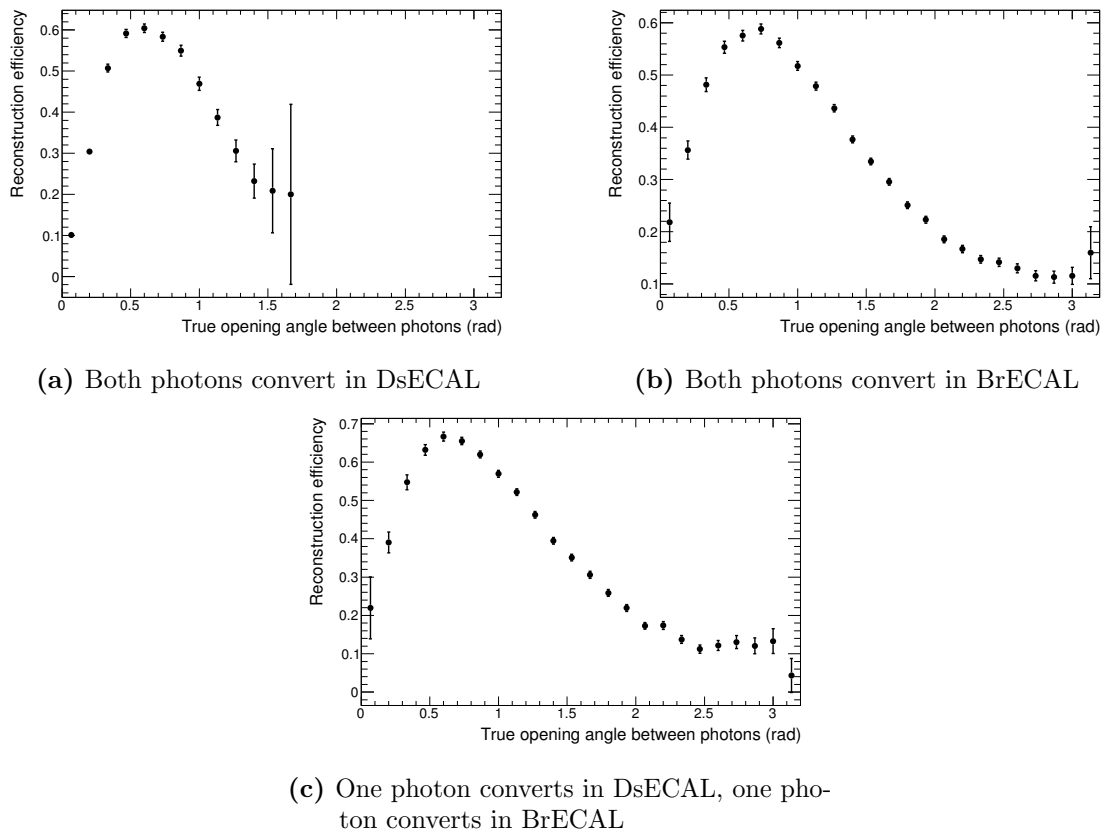


Figure 4.8.: Reconstruction efficiency of photons from NC $1\pi^0$ interactions in FGD1 and FGD2 as a function of the true photon opening angle between ECAL clusters. The plots were made using cherry picked Monte Carlo.

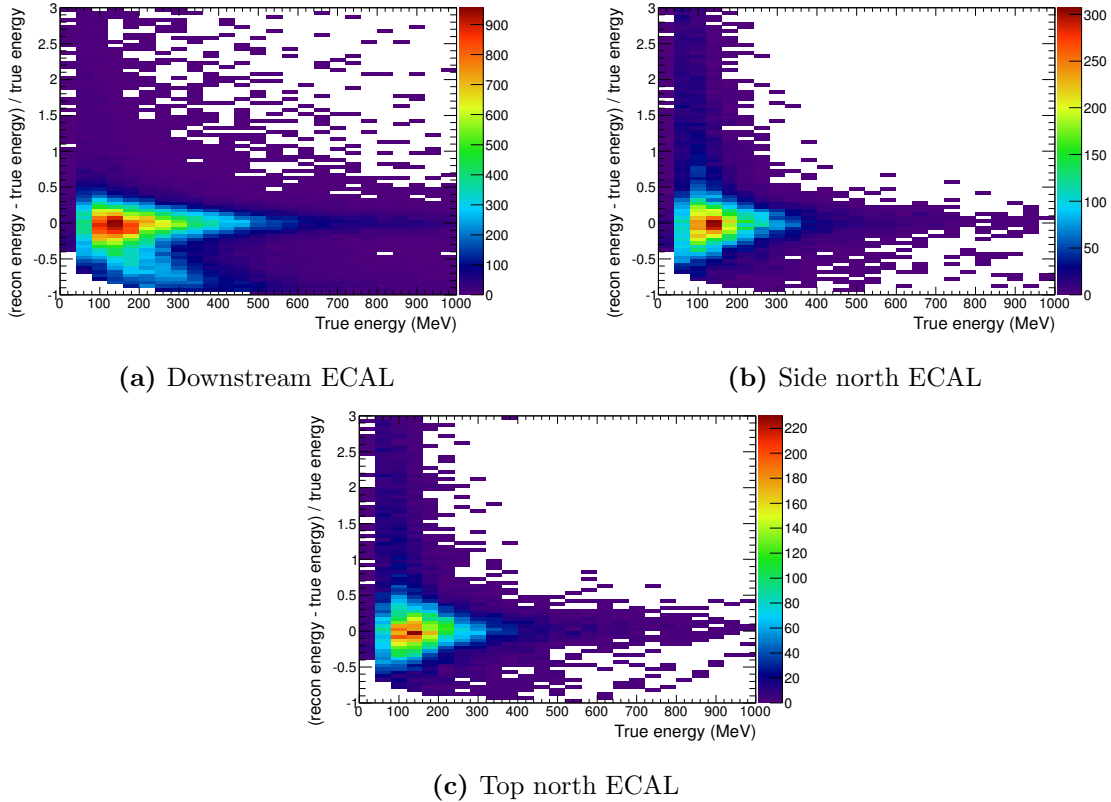


Figure 4.9.: Comparison of true and reconstructed energy for photons converting in the ECAL from NC $1\pi^0$ interactions in FGD1 and FGD2. The plots were made using cherry picked Monte Carlo.

As photon reconstruction in the ECAL is the main focus of this thesis, a comparison between true and reconstructed photon energy can be found in Figure 4.9³. The plot was made using Monte Carlo equivalent to 2.266×10^{23} POT for true NC $1\pi^0$ interactions in FGD1 and FGD2 where both photons from the π^0 convert in the ECAL. All ECAL modules show good agreement between true and reconstructed photon energy. However, the energy reconstruction for the downstream ECAL (Figure 4.9a) shows that for a significant number of photons, the reconstructed energy is an underestimate. Investigation into this discrepancy finds that 77% (85%) of the high (low) energy photons contributing to the underestimate are from interactions in FGD 1. This is not surprising as energy losses are expected as the photon travels through TPC2, FGD2 and TPC3 before converting in the downstream ECAL.

³ The modules shown are the top north, side north and downstream ECAL, for reasons explained in Section 4.5.2.

4.5.4. Particle identification

The particle identification in the ECAL aims to separate track-like clusters from those that resemble showers.

The fitting of shower-like objects, i.e. those created by electrons and photons, is centred around a three dimensional PCA. The (three dimensional) position of each hit is added to the PCA a number of times based on its charge; this ensures the hits that have the highest charge are given the most weight. The track fitting algorithm, which is best suited for clusters created by MIPs, first fits tracks to the two dimensional views of the clusters. These tracks are then combined and refit in three dimensions.

A discriminator called track/shower value was developed to distinguish between track- and shower-like clusters. All reconstructed three dimensional clusters are fitted with both the track and shower fitting algorithms, which means analysis-level decisions can be made for the PID. The algorithm used to produce the track/shower value is an artificial neural network (ANN) implemented using the TMVA package in ROOT. The ANN input variables are the axis max ratio, max ratio, EM likelihood, shower angle and shower width.

The axis max ratio (AMR) is calculated by taking the mean of the ratio of the primary and secondary components of the PCA for each two dimensional cluster. The ratio is bounded between 0 and 300, as the ratio can approach infinity for objects with a very small width (secondary component). Thus, shower-like clusters have a low AMR, whereas tracks-like clusters have a large AMR.

The max ratio is a ratio of the charge in the layers with the largest and smallest total charge, neglecting layers with no charge deposited. Track-like clusters are expected to have a max ratio of approximately one. Shower-like clusters are likely to have both a high and low charge density region, meaning the max ratio should be larger than the value calculated for tracks.

The EM likelihood is the result of the energy fit described in Section 4.5.3. Shower-like events have an EM likelihood near zero whilst track-like events have larger values.

The shower angle is the arctan of the ratio of the secondary and primary components from a three dimensional PCA of the cluster. By construction, this angle is bounded between zero (track-like) and one (shower-like).

The shower width is the (normalised) tertiary component produced in the three dimensional PCA of the cluster and thus varies between zero and one. Shower-like clusters have a larger physical width than track-like clusters, meaning that they are expected to have a larger shower width than tracks.

The variable track/shower value is the output of the ANN and is loosely bounded between zero (shower-like) and one (track-like), as it is an approximation of a likelihood. The analysis detailed in Chapter 6 uses the track/shower value to select photons in the ECAL from NC $1\pi^0$ interactions in FGD1 and FGD2. Photons, especially the low energy photon from π^0 decay, often appear to be track-like, this is due to the fact that many clusters are formed in the re-clustering (Section 4.5.1) stage of the ECAL reconstruction and, as a result, have a small number (4 – 6) of hits per cluster.

New particle identification variables are in the final stages of verification and development at the time of writing and will be available for use in all future official ND280 data and MC productions. The new particle identification variables are based on low-level quantities combined with a likelihood-based method and provide a discriminator to tag showering π^\pm in a sample of MIP-like clusters and to separate electrons from protons.

4.5.5. Direction reconstruction

Good direction reconstruction in the ECAL is especially important when trying to select NC $1\pi^0$ interactions in FGD1 or FGD2 where the decay photons from the π^0 convert in the ECAL. Often there will be no tracks or unclustered FGD hits to use to locate a vertex, generally the only information available for vertex finding is that from the ECAL. The reconstructed direction of the cluster can be used to point the clusters back into the tracker to try and reconstruct a vertex.

There are two different methods used to produce sets of variables that can be used to infer the direction of a cluster. The first method uses the eigenvectors output from a PCA of the charge weighted hits in the cluster, where the primary eigenvector (the one with the largest eigenvalue) is the direction along the longest axis of the cluster. A second method for direction determination of ECAL clusters⁴ is to use an adaptation of a (jet physics) “thrust” algorithm. This method makes the prior assumption that the particle is travelling from the centre of the ND280 outward, i.e. the local z component

⁴ This method was developed especially for selecting photons from NC $1\pi^0$ interactions in the ECAL. Further information regarding development and performance can be found in [66]

increases with time. Whilst this is a fair assumption for neutrino-induced interactions inside the tracker, it removes the possibility of rejecting interactions of neutrinos and cosmic rays in the magnet or within the ECAL. The thrust, t , is defined as

$$t(\theta, \phi) = \frac{\sum_i q_i |\vec{n}_{\theta, \pi} \cdot (\vec{x}_i - \vec{o})|}{\sum_i q_i |\vec{x}_i - \vec{o}|}, \quad (4.3)$$

where \vec{o} is the thrust origin, defined as the charge weighted mean position of hits in the innermost layer (i.e. the layer with the smallest local z coordinate), $\vec{n}_{\theta, \pi}$ is a unit vector with polar angles θ and ϕ and q_i and \vec{x}_i are the charge and three dimensional position of the i th hit in the cluster, respectively. The “thrust axis”, which is said to be the direction of the cluster, corresponds to $\vec{n}_{\theta, \pi}$ when the value of t is maximal.

The thrust axis is used to estimate the photon direction in the NC $1\pi^0$ analysis presented in this thesis. A comparison between true and reconstructed angle can be found in Figure 4.10⁵.

⁵ The modules shown are the top north, side north and downstream ECAL, for reasons explained in Section 4.5.2.

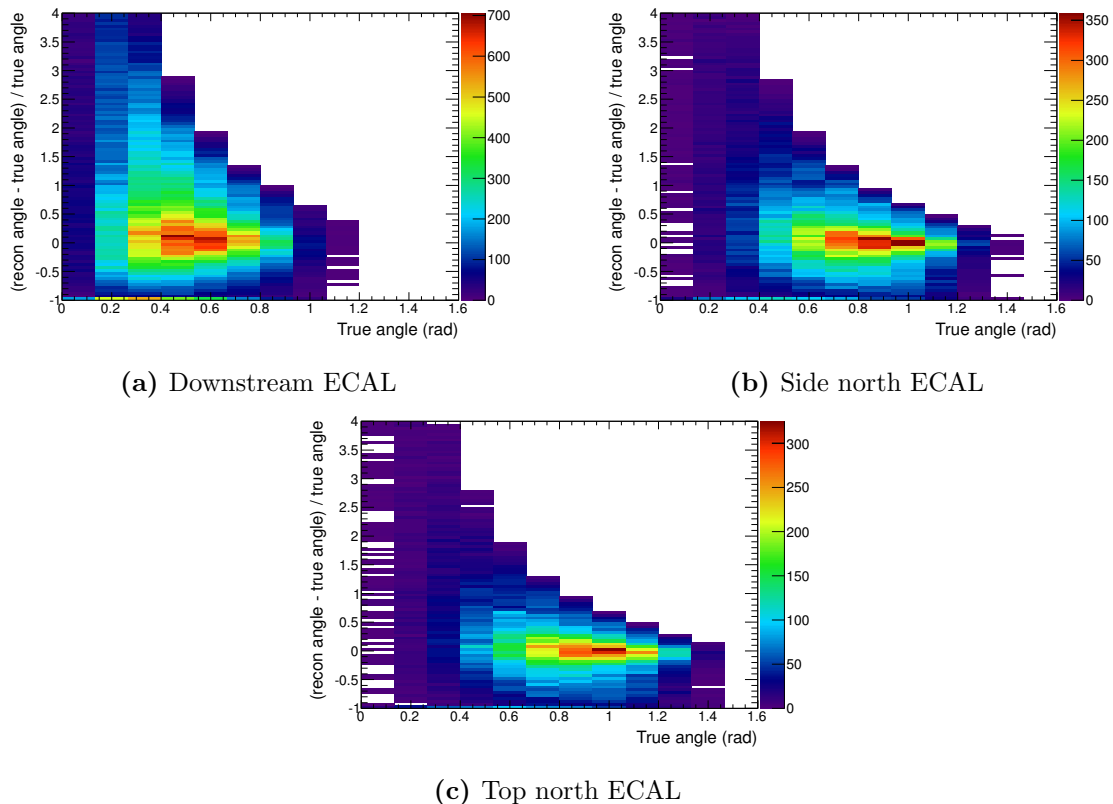


Figure 4.10.: Comparison of true and reconstructed angle for photons converting in the ECAL from NC $1\pi^0$ interactions in FGD1 and FGD2. The angle was calculated using the local z coordinate of the thrust axis. The plots were made using cherry picked Monte Carlo.

Chapter 5.

Calibration of the barrel and downstream ECAL time offsets

Good time calibration of the ECAL is essential for effective clustering, the rejection of noise hits and particle direction determination. This section describes the calibration of the time offsets for the barrel and downstream ECAL modules arising as a result of differing cable lengths between the MCM and RMMs (called RMM offsets) and each RMM and the TFBs connected (called TFB offsets), as described in Section 3.3.3. The PODECAL is not calibrated using the method outlined in this chapter, as its structure is simpler than the barrel and downstream ECAL.

5.1. Data samples

This calibration uses inter-spill cosmic muon data from a selection of the Run 2 data, taken between November 2010 and March 2011. Inter-spill cosmic muon data is used, as opposed to beam spill data, as it provides a uniform distribution of hits over the whole ECAL. This uniformity is achieved by pre-scaling certain cosmic trigger configurations during data taking. To ensure ample statistics, approximately 20 sub-runs, where one sub-run corresponds to approximately 20 minutes of data taking, are required to produce an accurate set of offsets¹. Only runs with 25 sub-runs or more are used in this calibration. The first reason for this condition is that 10 ns shifts in the time of the RMMs have been

¹ For completion, the runs used to determine the RMM and TFB time offsets are: 6462, 6466, 6474, 6520, 6552, 6604, 6606, 6754, 6778, 6784, 6830, 6834, 6838, 6870, 6906, 6914, 6916, 6924, 6930, 6932, 6944, 6948, 6958, 6960, 6964, 6966, 6462, 7360, 7394, 7406, 7418, 7420, 7432, 7454, 7456, 7458, 7480, 7490, 7492, 7496, 7504, 7508, 7616, 7622, 7626, 7668, 7672, 7680, 7688, 7694, 7700, 7702, 7728, 7736,

found to occur. Initially it was thought to be a result of power-cycling of the electronics, but further investigation has shown that these 10 ns time jumps occur as a result of temporary optical link losses in the Rocket I/O cables that connect the MCM to the SCM and, subsequently, to the RMMs. Using sub-runs from the same run was thought to reduce the likelihood of large time discrepancies. The second reason for the requirement is that, unfortunately, no official data quality information regarding the status of the ND280 detector is available for this data. Data quality information is made available in the oaAnalysis package. The data used to determine the time offsets is not reconstructed using the whole ND280 reconstruction software, as it was deemed unreliable at the time this study was undertaken, and as a result, cannot be processed through the oaAnalysis package. The assumption was made that longer runs would prove to be of a good quality. The logs made by ND280 shifters at the time of data taking were also studied to ensure good quality.

First the raw data is calibrated. At the time of this study there was already a basic calibration method in place for the downstream ECAL, the offsets of which were produced using raw (i.e. no calibration or reconstruction was applied) Run 1 data taken between March 2010 and June 2010, when only the DsECAL was *in situ*. Thus, it was important to ensure the time offsets for both the TFBs and RMMs are not applied during calibration. Next, the calibrated data is reconstructed using a simple track fitting algorithm. This track fitting algorithm uses the basic clustering, described in Section 4.5.1, but no timing information and only the position of hits in the ECAL module to fit a track to hits in the event. To ensure the rejection of noise hits an additional charge cut requiring hits to be greater than 8 PEU is imposed.

Unfortunately it is not possible to optimise and verify the accuracy of the method outlined in this chapter using cosmic Monte Carlo (MC). The hit time distribution of the cosmic MC is flat and therefore does not resemble that seen in the data, meaning measurable time offsets cannot be introduced to the MC. Thus, all plots in this chapter were made using the Run 2 data detailed previously.

7744, 7746, 7750, 7752. Only runs with even run numbers are used to produce the constants. Runs with odd numbers are used to validate the method and determine the resolution.

RMM	Number of TFBs	ECAL module
0	28	Downstream
1	28	Downstream
2	15	P0D South
3	44	Barrel Top South
4	44	Barrel Bottom South
5	26	Barrel Side South
6	26	Barrel Side South
7	15	P0D North
8	26	Barrel Side North
9	26	Barrel Side North
10	44	Barrel Bottom North
11	44	Barrel Top North

Table 5.1.: Location and number of TFBs connected to each ECAL RMM.

5.2. Method for calculating TFB offsets

There were several factors to consider when deciding upon a method to calculate the TFB offsets. The SMRD towers used for triggering have different cable lengths, which could introduce a latency and affect the hit time relative to trigger. As a result of this latency, it is not possible to compare hit times from different events, as they may have triggered on different towers. Also, cosmic muons with different ECAL detector combinations have different times. Consider a track that propagates through the top ECAL module and then the DsECAL, this results in late hit times in the DsECAL. However, a track going through the DsECAL and then the bottom ECAL module will have early hit times in the DsECAL. Thus, the actual hit time on a TFB cannot be used as a comparison, only the time difference between TFBs.

For completeness, the location and number of TFBs on each ECAL RMM can be found in Table 5.1.

First for all hits in the data sample, the unknown coordinate is determined using the equation of the line fit to the reconstructed track in that event. The need to infer one spatial coordinate arises from the nature of the ECAL bars. A correction is also made to

each hit to account for the time of flight within a module. To make this correction it is assumed that the cosmic muon is travelling downward and that it travels at the speed of light. The entry position of the cosmic ray into an ECAL module, \vec{a} , is determined using an extrapolation of the fitted track. Thus, the time of flight of the muon, t_i , for each hit i is determined using

$$t_i = \frac{|\vec{a} - \vec{x}_i|}{c}, \quad (5.1)$$

where \vec{x}_i is the 3-dimensional position of the i th hit. The hit time is also corrected to take into account the time taken for the light to travel down the bar to the MPPC.

Next, the time difference between TFBs in each event must be calculated. As there are no events that illuminate every TFB on an RMM with hits², it is necessary to correct TFB a back to TFB b for each event in which the combination occurs, for all TFBs on an RMM. A slightly adapted version of Prim's algorithm [67] is used to determine a mapping of TFB combinations that occur together most frequently. A weighted graph is produced using each TFB combination present in the data, where the weight is the number of times that a specific TFB combination occurred. Then, starting at a TFB chosen at random, a map (spanning tree) between TFBs is constructed by maximising the weight between TFBs, as shown in Figure 5.1. This mapping of TFBs is determined using all good hits³ for all events in the 20 sub-runs and is determined every time the offsets are calculated. This need to redetermine the map arises as data taking trigger configurations and prescales can be changed and may result in a change in the occupancy of hits on a TFB. By iterating over all hits in an event the pairs of TFBs specified by Prim's algorithm are found. The mean time for each TFB is determined, as there are often a number of hits per TFB per event, and the time difference between TFB pairs is saved. This is repeated for all events.

After searching through every event for TFB pairs, a distribution of hit time differences is built up, an example of which can be seen in Figure 5.2. To determine the offset, O_i , for TFB i with respect to TFB c (usually TFB 0) on that RMM, the local offsets between TFBs are added according to the result of Prim's algorithm,

² The ECAL does have a light injection (LI) system that would allow a flash of light be applied to each TFB at the same time. However, at the time of writing this system has not been fully commissioned.

³ A good hit has a valid time and charge and is part of the track fit using the simple track fitting algorithm.

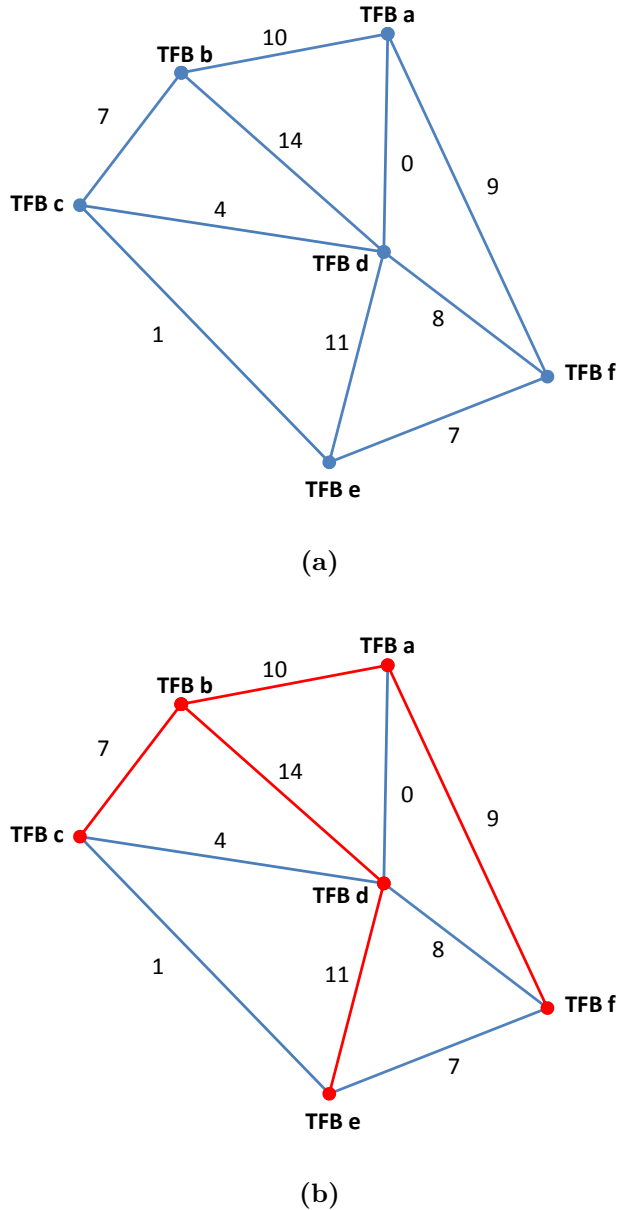


Figure 5.1.: (a) is an illustrative example of a weighted graph. The number of times specific TFB combinations occur in data is used to produce weights between TFBs. For example, the graph shows that there are eleven events that produce hits on both TFB d and TFB e, whereas no events produce hits on both TFB a and TFB d. The red lines connecting TFBs in (b) represent the spanning tree constructed by maximising the weighted graph in (a). To make the maximum spanning tree, first a vertex (TFB a) is chosen at random and the edge with the largest weight (ten) connected to the vertex is selected. This edge connects TFB a to TFB b. Next, all edges connected to vertices TFB a and TFB b are considered and the edge with the largest weight (TFB b – TFB d) is selected. All edges connected to vertices TFB a, TFB b and TFB d are then considered and the edge with the largest weight (TFB d – TFB e) is selected. This process of selecting the edge with the largest weight continues until all vertices (TFBs) are connected, as shown in (b).

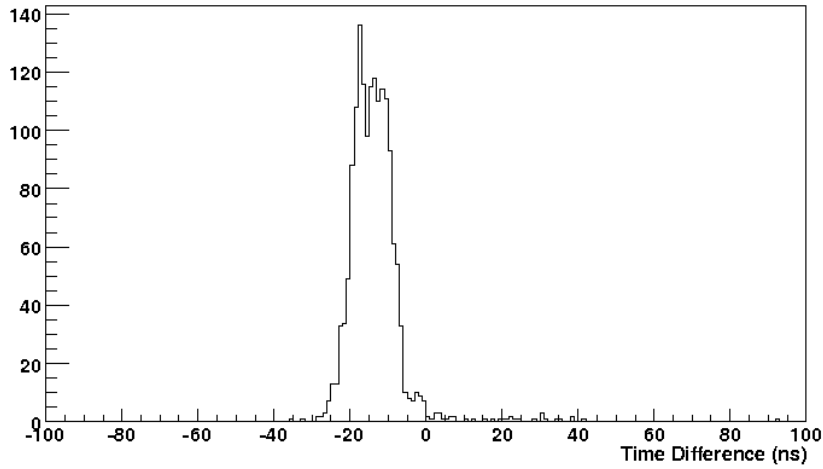


Figure 5.2.: Time difference between hits on TFB 23 and TFB 13 on RMM 3. This was randomly selected for run 7627, which had approximately 35,000 useable events (from 20 sub-runs). There are 1601 entries in this distribution, with an rms of 7.4 ns and a truncated mean of -14.2 ns. The mean of this distribution is used to calculate the global offset between a given TFB and the first TFB on that RMM according to Equation 5.2

$$O_i = o_{(c-k)} + o_{(k-j)} + \dots + o_{(m-i)}, \quad (5.2)$$

where $o_{(k-j)}$ is the local offset between TFB k and TFB j . Due to the nature of Prim's algorithm there is only one unique path of local offsets for each global offset. To clarify, an example path to calculate the offset for TFB 8 with respect to TFB 0 is

$$O_8 = o_{(0-6)} + o_{(6-7)} + o_{(7-8)}, \quad (5.3)$$

where $o_{(0-6)}$ is the offset between TFB 0 and TFB 6, $o_{(6-7)}$ is the offset between TFB 6 and TFB 7 and $o_{(7-8)}$ is the offset between TFB 7 and TFB 8.

To increase stability of the offsets, in the event of a TFB malfunctioning, each offset is then corrected to the mean TFB offset for that RMM.

RMM	Trigger Mask
0	All Top SMRD towers + DsECAL
1	All Top SMRD towers + DsECAL
2	Offset not calculated
3	All Top SMRD towers + all Bottom SMRD towers
4	All Top SMRD towers + all Bottom SMRD towers
5	Upper South SMRD towers + Lower North SMRD towers ¹
6	Upper South SMRD towers + Lower North SMRD towers ¹
7	Offset not calculated
8	Lower South SMRD towers + Upper North SMRD towers ²
9	Lower South SMRD towers + Upper North SMRD towers ²
10	All Top SMRD towers + all Bottom SMRD towers
11	All Top SMRD towers + all Bottom SMRD towers

Table 5.2.: Cosmic trigger masks used to select events with a certain topology to calculate RMM offsets.

5.3. Method for calculating RMM offsets

The RMM offsets are not calculated on an event-by-event basis because the global timing requires the time on each ECAL RMM is corrected back to the mean time of RMM 0 and RMM 1 (i.e. the downstream ECAL), which is not achievable using the method described in Section 5.2. To calculate these offsets all good hits in all events are used, provided the event had a specific track topology. Trigger masks⁴ are used to ensure the hit time distributions are not double peaked. For example, to calculate the offset for RMM 5, which is located in the left side module in the barrel ECAL, only events that triggered on the upper part (i.e. large, positive global y) of the south side SMRD towers and the lower part (i.e. large, negative global y) of the north side SMRD towers are used. Details of the specific trigger masks used for all ECAL RMMs can be found in Table 5.2.

⁴ The ND280 cosmic trigger uses the SMRD, DsECAL and P0D subdetectors. Each subdetector is split into a grid where each square of the grid is called a tower. Trigger masks are used to select cosmic rays that travel through specific towers in a subdetector.

First, to reduce the spread of hit times on an RMM, the TFB offsets are applied to the data. Events are used if they contain one or two tracks in an ECAL module, i.e. a cosmic muon spanning one ECAL module or two. If the event contains two tracks, the time of flight between ECAL modules is corrected for. To make this time of flight correction, first the assumption is made that all cosmic muons are travelling downward. Thus, the earlier track is the one with the highest y -position in the global geometry. Then, the distance between the exit position of the upper track and the start of the lower track is determined and added to the exit position of the upper track. The exit position of the extrapolated track is compared to the start position of the lower track; if they agree within 400 mm, the tracks are said to be matched and from the same cosmic muon. The calculation for the time of flight, t , becomes

$$t = \frac{\vec{x}_{\text{upper}} - \vec{x}_{\text{lower}}}{c}, \quad (5.4)$$

where $\vec{x}_{\text{upper}} (\text{lower})$ is the 3-dimensional position of the end (start) of the upper (lower) track and the muon is assumed to be travelling at the speed of light, c . It should be noted that this method does not take into account any curvature of the track caused by the magnetic field.

As some distributions have a non-Gaussian tail, the truncated mean of the hit time distribution for each RMM is taken. The truncated mean is calculated for ± 50 bins either side of the maximum bin. An example of the hit time distribution for RMM 3 can be found in Figure 5.3. Then, an offset is calculated which, when applied, corrects the mean time of each RMM to the mean time of RMM 0 and RMM 1.

5.4. Method validation

To validate this method for calculating the time offsets, the TFB and RMM offsets were applied to data from a run that was not used to calculate the offsets. This run was randomly chosen because it had more than 25 sub-runs and the shift logs suggested no

¹Upper South SMRD towers refers to towers: 2, 3, 6, 7, 10, 11, 14, 15, 18, 19, 22, 23, 26, 27, 30, 31 in the South SMRD module. Lower North SMRD towers refers to towers: 0, 1, 4, 5, 8, 9, 12, 13, 16, 17, 20, 21, 24, 25, 28, 29 in the North SMRD module.

²Lower South SMRD towers refers to towers: 0, 1, 4, 5, 8, 9, 12, 13, 16, 17, 20, 21, 24, 25, 28, 29 in the South SMRD module. Upper North SMRD towers refers to towers: 2, 3, 5, 6, 10, 11, 14, 15, 18, 19, 22, 23, 26, 27, 30, 31 in the North SMRD module.

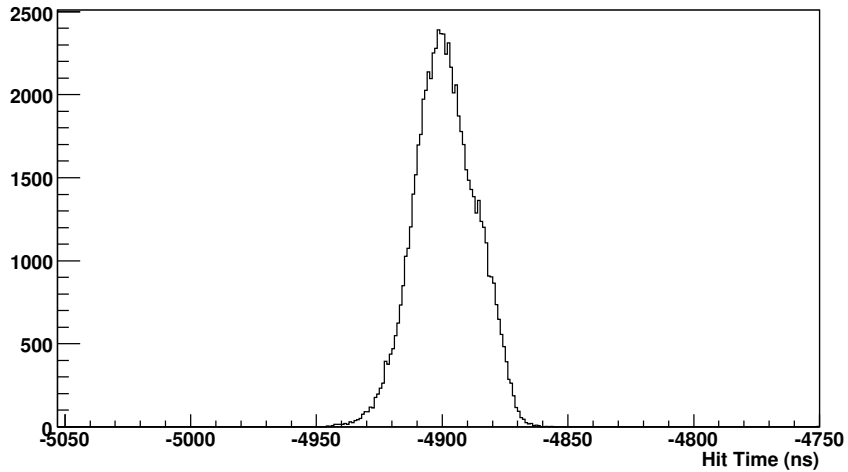


Figure 5.3.: An example of the hit time distribution for an RMM after the TFB offsets have been applied. This specific distribution is for RMM 3 and the data was from run 7626.

issues arose during data taking. Selecting a run not used to determine the offsets gives an indication of the validity of the offsets from one run to another.

The mean time on a TFB before and after offsets from the database were applied can be seen in Figure 5.4. Whilst the shape of the black curve, which represents the mean time on a TFB before RMM and TFB offsets were applied, appears double peaked, there is no physical significance, as it is just the mean of the hit time distribution for a TFB plotted for all barrel and downstream ECAL TFBs. It is clear that the width of the distribution is significantly reduced from 11.7 ns before the offsets were applied to 6.6 ns afterwards, thus showing that applying the offsets reduces the spread in times between TFBs.

5.5. Offset stability over time

The residual offset, i.e. the difference between the mean offset calculated over a period of time and the offset at a given time, is plotted for each RMM and can be seen in Figures 5.5 and 5.6. Most TFBs on an RMM have offsets which are constant to within 2.5 ns (this is the accuracy of the timestamp described in Section 3.3.3, an example of which can be found in Figure 5.6c). However some RMMs, for example RMM 9 in Figure 5.5h, have TFB offsets that are only constant to within 5 ns. The reason some

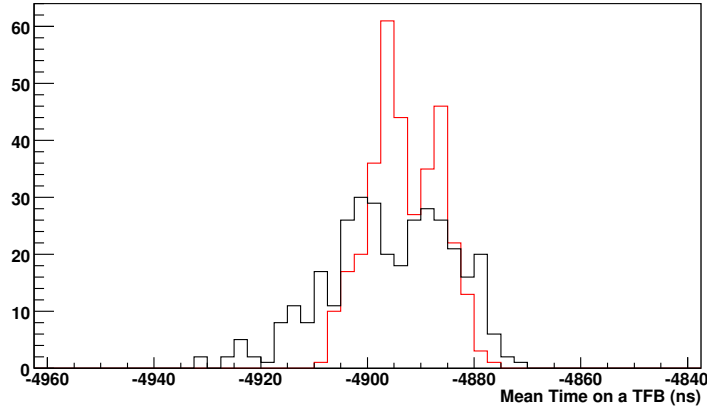


Figure 5.4.: Mean time on a TFB before (black) and after (red) TFB and RMM offsets calculated from run 7616 were applied to data from run 7617.

offsets are constant to within 2.5 ns and others only 5 ns remains unclear; it is thought that increased statistics may improve this, but this is difficult to achieve as few runs have greater than 20 sub-runs and the processing of these runs is very time consuming and computationally intensive. Some TFB offsets exhibit an oscillatory nature, as seen in Figure 5.5i, which this is thought to be due to the chosen method. To remove these oscillations every single possible combination of local offsets would need to be added together to determine the global offset. Unfortunately this is not possible, as the statistics for some TFB combinations are severely limited.

5.6. Timing resolution

The timing resolution is calculated using inter-spill cosmic data that has been calibrated and reconstructed using the simple track fitting algorithm with the RMM and TFB offsets turned both on and off. There is also a requirement that the run in question is not used to calculate the TFB and RMM offsets, to try to get the most accurate value of the resolution, rather than the best possible.

The time of flight and light propagation times are corrected for, as described in Section 5.2. This means that for the files where TFB and RMM offsets are applied one would expect every hit to have the same time. Then for each event, the hit with the highest charge is chosen as a reference hit, as the resolution is best for high charge hits, and the time of every other hit in that event is subtracted from the reference hit time.

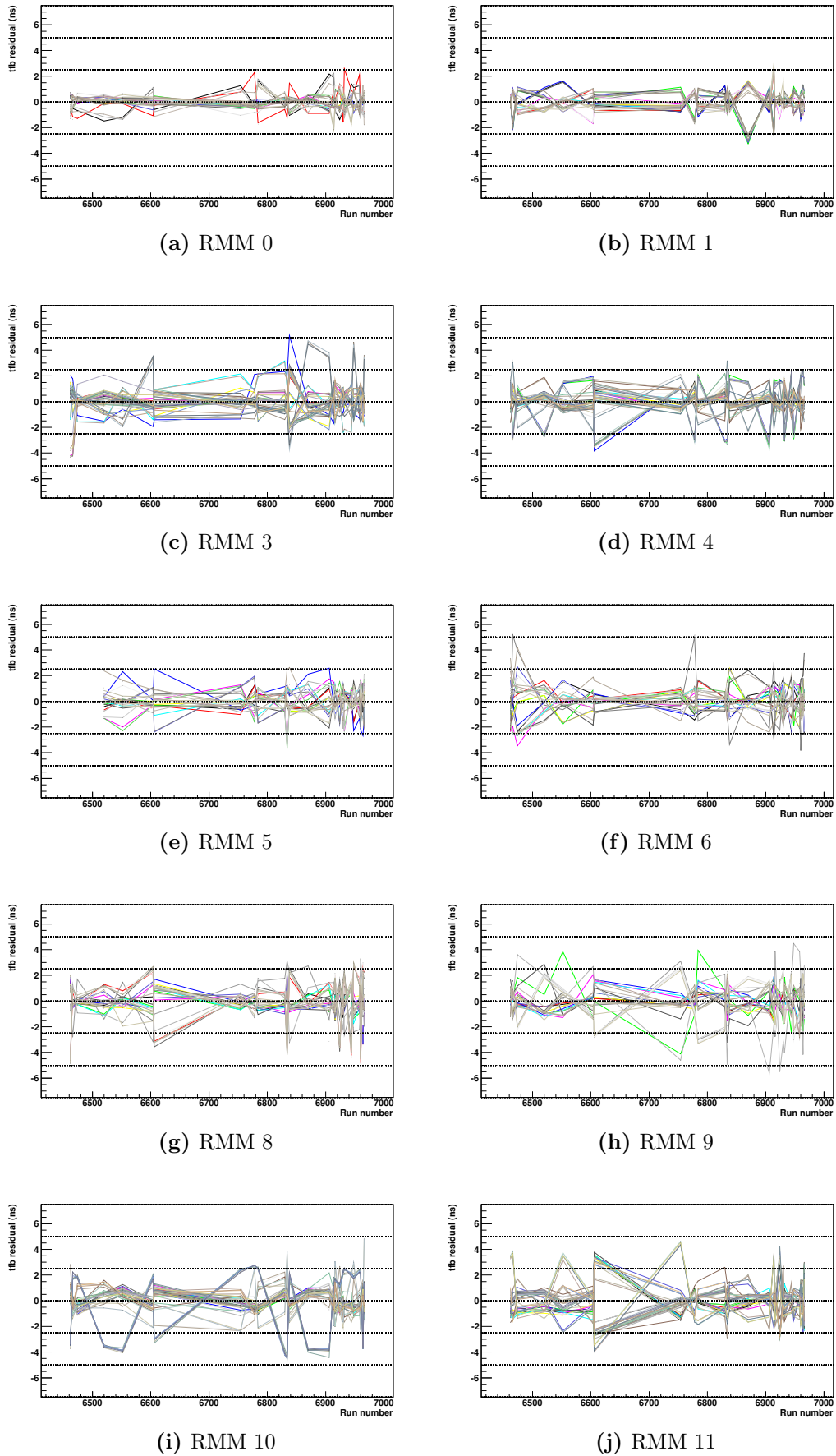


Figure 5.5.: Residual TFB offsets for all barrel and downstream ECAL RMMs for the 6000 ND280 data runs.

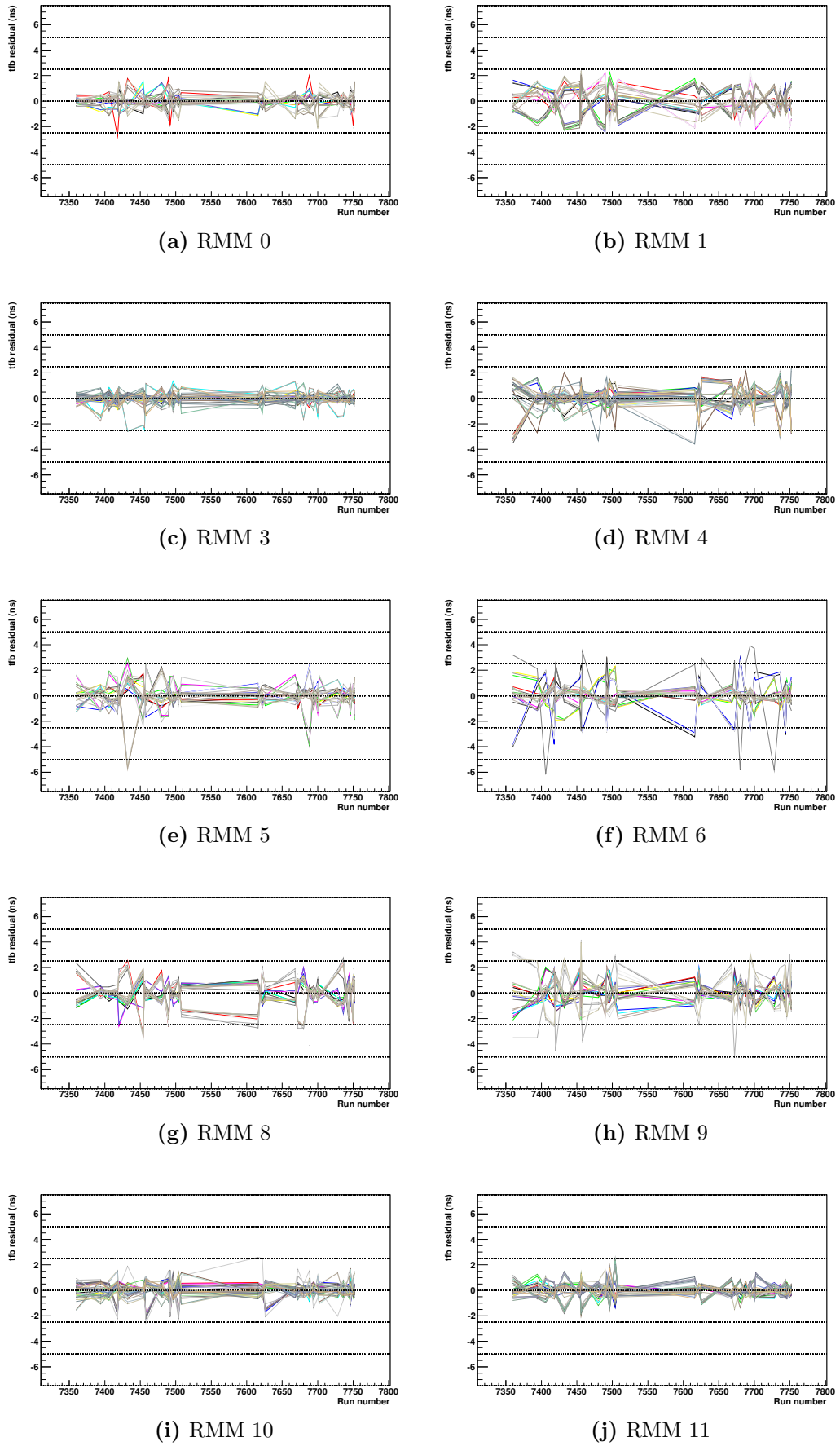


Figure 5.6.: Residual TFB offsets for all barrel and downstream ECAL RMMs for the 7000 ND280 data runs.

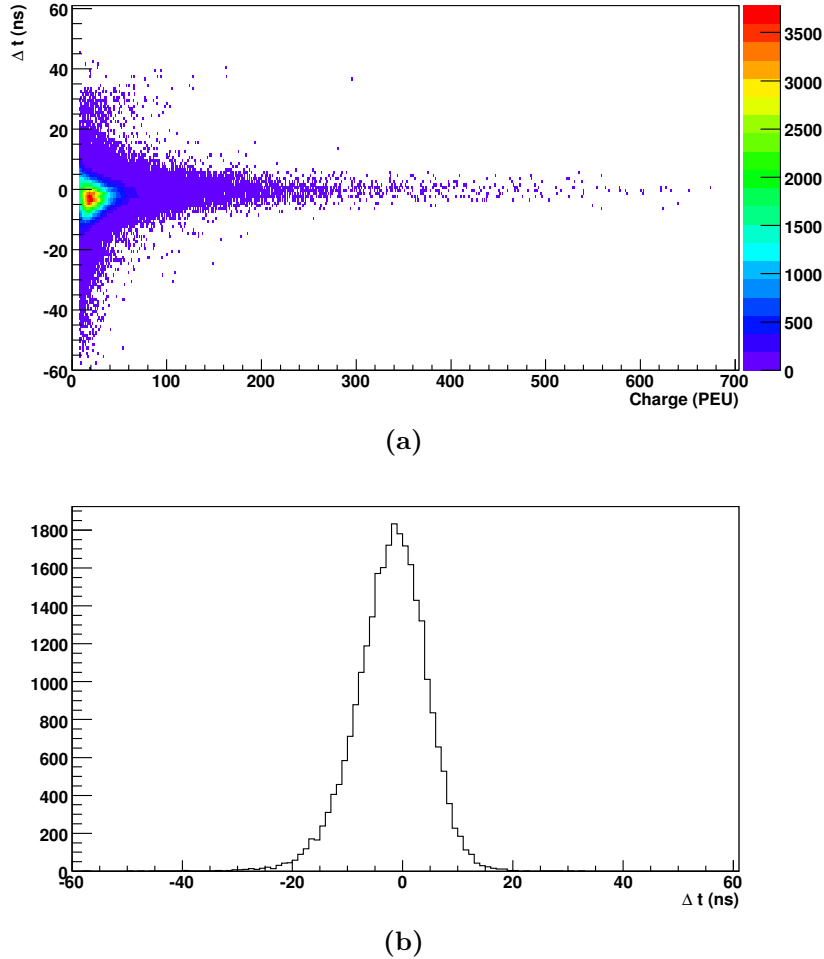


Figure 5.7.: Time difference between the highest charge hit in an event and all other hits in that event, for all useable events in run 7491 with TFB and RMM offsets from the database applied. (a) shows the time difference for all charges in that event, whereas (b) shows the time difference for all hits with a charge of 10 PEU.

This difference is plotted as a function of charge, an example of which can be seen in Figure 5.7. Finally, to calculate the resolution, defined as

$$\text{resolution} = \frac{\text{rms}}{\sqrt{2}}, \quad (5.5)$$

where the rms of the distribution was obtained without making a Gaussian fit to the data, as only distributions with all corrections applied are Gaussian.

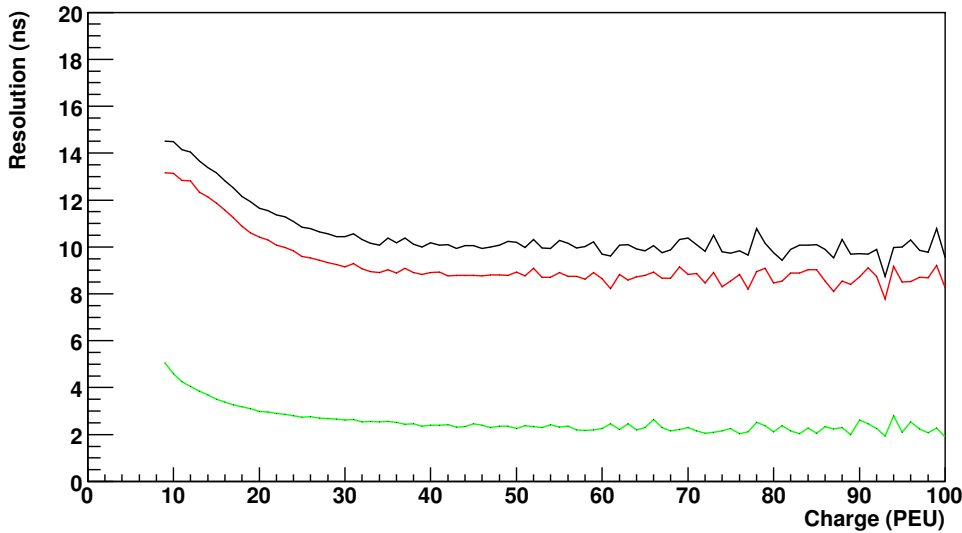


Figure 5.8.: Timing resolution for ND280 data run 7491. The black curve represents the resolution before the time of flight and light propagation corrections were made, there are also no TFB or RMM offsets applied. The red (green) curve has time of flight and light propagation corrections and is plotted without (with) TFB and RMM offsets.

The timing resolution for the randomly chosen run 7491 can be seen in Figure 5.8. It is clear that the application of TFB and RMM offsets improve the resolution from approximately 9 ns (red curve, with time of flight and light propagation corrections applied) to approximately 2.5 ns, for high charge hits. It is thought that increased statistics will make the curves smoother.

Figures 5.9 and 5.10 show the resolution over the whole Run 2 data set without and with offsets from the database being applied, respectively. The figures show that the resolution for high charge hits is approximately 2.5 ns, whereas low charge hits have a poorer resolution of roughly 5 ns. There are some runs where the resolution appears to be noticeably worse regardless of the charge; it is thought that the more frequent production of constants may improve the resolution of these runs. However, it is important to note that runs 6691 → 6945 have relatively poorer resolution before the TFB and RMM offsets are applied; this suggests that the problem could lie with other areas of the calibration or that the run, although deemed good, was not suitable for calibration purposes. Furthermore, many runs use the same constants, for example 6691 → 6713, which suggests producing constants more frequently will improve the resolution.

It should also be noted that the timing of the Trip-t detectors was realigned after run 6945; this realignment seems to improve the resolution.

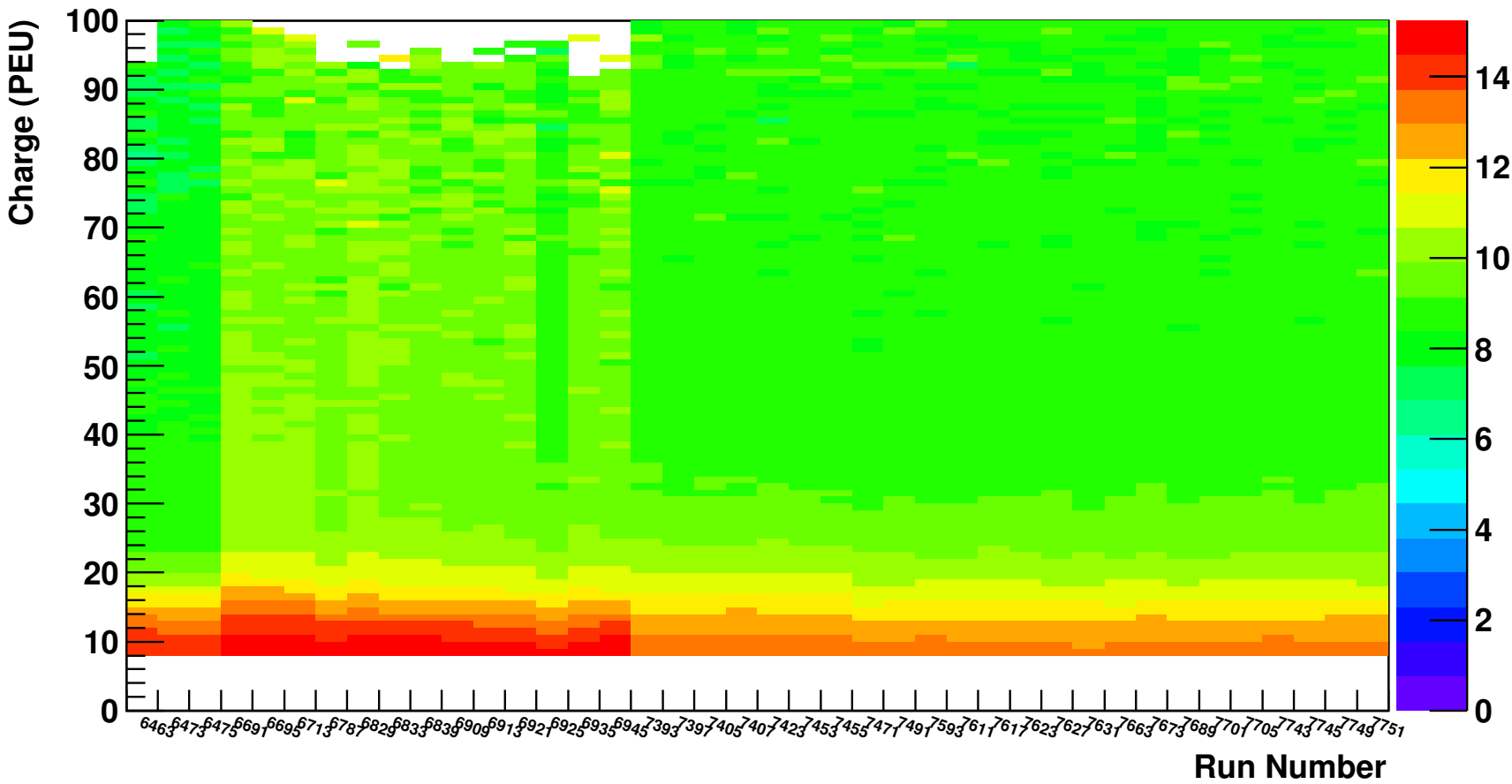


Figure 5.9.: Timing resolution as a function of charge for a selection of runs from the Run 2 data set. The colour (z-axis) represents the resolution in ns. No TFB and RMM offsets have been applied, but time of flight and light propagation corrections have been made. These runs were not used to produce the calibration constants.

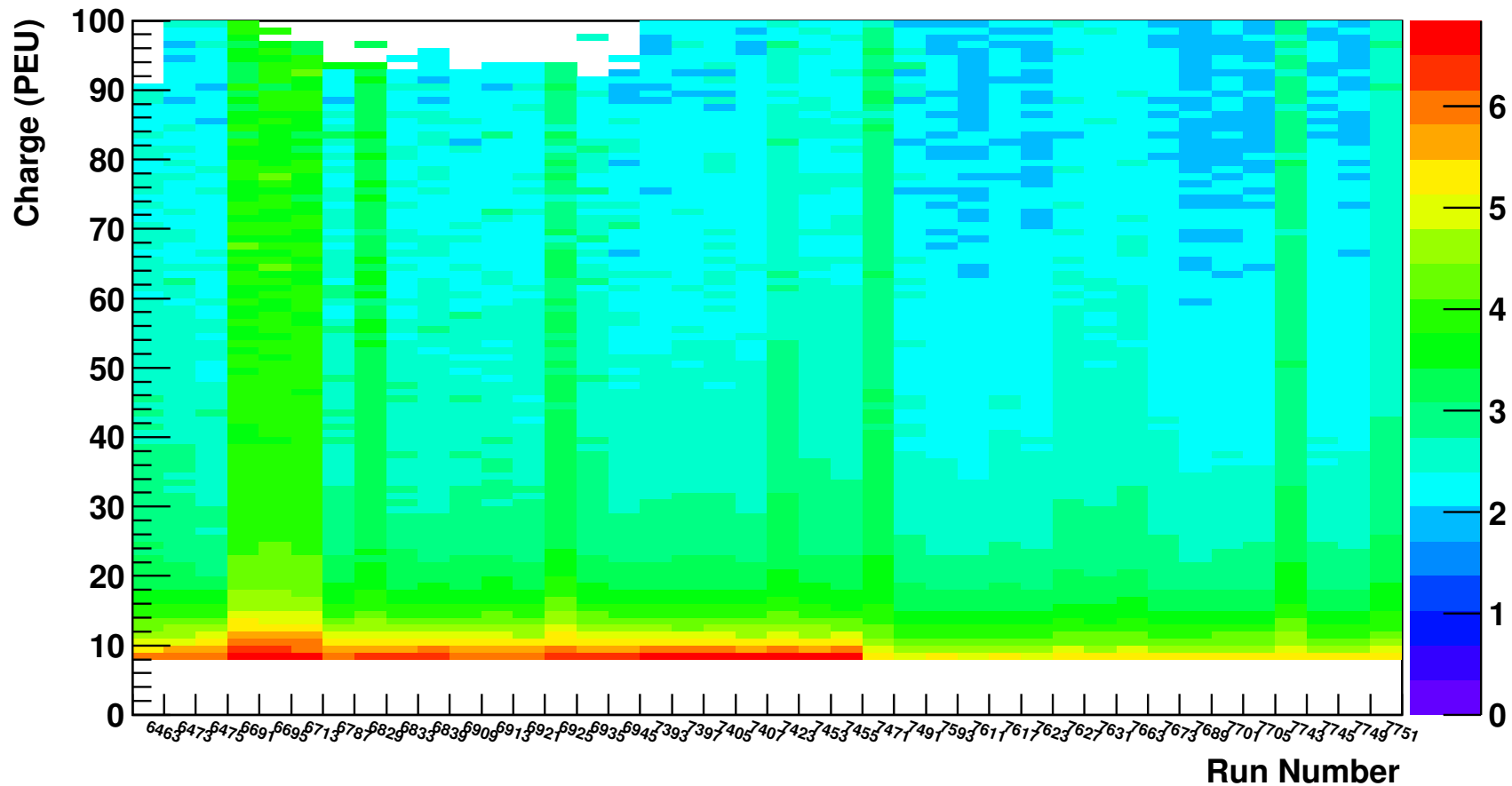


Figure 5.10.: Timing resolution as a function of charge for a selection of runs from the ND280 Run 2 data set. The colour (z-axis) represents the resolution in ns. The TFB and RMM offsets which were uploaded to the database have been applied, in addition to time of flight and light propagation corrections. These runs were not used to produce the calibration constants.

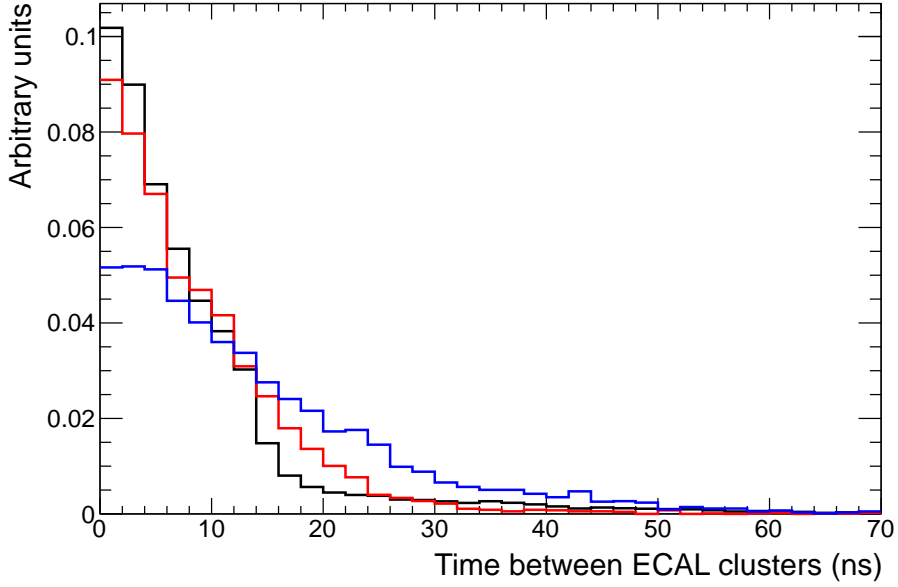


Figure 5.11.: Time difference between ECAL clusters in a bunch. The black curve shows the true time difference between ECAL clusters for a sample of neutrino-induced interactions simulated using magnet Monte Carlo (see Section 6.2 for a complete description of this MC sample). The red (blue) curve represents the time difference between ECAL clusters in data, for beam spill interactions in ND280 run 7491, with (without) the RMM and TFB offsets applied.

5.7. Impact of improved timing

The improvement of the timing resolution for high charge hits from approximately 9 ns to 2.5 ns is essential for the next official production of ND280 Monte Carlo. Future analyses aim to use the global ND280 timing to determine the direction of tracks; this will help to remove background events with interaction vertices originating from outside of the FGD. However, good global timing can only be achieved in conjunction with good individual subdetector timing.

It is important that the timing in the Monte Carlo simulation is an accurate representation of that seen in data. Figure 5.11 shows the time difference between ECAL clusters for both beam data, with and without the RMM and TFB offsets applied, and Monte Carlo. Applying the RMM and TFB offsets reduces the spread in times between ECAL clusters and ensures better agreement between data and MC. Future official productions will have improved electronics simulation with regards to the time walks, which should improve the agreement between data and MC further.

The analysis presented in Chapter 6 aims to select NC $1\pi^0$ interactions in the FGD when both π^0 decay photons convert in the ECAL. Currently, a loose cut requiring that the time between isolated ECAL clusters is less than 200 ns is made. However, when the Monte Carlo properly simulates the timing seen in data it will be possible to make the time cut tighter. A Monte Carlo study was undertaken to assess the impact of reducing the time cut between isolated ECAL clusters on the final purity for selecting these NC $1\pi^0$ interactions (detailed in Chapter 6). Figure 5.12 shows that the selection purity increases (the efficiency remains constant and is not plotted) as the time cut is decreased. Thus, by requiring the time between isolated ECAL clusters is less than or equal to 10 ns the purity of events where one photon converts in the BrECAL and one in the DsECAL is increased by approximately 4%, in comparison with the selection applying a loose time cut. Furthermore, by making a time cut of 10 ns instead of 200 ns, the selection purity for the case when both photons convert in either the barrel or downstream ECAL is increased by over 1.5%.

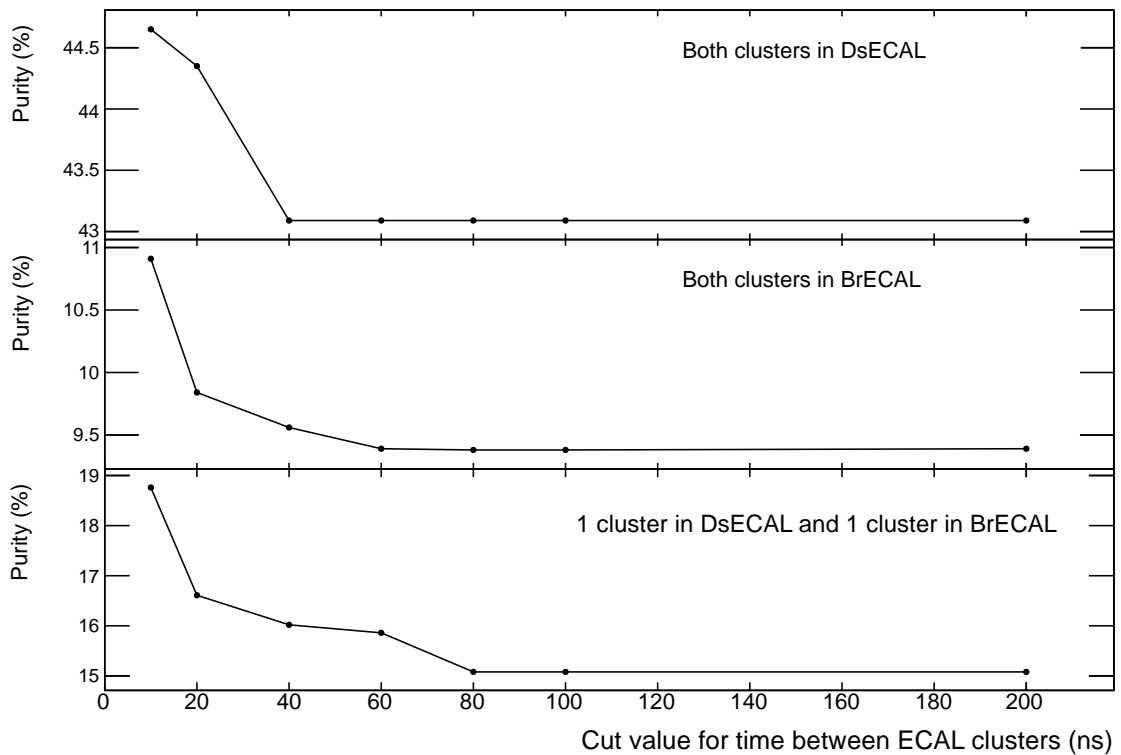


Figure 5.12.: The final purity for selecting NC $1\pi^0$ interactions in the FGD (for full details of the selection see in Chapter 6) for varying time cuts between ECAL clusters for different photon conversion topologies. The final selection efficiency remained constant and so is not shown. (The selection, in addition to the signal definition, used to make these plots is identical to that detailed in Chapter 6, apart from the change in requirement of the time between isolated ECAL clusters.)

Chapter 6.

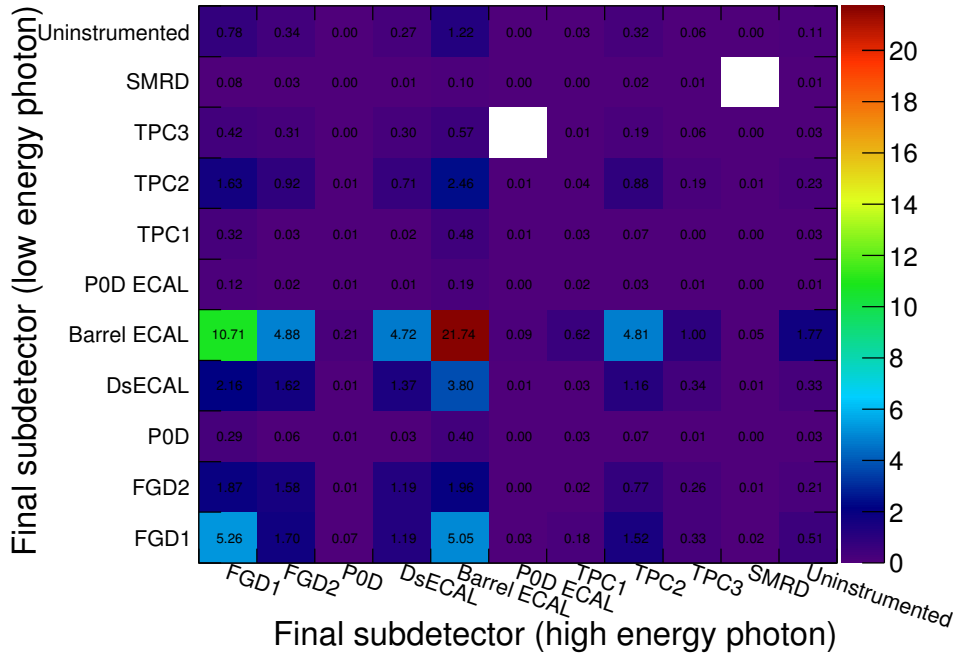
Selecting neutral current π^0 interactions in the FGD

This analysis aims to select neutrino-induced neutral current interactions occurring in the fiducial volumes of FGD1 or FGD2 that produce only one π^0 in the final nuclear state, in addition to any number of nucleons and photons, from the recoil of the nucleus. The selection outlined in this chapter is optimised to selecting NC $1\pi^0$ decay photons that convert in the barrel and downstream ECAL, whilst other complimentary ND280 analyses focus on photon conversion in other subdetectors. As can be seen in Figure 6.1, the photon topology in this analysis accounts for 31.6% of NC $1\pi^0$ events in FGD1 and 51.7% in FGD2 and samples the whole phase space of NC $1\pi^0$ interactions in the FGD, as shown in Figure 6.2.

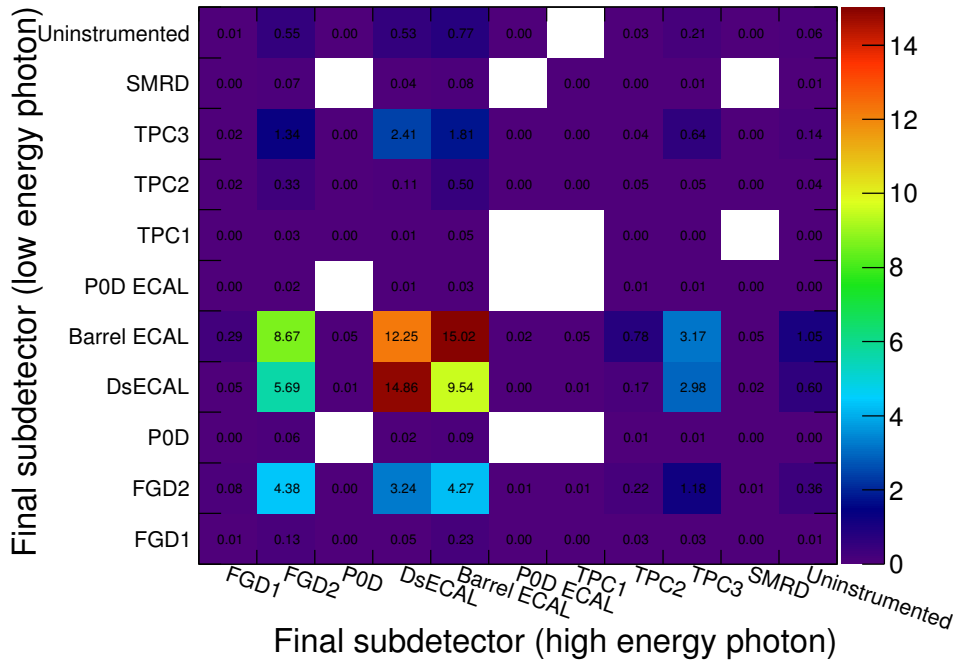
The strategy for selecting NC $1\pi^0$ interactions, outlined in Figure 6.3, is first to isolate the potential NC $1\pi^0$ candidates by making an ECAL cluster pre-selection on a bunch-by-bunch basis. Then, after P0D and TPC1 vetoes are applied, all tracks in the tracker are required to be proton-like. Using ECAL variables in a multi-variate analysis framework, decay photons from NC $1\pi^0$ interactions are selected. Finally a vertex cut is made to ensure the interaction originated from within an FGD fiducial volume.

6.1. Signal definition

A signal neutrino interaction, as defined using NEUT Monte Carlo, is one that is neutral current (i.e. the NEUT interaction code is greater than or equal to 31 (for ν) or less than or equal to -31 (for $\bar{\nu}$)); occurred in the fiducial volume of FGD1 or FGD2 (see



(a) FGD1



(b) FGD2

Figure 6.1.: π^0 decay photon subdetector conversion location for NC $1\pi^0$ interactions in (a) FGD1 and (b) FGD2. Made using cherry picked MC.

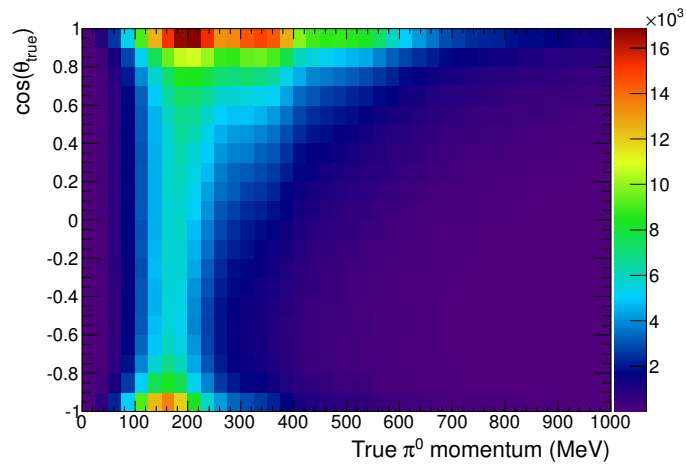
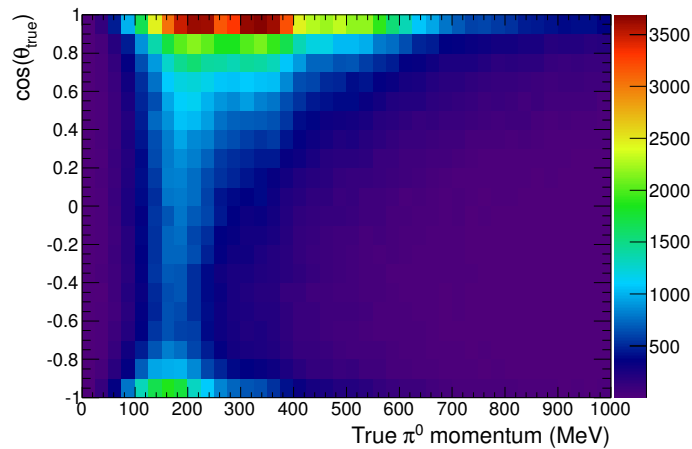
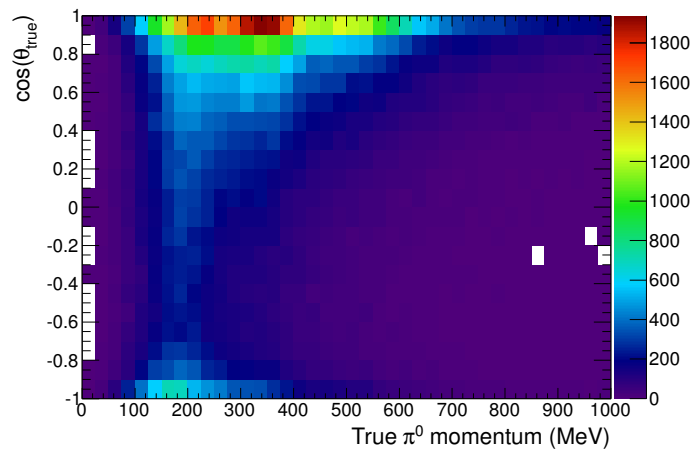
(a) All NC $1\pi^0$ interactions in FGD1 and FGD2(b) NC $1\pi^0$ interactions in FGD1 and FGD2 where both photons convert in the ECAL(c) NC $1\pi^0$ interactions in FGD1 and FGD2 where both photons convert and are reconstructed in the ECAL

Figure 6.2.: True π^0 momentum and angle (with respect to the beam direction), θ_{true} , for NC $1\pi^0$ interactions in the FGD. Made using cherry picked MC.

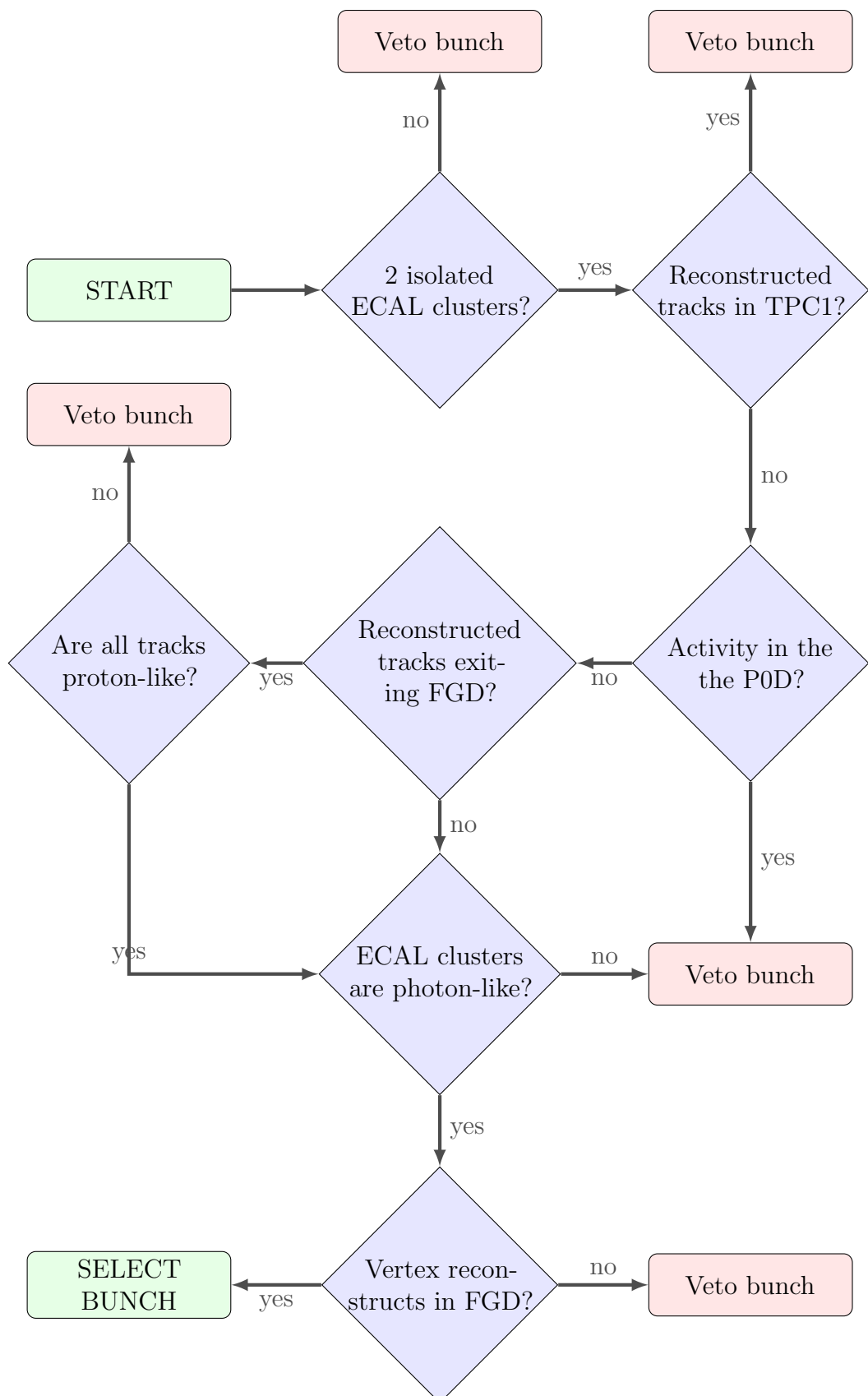


Figure 6.3.: Flowchart outlining the selection of NC $1\pi^0$ interactions in the FGD.

FGD	Min x	Max x	Min y	Max y	Min z	Max z
1	-832.20	832.20	-777.20	887.20	123.45	446.95
2	-832.20	832.20	-777.20	887.20	1481.45	1807.95

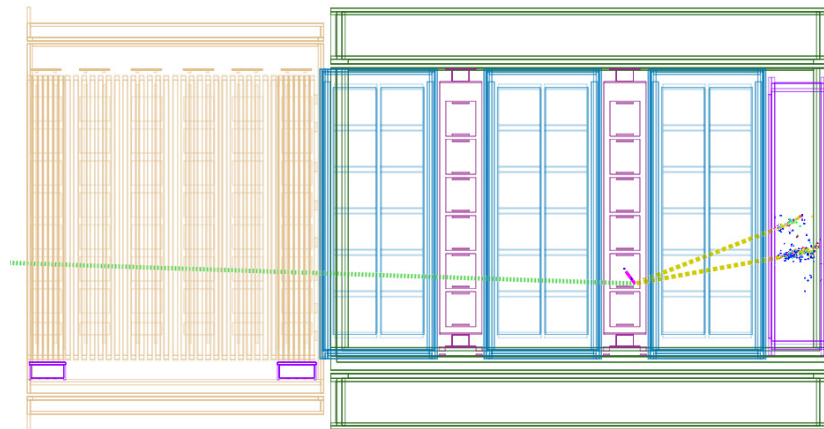
Table 6.1.: Global ND280 coordinates for the fiducial volume of FGD1 and FGD2 in millimetres.

Table 6.1 for the global ND280 coordinates); has only one π^0 and any number of nucleons exiting the nuclear environment and can have any number of photons from the recoil of the nucleus. The possible production mechanisms for such interactions are discussed in Section 2.5.1. To illustrate, some ND280 event displays for “golden” signal events can be found in Figure 6.4.

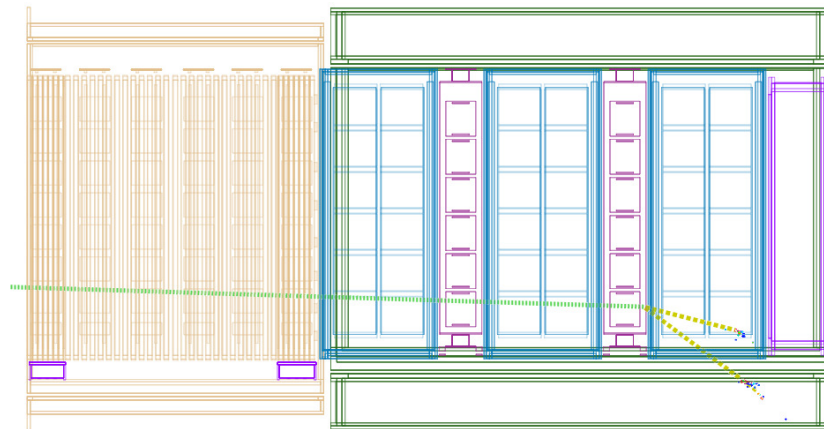
6.2. Data and Monte Carlo samples

This analysis uses the ND280 Run 2 data set which was taken between November 2010 and March 2011. Prior to use, two sets of quality cuts are applied to the data. The first cut, applied on a spill-by-spill basis, ensures the proton beam was running with stable conditions. The second cut, applied per sub-run of data, guarantees the whole ND280 detector was running in a steady mode. After data quality cuts, the number of protons on target used in this analysis is 7.832×10^{19} POT. The Run 1 (March 2010 – June 2010, 2.888×10^{19} POT) ND280 data was not used in this analysis. Data for Run 1 was taken when only the downstream ECAL was *in situ* and based on the selection efficiency detailed in Section 6.7 would constitute selecting only one signal and two background events. Unfortunately Run 3 data totalling 1.5702×10^{20} POT, which was taken between February and June in 2012, cannot be used for this analysis as the appropriate calibration constants and optimisations are not available at the time of writing.

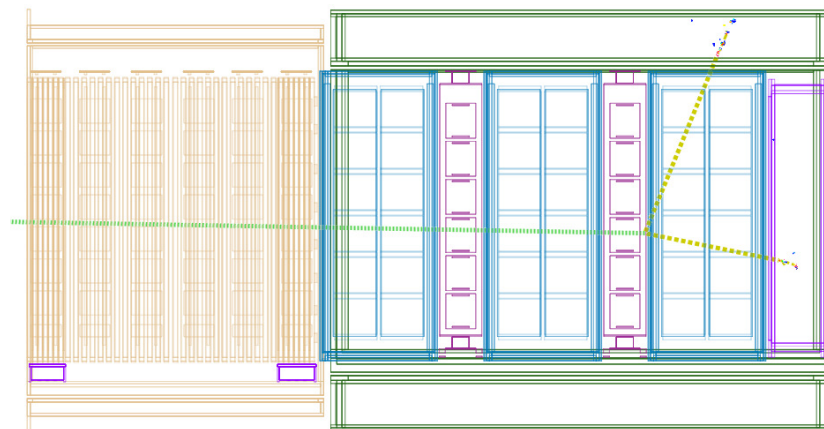
Several different Monte Carlo samples, produced using the method described in Section 4.1, were used in this analysis and are called “magnet”, “sand” and “cherry picked”. The bunch timing structure for the data, magnet and sand samples can be found in Figure 6.5.



(a) Both photons convert in the DsECAL



(b) Both photons convert in the BrECAL



(c) One photon converts in the DsECAL and one in the BrECAL

Figure 6.4.: Golden signal ND280 NC $1\pi^0$ interactions produced using cherry picked Monte Carlo. The neutrino beam is travelling from left to right and the side view of the ND280 is shown. The incoming neutrino (light green) interacts in an FGD to produce a π^0 and (in the case of (a)) a neutron (pink). The π^0 decays to two photons (yellow) which convert in the barrel (dark green) or downstream (purple) ECAL. Only MC truth information is shown.

To model neutrino-induced interactions over the whole ND280 geometry, including the UA1 magnet, the NEUT neutrino interaction generator is used. This MC sample, corresponding to 1.868×10^{21} POT, simulates a beam power of 120 kW, i.e. the average beam power during Run 2 data taking, and produces interactions anywhere in the ND280, including the magnet. A neutrino flux tuning¹, based on the most up to date flux estimates, is also applied to ensure good agreement between data and MC. This sample is hereby referred to as “Magnet MC”.

A separate MC sample, called “Sand MC”, which also uses the NEUT generator and simulates a higher beam power of 178 kW, totalling 3.650×10^{20} POT, is used to simulate neutrino-induced interactions in the sand in the cavern surrounding the ND280. It is important to note that this production is preliminary and the normalisation of these neutrino interactions does not exactly match that seen in data. The sand MC sample is always POT normalised to the magnet MC, except in Figure 6.5 and Table 6.2. Currently the sand and magnet MC are totally separate, in future MC productions the collaboration hopes to simulate magnet and sand interactions simultaneously.

The final MC sample used in this analysis is a stripped down version of the magnet MC totalling 2.266×10^{23} POT and is called “Cherry picked MC.” Events are selected to contain one neutrino interaction per spill and, in the case of the files used in this analysis, all interactions are NC $1\pi^0$. These files are used to ensure the likelihood-based multi-variate analysis, which is used to select photons in the ECAL (see Section 6.5), has an abundance of signal interactions.

6.3. ECAL preselection and vetoes

The information presented in Table 6.2 indicates that 44.1% of bunches containing a signal event have two spatially isolated ECAL clusters, i.e. the global reconstruction has deemed there are no other tracks or showers associated with the ECAL object in question. These two spatially isolated ECAL clusters form a π^0 candidate. It is important to note that 45.1% of signal bunches have only one isolated ECAL cluster, thus there is an immediate efficiency loss due to the low energy reconstruction capabilities of the ECAL, as discussed in Section 4.5.3. By requiring that bunches contain only two isolated ECAL clusters, 98.6% of the magnet background and 99.9% of the sand background is removed.

¹ Flux tuning version 11bv3.2 with normal binning is used.

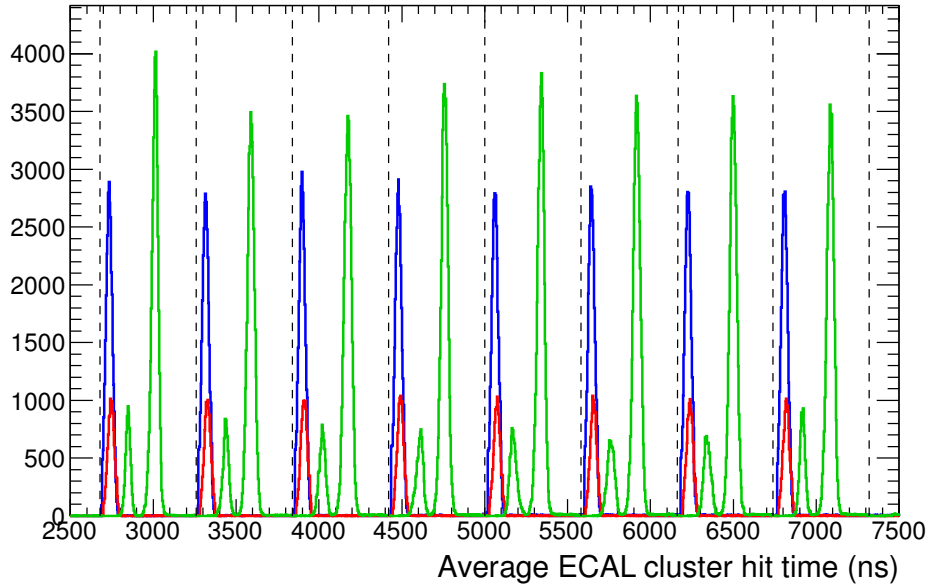


Figure 6.5.: Bunch timing structure for Run 2 data (green), 6.85×10^{19} POT magnet MC (blue) and 3.65×10^{20} POT sand MC (red). The double peak structure of the data is expected, as the global timing of ND280 was realigned during the run.

	Number of isolated ECAL clusters				
	0	1	2	3	4+
Background (magnet MC)	90.2	8.0	1.4	0.2	0.1
Background (sand MC)	98.5	1.4	0.1	0.0	0.0
Signal (magnet MC)	4.9	45.1	44.1	5.1	0.7

Table 6.2.: Percentage of isolated ECAL objects per bunch containing a signal or background interaction.

The next generation of this analysis will consider bunches with three isolated ECAL clusters, thus gaining 5% extra signal events.

In addition to requiring that the isolated ECAL clusters are in the same bunch, a loose time cut is applied. This time cut requires that the difference between cluster times is less than 200 ns. As shown in Figure 6.6, the time difference between most ECAL clusters in a π^0 candidate is less than the bunch width, as expected, thus this cut does not remove any signal events, but slightly reduces the backgrounds as it removes 0.8% of magnet and 0.7% of the sand background. It may be possible to use a tighter time cut

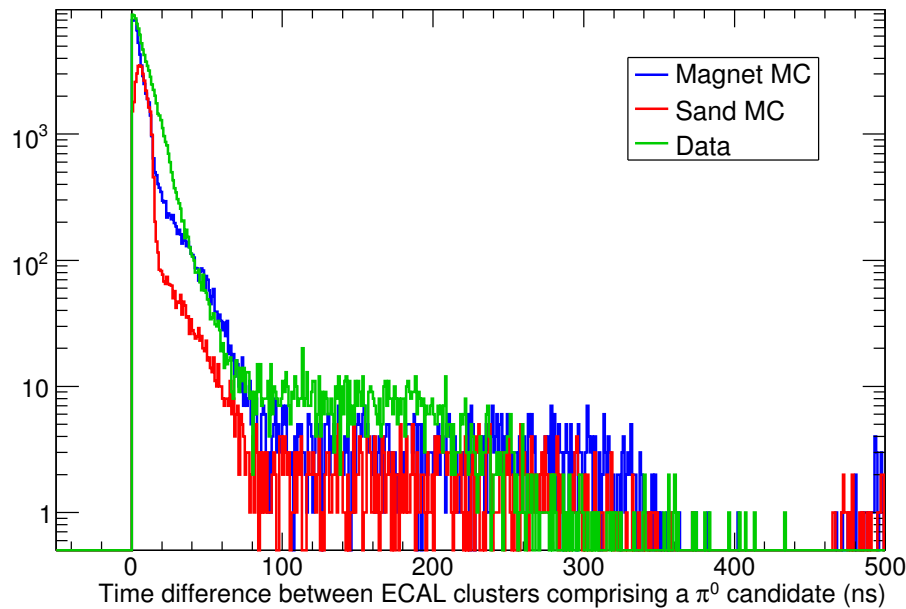


Figure 6.6.: Time difference between ECAL clusters in a π^0 candidate for Run 2 data (green), 6.85×10^{19} POT magnet MC (blue) and 3.65×10^{20} POT sand MC (red).

in future versions of this analysis, provided that the MC timing is a true reflection of that seen in the data.

Furthermore, to reduce the likelihood of selecting an interaction originating upstream of FGD1, a TPC1 and P0D veto are also made for each bunch containing only one π^0 candidate. The TPC1 veto requires that there are no reconstructed tracks in TPC1 and removes 6.4% of magnet, 4.7% of sand and only 1.5% of signal interactions. The P0D veto is based on the output of a specific clustering algorithm. By looking in the most downstream 50 cm of the P0D in windows of 100 ns, the algorithm iterates through fully calibrated hits and attempts to cluster them together. These clusters require a minimum number of four hits with a charge greater than 7 PEU, and are assigned a time corresponding to the mean time of the hits comprising the cluster. One or more of these P0D clusters occurring in the same bunch as the π^0 candidate will veto the bunch. The application of the P0D veto removes a further 3.7% of magnet and 6.2% of sand interactions whilst sacrificing only 1.3% of the signal events.

Particle	Signal (%)	Background (%)
Proton	75.1	16.5
Electron	15.5	34.9
Muon	4.2	19.8
Positron	1.8	15.7
π^+	4.2	7.3
π^-	1.0	4.1
Antimuon	0.6	1.2
Neutron	0.4	0.1
Other	0.0	0.2

Table 6.3.: True particle associated with reconstructed tracks in the tracker for bunches containing a signal or background interaction.

6.4. Selecting proton-like tracks

As per the signal definition in Section 6.1 only tracks made by protons, electrons and positrons, from pair-producing nuclear recoil photons, should be present in bunches with a signal interaction. However, given there is an average of nine (simulated NEUT) interactions in the whole ND280 per spill, it is possible there will be tracks from other neutrino-induced interactions present. Table 6.3 details the true particle composition of reconstructed tracks in signal and background bunches.

For bunches containing a signal event 75.1% of reconstructed tracks were created by a proton, 15.5% were from electrons and 1.8% from positrons. As expected, there are tracks from other neutrino-induced interactions namely muons (4.2%), π^+ (4.2%) and π^- (1.0%). For bunches containing only background interactions, only 16.5% of tracks correspond to protons. Thus, this selection requires all tracks to be proton-like.

There are three sources of information that can be used to select proton-like tracks depending on the track topology. If the track goes through a TPC, the TPC pulls can be used; if the track is isolated to an FGD, the FGD pulls are used; if the track has an FGD and ECAL, but no TPC, component, ECAL variables can be used for particle identification. At the time of writing there are no fully developed ECAL particle identification methods, however using the charge per unit length of the track proves effective, as discussed in Section 6.4.3.

PID information	% tracks (signal)	% tracks (background)
TPC pulls	64.6	78.4
FGD pulls	33.7	19.4
ECAL variables	1.7	2.2

Table 6.4.: PID information available for reconstructed tracks originating from the tracker (after quality cuts) for bunches containing a signal or background interaction.

The percentage of good quality tracks falling into each category mentioned above, for bunches containing signal and background events, can be found in Table 6.4. It should be noted that it is unsurprising that the percentage of tracks traversing an FGD and entering an ECAL is low; the current global reconstruction (see Section 4.4) has no fully developed algorithm to match FGD tracks to an ECAL module.

6.4.1. TPC particle identification

If a reconstructed track has a TPC component that passes a quality cut requiring that at least one TPC constituent has 18 hits or more, it is possible to use the TPC pulls (see Section 4.4) for particle identification. Figure 6.7 shows the POT normalised pulls for both data and magnet and sand MC. It is unsurprising the some pulls have a poor agreement between data and MC as there is a TPC calibration issue, affecting mainly true electrons, in the software production used in this analysis.

To determine which TPC pull would produce the cleanest sample of protons, the cut value for each pull was varied and the figure of merit efficiency \times purity ($\epsilon \times \pi$) was used to rank each proton identification candidate. For completeness, the definition of efficiency is

$$\epsilon = \frac{\text{number of protons selected with useable TPC information}}{\text{total number of protons with useable TPC information}}. \quad (6.1)$$

Similarly, purity is defined as

$$\pi = \frac{\text{number of protons selected with useable TPC information}}{\text{number of tracks selected with useable TPC information}}. \quad (6.2)$$

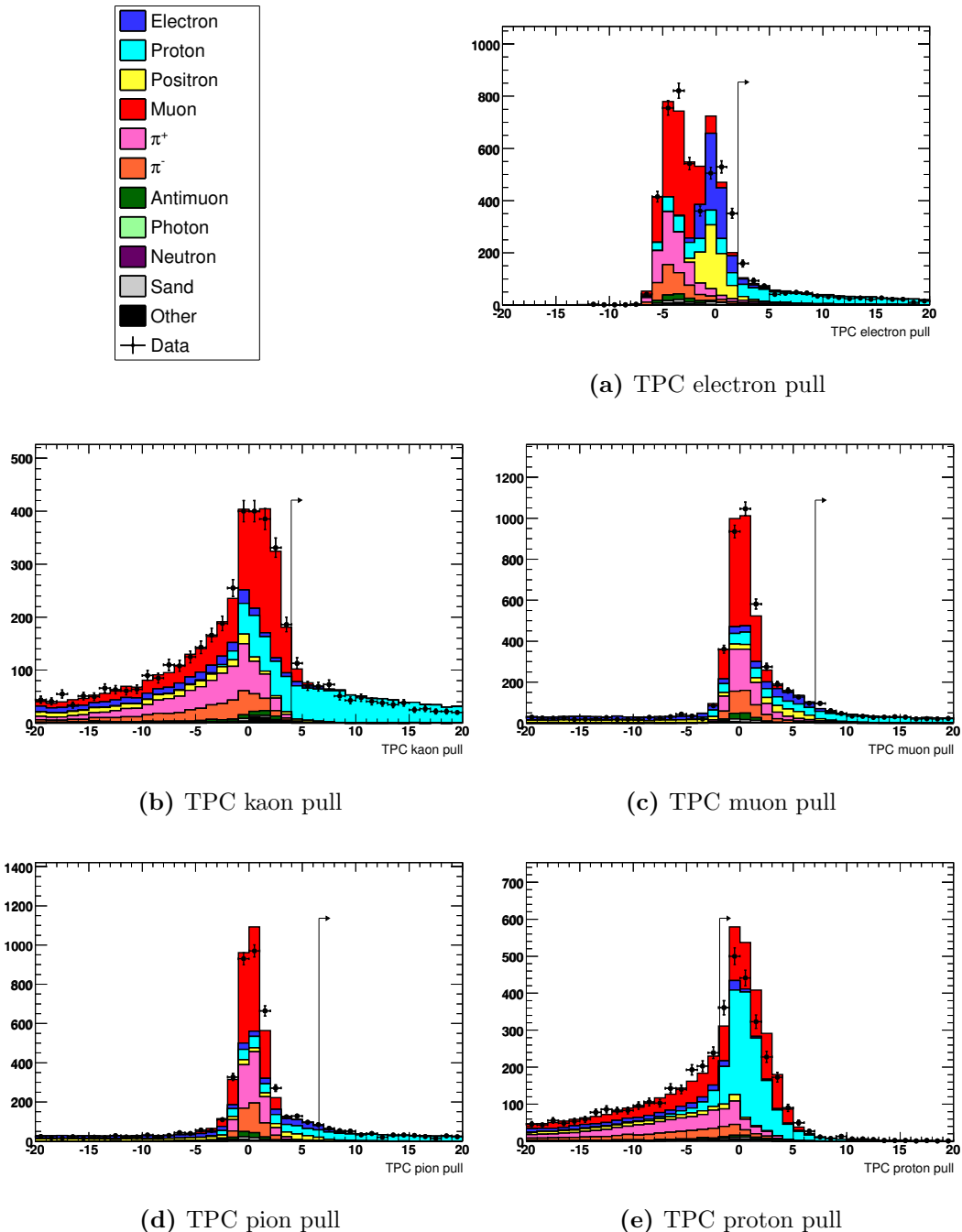


Figure 6.7.: TPC pull distributions produced using magnet and sand MC, POT normalised to data.

Type of pull	Max($\epsilon \times \pi$)	Efficiency (%)	Purity (%)	Cut value
Electron	26.92	33.16	81.16	2.05
Kaon	34.05	36.52	93.22	3.95
Muon	28.81	31.85	90.46	7.05
Proton	23.07	43.53	53.00	-1.90
Pion	30.94	33.26	93.01	6.55

Table 6.5.: Efficiency and purity for TPC pulls optimised to select protons.

The results of this study can be seen in Figure 6.8 and Table 6.5. It should be noted that the efficiency for selecting protons using the TPC pulls is never greater than $\sim 50\%$. This is a result of the global reconstruction algorithms, which do not save tracks that have no FGD component and only one TPC component, as they assume they are delta rays. After consideration of the results of this study it was decided that the kaon pull would provide the best sample of proton-like tracks.

6.4.2. FGD particle identification

If a reconstructed track begins and ends in an FGD, the FGD pulls can be used for particle identification (see Section 4.4 for further information about the pull calculation). The POT normalised muon, pion and proton pull distributions can be found in Figure 6.9.

Similarly to the TPC pulls, the efficiency and purity for varying cut values for each pull, defined as

$$\epsilon = \frac{\text{number of protons selected with useable FGD information}}{\text{total number of protons with useable FGD information}}, \quad (6.3)$$

and

$$\pi = \frac{\text{number of protons selected with useable FGD information}}{\text{number of tracks selected with useable FGD information}}, \quad (6.4)$$

respectively were plotted for varying cut values of FGD pulls. The results from this study can be seen in Figure 6.10. Details of the maximum value of $\epsilon \times \pi$ for each pull variable

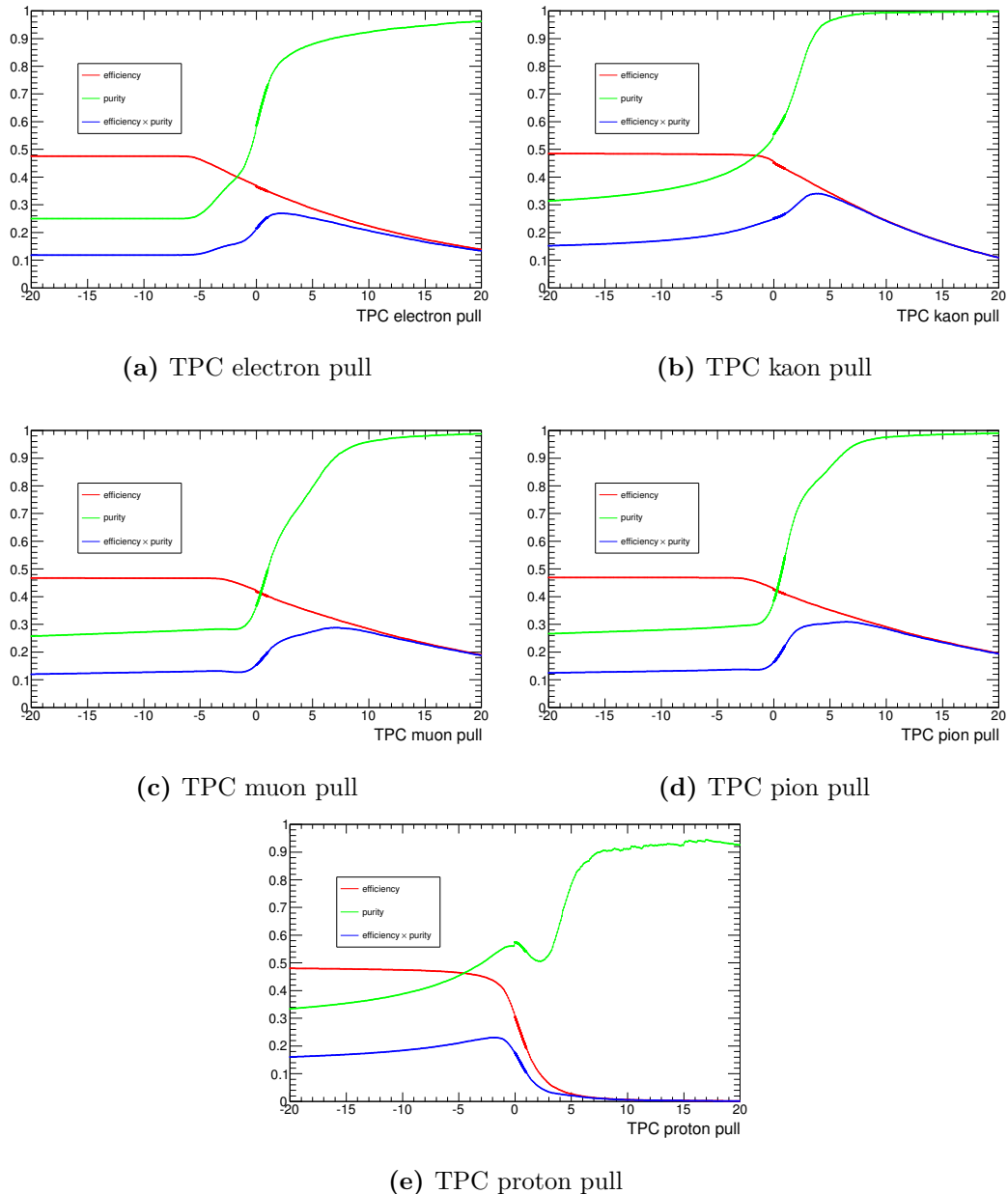


Figure 6.8.: Efficiency, purity and efficiency \times purity curves for selecting protons using a variety of TPC pulls.

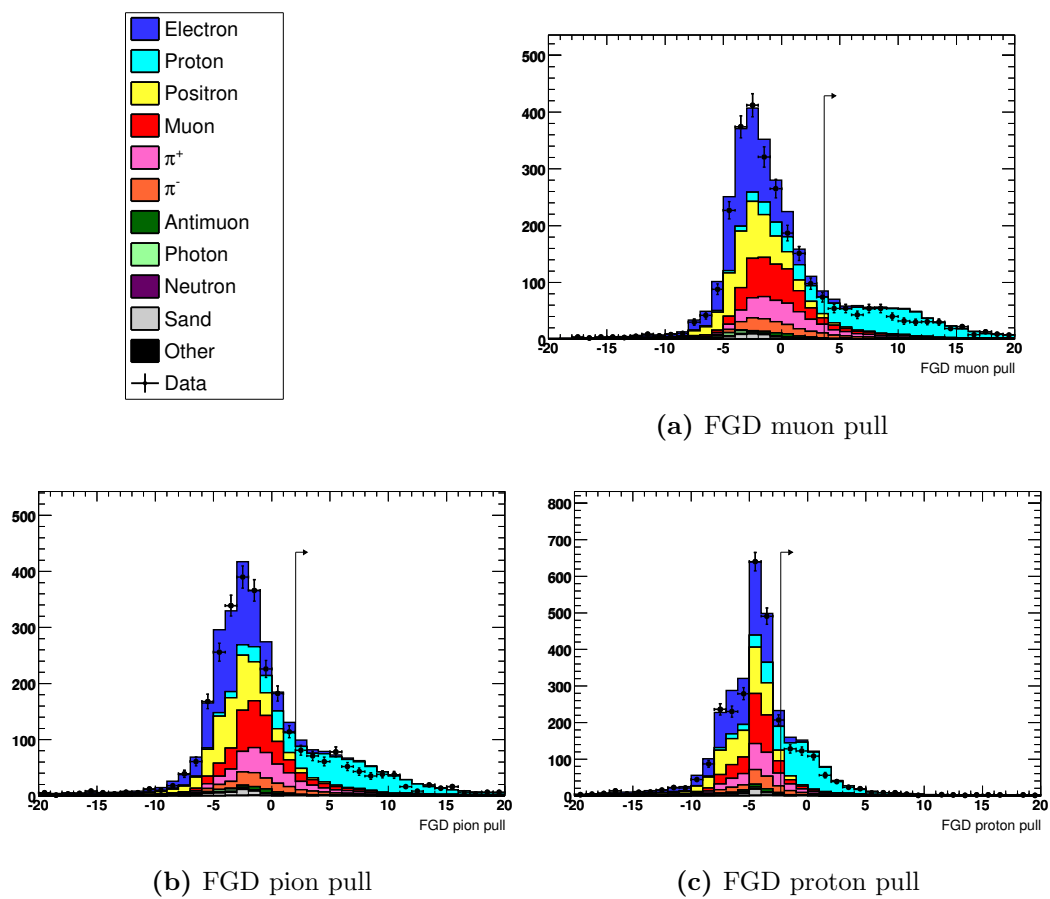
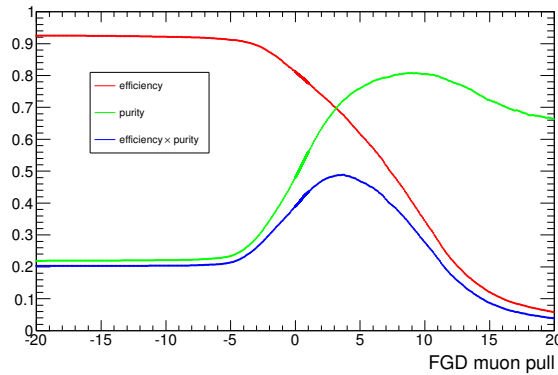
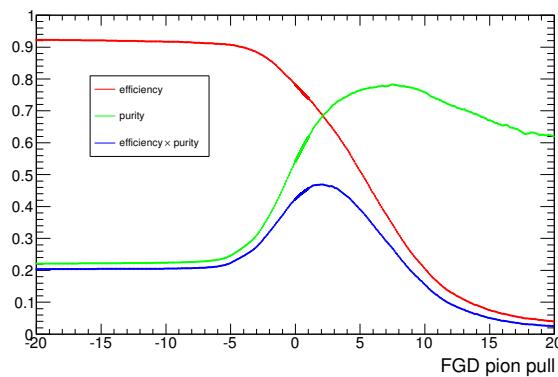


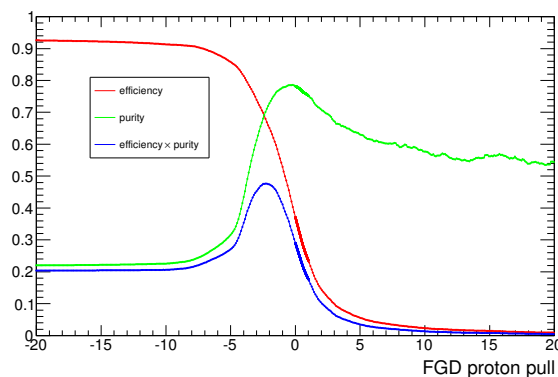
Figure 6.9.: FGD pull distributions produced using magnet and sand MC, POT normalised to data.



(a) FGD muon pull



(b) FGD pion pull



(c) FGD proton pull

Figure 6.10.: Efficiency, purity and efficiency \times purity curves for selecting protons using FGD pulls.

and the corresponding cut value can be found in Table 6.6. Hence it was decided that using the muon pull would produce the best sample of protons.

Type of pull	Max($\epsilon \times \pi$)	Efficiency (%)	Purity (%)	Cut value
Muon	48.86	67.84	72.01	3.65
Proton	47.63	67.96	70.09	-2.30
Pion	46.91	68.88	68.10	2.05

Table 6.6.: Efficiency and purity for FGD pulls optimised to select protons.

6.4.3. ECAL particle identification

Provided that the reconstructed object in the ECAL is deemed track-like (i.e. the ECAL variable track/shower (see Section 4.5.4) is required to be greater than or equal to 0.5), particle identification can be performed on the tracks that are reconstructed and travel through both the FGD and ECAL without traversing a TPC. The variable used to discriminate between protons and other particles is the charge per unit length of an ECAL track. Once again, the figure of merit chosen is efficiency \times purity, where the definitions of efficiency and purity are

$$\epsilon = \frac{\text{number of protons selected with useable ECAL information}}{\text{total number of protons with useable ECAL information}}, \quad (6.5)$$

and

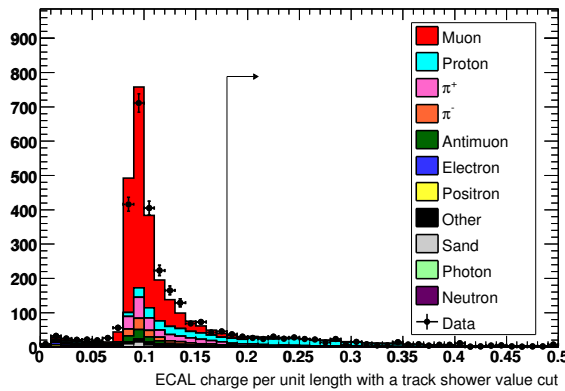
$$\pi = \frac{\text{number of protons selected with useable ECAL information}}{\text{number of tracks selected with useable ECAL information}}, \quad (6.6)$$

respectively. To increase the number of statistics in this sample, the quantity was optimised using *any* track entering the ECAL. Results are shown in Figure 6.11.

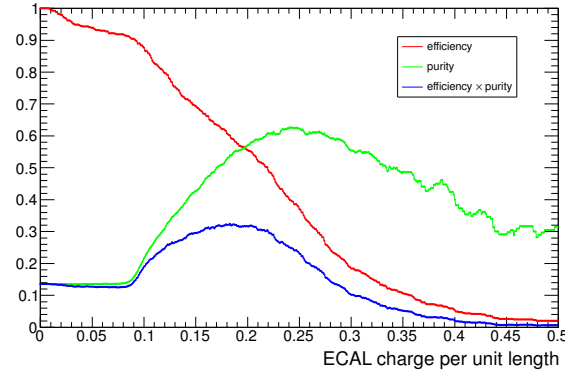
It was found that the maximum value of efficiency \times purity is 32.45% for a cut value of 0.18. The corresponding values of efficiency and purity are 60.08% and 54.02%, respectively.

6.4.4. Effectiveness of proton cuts

Table 6.7 shows the selection efficiency and purity information for each selection cut made thus far. As a result of the large number of background interactions, selection cuts



(a) ECAL charge per unit length



(b) ECAL charge per unit length

Figure 6.11.: (a) shows the ECAL charge per unit length for all track-like particles entering the ECAL. This plot was produced with magnet and sand MC and is POT normalised to data. (b) shows the efficiency, purity and efficiency \times purity curves for selecting protons in the ECAL.

Cut	Description	Total	Magnet	Sand	Signal	Efficiency (%)	Purity (%)
1	π^0 candidates	2335721	2148620	185809	1293	100.00	0.06
2	200 ns time cut	2317799	2132089	184417	1293	100.00	0.06
3	TPC1 veto	2171729	1994650	175806	1273	98.50	0.06
4	P0D veto	2086720	1920556	164908	1256	97.15	0.06
5	Proton-like tracks	1835546	1675468	159009	1070	82.73	0.06

Table 6.7.: Selection efficiency and purity after the cut requiring reconstructed tracks are proton-like is made.

2 – 5 do not noticeably increase the selection purity. However, the cuts do remove 22.0% (14.4%) of the magnet (sand) background interactions with a 17.2% loss of signal. The cut requiring all tracks are proton-like (cut number 5) removes 12.8% (3.6%) of magnet (sand) background events with a 14.8% loss of signal interactions. This loss of signal interactions is expected as only 75.1% of reconstructed tracks in the tracker for bunches containing a signal interaction were made by protons, as shown in Table 6.3. To justify implementing cuts 3 – 5 the whole analysis was performed both with and without cuts 3 – 5 applied and it was found that the final selection efficiency and purity was higher when cuts 3 – 5 were applied. This improved efficiency and purity when making cuts 3 – 5 is thought to arise because the cuts remove parts of the phase space corresponding to interactions occurring upstream of FGD1 and those interactions that are charged current. By making these cuts the difference in shape between signal and background ECAL variable distributions is increased and thus improves the separation of signal and background interactions achieved using TMVA.

6.5. Using the ECAL to select photons from NC $1\pi^0$ interactions

To select π^0 decay photons from NC $1\pi^0$ interactions in the FGD, specific variables (listed in Table 6.8) associated with the ECAL clusters selected in Section 6.3 are given to a multi-variate analysis (specifically the TMVA package in ROOT). A multi-variate analysis is used instead of a simple cuts-based analysis because the ECAL variable

distributions for signal and background interactions, shown in Figure 6.12, have a distinct difference in shape. There is no cut that can be made to each of the distributions that will reduce the number of background interactions without a significant signal loss. Ideally, a boosted decision tree (BDT)² would be used instead of a likelihood estimator. A BDT would naturally take into account the different ECAL cluster positions, discussed later in this section, and was found to produce a greater separation between signal and background interactions. Unfortunately a BDT is not used in this analysis because the amount of cherry picked MC files, used to provide the signal sample in TMVA, available (see Section 6.2) is not sufficient to ensure there is no overtraining. A TMVA likelihood estimator³ is used in this analysis as it was found that no overtraining occurred when using this method. The likelihood estimator works by building probability density functions (PDFs) that reproduce the signal and background variable distributions, ignoring correlations. The likelihood ratio $y_L(i)$ for an event i is defined by

$$y_L(i) = \frac{L_S(i)}{L_S(i) + L_B(i)}, \quad (6.7)$$

where

$$L_{S(B)}(i) = \prod_{k=1}^{n_{\text{var}}} p_{S(B),k}(x_k(i)), \quad (6.8)$$

and $p_{S(B),k}$ is the signal (background) PDF for the k th input variable x_k . The likelihood is then transformed using the function

$$y_L(i) \rightarrow y'_L(i) = \ln(y_L^{-1} - 1)/15, \quad (6.9)$$

to provide a more suitable output to place a cut, as shown in Figure 6.15. This transformed response is used throughout the analysis.

To improve the separation power of the variables, listed in Table 6.8, that are used in the multi-variate analysis, the ECAL clusters are split into three categories depending on their location within the ECAL:

² See Section 8.12 of the TMVA User's Guide for further information about boosted decision trees.

³ For more information about the likelihood estimator see Section 8.2 of the TMVA User's Guide.

- Category one: two clusters in the downstream ECAL,
- Category two: two clusters in the barrel ECAL,
- Category three: one cluster in the DsECAL and one in the BrECAL.

For categories one and two the potential inputs are split into two subcategories: high and low energy cluster, whereas for category three the splitting is: BrECAL and DsECAL cluster.

Some preliminary (pre-TMVA) cuts, detailed in Section 6.5.2, are made to remove background events with minimal loss to signal.

6.5.1. ECAL variables used in TMVA

To ensure the highest efficiency and purity is achieved it is essential to use ECAL variables with good signal/background separation. The variables used in the multi-variate analysis are listed in Table 6.8.

Label	Variable name	Description
a (f)	High / BrECAL (low / DsECAL) most ‘outside’ layer	Layer number in the cluster with the largest local z coordinate
b (g)	High / BrECAL (low / DsECAL) incidence angle (rad)	Local z component of the thrust axis (see Section 4.5.5)
c (h)	High / BrECAL (low / DsECAL) number of hits	Number of reconstructed hits in the cluster (minimum of 4 hits required to form a cluster)
d (i)	High / BrECAL (low / DsECAL) track/shower value	See Section 4.5.4
e (j)	High / BrECAL (low / DsECAL) most ‘inside’ layer	Layer number in the cluster with the smallest local z coordinate
k	Angle between clusters (rad)	Angle between the (3D) thrust axes of the clusters
l	Distance between clusters (mm)	Magnitude of the difference between thrust origins of the clusters (see Section 4.5.5)
m	Energy asymmetry	$(E_{h(b)} - E_{l(d)}) / (E_{h(b)} + E_{l(d)})$ where $h(b)$ and $l(d)$ refers to the high energy (barrel) and low energy (downstream) cluster, respectively, and E is the reconstructed energy

Table 6.8.: ECAL variables used in the TMVA. (For geometry information see Section 4.2, whereas for specific ECAL variable information see Section 4.5.)

6.5.2. Pre-TMVA cuts made to ECAL variables

To ensure the separating power of the multi-variate analysis is maximal preliminary cuts are made to the ECAL variables to remove background events with minimal loss of signal. Variable distributions for signal and background samples prior to these pruning cuts can be found in Figures A.1, A.2 and A.3.

The first cut, made for all ECAL cluster position categories, requires that there are no Michel electrons in the ECAL. Michel electron candidates are determined by first identifying a stopping muon candidate in the ECAL and then looking for energy deposits, in the form of unclustered hits, that are delayed in time. In addition to the fact that when selecting photons we expect there to be no Michel electrons, Figures A.1c, A.1i, A.2c, A.2i, A.3c and A.3i show that there is a distinct difference between signal and background distributions for this variable.

The requirement that the invariant mass is less than 500 MeV is also made. The invariant mass is defined as

$$\sqrt{2E_{h(b)}E_{l(d)}(1 - \cos(\theta_{hl(bd)}))}, \quad (6.10)$$

where $E_{h(b)}$ refers to the reconstructed energy for the high energy (barrel) cluster, similarly, $E_{l(d)}$ is the energy of the low energy (downstream) cluster and $\cos(\theta_{hl(bd)})$ is the angle between the high and low energy (barrel and downstream) cluster. As the interaction vertex has not been reconstructed at this stage of the selection the angle is calculated using the thrust axes of the ECAL clusters. Additional pre-TMVA cuts, listed in Table 6.9, are made to remove only background events.

Label	Category one	Category two	Category three
a	Must be > 2	No cut	No cut
b	No cut	No cut	No cut
c	No cut	Must be < 80	Must be < 80
d	Must be < 1.05	Must be < 1.10	Must be < 1.10
e	No cut	No cut	No cut
f	Must be > 2	No cut	No cut
g	No cut	No cut	No cut
h	No cut	No cut	No cut
i	Must be < 1.1	Must be < 1.1	Must be < 1.05
j	No cut	No cut	No cut
k	No cut	No cut	No cut
l	No cut	No cut	No cut
m	No cut	No cut	No cut

Table 6.9.: Pre-TMVA cuts for various cluster position categories. For label definitions see Table 6.8. The events passing these cuts are used in the TMVA analysis.

6.5.3. Distribution of ECAL variables used in TMVA

The final ECAL variable distributions for signal, magnet background and sand background interactions for category two can be found in Figure 6.12. To avoid repetition the same distributions for categories one and three can be found in Figures A.4 and A.5, respectively.

As a multi-variate analysis uses shape differences to distinguish between signal and background events, it is important to show there is reasonable to good agreement between data and MC for the ECAL variables used (a systematic error is also applied to account for any discrepancies, see Section 6.8.4). The area normalised plots for the input variables for category two can be found in Figure 6.13. Again, to avoid repetition the data and MC distributions for categories one and three can be found in in Figures A.6 and A.7, respectively. The POT normalised plots for all cluster categories can also be found in Figures A.8, A.9 and A.10. It is unsurprising that there is a poor agreement between the data and POT normalised MC, as the sand MC is still in the preliminary stages of development and currently does not have the correct normalisation.

The correlation matrix for input ECAL variables given to TMVA for each cluster location category can be found in Figure 6.14. The matrices show that there is generally little correlation between input variables.

6.5.4. TMVA response

As shown in Figure 6.15, the transformed likelihood response function shows there is a good separation of signal and background interactions for each cluster category. The cut value was varied across the transformed likelihood range and the value of

$$\frac{\text{number of signal events selected for a given cut value}}{\sqrt{(\text{total number of signal events}) + (\text{total number of background events})}}, \quad (6.11)$$

was used to optimise the cut⁴. Results for varying cut values can be found in Figure 6.16, whereas Table 6.10 details the cut value chosen for each cluster position category.

⁴ It should be noted that the number of signal and background events used in this study is the number remaining after all previous cuts are made and is not the original number of events before any cuts were made.

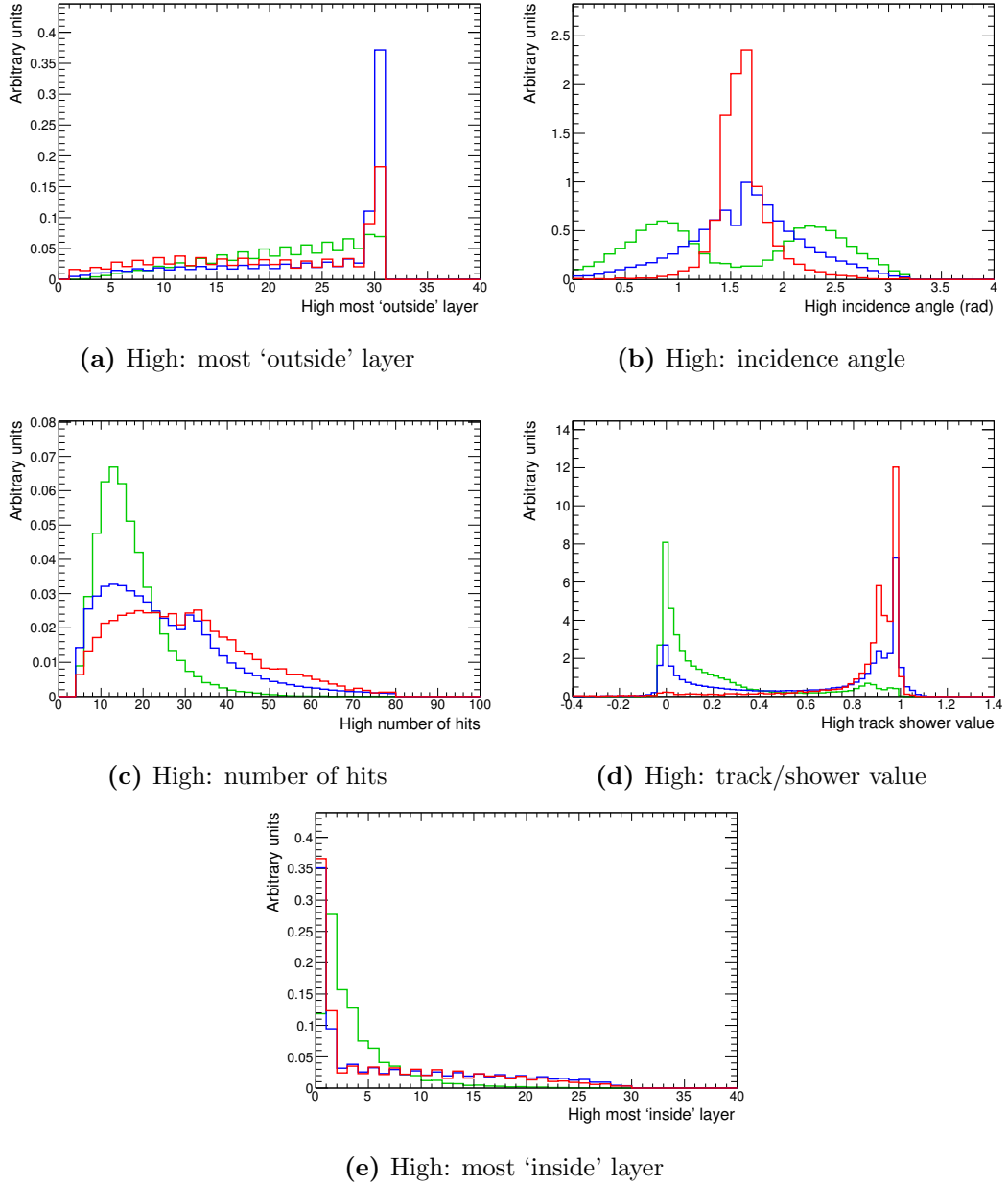


Figure 6.12.: Signal (green), magnet background (blue) and sand background (red) distributions for ECAL variables used in TMVA for the high energy cluster in category two (both clusters in the BrECAL) after the pre-TMVA cuts are made. For label definitions see Table 6.8.

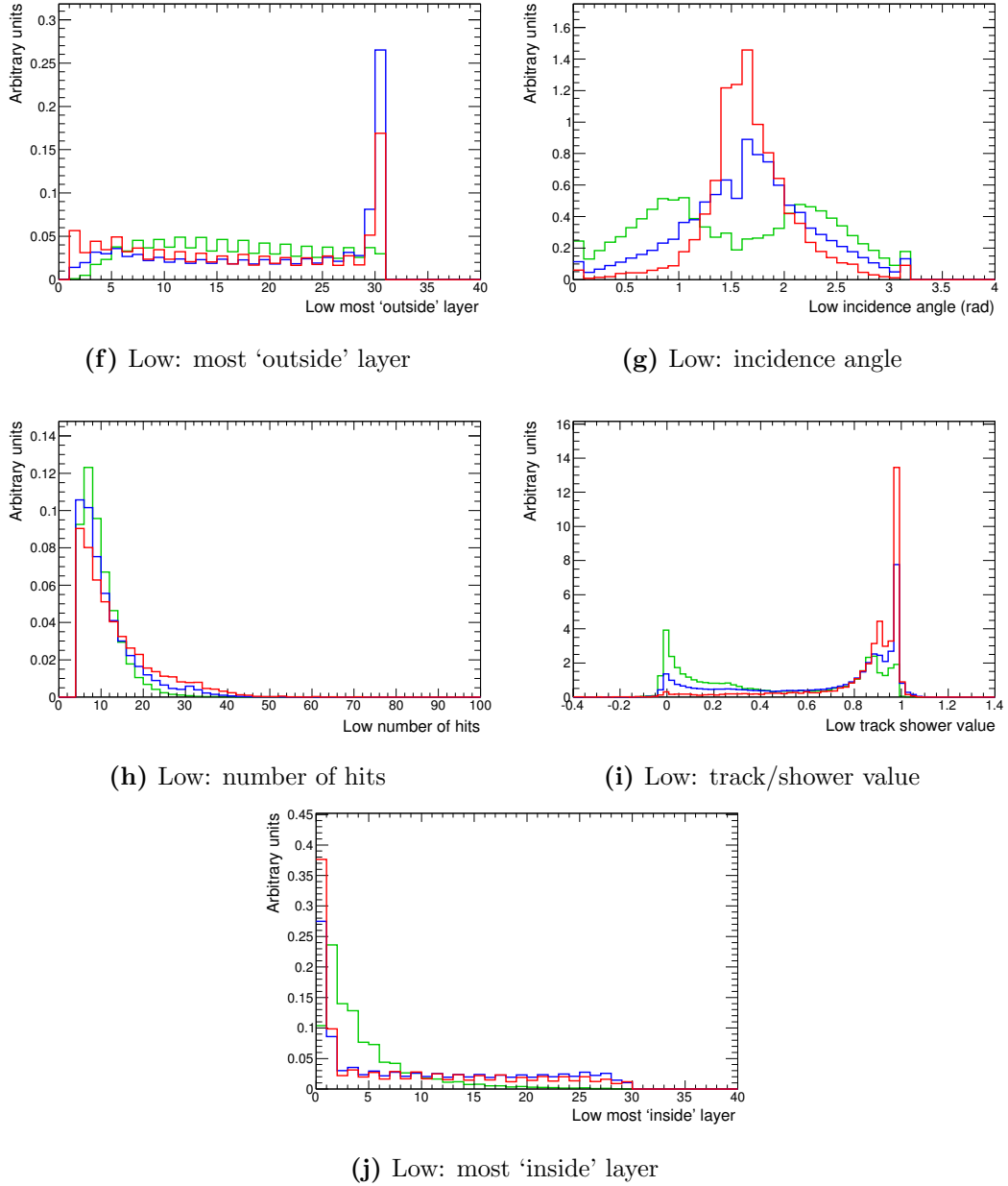


Figure 6.12.: Signal (green), magnet background (blue) and sand background (red) distributions for ECAL variables used in TMVA for the low energy cluster in category two (both clusters in the BrECAL) after the pre-TMVA cuts are made. For label definitions see Table 6.8.

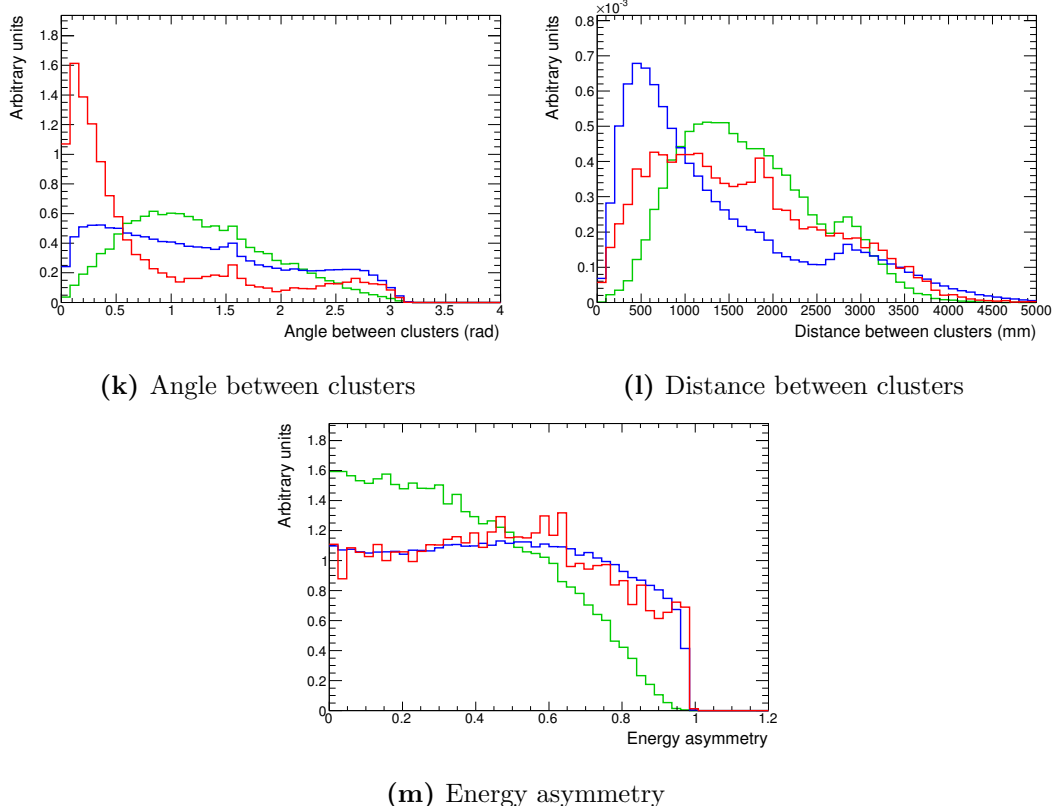


Figure 6.12.: Signal (green), magnet background (blue) and sand background (red) distributions for ECAL variables used in TMVA for category two (both clusters in the BrECAL) after the pre-TMVA cuts are made. For label definitions see Table 6.8.

Position category	$\frac{\text{signal}}{\sqrt{(\text{signal}+\text{background})}}$	Signal	Background	Cut value
one	4.80	75	169	0.248
two	1.87	78	1665	1.478
three	3.89	154	1413	0.756

Table 6.10.: Optimum TMVA cut value for each ECAL position category and corresponding numbers of signal and background interactions selected. The optimum cut value was determined by maximising the figure of merit $\frac{\text{signal}}{\sqrt{\text{signal} + \text{background}}}$, using magnet and sand MC.

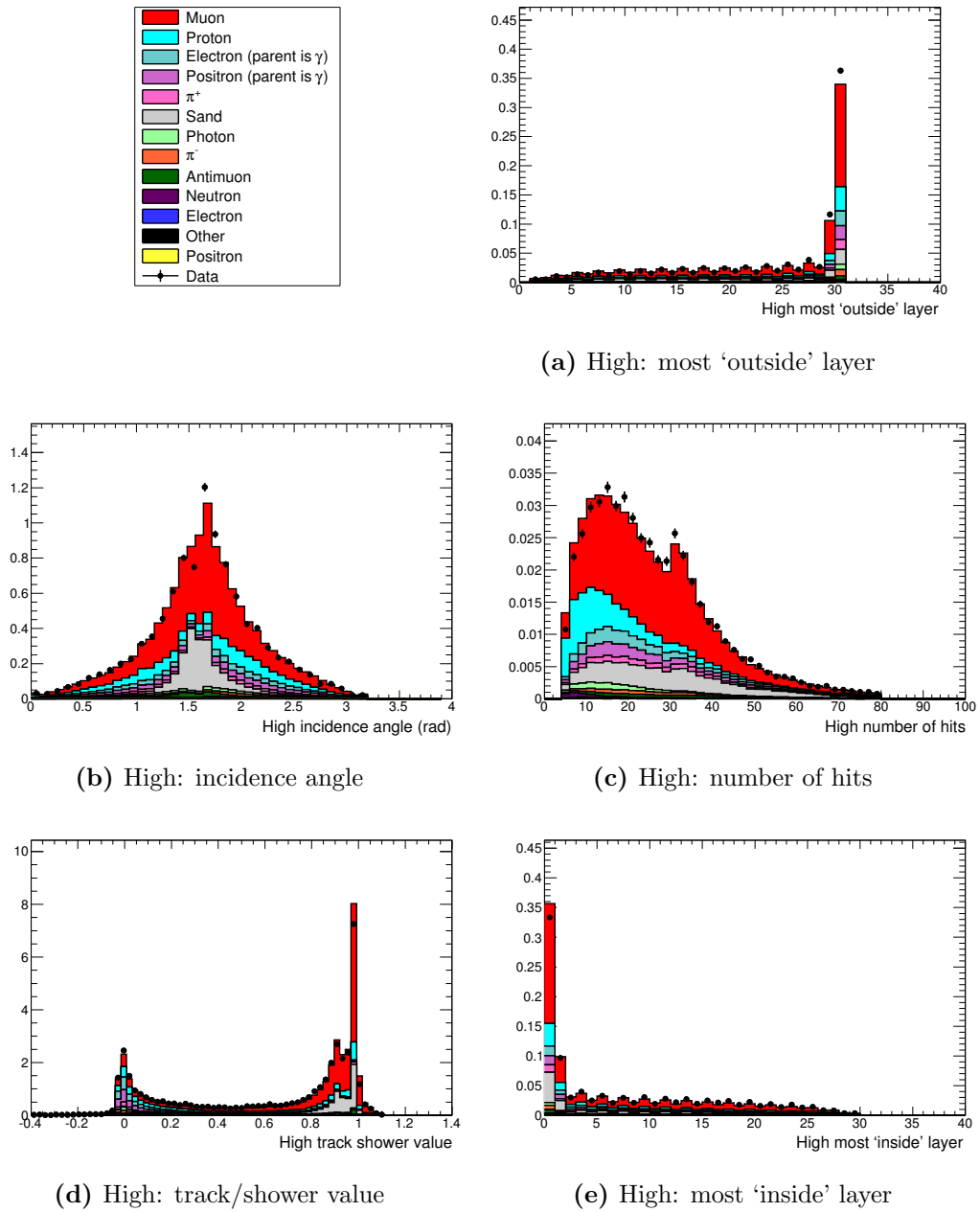


Figure 6.13.: Data and MC distributions of ECAL variables used in TMVA for the high energy cluster in category two. Plots are area normalised. For label definitions see Table 6.8.

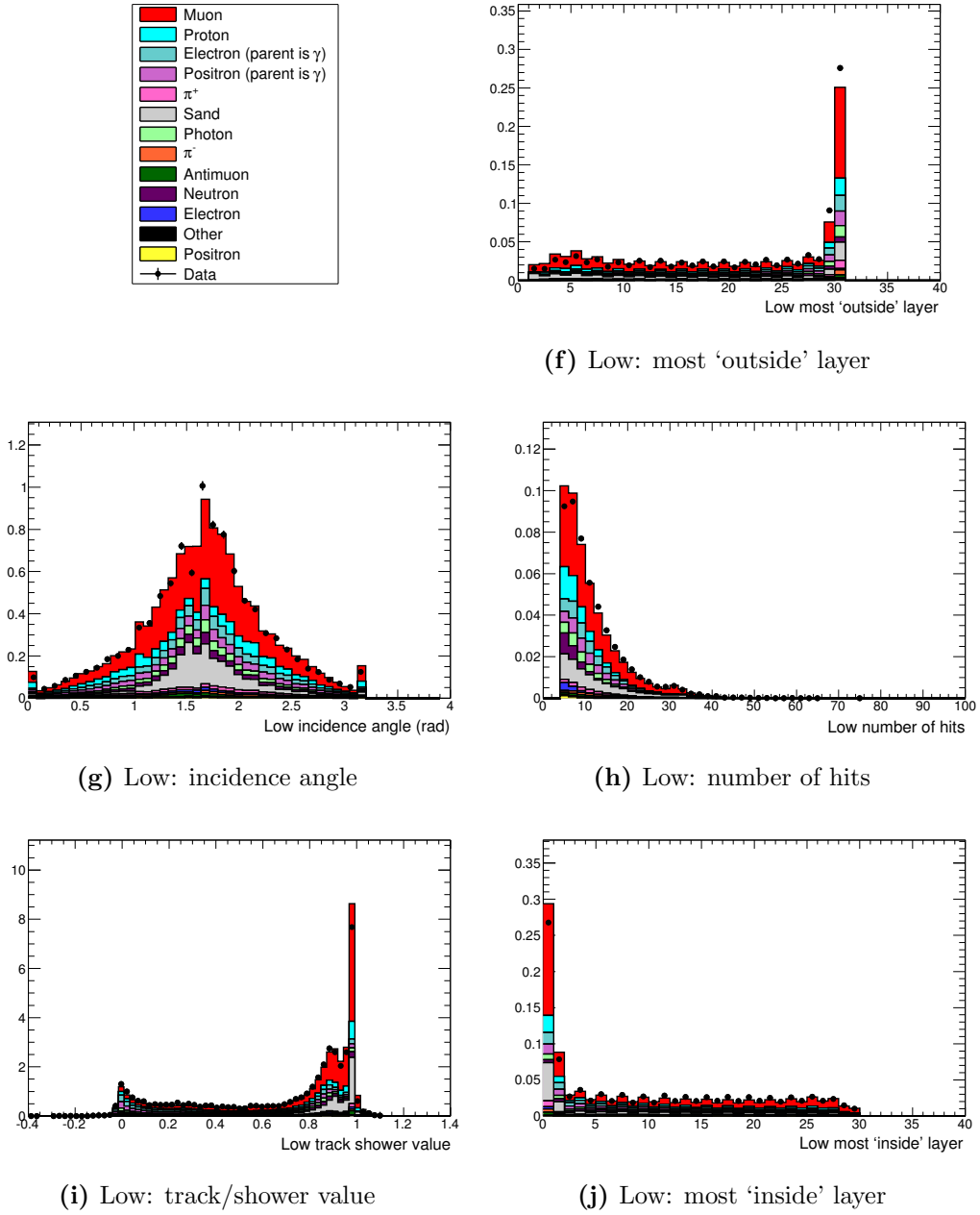
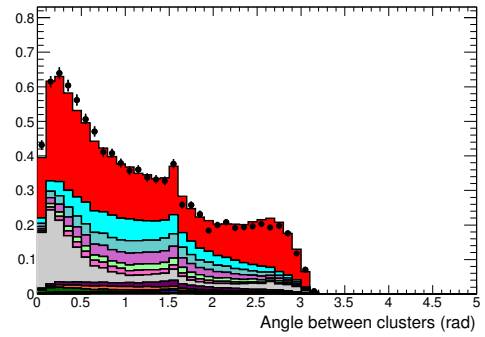
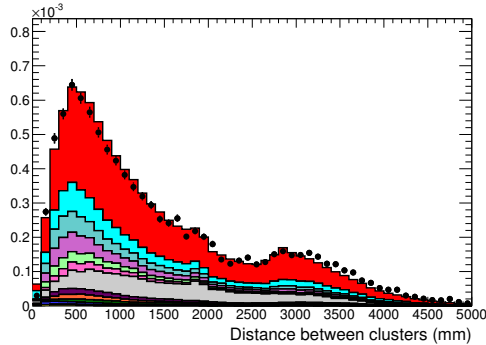


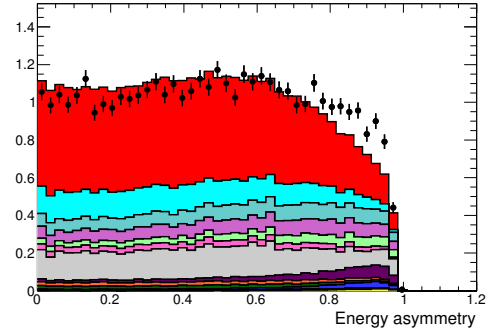
Figure 6.13.: Data and MC distributions of ECAL variables used in TMVA for the low energy cluster in category two. Plots are area normalised. For label definitions see Table 6.8.



(k) Angle between clusters



(l) Distance between clusters



(m) Energy asymmetry

Figure 6.13.: Data and MC distributions of ECAL variables used in TMVA for category two. Plots are area normalised. For label definitions see Table 6.8.

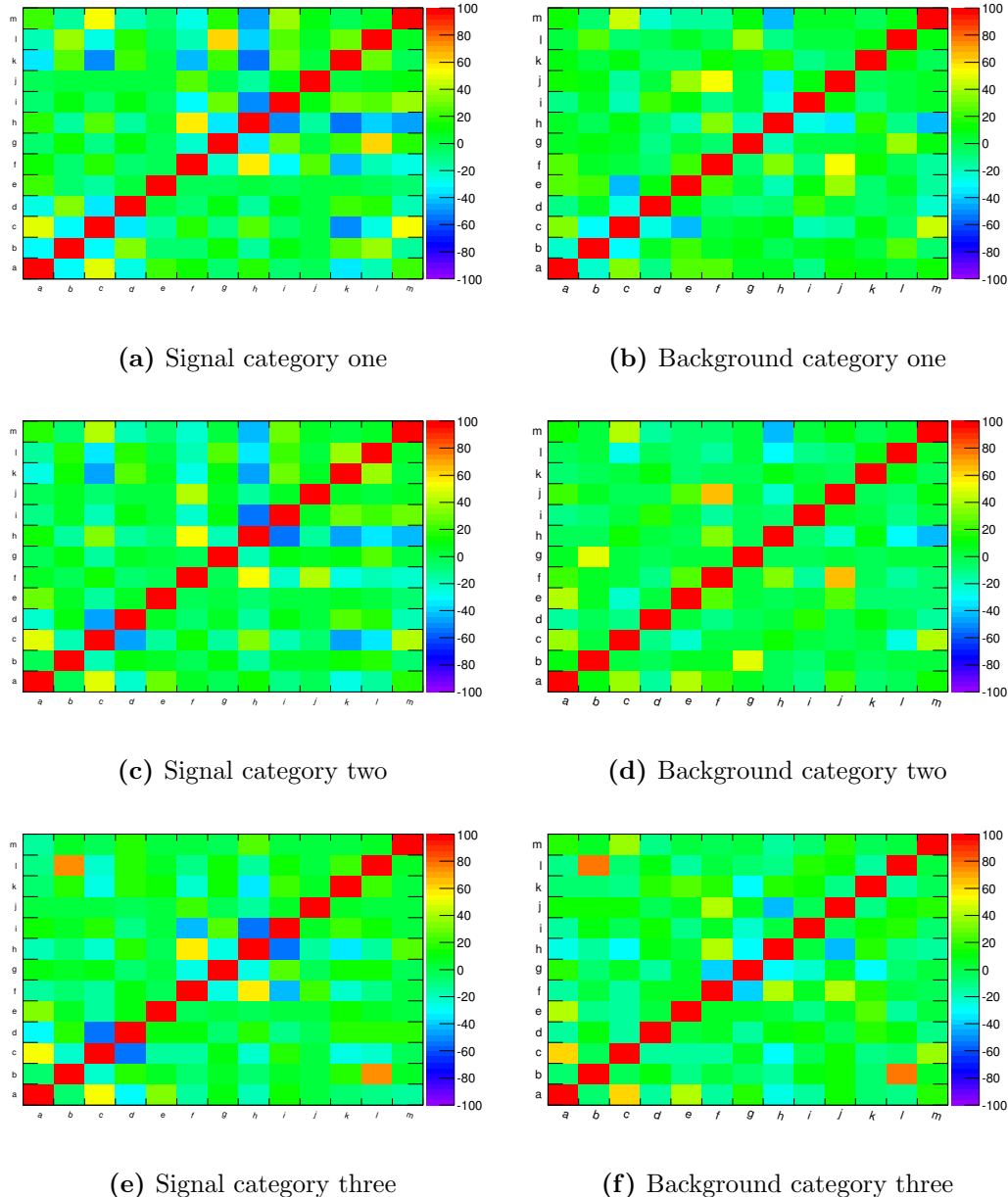


Figure 6.14.: Signal and background correlation matrices for ECAL variables used in TMVA for all cluster categories.

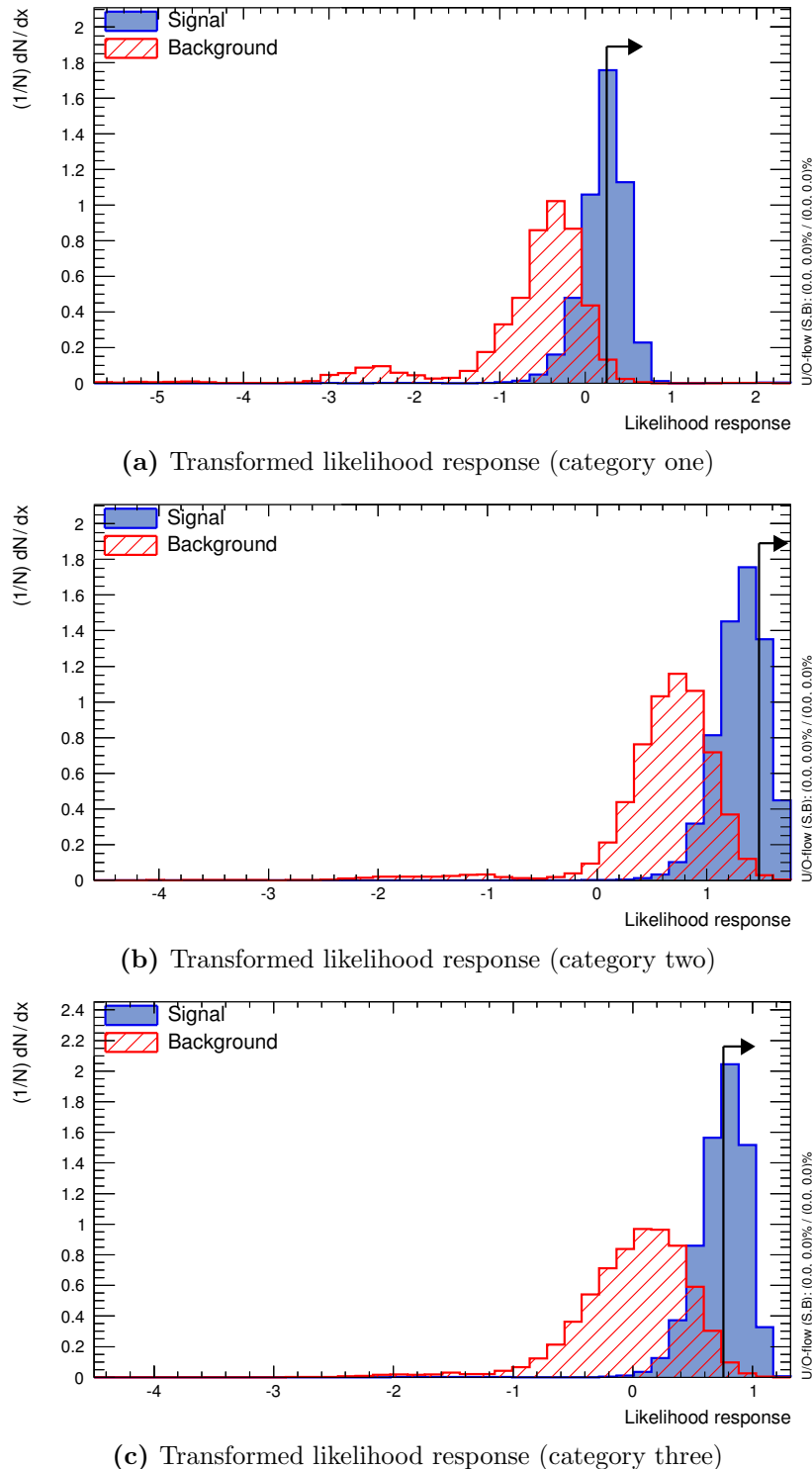
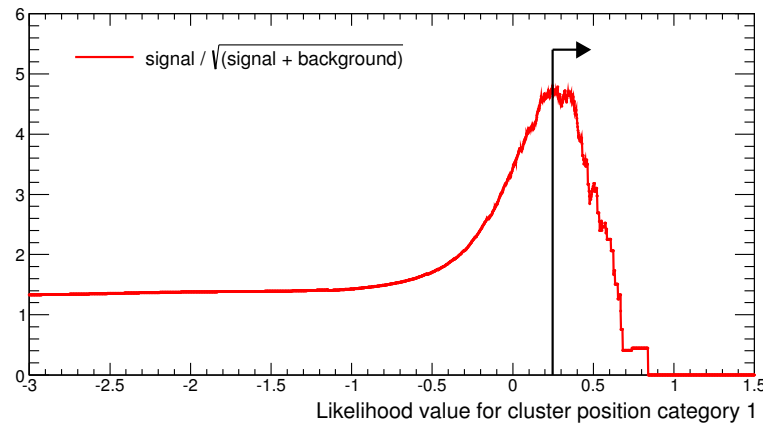
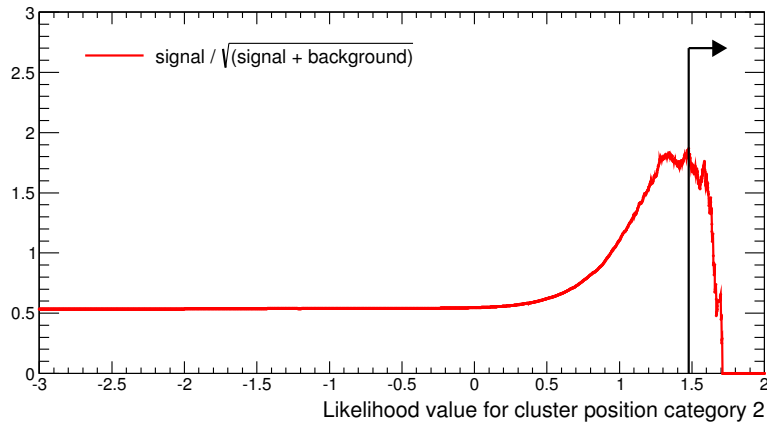


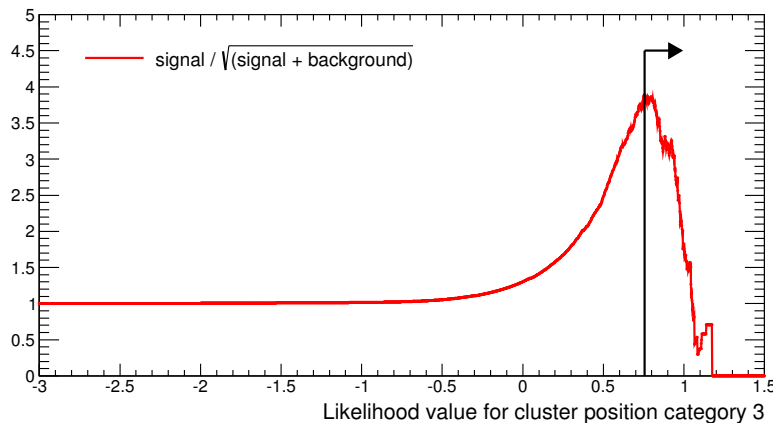
Figure 6.15.: (a), (b) and (c) show the signal/background separation of the transformed likelihood (and chosen cut value based on an optimisation study) for categories one, two and three, respectively.



(a) Category one



(b) Category two



(c) Category three

Figure 6.16.: The value of the discriminator $\frac{\text{signal}}{\sqrt{\text{signal} + \text{background}}}$ for various cut values of the transformed likelihood response from TMVA. All of the magnet and sand MC was used to make these plots (1.868×10^{21} POT and 3.650×10^{20} POT, respectively).

Information available	% signal events	% background events
1 tracker track	19.9	4.2
>1 tracker tracks	3.2	0.7
Unused FGD hits	16.1	19.9
No tracker information	60.8	75.2

Table 6.11.: Tracker information available to use to reconstruct the interaction vertex after making a cut on the TMVA transformed likelihood response.

6.6. Determining an interaction vertex

The method used to determine an interaction vertex is dependent on the information available in the tracker. Table 6.11 shows that only 19.9% (3.2%) of bunches containing a signal interaction have (more than) one reconstructed track in the tracker, whereas for the background case this is significantly lower at 4.2% (0.7%). Also, 16.1% (19.9%) of bunches containing a signal (background) interaction have unused hits in the FGD that can be used to reconstruct a vertex. Finally, 60.8% (75.2%) of signal (background) interactions have no tracker information that can be used to reconstruct a vertex and, as a result, the direction of the reconstructed ECAL clusters must be used to infer the vertex location.

6.6.1. Reconstructed tracks in the TPC and FGD

If there is more than one reconstructed track in the tracker for the bunch containing the π^0 candidate, the start position of the TPC track with the highest momentum is used. If there are no tracks in the TPC, the start position of the FGD track with the most hits is used. If there is only one track, the start position of that track is used as a vertex.

6.6.2. Unused FGD hits not associated with a reconstructed tracker object

If there are no reconstructed tracks in the FGD or the TPC, there is still useable information in the FGD. The FGD stores any unused hits or hits that were part of a 2D

track that could not be made into a 3D track. The charge weighted position of these unused hits is used to estimate the vertex position. If there are unused hits in both FGD1 and FGD2, the charge weighted position in the FGD with the highest total charge deposited is used.

6.6.3. Information from ECAL clusters only

If there are no reconstructed tracks in the tracker or unused FGD hits, information gained solely from the ECAL clusters is used to try to reconstruct a vertex. As discussed in Section 4.5.5, as a result of the small number of hits in a reconstructed photon cluster, the direction reconstruction is often inaccurate. These inaccuracies mean that it is not possible to extrapolate both clusters back into the tracker and expect them to converge on a single point.

To try to reconstruct a vertex it is necessary to decide which FGD to try first. If the global z position of the cluster is less (greater) than the centre of FGD1 (FGD2) then the vertex reconstruction is attempted in FGD1 (FGD2). However, if the z position of the cluster is greater than the centre of FGD1 and less than the centre of FGD2 the thrust axis is used to determine the vertex. If the z coordinate of the thrust axis is positive (negative) vertex reconstruction attempts are made in FGD1 (FGD2).

As a first attempt the high energy cluster is used. Once the FGD has been decided, using the method described above, the thrust axis is extrapolated to the global z coordinate corresponding to the centre of that FGD. If the corresponding x and y coordinates of the extrapolated track are inside the FGD, that position is used. If the vertex is not inside the FGD the high energy cluster is used, but the alternate FGD is considered. If a vertex has not successfully been reconstructed using the high energy cluster, the process is repeated using the low energy cluster.

6.6.4. Performance of vertexing methods

The vertex reconstruction efficiency for signal interactions when there is one or more reconstructed track(s) is approximately 95%. For the case where unused FGD hits are used to reconstruct the vertex, the reconstruction efficiency is lower at approximately 87%. The final case, where no tracker information is available and, as a result, the vertex

is reconstructed using information from the ECAL clusters, has the lowest the efficiency of 77%.

The vertex reconstruction performance for the various methods can be found in Figure 6.17. As a result of low statistics in magnet MC, these plots were made using events passing all previously mentioned cuts for cherry picked MC and thus are for true signal interactions only. The plots show that the method using the start position of a track is the most accurate and that the others perform less well, as expected. Figure 6.17c highlights the fact that the method using unused FGD hits often selects the wrong FGD, as there are a large number of events peaked at ~ 1400 mm. Whilst it appears that the method using only ECAL information is better than the FGD unused hits, it should be noted that the loss in selection efficiency as a result of vertex reconstruction comes primarily from the method using ECAL information only. Whilst the FGD unused hits often choose the wrong FGD, this method still selects some signal interactions.

6.7. Efficiency and purity for selecting NC $1\pi^0$ interactions

Overall, neglecting reconstruction efficiency, an efficiency of 22.24% and purity of 15.66%, for selecting NC $1\pi^0$ interactions in FGD1 and FGD2 where both π^0 decay photons convert in the ECAL, is obtained. For ECAL cluster position categories one, two and three the efficiency and purity information after each selection cut can be found in Table 6.12, 6.13 and 6.14, respectively⁵.

Interactions where at least one photon converts in the downstream ECAL have the highest efficiency and purity. For the case where both photons convert in the DsECAL (category one) the efficiency is 33% and the purity is 43%. When only one of the π^0 decay photons convert in the DsECAL (category three) the efficiency is 29% and the purity is 16%. However, if both reconstructed clusters are in the barrel ECAL (category two) an efficiency and purity of 12% and 9% is achieved, respectively. It is not surprising that photon topologies including the DsECAL have a higher efficiency and purity than those solely in the barrel. There are fewer backgrounds in the DsECAL, as it is not

⁵ When reading the table it is important to note that the number of events refers to the number remaining after the cut was applied.

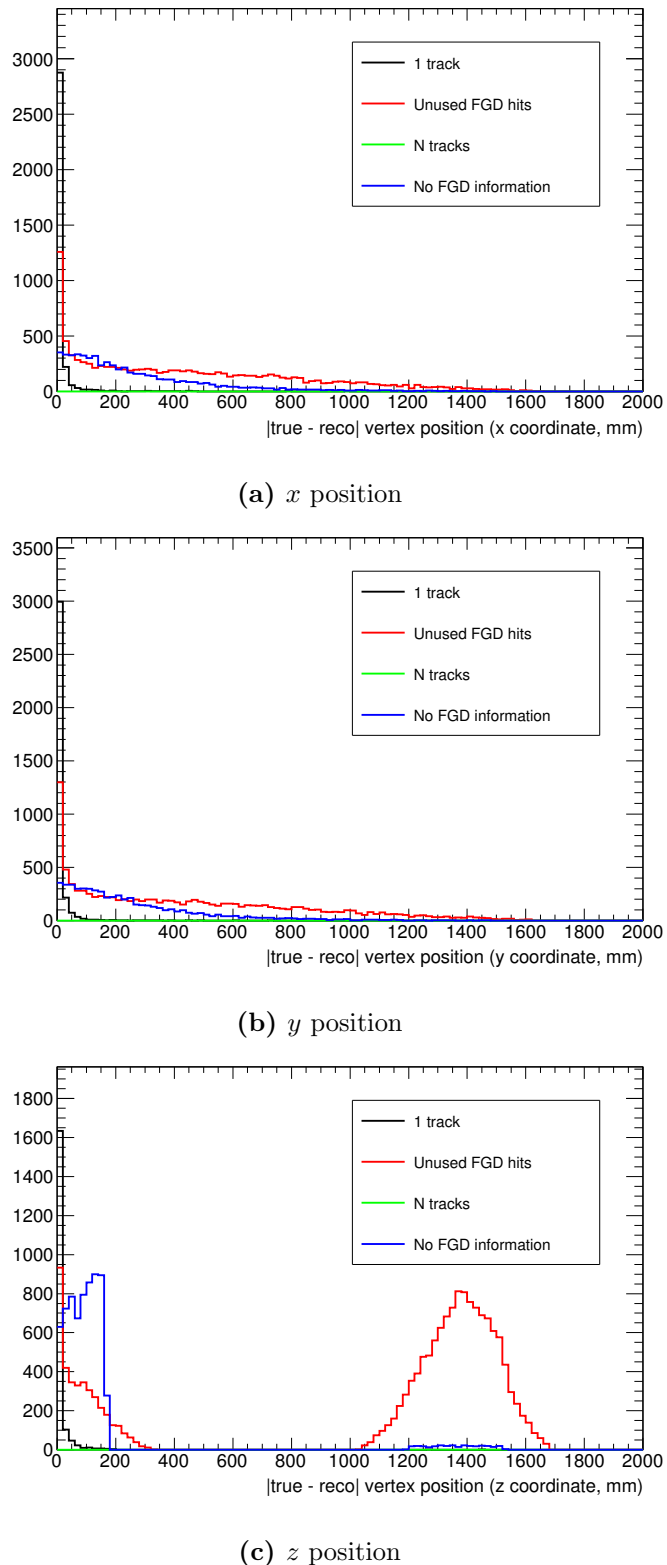


Figure 6.17.: Magnitude of the difference between true and reconstructed vertex position, which was obtained using a variety of methods. To ensure ample statistics, this plot was made using cherry picked MC and is for true signal interactions only.

Cut	Description	Total	Magnet	Sand	Signal	Efficiency (%)	Purity (%)
1	π^0 candidates	39481	38328	931	222	100.00	0.56
2	200 ns time cut	38129	36996	911	222	100.00	0.58
3	TPC1 veto	34782	34017	547	218	98.05	0.63
4	P0D veto	33947	33300	430	217	97.55	0.64
5	Proton-like tracks	26356	25844	322	189	85.02	0.72
6	Pre-TMVA	12041	11631	256	154	69.33	1.28
7	Transformed likelihood	294	207	0	88	39.52	29.81
8	Vertex in FGD	169	96	0	73	32.85	43.09

Table 6.12.: Efficiency and purity for each selection cut for ECAL cluster position category one (both clusters in the DsECAL).

encased by the SMRD, like the BrECAL is. Also, the variables output by the ECAL reconstruction were developed and optimised using the DsECAL.

The POT normalised π^0 invariant mass distributions for all ECAL position categories can be found in Figure 6.18; the signal is in cyan and the backgrounds are displayed based on the interaction type⁶ (for a full breakdown of the backgrounds including the interaction location and type, see Tables A.1, A.2 and A.3). There is a good agreement between data and MC at the 68% confidence level. The total number of (signal and backgrounds) events predicted for the Run 2 data set for category one, two and three is 7, 32 and 38, respectively. The number of events selected in data is 5, 22 and 31 for categories one, two and three, respectively. Thus, neglecting errors, data and MC are in agreement to within 1σ .

The largest background for events falling into category one is from charged current interactions in the ECAL, whereas for categories two and three the main backgrounds are a result of both charged current and neutral current interactions in the ECAL.

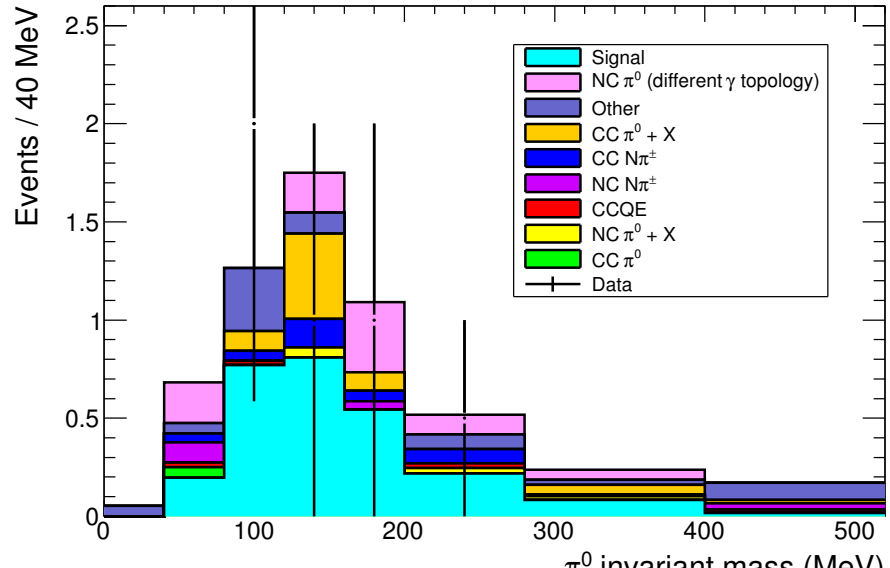
⁶ It should be noted that “NC $1\pi^0$ (different γ topology)” refers to an NC $1\pi^0$ interaction occurring *anywhere* in the ND280 where both photons do not convert in the ECAL.

Cut	Description	Total	Magnet	Sand	Signal	Efficiency (%)	Purity (%)
1	π^0 candidates	1854198	1692190	161429	580	100.00	0.03
2	200 ns time cut	1839116	1678464	160073	580	100.00	0.03
3	TPC1 veto	1723201	1569080	153549	572	98.59	0.03
4	P0D veto	1649762	1505549	143649	564	97.20	0.03
5	Proton-like tracks	1479899	1339083	140344	472	81.39	0.03
6	Pre-TMVA	481911	423460	58056	395	68.08	0.08
7	Transformed likelihood	2017	1888	41	89	15.29	4.39
8	Vertex in FGD	755	669	15	71	12.21	9.38

Table 6.13.: Efficiency and purity for each selection cut for ECAL cluster position category two (both clusters in the BrECAL).

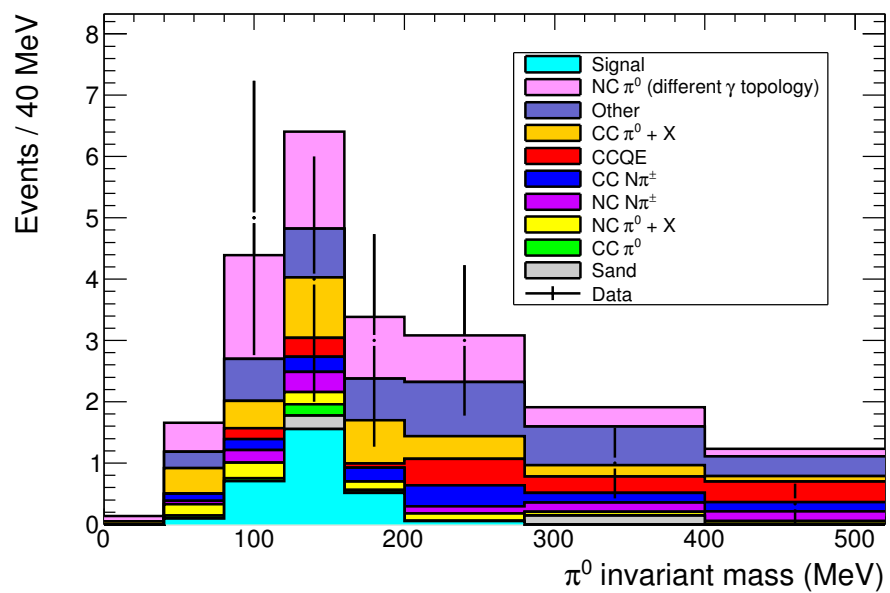
Cut	Description	Total	Magnet	Sand	Signal	Efficiency (%)	Purity (%)
1	π^0 candidates	442041	418102	23449	491	100.00	0.11
2	200 ns time cut	440554	416630	23433	491	100.00	0.11
3	TPC1 veto	413746	391553	21709	484	98.60	0.12
4	P0D veto	403011	381707	20829	476	96.92	0.12
5	Proton-like tracks	329291	310540	18342	409	83.29	0.12
6	Pre-TMVA	102180	94728	7112	340	69.27	0.33
7	Transformed likelihood	1831	1645	10	175	35.70	9.57
8	Vertex in FGD	912	763	5	144	29.29	15.78

Table 6.14.: Efficiency and purity for each selection cut for ECAL cluster position category three (one cluster in the DsECAL, one cluster in the BrECAL).



(a)

Figure 6.18.: Final π^0 invariant mass distribution for ECAL cluster position category one. Sand and magnet MC are POT normalised to the Run 2 data.



(b)

Figure 6.18.: Final π^0 invariant mass distribution for ECAL cluster position category two. Sand and magnet MC are POT normalised to the Run 2 data.

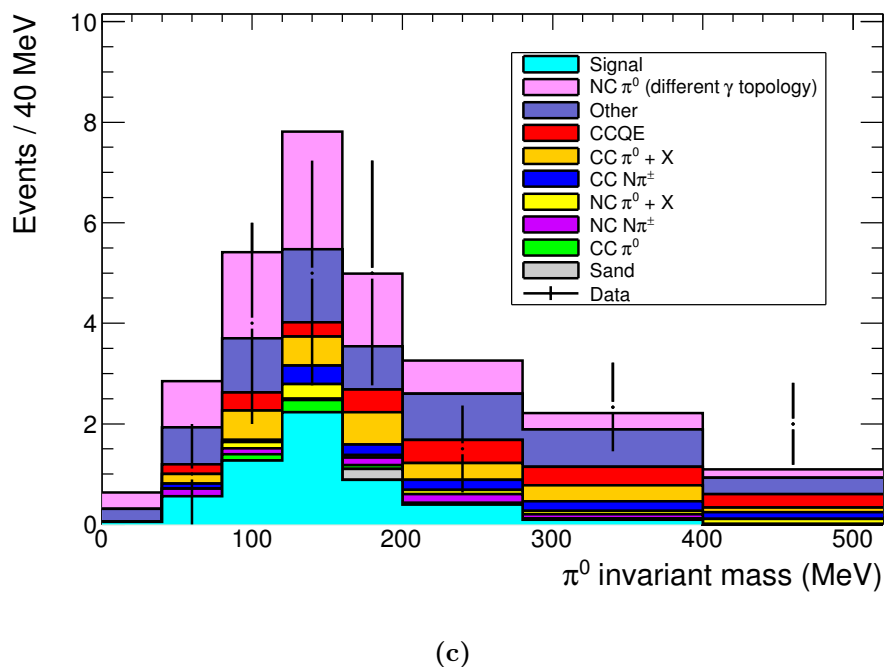


Figure 6.18.: Final π^0 invariant mass distribution for ECAL cluster position category three. Sand and magnet MC are POT normalised to the Run 2 data.

6.8. Systematic uncertainties

Several sources of systematic error are considered in this analysis namely, cross-section model parameter and final state interaction (FSI) errors, described in Sections 6.8.1 and 6.8.2, respectively; neutrino flux prediction errors (Section 6.8.3) and an estimate of the systematic uncertainty associated with the multi-variate analysis resulting from the shape discrepancy between data and MC (Section 6.8.4). Whilst it is not possible to include a full set of detector systematics at this time, a qualitative discussion of these systematics is presented in Section 6.8.6.

6.8.1. Cross-section model parameter systematic errors

Event reweighting is used to estimate the effect of the uncertainty in cross-section model parameters on the π^0 invariant mass distribution. Reweighting is a convenient way to vary underlying cross-section parameters for an event without needing to rerun the MC simulation, which is computationally intensive. Also, reweighting has the benefit of not conflating systematic errors with the MC statistical errors associated with independent data sets. A full description of the machinery used, called T2KReWeight, can be found in [68] and [69]. However, the basic principle behind event reweighting is as follows: for an event i , a weight,

$$w_i = \frac{\sigma(\vec{x}^i)}{\sigma(\vec{x})}, \quad (6.12)$$

is calculated to model a change in cross-section parameters where $\sigma(\vec{x})$ is the nominal cross-section and $\sigma(\vec{x}^i)$ is the updated cross-section for the changed parameters. By applying these individual weights to the selected events it is possible to achieve a similar output to a regenerated MC sample.

The official model parameters, errors and applicable energy ranges used in reweighting can be found in Table 6.15. All parameters are considered to be uncorrelated, apart from M_A^{RES} , CC 1π E1 and NC $1\pi^0$, as shown in the covariance matrix in Figure 6.19a. These cross-section parameter values and errors were determined using mainly neutrino-nucleus scattering data from the MiniBooNE experiment, however future studies will use data from SciBooNE, K2K and NOMAD. This need for external data arises because current

Parameter	E_ν range (GeV)	Best fit value	Fractional error
M_A^{QE}	all	1.21 GeV	0.37
M_A^{RES}	all	1.16 GeV	0.18
SF	all	0 (off)	1 (on)
E_b	all	25 MeV	0.36
p_F	all	217 MeV	0.14
CCQE E1	$0 < E_\nu < 1.5$	1.0	0.11
CCQE E2	$1.5 < E_\nu < 3.5$	1.0	0.3
CCQE E3	$E_\nu > 3.5$	1.0	0.3
CC 1π E1	$0 < E_\nu < 2.5$	1.63	0.32
CC 1π E2	$E_\nu > 2.5$	1.0	0.4
CC other	all	0.0	0.4
NC $1\pi^0$	all	1.19	0.33

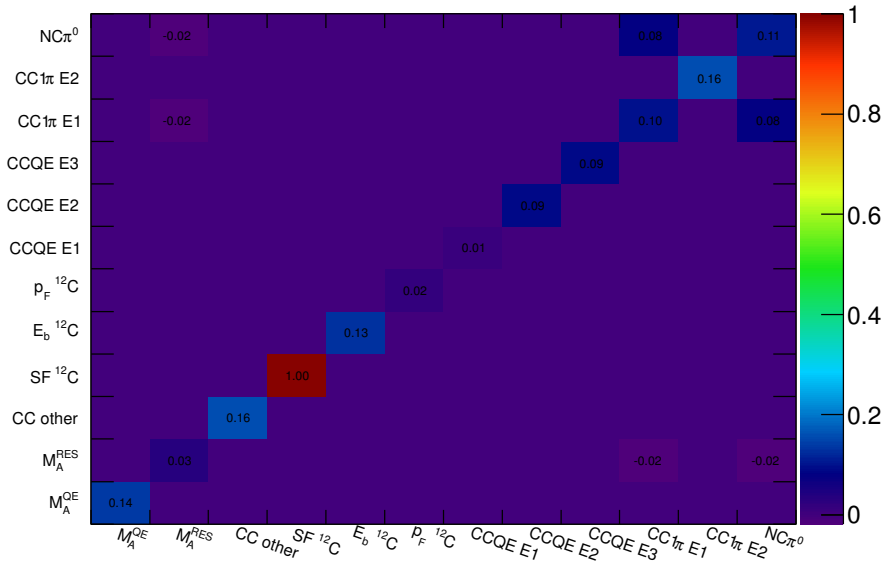
Table 6.15.: Official T2K NEUT cross-section parameters and errors, taken from [70]

ND280 data sets do not cover the full phase space of neutrino interactions and also do not include information on the kinematics of secondary tracks. Once ND280 data analyses are expanded, the reliance on external data will be reduced but not removed, as independent measurements with different systematics could still add value to model constraints. For a complete account of the procedure used to determine these errors, see [69] and [70], however a brief summary for each cross-section parameter is given below.

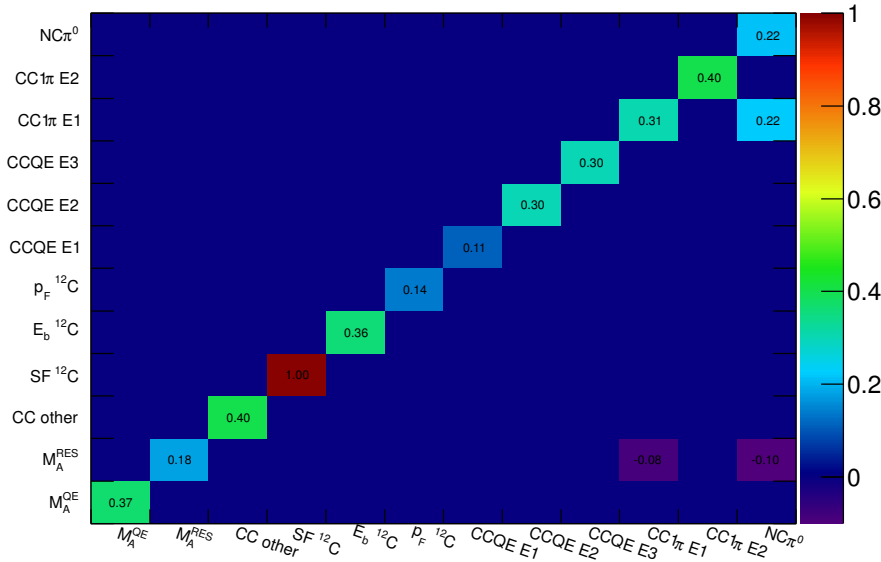
M_A^{QE} and low energy CCQE normalisation (CCQE E1)

An FSI-corrected sample of MiniBooNE CCQE data⁷ (presented as a double - differential cross-section, as a function of the angle between the incoming and outgoing leptons and the kinetic energy of the outgoing lepton) is fit to true CCQE interactions produced using NEUT MC using a χ^2 minimisation. The fit varies the values of M_A^{QE} , the axial mass in the axial vector form factor for CCQE interactions, and the low energy CCQE normalisation, which is included as the uncertainty on

⁷ This FSI-corrected sample of CCQE events was obtained by first using a sample of CCQE-like events i.e. events with a muon and no pions. These CCQE-like events are comprised of mostly CCQE interactions but there is a significant contribution from CC $1\pi^+$ and other modes that produce a pion that re-interacts in the nucleus and so is not seen exiting the nucleus. By using dedicated samples of these other modes, the contaminating components can be removed from the CCQE-like sample leaving a CCQE-corrected data set.



(a) Input covariance matrix of cross-section parameters



(b) Cholesky decomposed covariance matrix

Figure 6.19.: Input cross-section parameter covariance matrix and the Cholesky decomposition of that matrix.

the MiniBooNE flux is 10.7%. The fitted value of M_A^{QE} obtained is 1.64 ± 0.03 GeV whereas the low energy normalisation, CCQE E1, is found to be 0.88 ± 0.02 . The fitted value of M_A^{QE} is significantly larger than previously published results, which is thought to arise from a difference in the technique used to model low Q^2 (momentum transfer to the hadronic system) behaviour. Unfortunately, due to the absence of a covariance matrix supplied with the MiniBooNE data, the error on M_A^{QE} cannot be accurately reported. Thus, the difference between the fitted value of M_A^{QE} and the nominal (in NEUT this is 1.21 GeV) plus the fitted error is said to be the uncertainty (i.e. $1.64 - 1.21 + 0.03 \simeq 0.45$ GeV) for M_A^{QE} . For the CCQE E1 normalisation, the MiniBooNE flux error is used (11%) with the nominal value (1.0).

M_A^{RES} , low energy CC 1π normalisation (CC 1π E1) and NC $1\pi^0$

The parameter values and errors for M_A^{RES} , the axial mass for resonant interactions, the low energy CC 1π normalisation and the NC $1\pi^0$ normalisation are estimated using three different MiniBooNE data sets, with no FSI corrections: CC $1\pi^0$ [71], CC $1\pi^+$ [72] and NC $1\pi^0$ [73], as they are connected by common parameters in NEUT.

A simultaneous fit is performed using a χ^2 minimisation of nine parameters including: M_A^{RES} ; the “W shape” parameter, an empirical parameter that allows the spectrum of absolute momentum of π^0 from NC $1\pi^0$ interactions to be modified to improve agreement with data; “CC other”, a shape parameter that modifies a combination of CC cross-section channels (multi- π , DIS and resonant $\eta/K/\gamma$ production) as a function of neutrino energy and normalisation factors for NC coherent, NC $1\pi^0$, NC 1π and other neutral current interaction modes (“NC other”). Unfortunately the fit cannot constrain the normalisation parameters NC 1π , CC other and NC other as they contribute negligible amounts to the samples. Additionally, the NC coherent parameter cannot be constrained independently of the normalisation for NC $1\pi^0$ because there is no shape difference in the absolute π^0 momentum spectrum. Thus penalty terms are included in the χ^2 fit for these parameters. The procedure does not take into account correlations between data samples or the bin-by-bin correlations between data points in the CC $1\pi^+$ and NC $1\pi^0$ samples, as this information is not available. However, the full covariance matrix for the CC $1\pi^0$ sample is used, thereby enabling the use of a simple *ad hoc* scaling procedure to alter the size of the errors in order to reproduce the MiniBooNE flux-integrated cross-section errors.

The best fit value and error for M_A^{RES} , CC 1π E1 and NC $1\pi^0$ can be found in Table 6.15, whereas the covariance between these parameters is shown in Figure 6.19a. Whilst the value of W shape is not used in official T2K analyses at this time, for completeness, the best fit value obtained is 42.4 MeV compared to a nominal value of 87.7 MeV. This large discrepancy between fitted and nominal values of W shape is thought to reflect the need for a general model change.

Fermi gas parameters: p_F , E_b and SF

In the CCQE cross-section model in NEUT, the target nucleus is described using a relativistic Fermi gas model (FGM). The FGM characterises the nuclear potential using two nucleus-dependent parameters: p_F , the Fermi momentum and E_b , the nuclear binding energy, which are determined using electron scattering data [74].

Electron scattering data suggests that a more complicated model, called the spectral function (SF) [75], better describes the nuclear potential. The SF defines a probability distribution of nucleon momenta and energies required to remove a nucleon. The SF approach is more realistic than the Fermi gas model as the FGM assumes a uniform distribution of nucleons inside the Fermi sphere with constant binding energy. The systematic uncertainty for these parameters is the difference between observables simulated with both the Fermi gas and SF model and is either turned on (1) or off (0) in the reweighting software. As described later, the method used to determine the covariance matrices makes many throws. For the SF systematic, if the thrown value is positive, the value is set to 1, if it is negative the SF is turned off (0).

High energy normalisation parameters: CCQE E2, CCQE E3 and CC 1π E2

The high energy normalisations for CCQE E2 ($1.5 < E_\nu < 3.5$), CCQE E3 ($E_\nu > 3.5$) and CC 1π E2 ($E_\nu > 2.5$) are not constrained using MiniBooNE or ND280 data due to the small flux of neutrinos at these energies. The CCQE normalisations are assigned an uncertainty of 30% to try to account for the discrepancy seen between MiniBooNE data [76], collected with an average neutrino energy of ~ 0.8 GeV, and the data from the NOMAD experiment [77], which operates with a range of neutrino energies from 3 to 100 GeV. Comparison of the MiniBooNE CC $1\pi^+$ data set and the nominal NEUT MC at high neutrino energies (~ 2 GeV) gives a systematic uncertainty of 40% .

Shape uncertainty parameters: CC other

As mentioned previously, the CC other parameter is energy dependent and is defined

for a combination of charged current cross-section channels, namely multi- π , DIS and resonant $\eta/K/\gamma$ production. The total CC-inclusive cross-section results published by the MINOS collaboration [78] indicate that the uncertainty is of the order of 10% at 4 GeV. Using this as a reference, the error is defined as

$$\sigma_{\text{CC other}} = \frac{0.4}{E_\nu}, \quad (6.13)$$

where E_ν is the neutrino energy in GeV. As the interactions in question have an energy threshold of ~ 0.6 GeV, obtaining an infinite error is not a concern.

To build a covariance matrix describing the impact of the cross-section model parameter errors on the π^0 invariant mass distribution the following steps were taken. First the model parameter covariance matrix shown in Figure 6.19a was Cholesky decomposed (this is the equivalent of doing the square root of a matrix), as seen in Figure 6.19b. Then, 5000 throws of this matrix were made, where one throw constitutes the multiplication of the matrix by a vector of random Gaussian numbers, centred on zero with a width of one. The resultant vector from the multiplication contains the parameter error values that are given to T2KReWeight. In addition to these errors the events selected in Section 6.7 are given to the reweighting software. The result from the throws is 5000 π^0 invariant mass distributions, each produced with slight variations of the underlying cross-section parameters; an example of one throw compared to the nominal value can be seen in Figure 6.20. To construct a fractional covariance matrix, $v(i, j)$, to describe the correlations between π^0 invariant mass bins, the following equation is used

$$v(i, j) = \frac{1}{N_t} \sum_{N_t} \frac{\sum_{i,j} (x_i - n_i)(x_j - n_j)}{n_i n_j}, \quad (6.14)$$

where N_t is the number of throws, i (j) corresponds to the i th (j th) bin in the invariant mass distribution, n_i (n_j) is the number of entries in the i th (j th) bin in the nominal π^0 invariant mass and x_i (x_j) is the number of entries in the i th (j th) bin in the π^0 invariant mass for the throw in question. The resultant fractional covariance and correlation matrices for cluster position category one can be found in Figure 6.21, position categories two and three are in Figure B.1. For cluster position category one, the largest error, associated with the π^0 invariant mass peak, is $\sim 28\%$, whereas for categories two and

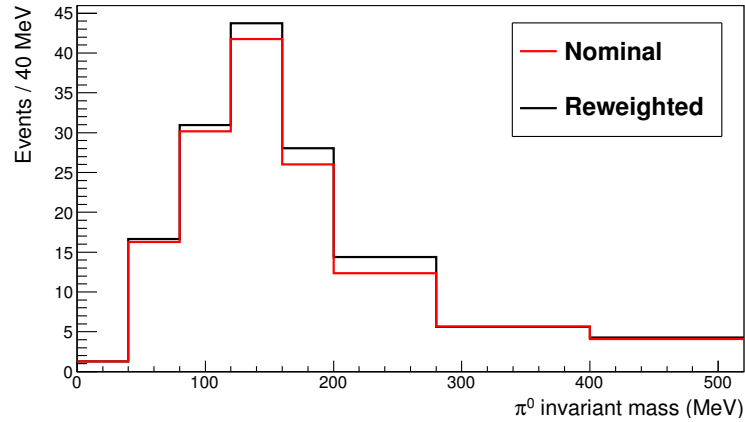
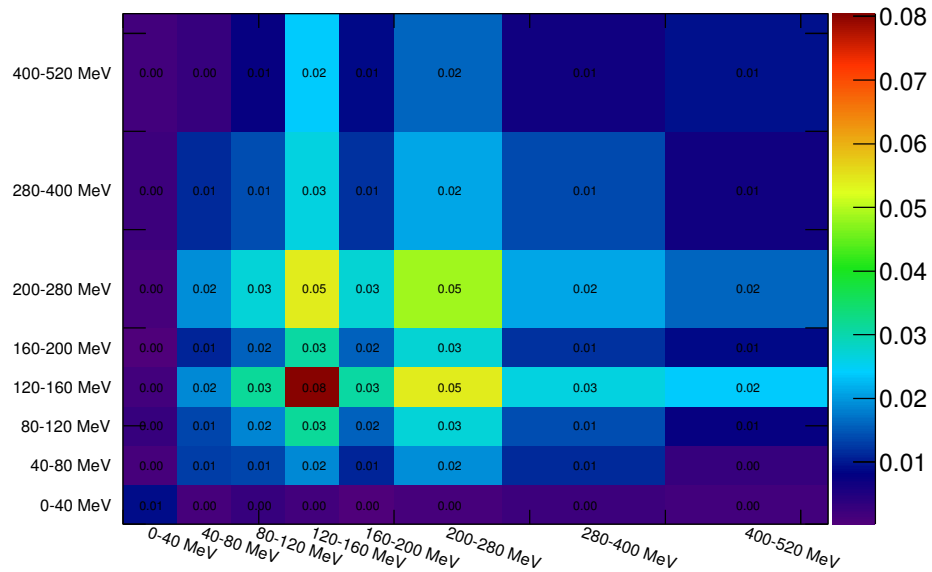
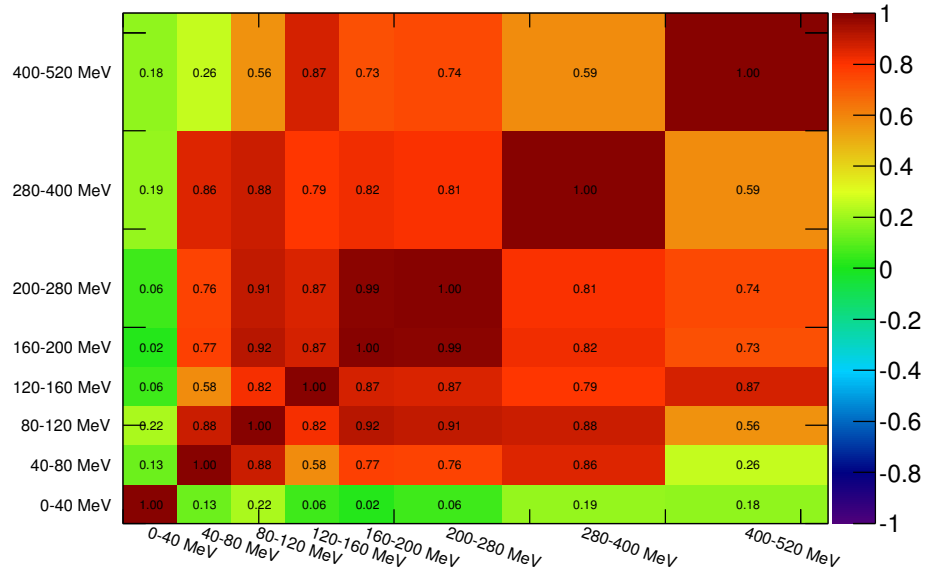


Figure 6.20.: π^0 invariant mass distribution for selected events (magnet and sand MC) in cluster position category one, with and without the thrown cross-section parameter errors applied.

three the largest errors occurring at the peak of the distribution are $\sim 17\%$ and $\sim 14\%$, respectively.



(a) Fractional covariance matrix for category one



(b) Correlation matrix for category one

Figure 6.21.: Fractional covariance and correlation matrices illustrating the impact of applying the cross-section parameter errors on the π^0 invariant mass distribution for cluster position category one.

6.8.2. Cross-section final state interaction systematic errors

The term final state interaction (FSI) refers to the re-interaction, via the strong force, of hadrons produced in neutrino-nucleon interactions as they exit the nucleus. NEUT uses a microscopic cascade model to simulate pion FSI; a description of this model and validation to external pion scattering data are detailed in [79]. Processes causing these re-interactions are categorised as: charge exchange, absorption, scattering and particle production [80]. For pions produced with momenta less than 500 MeV, which accounts for $\sim 70\%$ of those produced in the initial neutrino interaction at T2K, only absorption, charge exchange and scattering processes occur. Whereas, pions with momenta greater than 500 MeV have sufficient energy for particle production, in addition to absorption, charge exchange and scattering. Figure 6.22 shows the fate of a π^0 produced in a neutrino-induced interaction on ^{16}O as a function of true momentum. For further information regarding the implementation of these processes in NEUT see [79] and [81].

When a pion undergoes charge exchange it interacts with a nucleus to produce a pion that differs in charge by one unit (e.g. $\pi^\pm \rightarrow \pi^0$). It is also possible for a pion to undergo double charge exchange, i.e. $\pi^\pm \rightarrow \pi^\mp$, before exiting the nucleus. The defining feature of absorption is that the pion produced by the initial neutrino interaction is completely absorbed by the nucleus, resulting in no pions escaping the nucleus in the final state. The scattering of pions off the nucleus is only inelastic, as the NEUT FSI model does not include elastic scattering. Particle production occurs 30% of the time for the T2K flux and refers to events with two or more pions in the final state.

The method for producing event weights, to take into account the FSI errors, is similar to that previously outlined. Table 6.16 contains the “one sigma” errors that span the whole FSI parameter space for the following parameters: low energy quasi-elastic (QE) scattering (FSIQEL); high energy QE scattering (FSIQEH); pion production (high momentum pions) (FSIINEL); absorption (FSIABS); low energy single charge exchange (FSICXL) and high energy single charge exchange (FSICXH). Two separate studies, described in [81], were performed to obtain these values.

As there is a non-linear relationship between interactions in the microscopic cascade (e.g. multiple scattering followed by absorption), 13^3 sets of pion scattering MC were generated to consider all combinations of low energy parameters (FSIQEL, FSICXL and FSIABS). These parameters were varied between 0.4 and 1.6 in steps of 0.1. Points lying near the one sigma lines were chosen to ensure all extreme correlations are taken

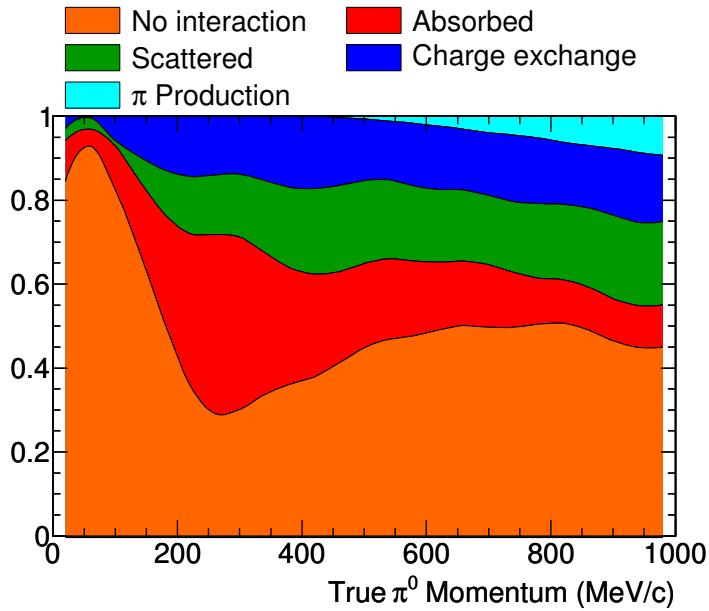


Figure 6.22.: The stacked probability as a function of true momentum for a given final fate π^0 produced in a neutrino-induced interaction on ^{16}O using the NEUT tuned FSI model. Figure taken from [79].

into account, for example the combined effect of increased scattering and absorption on the total absorption cross-section, or decreased absorption and increased scattering and charge exchange on the total charge exchange cross-section. Due to a lack of high energy data, a simpler method is implemented to extract the systematic uncertainties for each high energy interaction mechanism (FSIQEH, FSICXH and FSIINEL). The mean free path of the particle production and charge exchange mechanisms are simultaneously varied by $\pm 50\%$ while inversely varying the mean free path of QE scattering by 70% . The amount of variation of each parameter is also constrained by a data comparison.

The errors in each row of Table 6.16 are then given in turn to the reweighting engine, T2KReWeight, with each row forming a different throw. Then for each throw a π^0 invariant mass plot is made, as shown in Figures 6.23 and B.2. Using these 16 invariant mass plots, a fractional covariance matrix is constructed using Equation 6.14. The resultant covariance and correlation matrices for ECAL cluster position category one can be found in Figure 6.24. The covariance matrix shows that the maximum error is $\sim 48\%$, however this is not in the region of interest; the error around the peak is $\sim 14\%$. Similarly, the covariance and correlation matrix for categories two and three can be found in Figure B.3, for these categories the error around the peak is $\sim 17\%$.

Parameter set	Final state interaction parameter name					
	FSIQEL	FSIQEH	FSIINEL	FSIABS	FSICXL	FSICXH
Nominal	1.0	1.8	1.0	1.1	1	1.8
15	0.6	1.1	1.5	0.7	0.5	2.3
16	0.6	1.1	1.5	0.7	1.6	2.3
17	0.7	1.1	1.5	1.6	0.4	2.3
18	0.7	1.1	1.5	1.6	1.6	2.3
19	1.4	1.1	1.5	0.6	0.6	2.3
20	1.3	1.1	1.5	0.7	1.6	2.3
21	1.5	1.1	1.5	1.5	0.4	2.3
22	1.6	1.1	1.5	1.6	1.6	2.3
23	0.6	2.3	0.5	0.7	0.5	1.3
24	0.6	2.3	0.5	0.7	1.6	1.3
25	0.7	2.3	0.5	1.6	0.4	1.3
26	0.7	2.3	0.5	1.6	1.6	1.3
27	1.4	2.3	0.5	0.6	0.6	1.3
28	1.3	2.3	0.5	0.7	1.6	1.3
29	1.5	2.3	0.5	1.5	0.4	1.3
30	1.6	2.3	0.5	1.6	1.6	1.3

Table 6.16.: NEUT FSI parameters, representing a “one sigma” contour in the FSI parameter space, used in event reweighting. Official T2K values taken from [70].

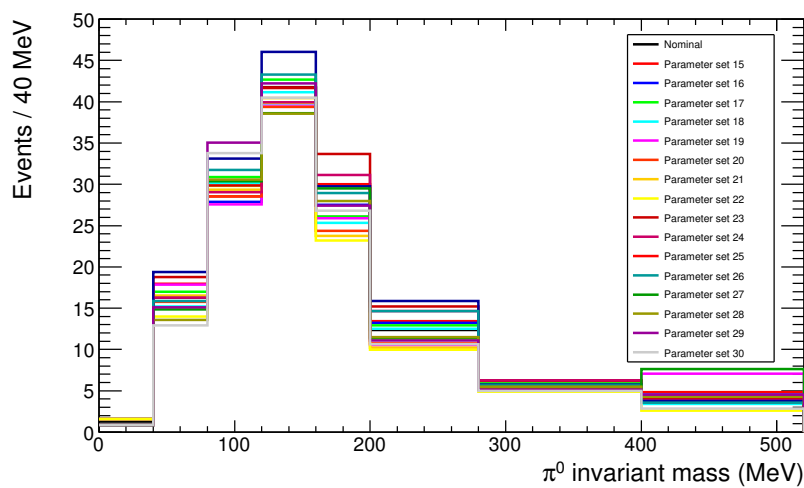
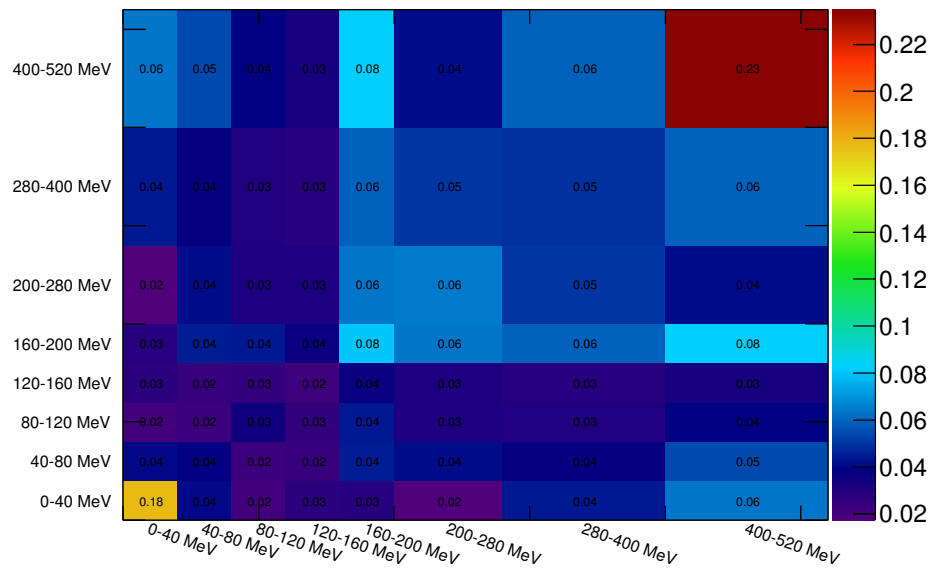
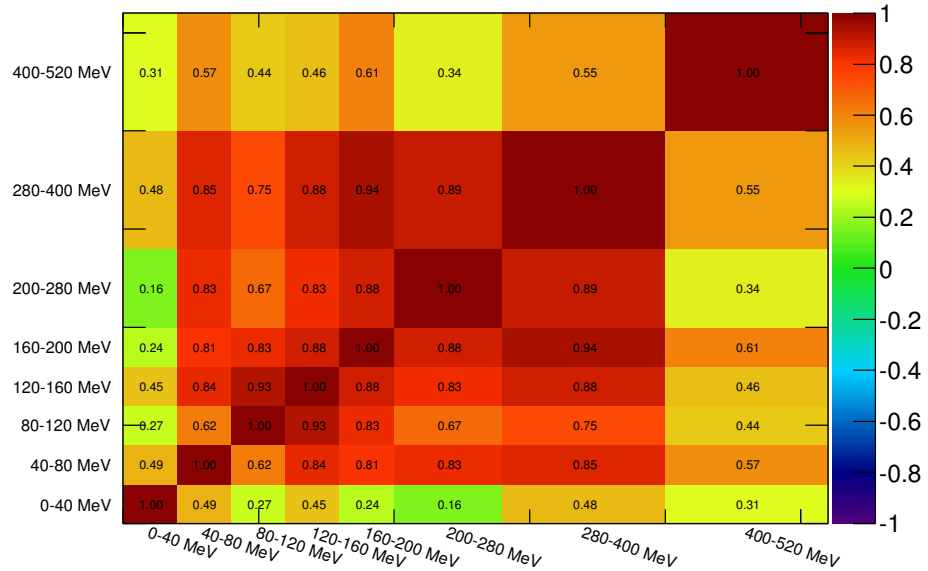


Figure 6.23.: The π^0 invariant mass, for ECAL cluster position category one, for all 16 throws of the FSI parameters and the nominal value.



(a) Fractional covariance matrix for category one



(b) Correlation matrix for category one

Figure 6.24.: Fractional covariance and correlation matrices illustrating the effect of the cross-section FSI parameters on the π^0 invariant mass distribution for cluster position category one.

6.8.3. Neutrino flux prediction systematic errors

To assess the impact of the neutrino flux systematics on the π^0 invariant mass distribution the same procedure is adopted as for the cross-section systematics. However, there is no need for the analyser to produce event weights for the selected sample, as the T2K beam group conveniently provide a covariance matrix⁸ as a function of neutrino species, true energy and detector (ND280 or Super-Kamiokande), as seen in Figure 6.26a. This covariance has 20 true neutrino energy bins for each detector/flavour (GeV): 0.0-0.1, 0.1-0.2, 0.2-0.3, 0.3-0.4, 0.4-0.5, 0.5-0.6, 0.6-0.7, 0.7-0.8, 0.8-1.0, 1.0-1.2, 1.2-1.5, 1.5-2.0, 2.0-2.5, 2.5-3.0, 3.0-3.5, 3.5-4.0, 4.0-5.0, 5.0-7.0, 7.0-10.0, >10.0 . The bin ordering is as follows,

- Bins 0 – 19: ν_μ ND280 bins,
- Bins 20 – 39: $\bar{\nu}_\mu$ ND280 bins,
- Bins 40 – 59: ν_e ND280 bins,
- Bins 60 – 79: $\bar{\nu}_e$ ND280 bins,
- Bins 80 – 99: ν_μ SK bins,
- Bins 100 – 119: $\bar{\nu}_\mu$ SK bins,
- Bins 120 – 139: ν_e SK bins,
- Bins 140 – 159: $\bar{\nu}_e$ SK bins.

The error sources considered when constructing the covariance matrix are: pion, kaon and secondary nucleon production; production cross-sections; off-axis angle and proton beam errors; horn and target alignment uncertainty; absolute horn current and the MC statistical uncertainty on the flux samples.

There are two approaches used to construct the covariance matrix. The first method is reweighting, which is used when an error source includes a number of correlated underlying parameters. This method is similar to those used to determine the effect of the cross-section systematic errors: throws (typically 500 or more) of the underlying flux parameters are made and the flux prediction is reweighted. The effect on the flux is then evaluated by constructing a covariance matrix from the throws. The uncertainties evaluated using this method are those of the hadron interaction and proton beam profile.

⁸ The flux covariance release used in this analysis is 11bv3.1.

The second method, used to evaluate uncertainties represented by variations in the flux as a result of changes to a single underlying parameter, is to re-simulate the flux for a $\pm 1\sigma$ variation in these parameters, which constitutes two throws. A covariance matrix is then constructed using these two throws. The combined uncertainty on the flux prediction is obtained through the addition of the covariances from each individual source of uncertainty, which are described below (for further information see [44]).

Hadron interaction uncertainties

The uncertainty in the modelling of the pion and kaon production multiplicity arises from a number of sources and is estimated using reweighting techniques. For both pions and kaons the sources are as follows: the uncertainty on the data used to reweight the pion/kaon multiplicity; the uncertainty on the incident particle momentum scaling used to apply the data to interactions with lower momentum incident nucleons and the uncertainty from the phase space that is not covered by the data. The pion [46] and kaon [82] data in question is predominantly that produced by the NA61/SHINE collaboration, but data from Eichten *et al.* [83] and Allaby *et al.* [84] are also used. There is an additional uncertainty for kaons arising from their production outside of the target.

Interactions of secondary protons and neutrons, i.e. those produced by the initial incident primary proton beam, in the target contribute approximately 16% and 5% to the neutrino flux, respectively. The high momentum protons are thought to be produced by QE scattering of the primary protons. Due to the lack of data in this high momentum region, a 100% error is assigned. Low momentum protons are thought to be produced alongside hadrons in the inelastic scatter of the primary protons; the uncertainty associated with this production is taken as the discrepancy between FLUKA predictions and the Eichten *et al.* and Allaby *et al.* data sets. It is found that only low momentum secondary neutrons make a significant contribution to the flux. Thus, assuming isospin invariance, the low momentum neutrons are assigned the same error as the low momentum protons.

A conservative systematic uncertainty, taken to be the magnitude of the QE correction that is applied to the total inelastic cross-section, is assigned to the production cross-section. This systematic uncertainty arises due an apparent discrepancy between cross-section measurements, thought to be a result of the difficulty in understanding whether experiments measure the inelastic or production cross-section.

In summary, the largest sources of uncertainty on the ν_μ neutrino flux at low energy are from secondary nucleon production and production cross-sections. At high energies, the uncertainty is dominated by the experimental errors on kaon production. New measurements from NA61/SHINE are expected to reduce the overall uncertainty on the neutrino flux prediction.

Proton beam and off-axis angle uncertainties

Sources of uncertainty on the proton beam average position and angle are: the alignment uncertainty of the beam monitoring devices; the alignment uncertainty between the primary beamline and the target station (secondary beamline) and the uncertainty in the position measurements made by the beam monitors. These uncertainties are estimated using reweighting techniques. Studies found that the only systematic errors to have a significant effect on the neutrino flux prediction are those for the vertical position and angle of the beam centre, as these parameters change the off-axis angle at the far detector. A 2% absolute flux uncertainty arises from errors on the proton beam intensity, measured by the proton beam monitor CT5.

Target and horn alignment uncertainties

To study the effect of the target alignment, the target was rotated in JNUBEAM by 1.3 (0.1) mrad in the horizontal (vertical) plane. The result of this simulation was a change in the predicted neutrino flux of a few percent. For the horn position alignment, only a shift in position along the y -axis resulted in a significant change (a few percent) in the predicted flux. Rotations of 0.2 mrad in both the horizontal and vertical plane were made to the horns, however only rotations of the first horn showed any sizeable effect on the predicted neutrino flux. In summary, the uncertainty due to the target and horn alignment are estimated to be <3% for neutrinos with energies below 7 GeV.

Horn current and magnetic field uncertainties

The total uncertainty of the measured horn current is 1.3% and the measured magnetic field strength is consistent with the predicted value to within 2%, this results in an overall uncertainty on the neutrino flux of 2%.

In summary, the total flux uncertainty on muon neutrinos at ND280, found in Figure 6.25, is dominated by hadron interaction uncertainties. However, there is a significant contribution from the proton beam, alignment and off-axis angle at the flux peak.

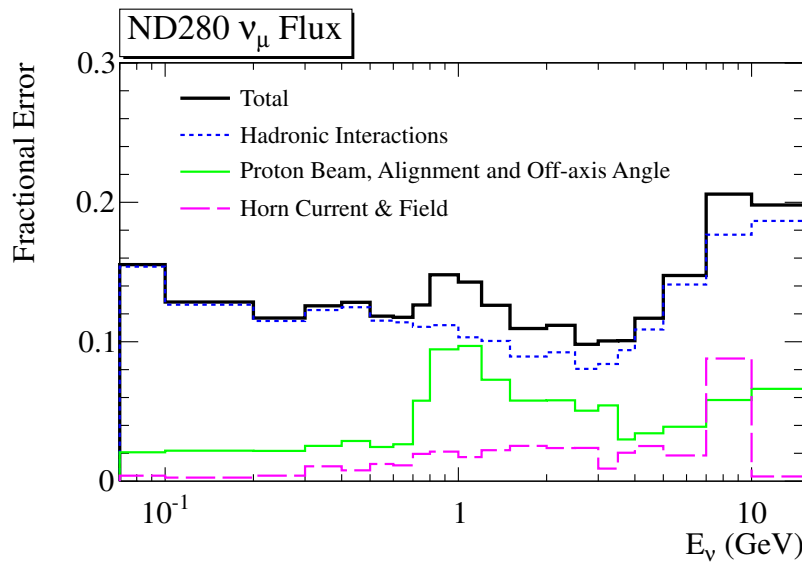
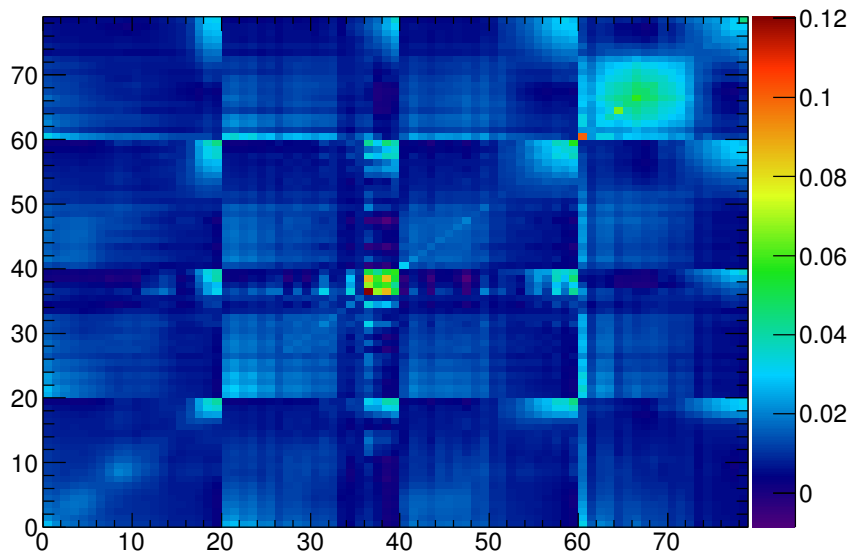
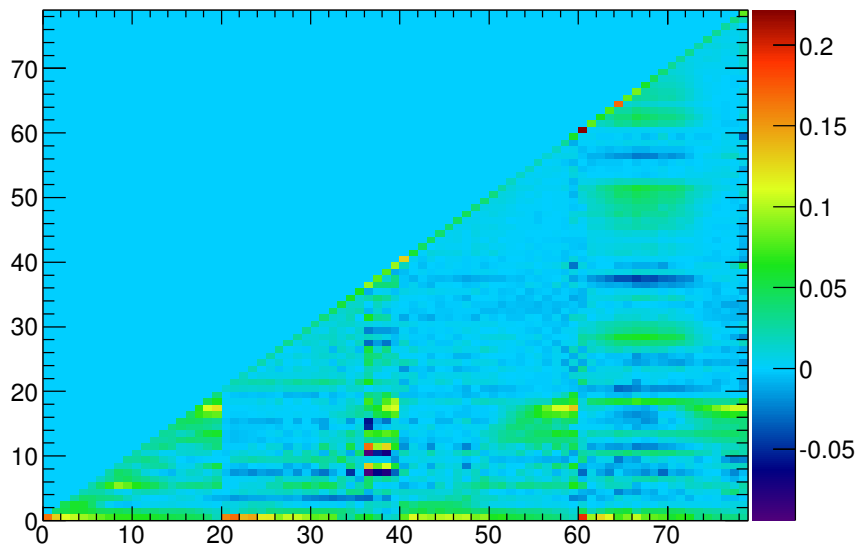


Figure 6.25.: Fractional flux error, including all sources of uncertainty, for ν_μ at ND280 [44].

To obtain a covariance matrix illustrating the effect of the flux systematics on the π^0 invariant mass distribution, first the flux covariance matrix (Figure 6.26a) is Cholesky decomposed (Figure 6.26b). This decomposed matrix is then multiplied by a vector of random Gaussian numbers (with a mean of zero and a width of one), constituting one throw of the matrix. For each selected event, using the true neutrino energy and species inducing the interaction, the relevant entry is selected from the throw. The event weight is obtained by adding the thrown parameter value to the nominal value (1). For each throw the π^0 invariant mass distribution is plotted, then after 5000 throws the π^0 invariant mass covariance matrix is calculated using Equation 6.14. The covariance and correlation matrix for ECAL cluster position category one, found in Figure 6.27, show that the error around the invariant mass peak is $\sim 10\%$. Similarly, the error at the peak for categories two and three (see Figure B.4) is $\sim 10\%$, as expected.

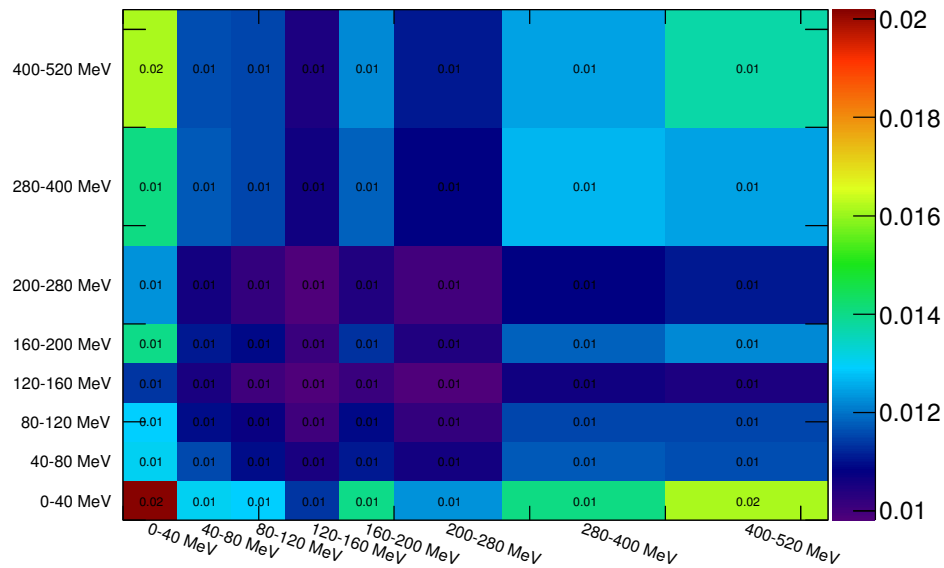


(a) Input flux covariance matrix

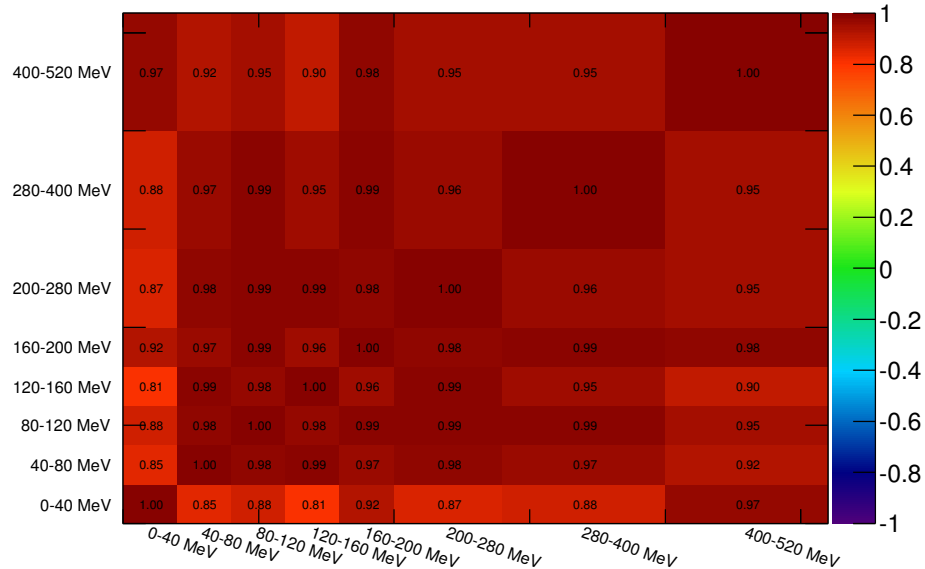


(b) Cholesky decomposition of the flux covariance matrix

Figure 6.26.: Input flux covariance matrix and the Cholesky decomposition of that covariance matrix.



(a) Fractional covariance matrix for category one



(b) Correlation matrix for category one

Figure 6.27.: Fractional covariance and correlation matrices illustrating the effect of the neutrino flux uncertainty on the π^0 invariant mass distribution for cluster position category one.

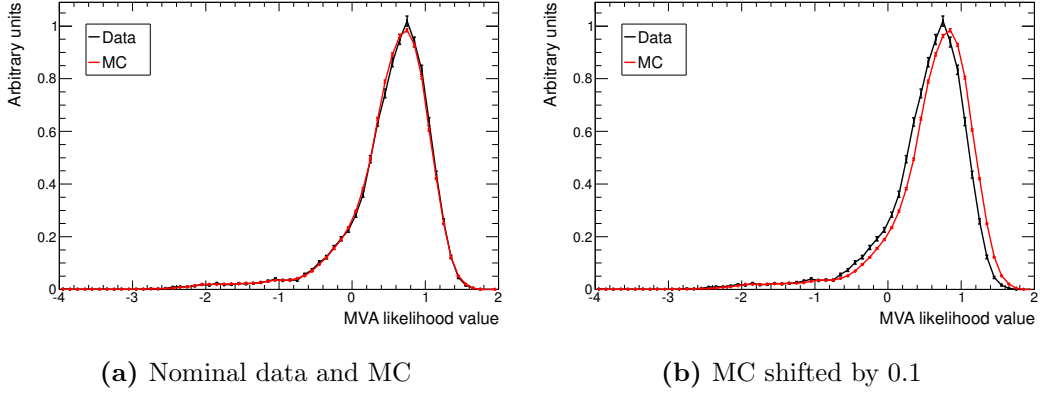


Figure 6.28.: An example of the histograms used to compare nominal and shifted MC to data for the transformed likelihood response for all categories combined. This figure is for illustration purposes, the actual error analysis uses the cluster position categories defined in Section 6.5.

6.8.4. Multi-variate analysis systematic errors

As seen in Figures 6.13, A.6 and A.7 there is a small shape discrepancy between data and MC. As the multi-variate analysis, used to select π^0 decay photons from NC $1\pi^0$ interactions, relies on shape differences between input variables to discriminate between signal and background interactions it is important to quantify the effect. The transformed likelihood response from TMVA is plotted for both data and MC, with the MC shifted between -0.5 and 0.5 in increments of 0.1 (0.01 around the minimum), as shown in Figure 6.28. The χ^2 value is then computed for each shift, as shown in Figure 6.29, and the distribution is fitted with a second order polynomial about the minimum. The error is then said to be the difference between the zero shift MC point and the minimum of the polynomial, displayed in Table 6.17. To see the effect of this error, the selection is repeated with the error added to the transformed likelihood response from TMVA for each event. The effect on the π^0 invariant mass distribution for ECAL cluster category two can be seen in Figure 6.30, for categories one and three see Figure B.5. Then, using Equation 6.14 the fractional covariance matrix is calculated, however the number of throws in this case is one. The resultant matrix and correlation matrix for cluster category two can be found in Figure 6.31; it shows that, around the invariant mass peak, the uncertainty is less than 14%. ECAL cluster categories one and three (Figure B.6) have several entries with zero error, this is due to the fact that many bins have the same number of entries with and without the multi-variate analysis errors applied.

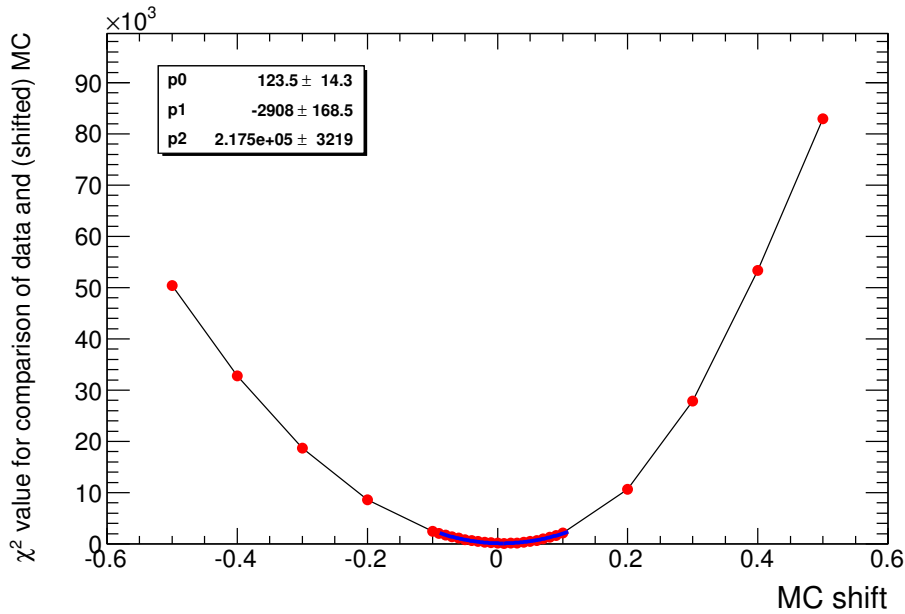


Figure 6.29.: χ^2 value for each shift of the MC transformed likelihood response in comparison to data for ECAL cluster position category two.

Category	Error
one	0.004
two	0.007
three	0.002

Table 6.17.: Systematic errors to account for the effect of the shape discrepancy between data and MC on the TMVA.

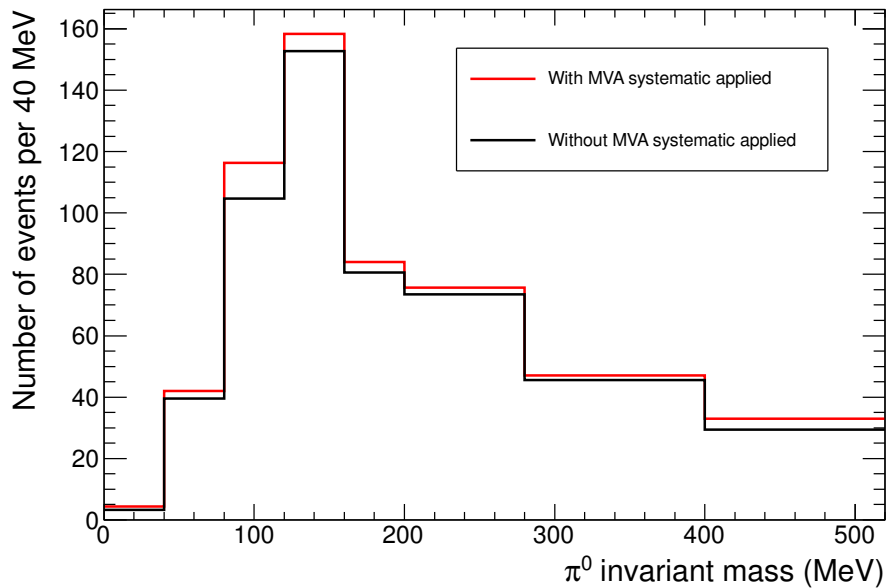
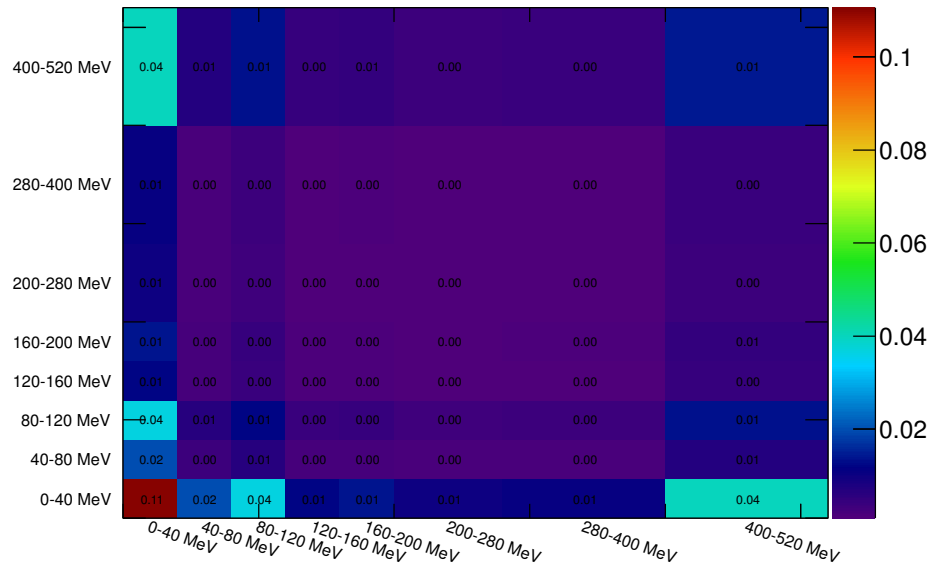


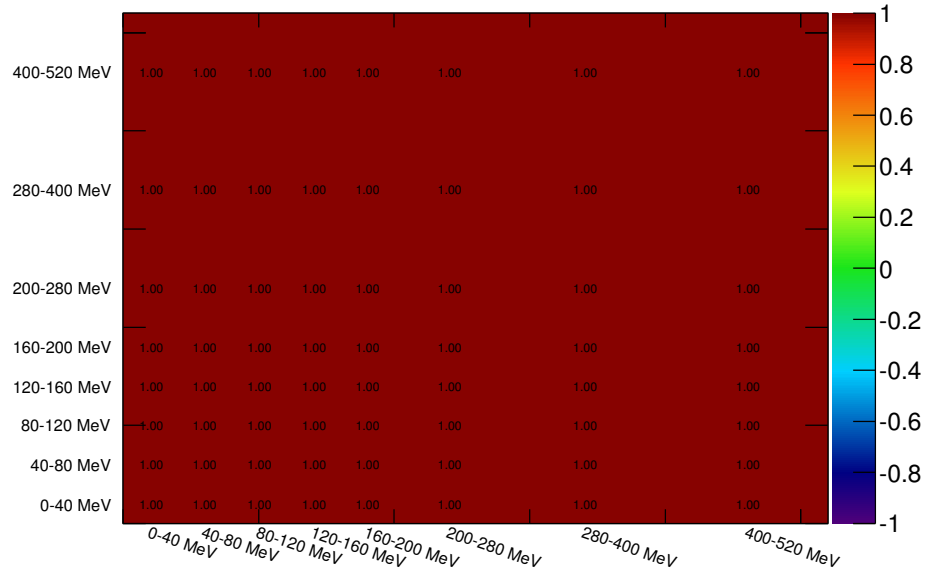
Figure 6.30.: π^0 invariant mass, for selected magnet and sand MC interactions, with and without the TMVA shape systematic applied for ECAL cluster category two.

6.8.5. Combined systematic error

This section presents the total combined error on the π^0 invariant mass distribution taking into account cross-section model parameter and FSI systematic uncertainties; neutrino flux prediction errors and the systematic error arising from a shape discrepancy in data and MC between ECAL variables used in TMVA. As seen in Figure 6.32, the total error around the peak of the invariant mass distributions for ECAL cluster position categories one, two and three is $\sim 35\%$, $\sim 26\%$ and $\sim 22\%$, respectively, with the largest contribution to the total error coming from cross-section systematics.

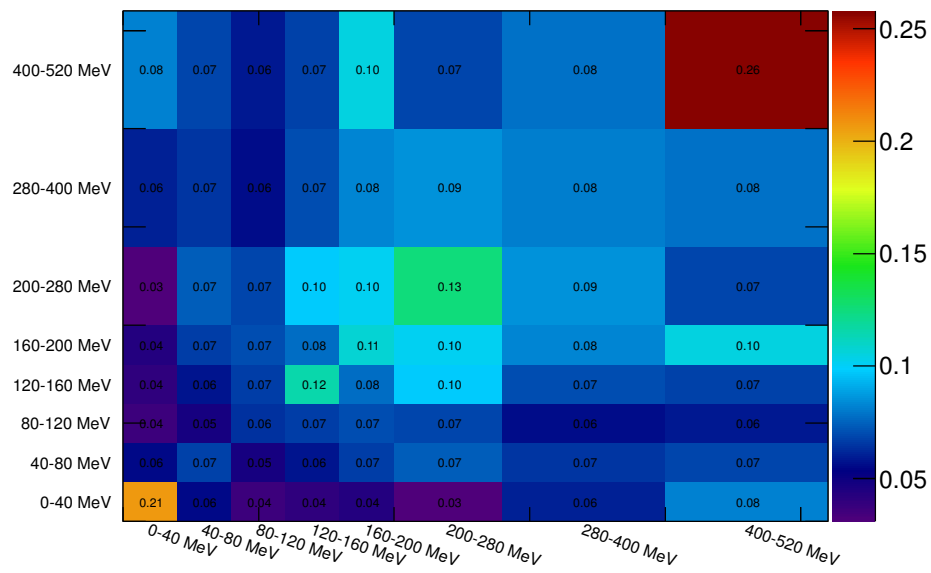


(a) Fractional covariance matrix for category two



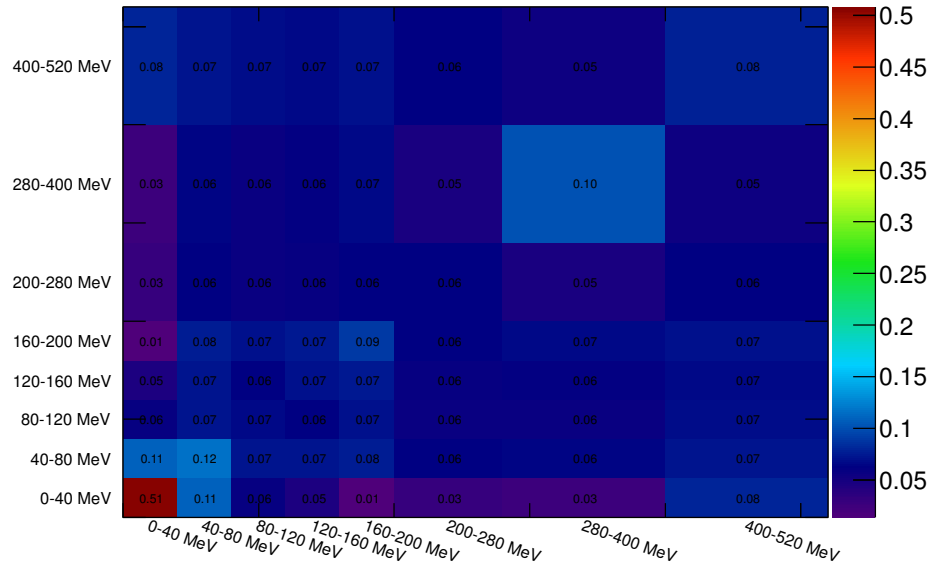
(b) Correlation matrix for category two

Figure 6.31.: Fractional covariance and correlation matrices illustrating the effect of the discrepancy between data and MC on the multi-variate analysis on the final π^0 invariant mass distribution for cluster position category two.



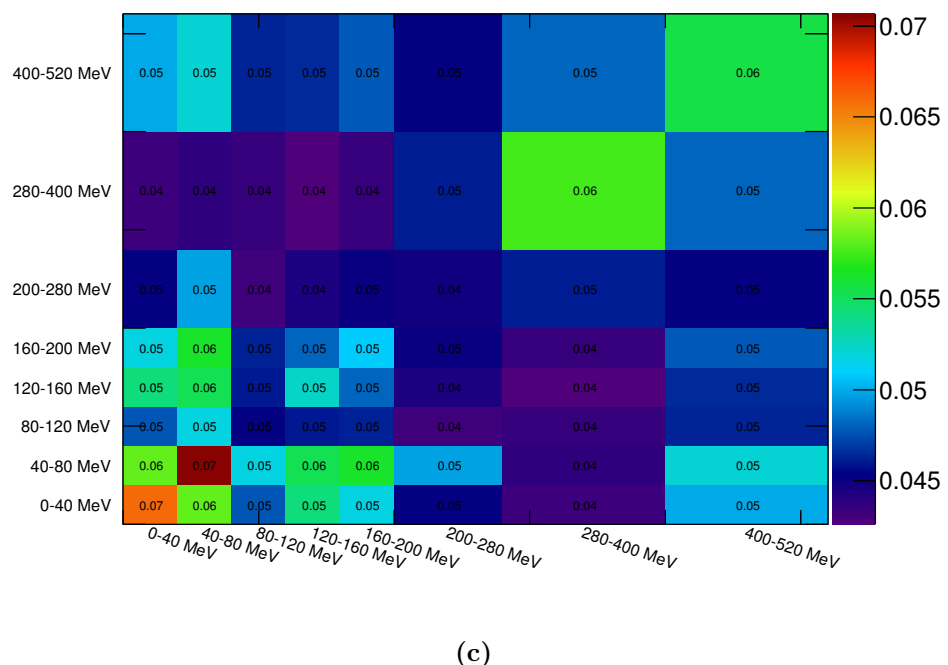
(a)

Figure 6.32.: Fractional covariance matrix illustrating the effect of all systematic errors on the final π^0 invariant mass distribution for ECAL cluster position category one.



(b)

Figure 6.32.: Fractional covariance matrix illustrating the effect of all systematic errors on the final π^0 invariant mass distribution for ECAL cluster position category two.



(c)

Figure 6.32.: Fractional covariance matrix illustrating the effect of all systematic errors on the final π^0 invariant mass distribution for ECAL cluster position category three.

6.8.6. Discussion of detector systematics

A quantitative assessment of ECAL and tracker detector systematics and a reweighting technique to assess the impact of these systematics on a selection are still in development. A qualitative discussion of the main systematics relevant to this analysis is presented below.

ECAL hit charge

Clustering and three dimensional hit reconstruction in the ECAL relies predominantly on the charge and position information of hits. As calibrated hits are only considered for reconstruction if their charge is greater than 3.5 photon equivalent units (p.e. units), variations in the charge of a hit prior to reconstruction is thought to have the biggest impact on both the number of reconstructed ECAL clusters (as a minimum of 4 hits are required to form a cluster) and on the number of hits in a cluster.

The effect of the detector charge response on the number of selected events can be estimated by smearing the calibrated charge of each ECAL hit. This smearing can be achieved by adding the value obtained by making a random throw from a Gaussian distribution, with a mean of zero and a width equal to the charge resolution of the ECAL (obtained by studying the variation of the most probable value for the charge of a single hit created by a MIP as a function of time), to the charge of the calibrated hit.

ECAL MPPC response

The Monte Carlo simulation of the MPPC response to photons can differ by up to 10% from data taken using LEDs to illuminate a WLS fibre at a fixed distance from an MPPC. A correction to ensure the MC response better matches that seen in data does not feature in the MC production used in this analysis, but will be present in future productions, thus a systematic uncertainty can be estimated by comparing the number of selected events with and without this MPPC response correction.

Noise in the ECAL

A comparison of cosmic MC and data can be used to estimate the systematic uncertainty arising as a result of the difference between the number of noise hits simulated in MC and present in data. By comparing the number of true noise hits simulated in cosmic MC to the estimated number of noise hits in cosmic muon data (found by subtracting the number of hits in three dimensional clusters from the

total number of hits in the ECAL in an event) a MC correction can be made. The effect of this MC correction on a selection can then be quantified.

ECAL component dimensions

The ECAL modules are simulated in the MC based on the design specification used during their construction. Thus, uncertainties on the thickness of the TiO_2 coating on the scintillator bars ($0.25 \text{ mm} \pm 0.13 \text{ mm}$); the volume of the scintillator bars ($40 \text{ mm} \pm 0.4 \text{ mm} \times 10 \text{ mm} \pm 0.4 \text{ mm} \times \text{length of bar} \pm 0.1 \text{ mm}$) and the volume of lead sheets ($\text{length} \pm 3 \text{ mm} \times \text{width} \pm 3 \text{ mm} \times \text{thickness} \pm 0.1 \text{ mm}$) could change the amount of active/dead material in the ECAL. The uncertainty of other materials used in the ECAL construction are thought to have a negligible effect on a selection as they constitute less than 1% of the total detector mass.

Tracker – ECAL matching efficiency

The method to obtain a systematic uncertainty for the matching efficiency (including an ECAL reconstruction efficiency) between the tracker and the ECAL is currently being developed. A high purity control sample is selected in data and MC (using new ECAL particle identification variables based on low-level quantities combined with a likelihood-based method, detailed in [85]) and the systematic uncertainty is said to be a combination of the difference in efficiency for data and MC and the statistical error on the data control sample.

Particle identification

A comparison of the dE/dx value for data and MC control samples should be used to assign a systematic uncertainty for the TPC and FGD PID. As the ECAL PID variable that distinguishes between tracks and showers (see Section 4.5.4) will not be used in future MC productions and, additionally, plays a small part in the analysis presented in this thesis (due to the small number of tracks that traverse from an FGD into an ECAL without entering a TPC) no study will be undertaken to assign a systematic uncertainty to this variable.

6.9. Summary

Neglecting the photon reconstruction efficiency in the ECAL, the efficiency and purity for selecting NC $1\pi^0$ interactions occurring the FGD1 and FGD2 with both photons converting in the ECAL is 22% and 16%, respectively. For ECAL cluster position categories one (both photons convert in the DsECAL), two (both photons convert in the BrECAL) and three (one photon converts in the DsECAL, the other in the BrECAL) the efficiency (purity) is 33% (43%), 12% (9%) and 29% (16%), respectively. The main backgrounds are from neutrino-induced charged current and neutral current interactions occurring in the ECAL. Interactions with at least one photon converting in the downstream ECAL have the highest efficiency and purity; this is expected as there are fewer backgrounds in the DsECAL, as it is not enclosed within the SMRD, like the BrECAL. Also, the variables output from the ECAL reconstruction were developed and optimised using the DsECAL.

The systematic uncertainties arising from cross-section parameters and final state interactions, the neutrino flux prediction and the shape discrepancy between data and MC are evaluated. Neglecting correlations between invariant mass bins in the total covariance matrix, the predicted total number of events for each ECAL position category are:

- Category one: 7.1 ± 2.3 (syst) ± 0.5 (stat),
- Category two: 31.6 ± 8.9 (syst) ± 1.2 (stat),
- Category three: 38.1 ± 8.7 (syst) ± 1.3 (stat).

The selected number of events in data for categories one, two and three is 5, 22 and 31, respectively, which agrees with the MC prediction within errors.

Chapter 7.

Conclusions

The T2K experiment is a long baseline neutrino oscillation experiment; the most intense accelerator muon neutrino beam ever built is produced at the J-PARC facility in Tokai, located on the east coast of Japan, and directed (2.5° off-axis) toward the Super-Kamiokande water Cherenkov detector, located 295 km away in the mountains of western Japan. The main physics goals of the T2K experiment are the discovery of the oscillation $\nu_\mu \rightarrow \nu_e$. By exploring this ν_e appearance channel T2K were the first experiment to report an indication of non-zero θ_{13} , the reactor/accelerator mixing angle, in June 2011. Additionally, T2K will achieve precision measurements of oscillation parameters in ν_μ disappearance achieving sensitivities of $\delta(\Delta m_{23}^2) = 10^{-4}$ and $\delta(\sin^2 2\theta_{23}) = 0.01$.

For the current T2K ν_e appearance analysis, 23% of the background at Super-Kamiokande is from neutral current interactions that produce one π^0 in the final state (NC $1\pi^0$). The π^0 subsequently decays to two photons and if there is a small opening angle between these two decay photons, or if one photon is not reconstructed, the NC $1\pi^0$ interaction can mimic a ν_e interaction at Super-Kamiokande, as the Cherenkov ring produced by a photon is similar to that produced by an electron. Thus it is important to study these backgrounds thoroughly to reduce systematic uncertainties.

The large neutrino flux at the T2K off-axis near detector ND280 enables NC $1\pi^0$ interactions to be studied. The analysis presented in this thesis selects neutrino-induced NC $1\pi^0$ interactions in FGD1 and FGD2 where both π^0 decay photons convert in the barrel and downstream ECAL. This topology is chosen as it accounts for 32% of NC $1\pi^0$ interactions in FGD1 and 52% of those occurring in FGD2.

After making selection cuts to veto neutrino-induced interactions occurring upstream of FGD1, the FGD and TPC pulls and the charge per unit length of an ECAL track

are used to require all reconstructed particle tracks are proton-like, thus ensuring the interaction is neutral current. Next, the selection is split into three categories based on the photon conversion location within the ECAL (barrel or downstream). After some pruning cuts to remove backgrounds, a likelihood estimator from the TMVA package in ROOT is used to select photons from NC $1\pi^0$ interactions in the ECAL. Finally, a requirement is made that the interaction vertex is reconstructed in either FGD1 or FGD2.

Overall, neglecting reconstruction efficiency, an efficiency of 22% and purity of 16%, for selecting neutrino-induced NC $1\pi^0$ interactions occurring the FGD1 and FGD2 where both photons convert in the ECAL, is obtained. The main backgrounds are from neutrino-induced charged current and neutral current interactions in the ECAL. For ECAL cluster position categories one (both photons convert in the DsECAL), two (both photons convert in the BrECAL) and three (one photon converts in the DsECAL, the other in the BrECAL) the efficiency (purity) is 33% (43%), 12% (9%) and 29% (16%), respectively. Interactions with at least one photon converting in the downstream ECAL have the highest efficiency and purity; this is expected as there are fewer backgrounds in the DsECAL, as it is not enclosed within the SMRD, like the BrECAL. Also, the variables output from the ECAL reconstruction algorithms were developed and optimised using the DsECAL.

The study presented in this thesis was conducted using ND280 Run 2 data totalling 7.832×10^{19} POT (protons on target) after data quality cuts (approximately 1% of the design number of POT). Based on Monte Carlo (MC) predictions a total of 77 events are expected to be selected. When the study was performed on data a total of 58 events were selected.

The systematic uncertainties arising from cross-section parameters and final state interactions, the neutrino flux prediction and the shape discrepancy between data and MC are evaluated. Neglecting correlations between invariant mass bins in the total covariance matrix, the predicted total number of events for each ECAL position category are:

- Category one: 7.1 ± 2.3 (syst) ± 0.5 (stat),
- Category two: 31.6 ± 8.9 (syst) ± 1.2 (stat),
- Category three: 38.1 ± 8.7 (syst) ± 1.3 (stat).

The selected number of events in data for categories one, two and three is 5, 22 and 31, respectively. Thus, data and MC agree within errors.

At the time of writing, the fit performed to ND280 data to constrain T2K flux and cross-section model parameters is done using only a sample of charged current inclusive interactions. By including the number of NC $1\pi^0$ interactions at ND280 into this fit it will be possible to reduce the systematic error assigned to the NC $1\pi^0$ cross-section in the T2K ν_e appearance analysis, which is currently 43%. Furthermore, this study of NC $1\pi^0$ interactions will eventually lead to an absolute or ratio cross-section measurement made at ND280, which will lead to improvements in neutrino interaction model predictions.

In addition to the selection of NC $1\pi^0$ interactions, the calibration of the time offsets for the barrel and downstream ECAL is also presented in this thesis. Good time calibration is essential for effective clustering, the rejection of noise hits and particle direction determination. Algorithms were developed to calculate TFB and RMM offsets, the application of which reduce the timing resolution from 9 ns to approximately 2.5 ns, for high charge hits.

Bibliography

- [1] B. Pontecorvo *J. Exptl. Theoret. Phys.*, vol. 33, p. 549, 1957.
- [2] Y. Fukuda *et al.*, “Evidence for oscillation of atmospheric neutrinos,” *Phys. Rev. Lett.*, vol. 81, pp. 1562–1567, 1998.
- [3] R. Davis, D. S. Harmer, and K. C. Hoffman, “Search for neutrinos from the sun,” *Phys. Rev. Lett.*, vol. 20, no. 21, pp. 1205–1209, 1968.
- [4] Q. R. Ahmad *et al.*, “Direct evidence for neutrino flavor transformation from neutral-current interactions in the Sudbury Neutrino Observatory,” *Phys. Rev. Lett.*, vol. 89, p. 011301, 2002.
- [5] B. T. Cleveland *et al.*, “Measurement of the solar electron neutrino flux with the Homestake chlorine detector,” *Astrophys. J.*, vol. 496, pp. 505–526, 1998.
- [6] W. Hampel *et al.*, “GALLEX solar neutrino observations: Results for GALLEX IV,” *Phys. Lett.*, vol. B447, pp. 127–133, 1999.
- [7] J. Abdurashitov *et al.*, “Measurement of the solar neutrino capture rate by SAGE and implications for neutrino oscillations in vacuum,” *Phys. Rev. Lett.*, vol. 83, pp. 4686–4689, 1999.
- [8] K. S. Hirata *et al.*, “Search for day-night and semiannual variations in the solar neutrino flux observed in the kamiokande-ii detector,” *Phys. Rev. Lett.*, vol. 66, pp. 9–12, 1991.
- [9] S. Fukuda *et al.*, “Constraints on neutrino oscillations using 1258 days of Super-Kamiokande solar neutrino data,” *Phys. Rev. Lett.*, vol. 86, pp. 5656–5660, 2001.
- [10] L. Wolfenstein, “Neutrino oscillations in matter,” *Phys. Rev. D*, vol. 17, pp. 2369–2374, 1978.
- [11] K. Eguchi *et al.*, “First results from KamLAND: Evidence for reactor anti-neutrino

disappearance,” *Phys. Rev. Lett.*, vol. 90, p. 021802, 2003.

[12] T. Araki *et al.*, “Measurement of neutrino oscillation with KamLAND: Evidence of spectral distortion,” *Phys. Rev. Lett.*, vol. 94, p. 081801, 2005.

[13] M. Apollonio *et al.*, “Search for neutrino oscillations on a long base-line at the CHOOZ nuclear power station,” *Eur. Phys. J.*, vol. C27, pp. 331–374, 2003.

[14] K. Abe *et al.*, “Indication of Electron Neutrino Appearance from an Accelerator-produced Off-axis Muon Neutrino Beam,” *Phys. Rev. Lett.*, vol. 107, p. 041801, 2011.

[15] F. An *et al.*, “Observation of electron-antineutrino disappearance at Daya Bay,” *Phys. Rev. Lett.*, vol. 108, p. 171803, 2012.

[16] J. Ahn *et al.*, “Observation of Reactor Electron Antineutrino Disappearance in the RENO Experiment,” *Phys. Rev. Lett.*, vol. 108, p. 191802, 2012.

[17] G. Fogli, E. Lisi, A. Marrone, A. Palazzo, and A. Rotunno, “Evidence of $\theta_{13} > 0$ from global neutrino data analysis,” *Phys. Rev.*, vol. D84, p. 053007, 2011.

[18] P. Adamson *et al.*, “Improved search for muon-neutrino to electron-neutrino oscillations in MINOS,” *Phys. Rev. Lett.*, vol. 107, p. 181802, 2011.

[19] Y. Abe *et al.*, “Indication for the disappearance of reactor electron antineutrinos in the Double Chooz experiment,” *Phys. Rev. Lett.*, vol. 108, p. 131801, 2012.

[20] J. Beringer *et al.*, “Review of Particle Physics (RPP),” *Phys. Rev.*, vol. D86, p. 010001, 2012. Section 13 (Neutrino Mass, Mixing, and Oscillations).

[21] H. Murayama, “Oscillation Parameter Plots, PDG Web Update,” <http://hitoshi.berkeley.edu/neutrino/>, 2011.

[22] Official plots provided by the T2K collaboration.

[23] J. Hartnell and the SNO+ Collaboration, “Neutrinoless Double Beta Decay with SNO+,” *Journal of Physics Conference Series*, vol. 375, no. 4, p. 042015, 2012.

[24] A. S. Barabash *et al.*, “SuperNEMO double beta decay experiment,” *Journal of Physics Conference Series*, 2011.

[25] Sarazin, X., “Review of double beta experiments,” *Manuscript for Accreditation to Supervise Research (Univ. Paris-Sud 11)*, 2012.

- [26] A. Osipowicz *et al.*, “KATRIN: A Next generation tritium beta decay experiment with sub-eV sensitivity for the electron neutrino mass. Letter of intent,” *arXiv:hep-ex/0109033*, 2001.
- [27] H. Minakata and H. Nunokawa, “Inverted hierarchy of neutrino masses disfavored by supernova 1987A,” *Phys. Lett.*, vol. B504, pp. 301–308, 2001.
- [28] D. Ayres *et al.*, “NO ν A: Proposal to build a 30 kiloton off-axis detector to study $\nu_\mu \rightarrow \nu_e$ oscillations in the NuMI beamline,” 2004.
- [29] S. F. King, “Neutrino mass,” *Contemporary Physics*, vol. 48, pp. 195–211, 2007.
- [30] C. Athanassopoulos *et al.*, “Evidence for $\bar{\nu}_\mu \rightarrow \bar{\nu}_e$ oscillations from the LSND experiment at LAMPF,” *Phys. Rev. Lett.*, vol. 77, pp. 3082–3085, 1996.
- [31] A. A. Aguilar-Arevalo *et al.*, “The MiniBooNE Detector,” *Nucl. Instrum. Meth.*, vol. A599, pp. 28–46, 2009.
- [32] A. A. Aguilar-Arevalo *et al.*, “Event Excess in the MiniBooNE Search for $\bar{\nu}_\mu \rightarrow \bar{\nu}_e$ Oscillations,” *Phys. Rev. Lett.*, vol. 105, p. 181801, 2010.
- [33] A. A. Aguilar-Arevalo *et al.*, “Unexplained Excess of Electron-Like Events From a 1-GeV Neutrino Beam,” *Phys. Rev. Lett.*, vol. 102, p. 101802, 2009.
- [34] K. Mahn *et al.*, “Dual baseline search for muon neutrino disappearance at $0.5 \text{ eV}^2 < \Delta m^2 < 40 \text{ eV}^2$,” *Phys. Rev.*, vol. D85, p. 032007, 2012.
- [35] Zeller, G. P., “Low-energy neutrino cross-sections: Comparison of various Monte Carlo predictions to experimental data,” *arXiv:hep-ex/0312061*, 2003.
- [36] J. B. et al. (Particle Data Group) *Phys. Rev.*, vol. D86, 2012.
- [37] G. Lopez and the P0D collaboration, “Measurement of Neutral Current Single Pi-Zero Production with the T2K Pi-Zero Detector (P0D).” T2K internal technical note (T2K-TN-056), 2012.
- [38] K. Gilje and the P0D collaboration, “Measurement of Neutral Current Single Pi-Zero Production on Water with the T2K Pi-Zero Detector (P0D).” T2K internal technical note in progress (T2K-TN-144), 2013.
- [39] D. Binosi, J. Collins, C. Kaufhold, and L. Theussl, “JaxoDraw: A Graphical user interface for drawing Feynman diagrams. Version 2.0 release notes,” *Com-*

put. Phys. Commun., vol. 180, pp. 1709–1715, 2009.

[40] S. Nakayama *et al.*, “Measurement of single pi0 production in neutral current neutrino interactions with water by a 1.3-GeV wide band muon neutrino beam,” *Phys. Lett.*, vol. B619, pp. 255–262, 2005.

[41] A. A. Aguilar-Arevalo *et al.*, “Measurement of ν_μ and $\bar{\nu}_\mu$ induced neutral current single pi0 production cross sections on mineral oil at $E_\nu \sim 1$ GeV,” *Phys. Rev.*, vol. D81, p. 013005, 2010.

[42] B. Osmanov, “MINERvA Detector: Description and Performance,” *arXiv:1109.2855 [physics.ins-det]*, 2011.

[43] K. Abe *et al.*, “The T2K experiment,” *Nucl. Instrum. Meth.*, vol. A659, pp. 106–135, 2011.

[44] K. Abe *et al.*, “The T2K Neutrino Flux Prediction,” *Phys. Rev.*, vol. D87, p. 012001, 2013.

[45] T. Nakamoto *et al.*, “Design of superconducting combined function magnets for the 50 gev proton beam line for the j-parc neutrino experiment,” *IEEE Transactions on Applied Superconductivity*, vol. 14, no. 2, pp. 616 – 619, 2004.

[46] N. Abgrall *et al.*, “Measurements of Cross Sections and Charged Pion Spectra in Proton-Carbon Interactions at 31 GeV/c,” *Phys. Rev.*, vol. C84, p. 034604, 2011.

[47] A. Ferrari, P. R. Sala, A. Fasso, and J. Ranft, “FLUKA: A Multi-Particle Transport Code,” in *CERN-2005-010*, 2005.

[48] R. Brun, F. Carminati, and S. Giani, “GEANT Detector Description and Simulation Tool,” in *W5013*, CERN, 1994.

[49] C. Zeitnitz and T. A. Gabriel, “GCALOR,” in *International Conference on Calorimetry in High Energy Physics*, p. 376, 1993.

[50] A. Vacheret, G. Barker, M. Dziewiecki, P. Guzowski, M. Haigh, *et al.*, “Characterization and Simulation of the Response of Multi Pixel Photon Counters to Low Light Levels,” *Nucl. Instrum. Meth.*, vol. A656, pp. 69–83, 2011.

[51] I. Giomataris, R. De Oliveira, S. Andriamonje, S. Aune, G. Charpak, *et al.*, “Micromegas in a bulk,” *Nucl. Instrum. Meth.*, vol. A560, pp. 405–408, 2006.

- [52] G. Arnison *et al.*, “Experimental observation of isolated large transverse energy electrons with associated missing energy at $s^{**}(1/2) = 540\text{-GeV}$,” *Phys. Lett.*, vol. B122, pp. 103–116, 1983.
- [53] J. Altegoer *et al.*, “The NOMAD experiment at the CERN SPS,” *Nucl. Instrum. Meth.*, vol. A404, pp. 96–128, 1998.
- [54] J. Estrada, C. Garcia, B. Hoeneisen, and P. Rubinov, “MCM II and the Trip chip,” in *FERMILAB-TM-2226 (D0 note 4009)*, 2002.
- [55] Y. Itow *et al.*, “The JHF-Kamioka neutrino project,” *arXiv:hep-ex/0106019*, pp. 239–248, 2001.
- [56] The ND280 calibration group, “Calibration of the ND280 scintillator detectors.” T2K internal technical note (T2K-TN-037), 2012.
- [57] A. Hillairet *et al.*, “ND280 Reconstruction.” T2K internal technical note (T2K-TN-072), 2011.
- [58] R. Brun and F. Rademakers, “ROOT: An object oriented data analysis framework,” *Nucl. Instrum. Meth.*, vol. A389, pp. 81–86, 1997.
- [59] S. Agostinelli *et al.*, “Geant4 - a simulation toolkit,” *Nucl. Instrum. Meth.*, vol. A506, no. 3, pp. 250 – 303, 2003.
- [60] C. Andreopoulos, A. Bell, D. Bhattacharya, F. Cavanna, J. Dobson, *et al.*, “The GENIE Neutrino Monte Carlo Generator,” *Nucl. Instrum. Meth.*, vol. A614, pp. 87–104, 2010.
- [61] Y. Hayato, “A Neutrino Interaction Simulation Program Library NEUT,” *Acta Physica Polonica B*, vol. 40, p. 2477, 2009.
- [62] N. Abgrall *et al.*, “Time Projection Chambers for the T2K Near Detectors,” *Nucl. Instrum. Meth.*, vol. A637, pp. 25–46, 2011.
- [63] T. T. T. collaboration, “Calibration of the ND280 TPCs and PID studies.” upcoming T2K internal technical note (T2K-TN-069), 2013.
- [64] A. C. Villanueva *et al.*, “RecPack: A General Reconstruction Package,” <http://ific.uv.es/recpack>.
- [65] C. Giganti and M. Zito, “Particle Identification with the T2K TPC.” T2K internal

technical note (T2K-TN-001), 2009.

[66] Paweł Guzowski, *Reconstruction of neutrino induced neutral current neutral pion events with the T2K ND280 Tracker and ECAL*. PhD thesis, Imperial College London, 2011.

[67] Narsingh Deo, *Graph Theory with Applications to Engineering and Computer Science*, pp. 61 – 64. Prentice-Hall of India Private Limited, 2005.

[68] C. Andreopoulos, J. Dobson, and S. Dytman, “Handling Neutrino Interaction Uncertainties using Event Reweighting.” T2K internal technical note (T2K-TN-007), 2012.

[69] P. de Perio *et al.*, “Implementation of the NIWG Cross Section Parametrization.” T2K internal technical note (T2K-TN-113), 2012.

[70] P. de Perio *et al.*, “Cross section parameters for the 2012a oscillation analysis.” T2K internal technical note (T2K-TN-108), 2012.

[71] A. A. Aguilar-Arevalo *et al.*, “Measurement of ν_μ -induced charged-current neutral pion production cross sections on mineral oil at for $0.5 \text{ GeV} < E_\nu < 2.0 \text{ GeV}$,” *Phys. Rev.*, vol. D83, p. 052009, 2011.

[72] A. A. Aguilar-Arevalo *et al.*, “Measurement of neutrino-induced charged-current charged pion production cross sections on mineral oil at $E_\nu \sim 1 \text{ GeV}$,” *Phys. Rev. D*, vol. 83, p. 052007, 2011.

[73] A. A. Aguilar-Arevalo *et al.*, “Measurement of ν_μ and $\bar{\nu}_\mu$ induced neutral current single π^0 production cross sections on mineral oil at $E_\nu \sim \mathcal{O}(1 \text{ gev})$,” *Phys. Rev.*, vol. D81, p. 013005, 2010.

[74] E. J. Moniz, I. Sick, R. R. Whitney, J. R. Ficenec, R. D. Kephart, and W. P. Trower, “Nuclear fermi momenta from quasielastic electron scattering,” *Phys. Rev. Lett.*, vol. 26, no. 8, pp. 445–448, 1971.

[75] A. M. Ankowski and J. T. Sobczyk, “Construction of spectral functions for medium-mass nuclei,” *Phys. Rev.*, vol. C77, p. 044311, 2008.

[76] A. A. Aguilar-Arevalo *et al.*, “First Measurement of the Muon Neutrino Charged Current Quasielastic Double Differential Cross Section,” *Phys. Rev.*, vol. D81, p. 092005, 2010.

- [77] V. Lyubushkin *et al.*, “A Study of quasi-elastic muon neutrino and antineutrino scattering in the NOMAD experiment,” *Eur. Phys. J.*, vol. C63, pp. 355–381, 2009.
- [78] P. Adamson *et al.*, “Neutrino and antineutrino inclusive charged-current cross section measurements with the minos near detector,” *Phys. Rev.*, vol. D81, p. 072002, 2010.
- [79] P. de Perio *et al.*, “NEUT Nuclear Effects.” T2K internal technical note (T2K-TN-033), 2011.
- [80] G. Bellettini, “Proton-nuclei cross sections at 20 GeV,” *Nucl. Phys.*, vol. 79, pp. 609–624, 1966.
- [81] P. de Perio *et al.*, “NEUT Systematic Studies for 2010a Analysis.” T2K internal technical note (T2K-TN-032), 2011.
- [82] N. Abgrall *et al.*, “Measurement of Production Properties of Positively Charged Kaons in Proton-Carbon Interactions at 31 GeV/c,” *Phys. Rev.*, vol. C85, p. 035210, 2012.
- [83] T. Eichten *et al.*, “Particle production in proton interactions in nuclei at 24 gev/c,” *Nuclear Physics B*, vol. 44, no. 2, pp. 333 – 343, 1972.
- [84] J. V. Allaby *et al.*, “High-energy particle spectra from proton interactions at 19.2 GeV/c,” in *Technical Report 70-12*, CERN, 1970.
- [85] D. Hadley *et al.*, “Second Generation Particle ID with the ND280 Tracker ECALs.” T2K internal technical note (T2K-TN-111), 2012.

Appendix A.

Supplementary information for selecting neutral current π^0 interactions in the FGD

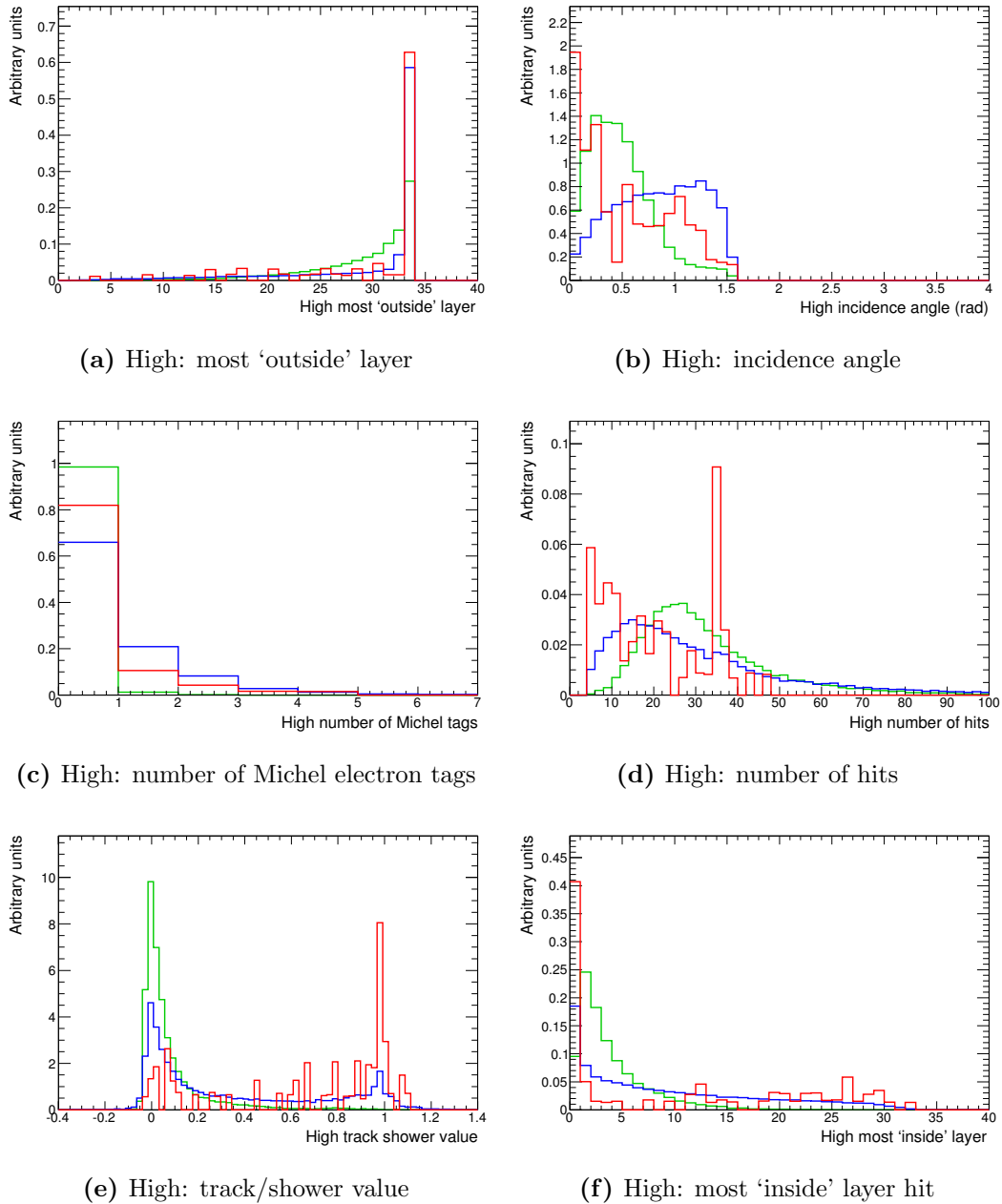


Figure A.1.: Signal (green), magnet background (blue) and sand background (red) distributions for ECAL variables used in TMVA for the high energy cluster in category one (both clusters in the DsECAL) before any pre-TMVA cuts are made. For label definitions see Table 6.8.

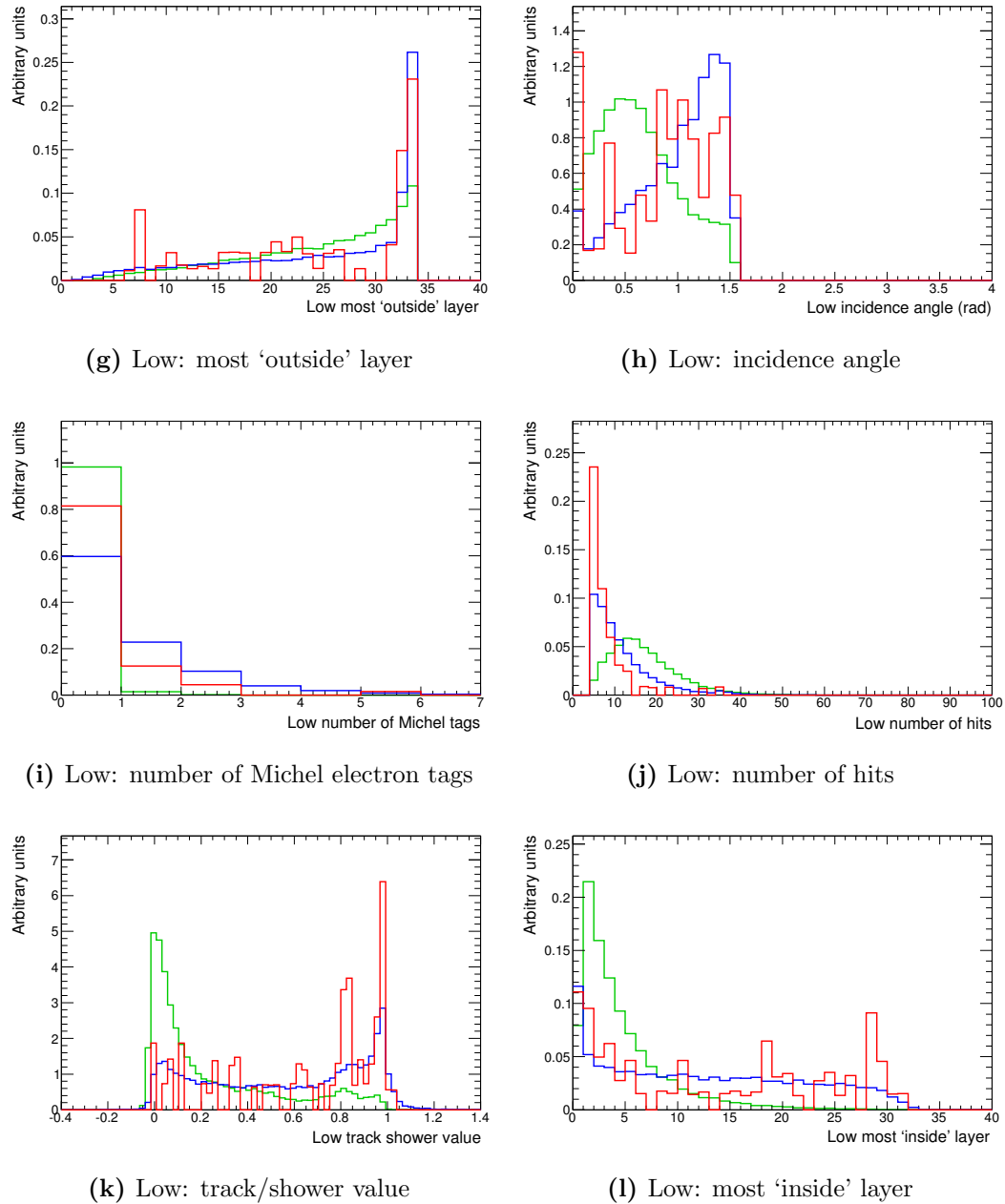


Figure A.1.: Signal (green), magnet background (blue) and sand background (red) distributions for ECAL variables used in TMVA for the low energy cluster in category one (both clusters in the DsECAL) before any pre-TMVA cuts are made. For label definitions see Table 6.8.

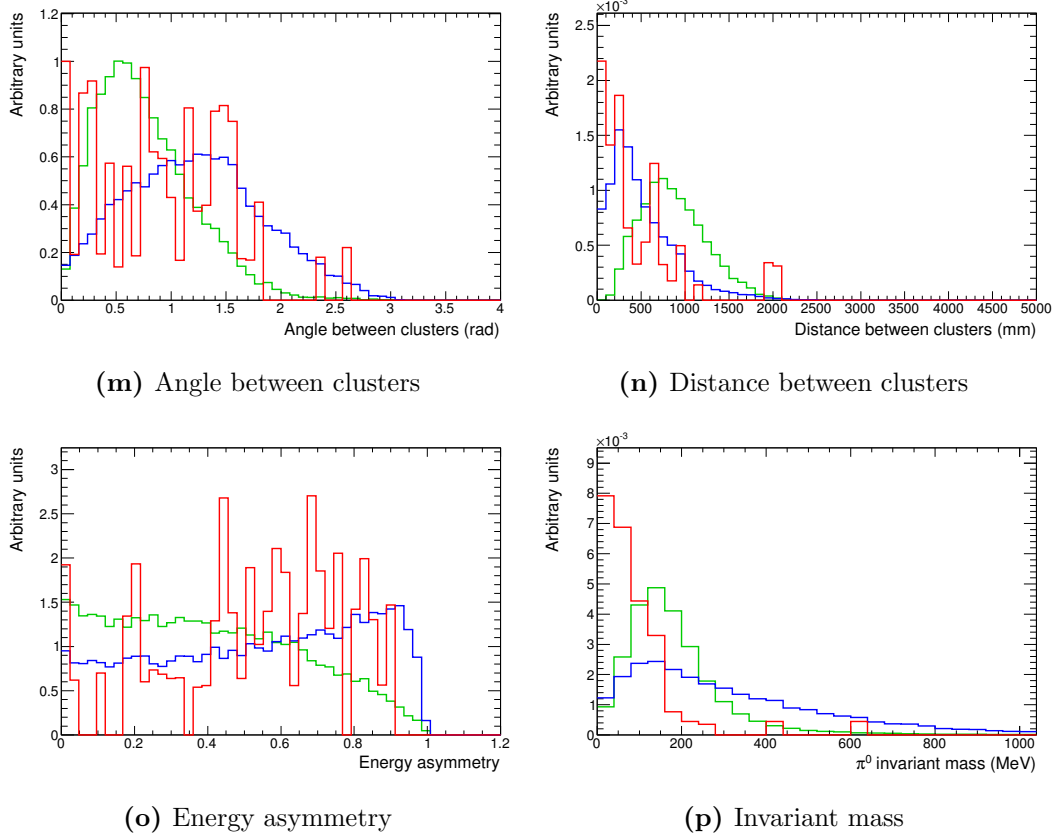


Figure A.1.: Signal (green), magnet background (blue) and sand background (red) distributions for ECAL variables used in TMVA for category one (both clusters in the DsECAL) before any pre-TMVA cuts are made. For label definitions see Table 6.8.

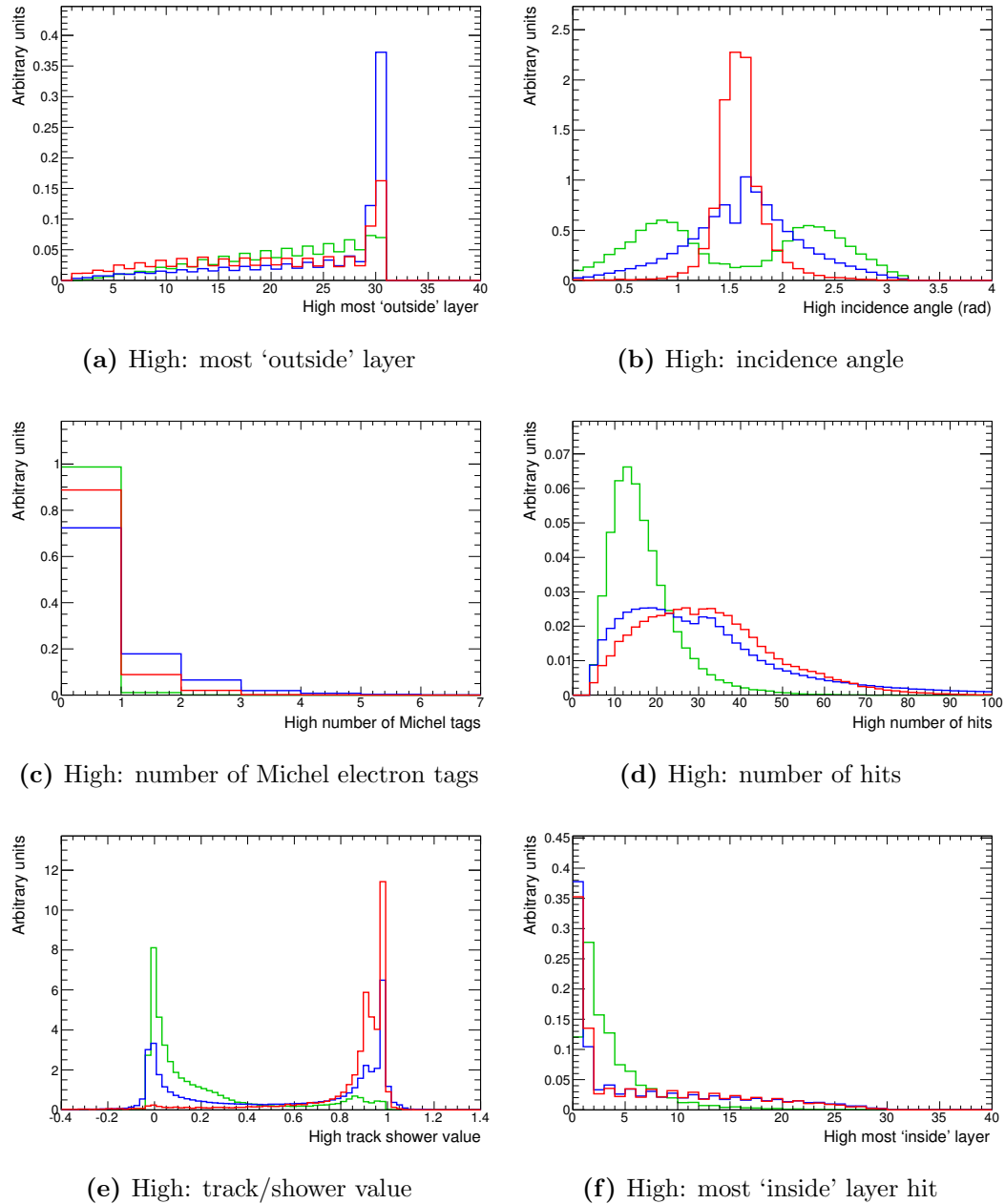


Figure A.2.: Signal (green), magnet background (blue) and sand background (red) distributions for ECAL variables used in TMVA for the high energy cluster in category two (both clusters in the BrECAL) before any pre-TMVA cuts are made. For label definitions see Table 6.8.

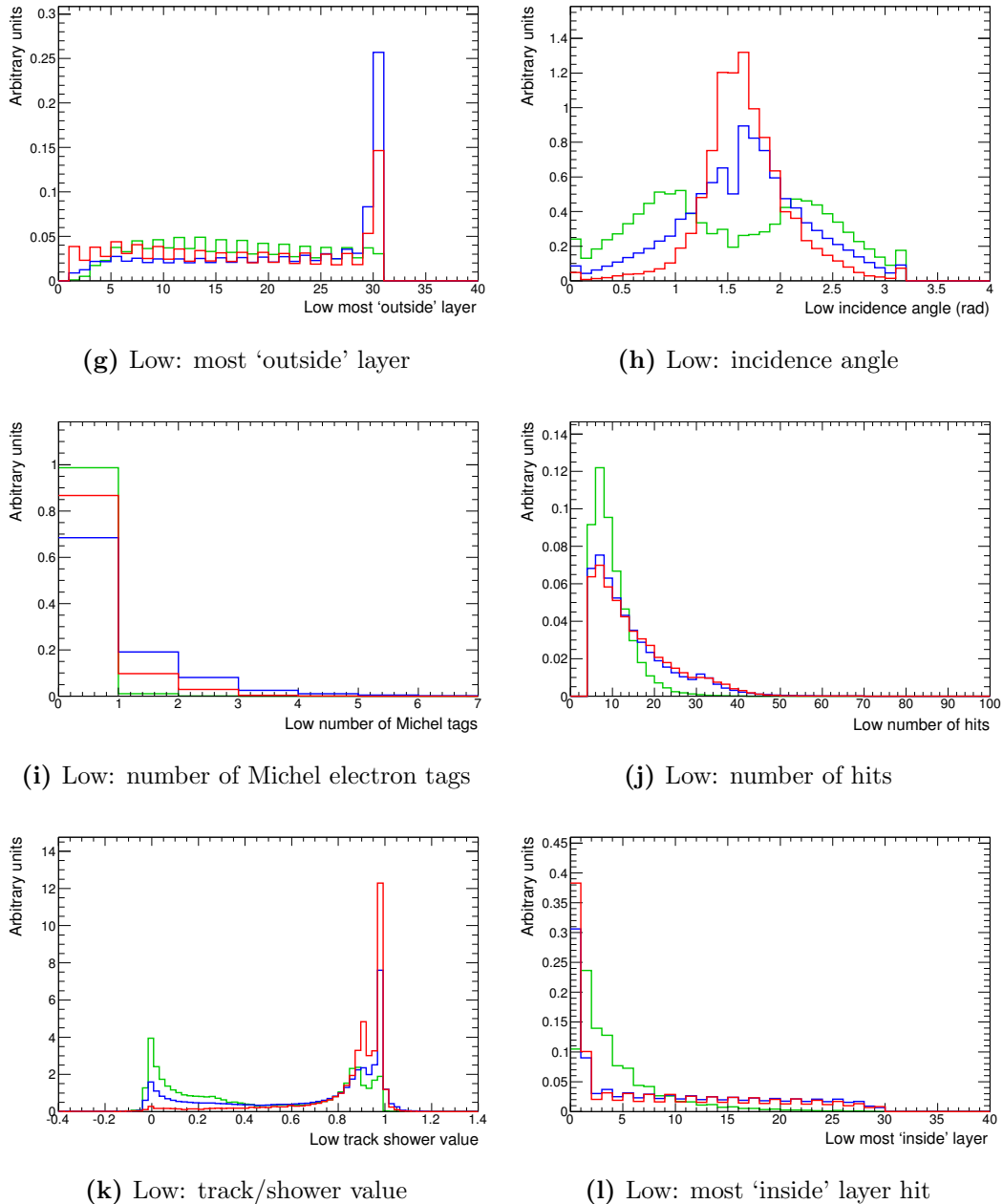


Figure A.2.: Signal (green), magnet background (blue) and sand background (red) distributions for ECAL variables used in TMVA for the low energy cluster in category two (both clusters in the BrECAL) before any pre-TMVA cuts are made. For label definitions see Table 6.8.

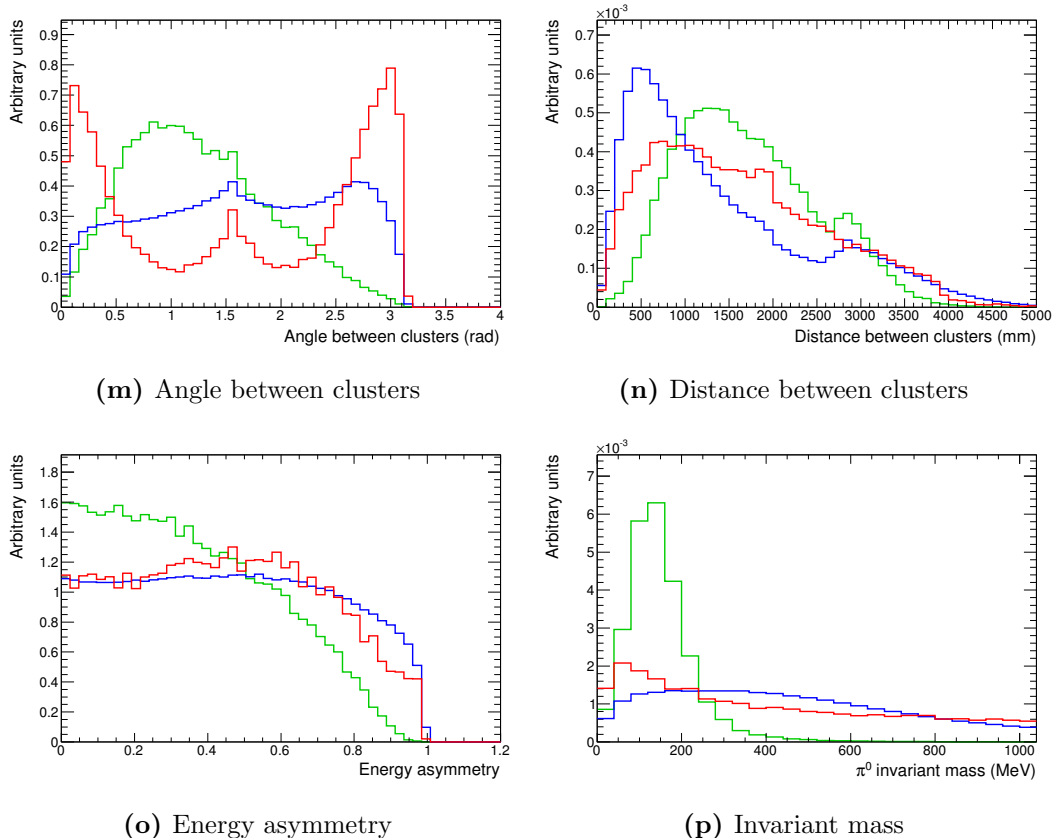


Figure A.2.: Signal (green), magnet background (blue) and sand background (red) distributions for ECAL variables used in TMVA for category two (both clusters in the BrECAL) before any pre-TMVA cuts are made. For label definitions see Table 6.8.

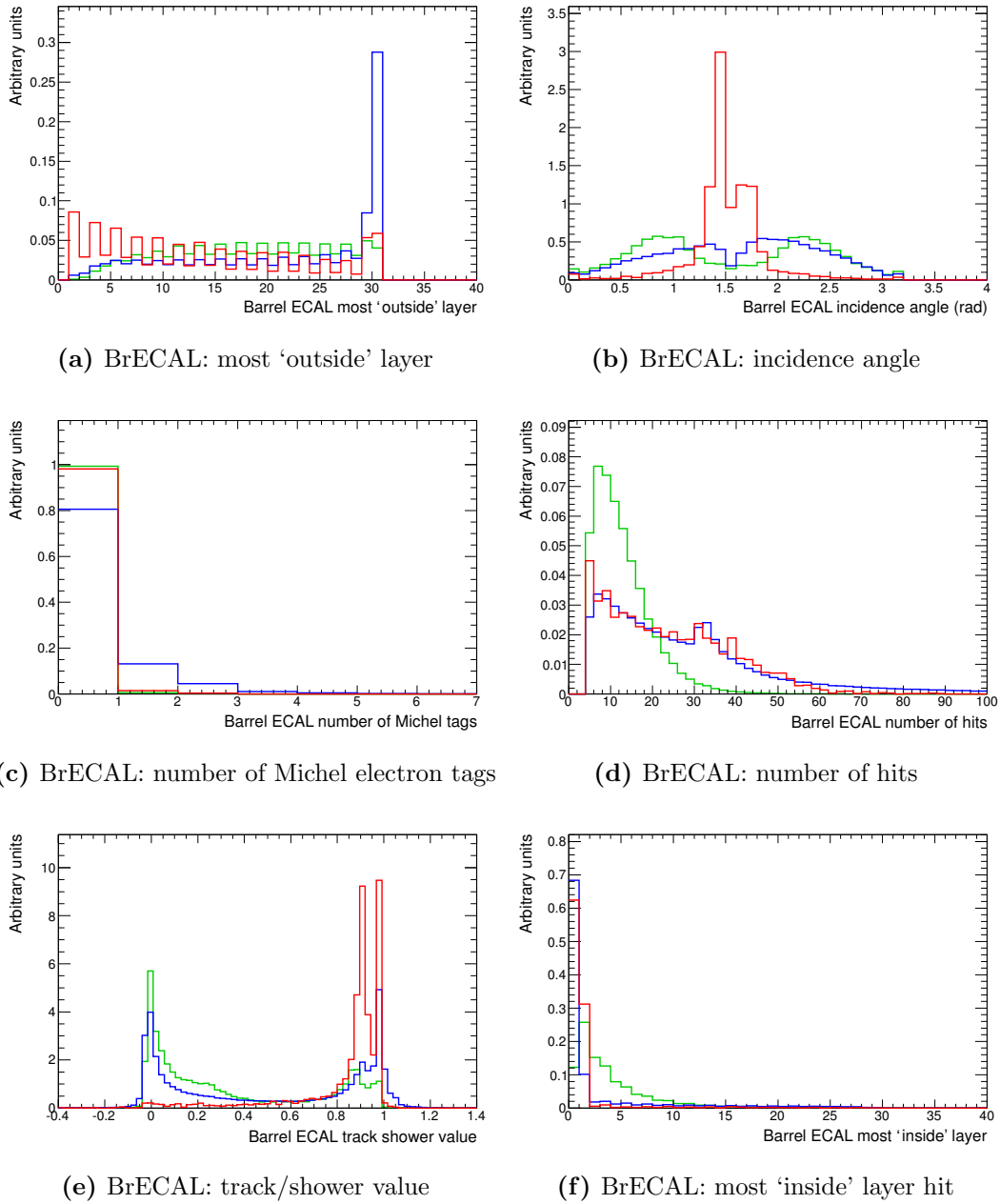


Figure A.3.: Signal (green), magnet background (blue) and sand background (red) distributions for ECAL variables used in TMVA for the BrECAL cluster in category three (one cluster in the DsECAL, one cluster in the BrECAL) before any pre-TMVA cuts are made. For label definitions see Table 6.8.

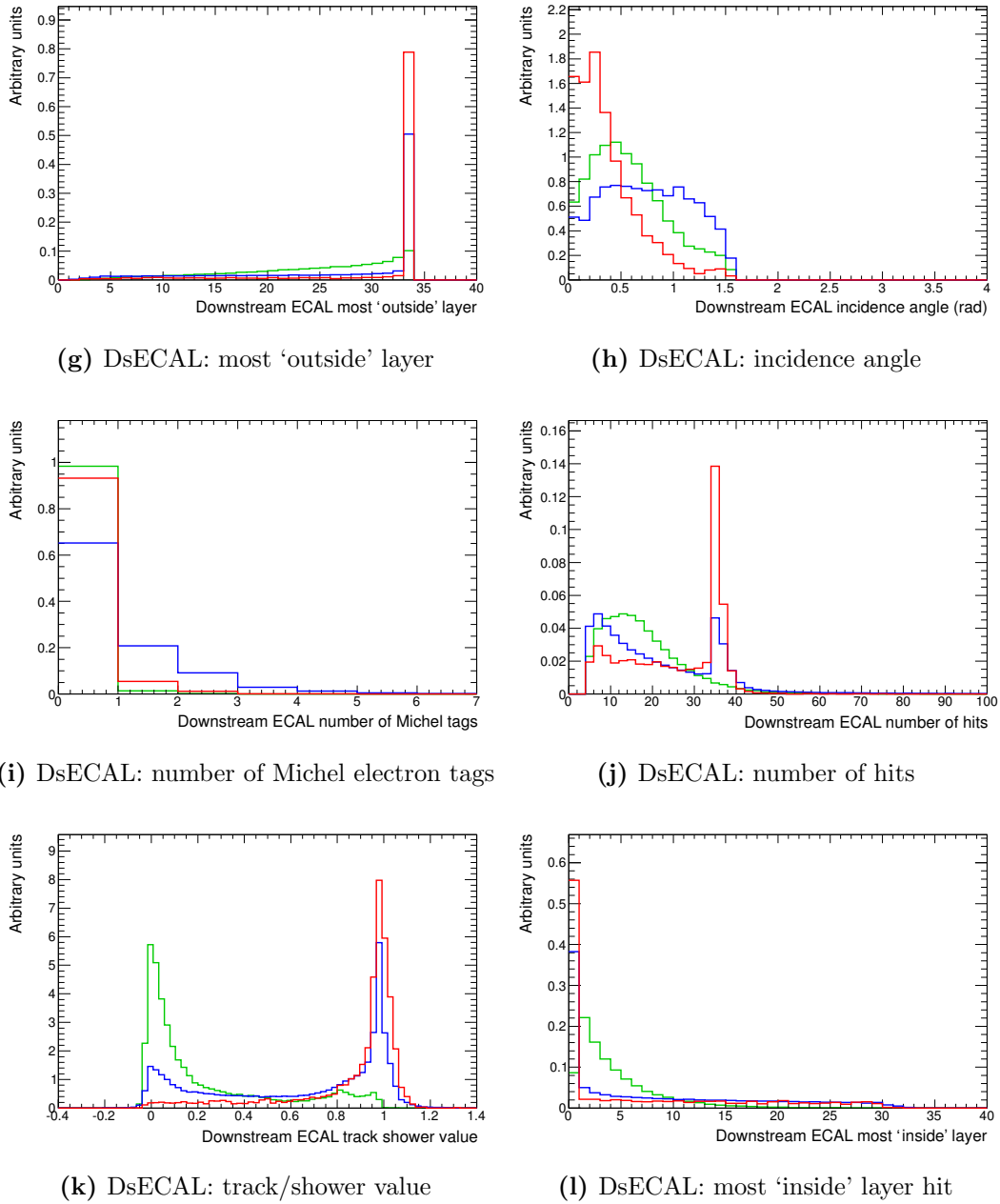


Figure A.3.: Signal (green), magnet background (blue) and sand background (red) distributions for ECAL variables used in TMVA for the DsECAL cluster in category three (one cluster in the DsECAL, one cluster in the BrECAL) before any pre-TMVA cuts are made. For label definitions see Table 6.8.

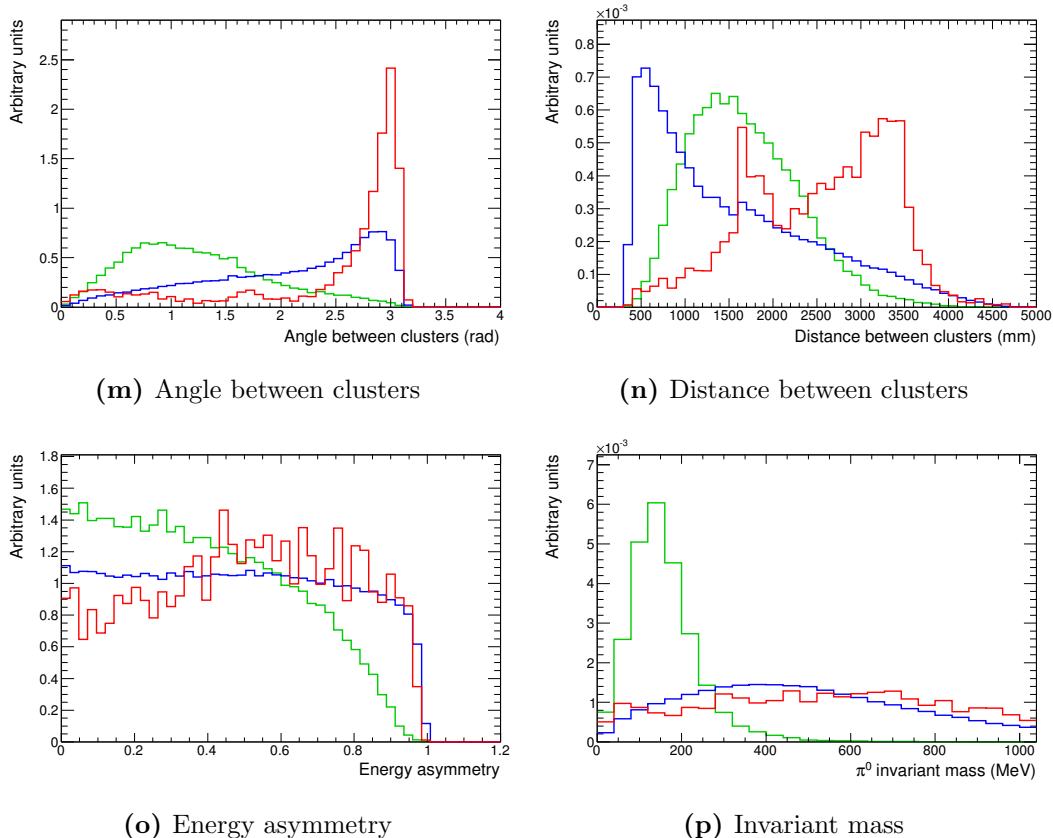


Figure A.3.: Signal (green), magnet background (blue) and sand background (red) distributions for ECAL variables used in TMVA for category three (one cluster in the DsECAL, one cluster in the BrECAL) before any pre-TMVA cuts are made. For label definitions see Table 6.8.

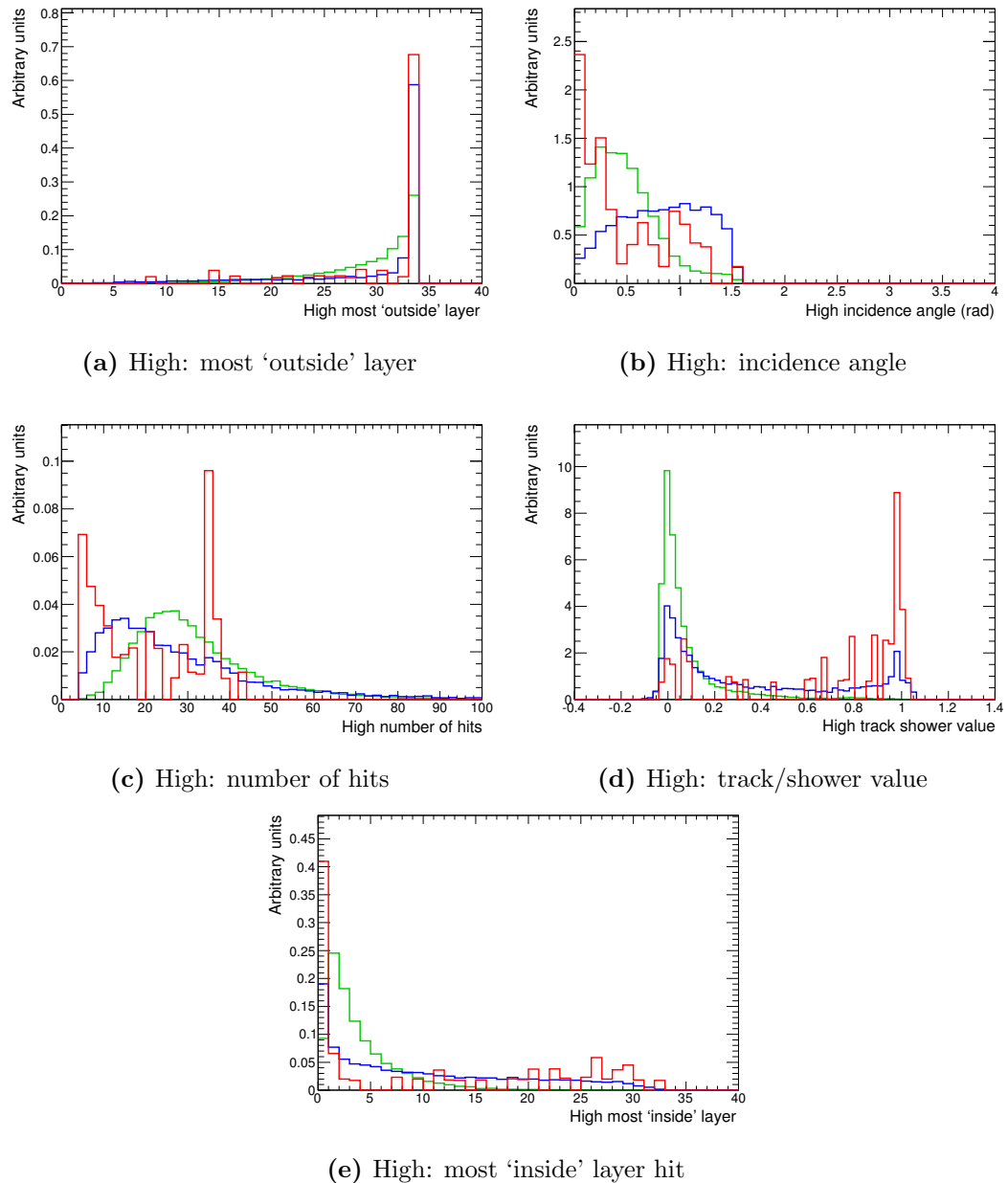


Figure A.4.: Signal (green), magnet background (blue) and sand background (red) distributions for ECAL variables used in TMVA for the high energy cluster in category one (both clusters in the DsECAL) after the pre-TMVA cuts are made. For label definitions see Table 6.8.

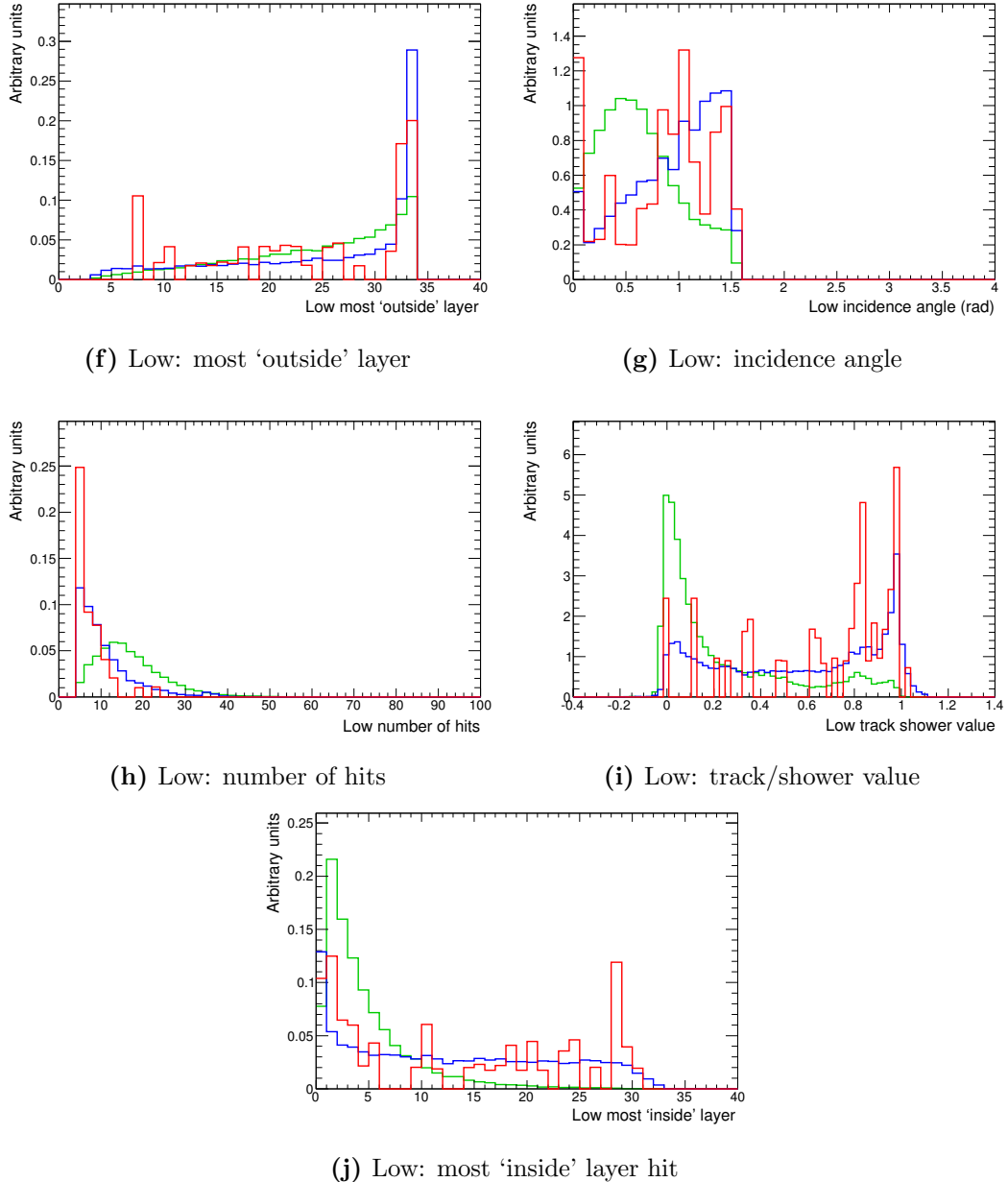


Figure A.4.: Signal (green), magnet background (blue) and sand background (red) distributions for ECAL variables used in TMVA for the low energy cluster in category one (both clusters in the DsECAL) after the pre-TMVA cuts are made. For label definitions see Table 6.8.

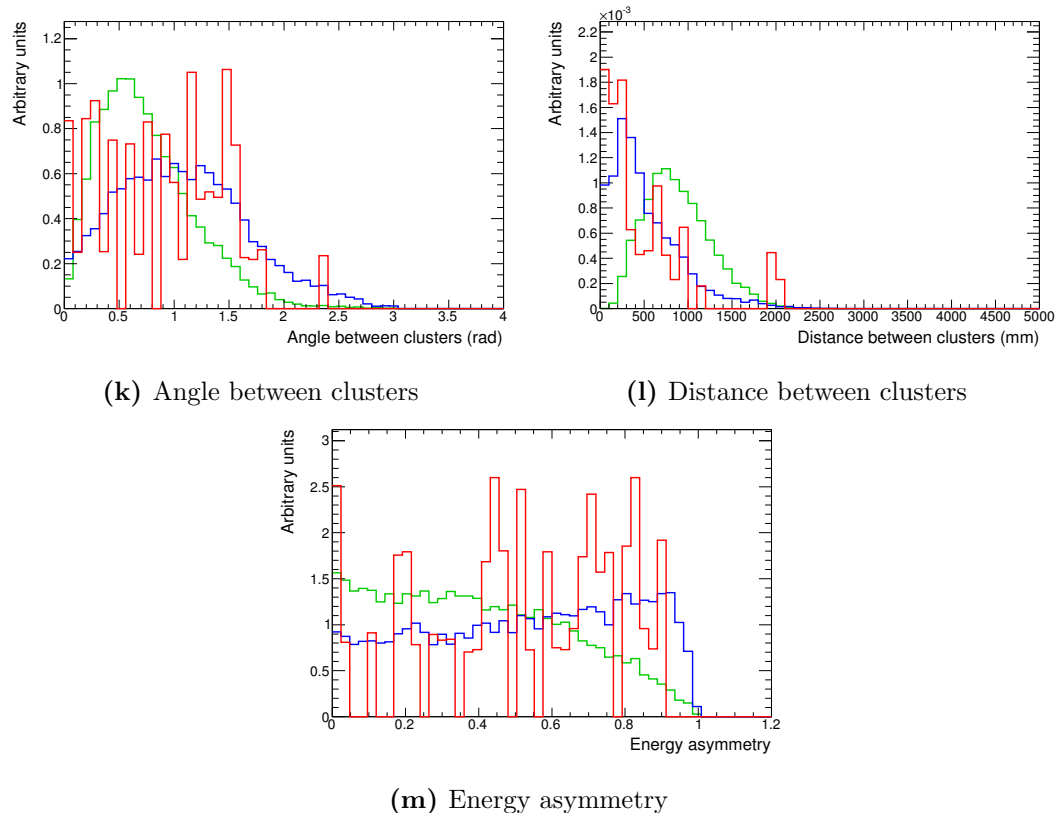


Figure A.4.: Signal (green), magnet background (blue) and sand background (red) distributions for ECAL variables used in TMVA for category one (both clusters in the DsECAL) after the pre-TMVA cuts are made. For label definitions see Table 6.8.

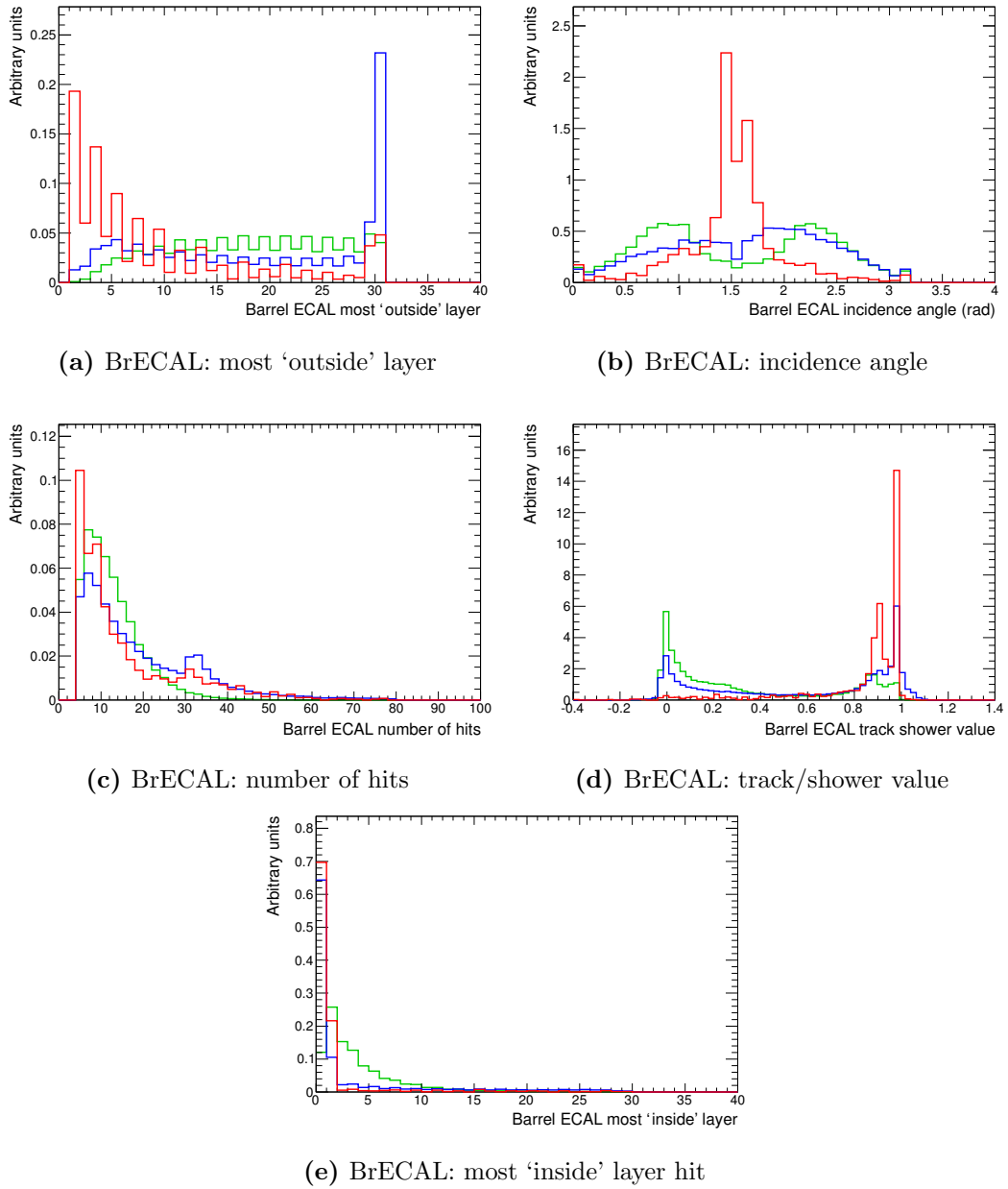


Figure A.5.: Signal (green), magnet background (blue) and sand background (red) distributions for ECAL variables used in TMVA for BrECAL cluster in category three (one cluster in the DsECAL, one in the BrECAL) after the pre-TMVA cuts are made. For label definitions see Table 6.8.

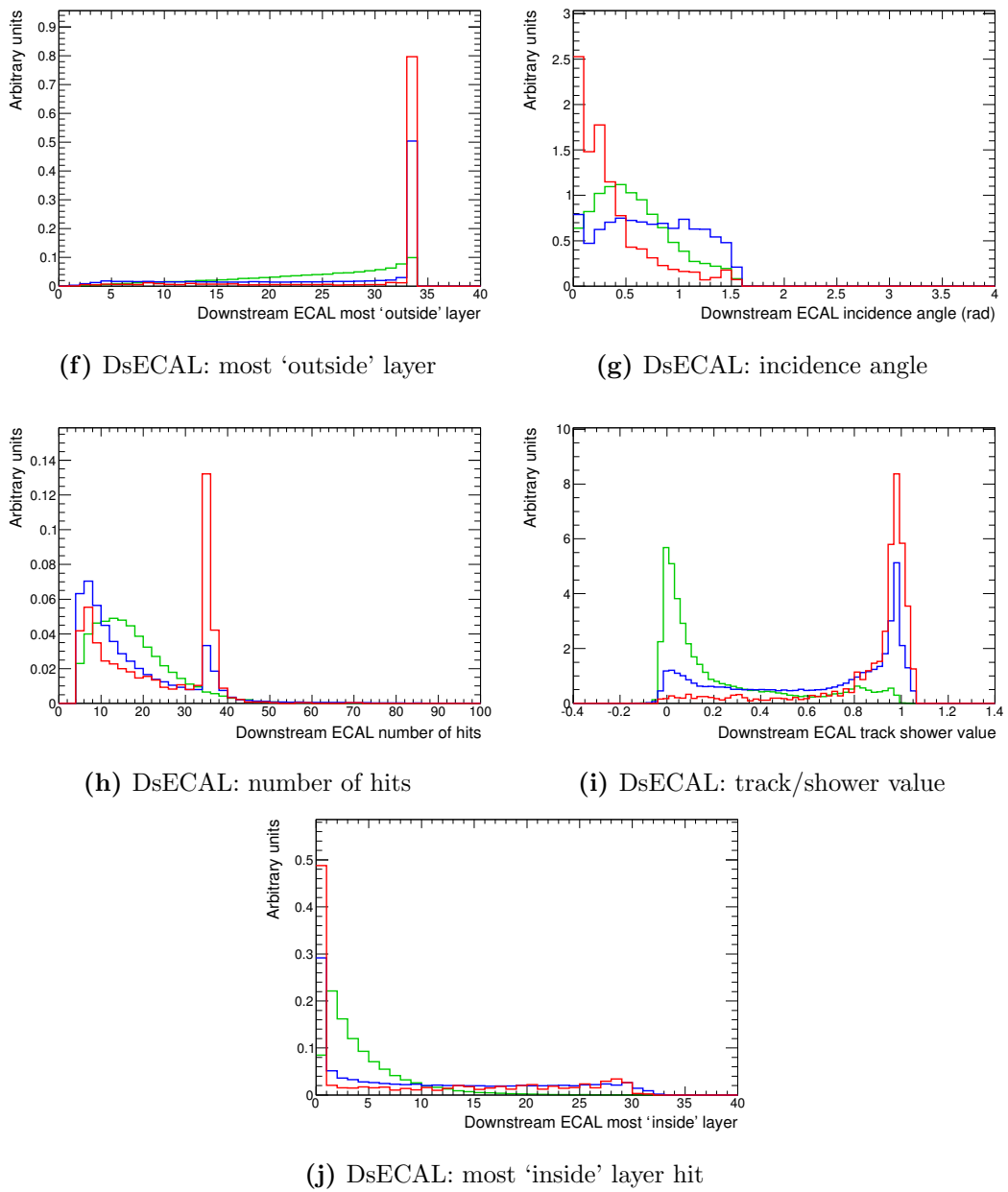


Figure A.5.: Signal (green), magnet background (blue) and sand background (red) distributions for ECAL variables used in TMVA for DsECAL cluster in category three (one cluster in the DsECAL, one in the BrECAL) after the pre-TMVA cuts are made. For label definitions see Table 6.8.

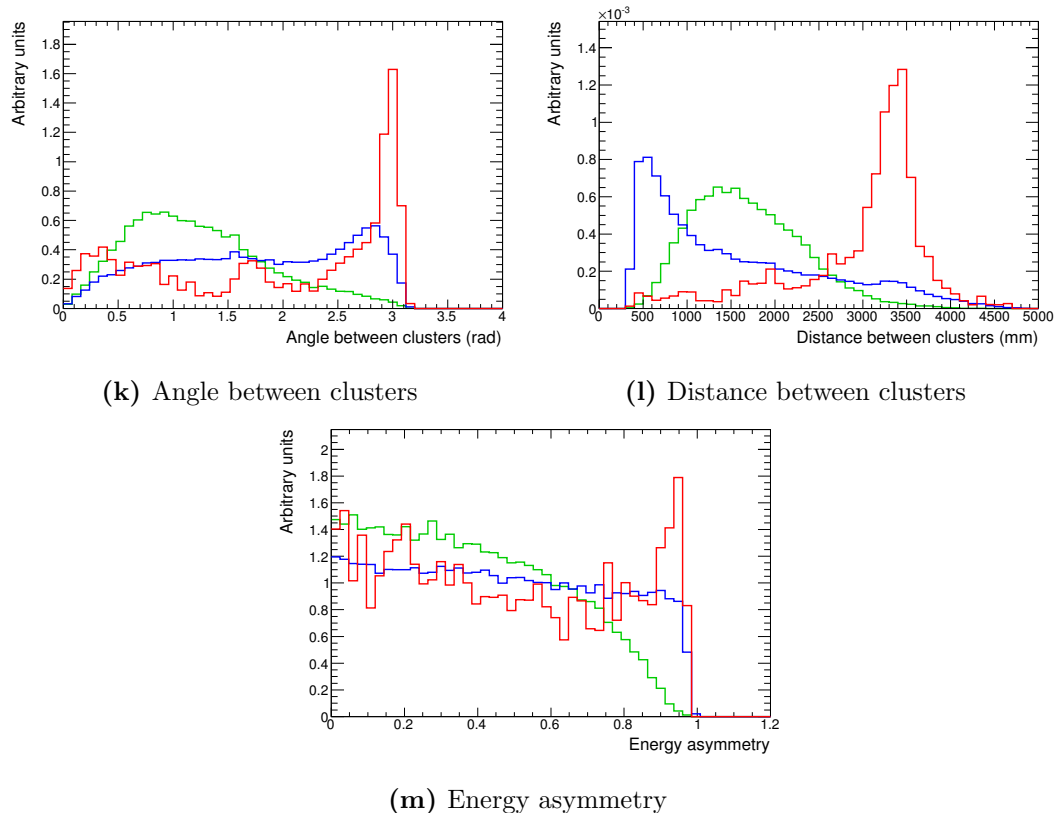


Figure A.5.: Signal (green), magnet background (blue) and sand background (red) distributions for ECAL variables used in TMVA for category three (one cluster in the DsECAL, one in the BrECAL) after the pre-TMVA cuts are made. For label definitions see Table 6.8.

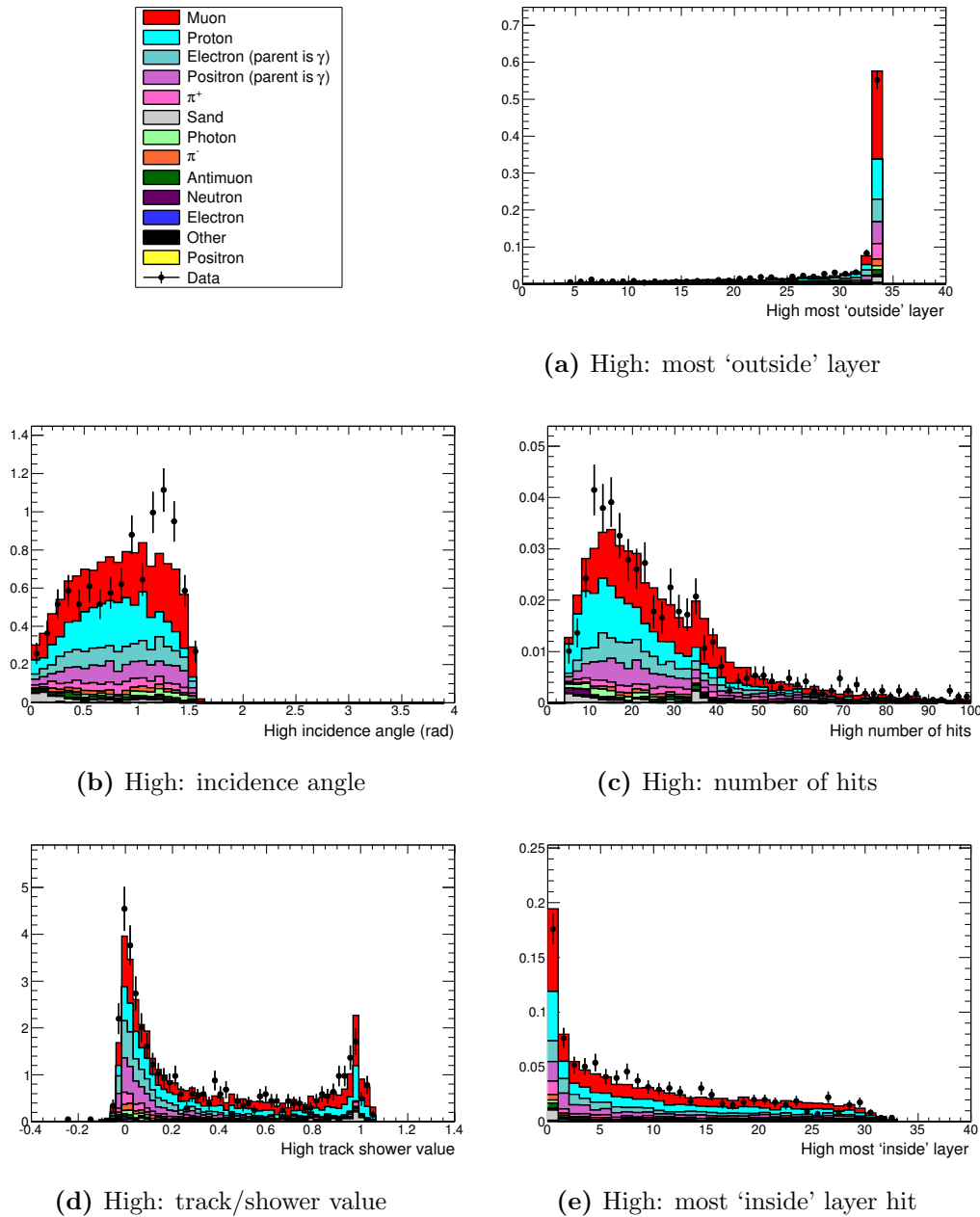


Figure A.6.: Data and MC distributions of ECAL variables used in TMVA for the high energy cluster in category one after pre-TMVA cuts. Plots are area normalised. For label definitions see Table 6.8.

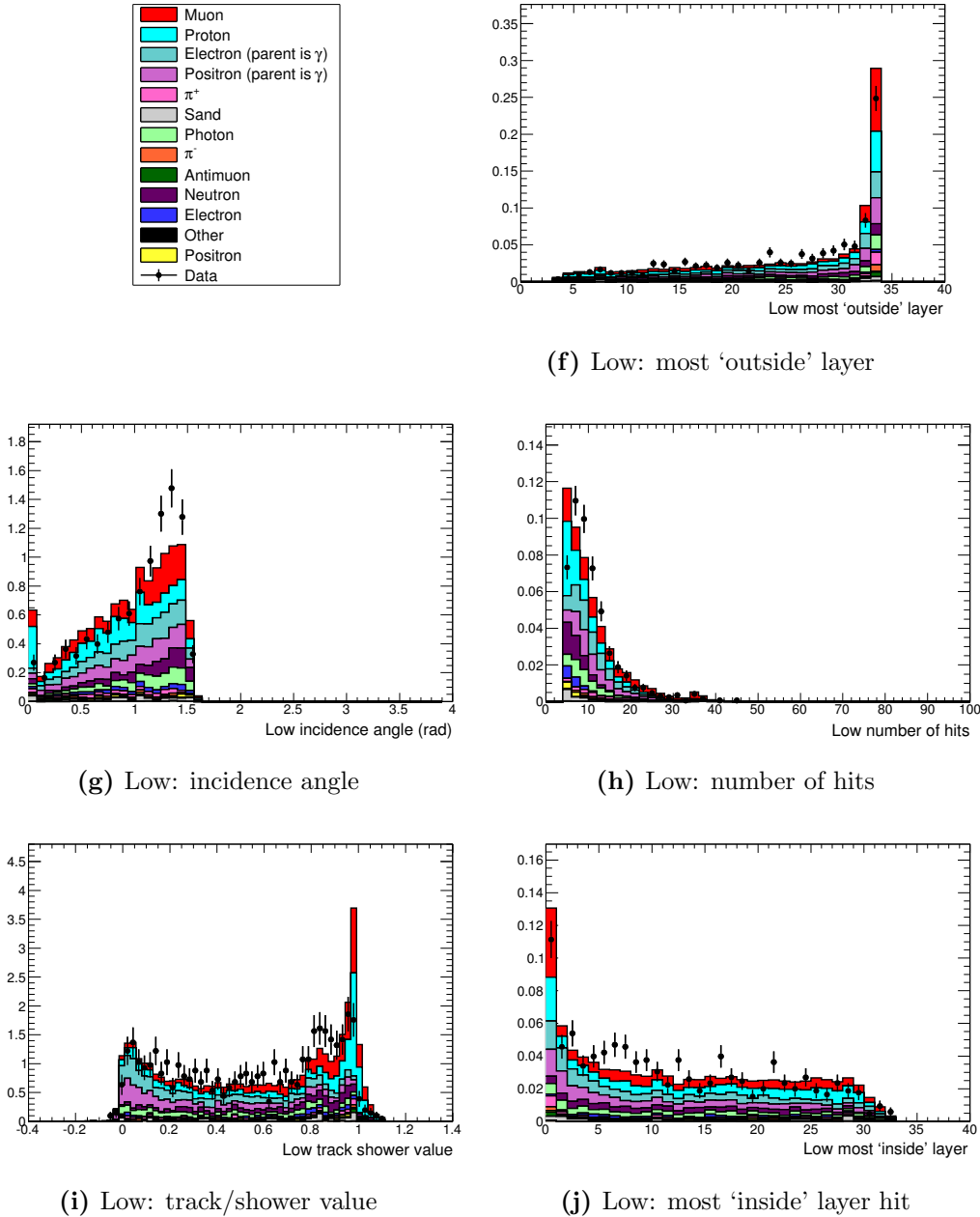
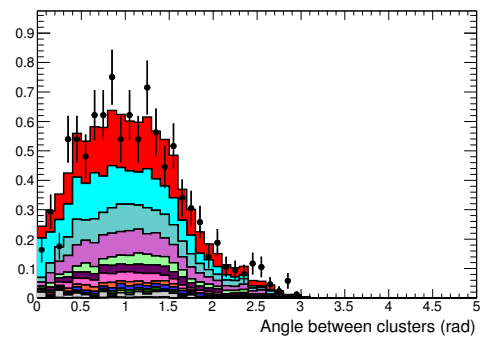
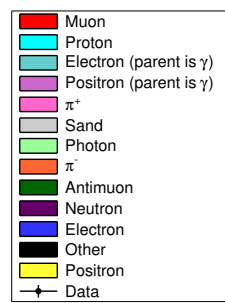
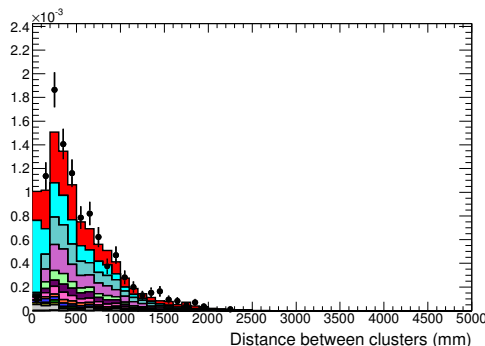


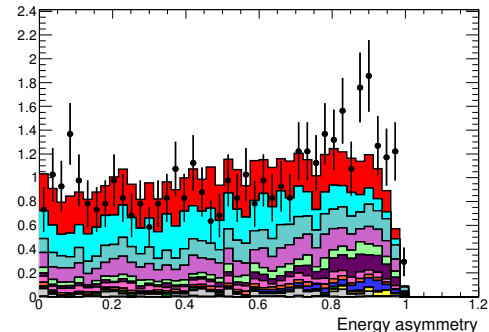
Figure A.6.: Data and MC distributions of ECAL variables used in TMVA for the low energy cluster in category one after pre-TMVA cuts. Plots are area normalised. For label definitions see Table 6.8.



(k) Angle between clusters



(l) Distance between clusters



(m) Energy asymmetry

Figure A.6.: Data and MC distributions of ECAL variables used in TMVA for category one after pre-TMVA cuts. Plots are area normalised. For label definitions see Table 6.8.

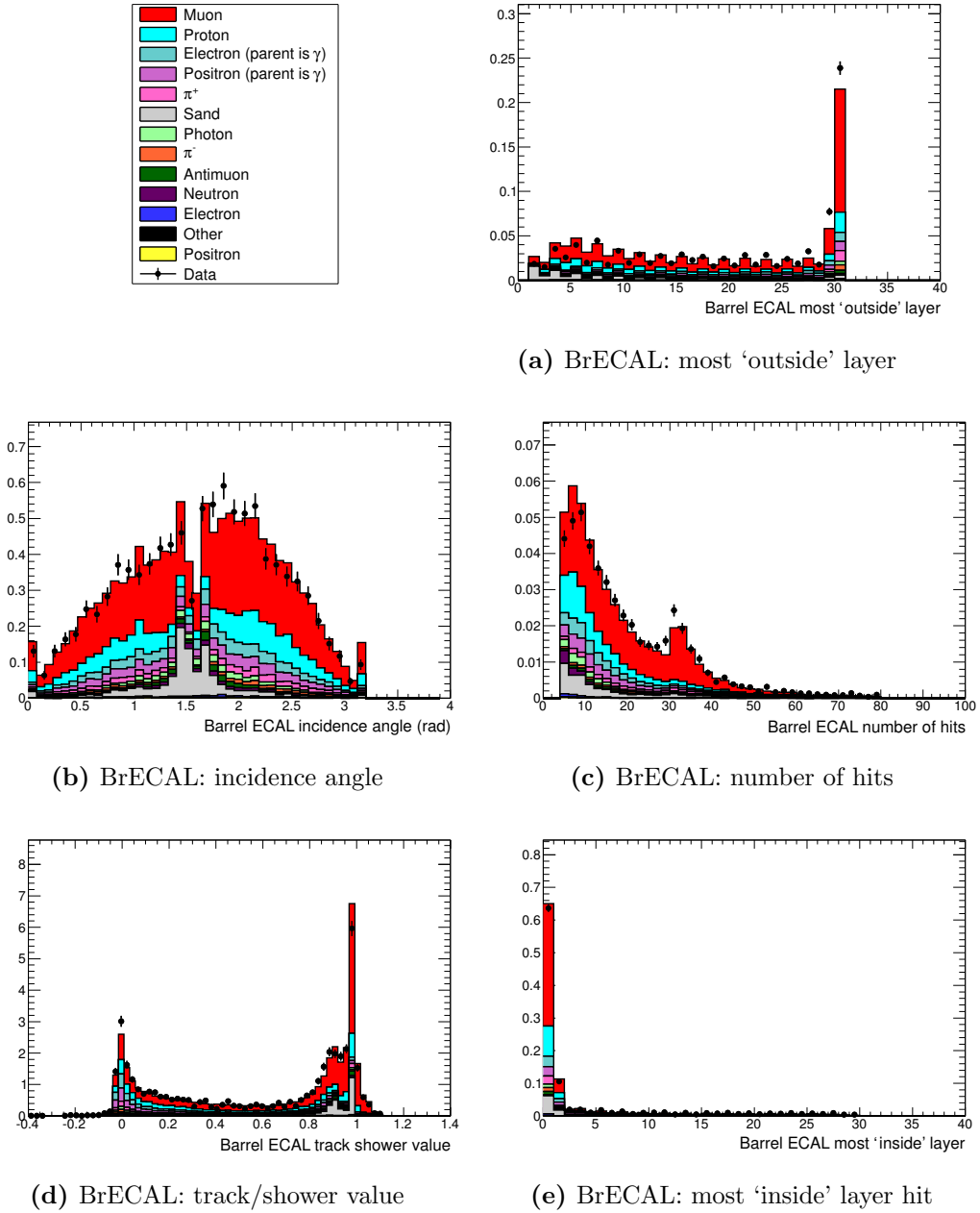


Figure A.7.: Data and MC distributions of ECAL variables used in TMVA for the BrECAL cluster in category three after pre-TMVA cuts. Plots are area normalised. For label definitions see Table 6.8.

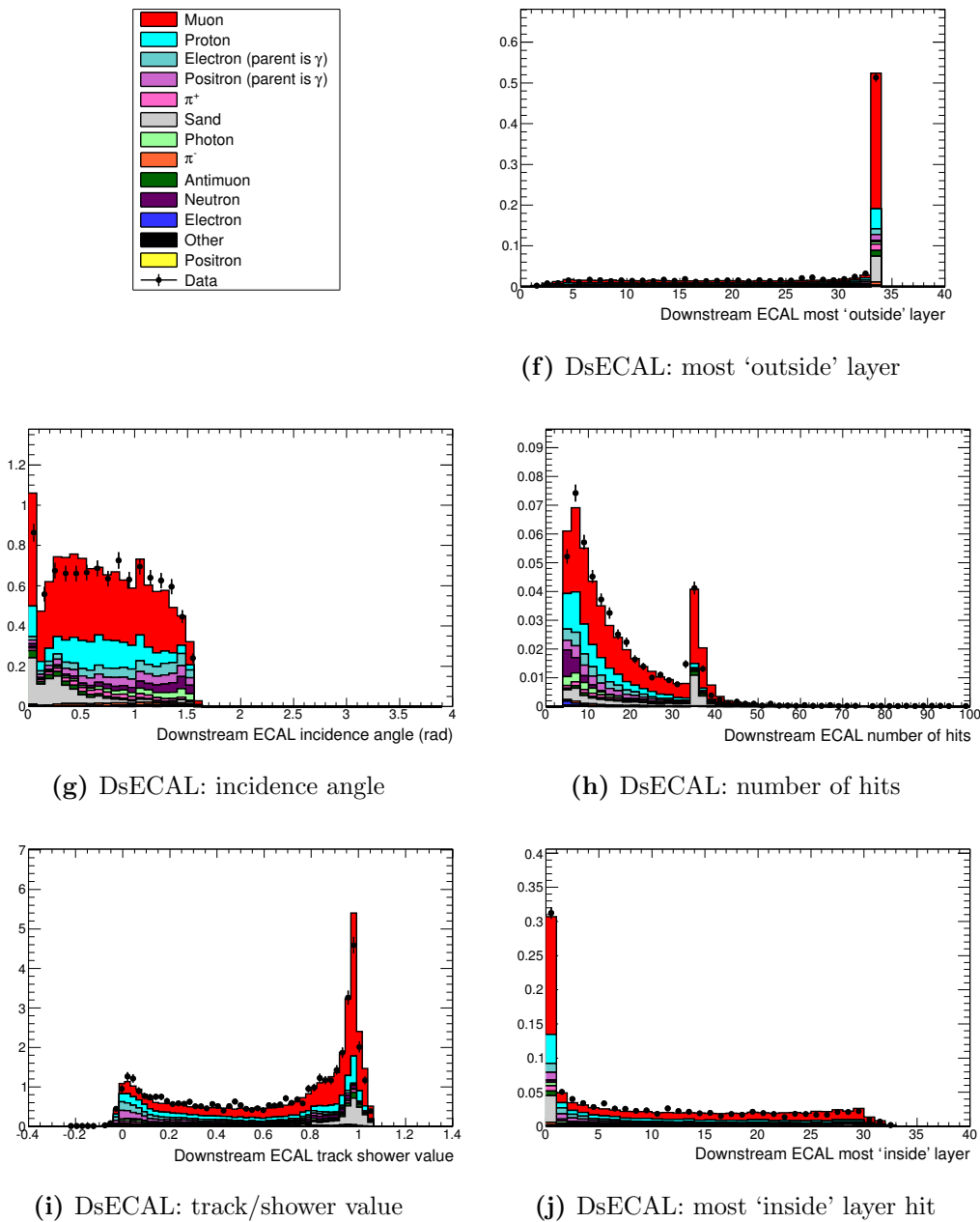
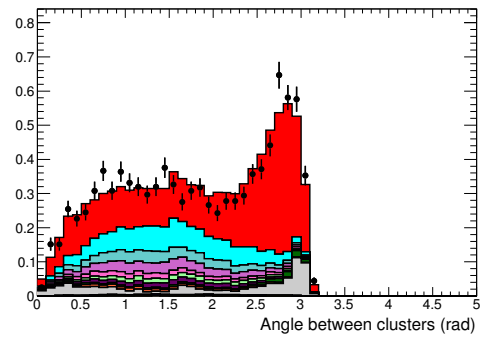
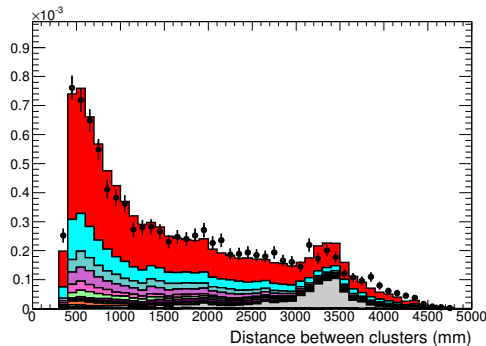


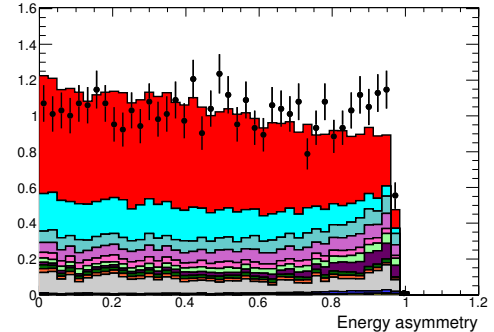
Figure A.7.: Data and MC distributions of ECAL variables used in TMVA for the DsECAL cluster in category three after pre-TMVA cuts. Plots are area normalised. For label definitions see Table 6.8.



(k) Angle between clusters



(l) Distance between clusters



(m) Energy asymmetry

Figure A.7.: Data and MC distributions of ECAL variables used in TMVA for category three after pre-TMVA cuts. Plots are area normalised. For label definitions see Table 6.8.

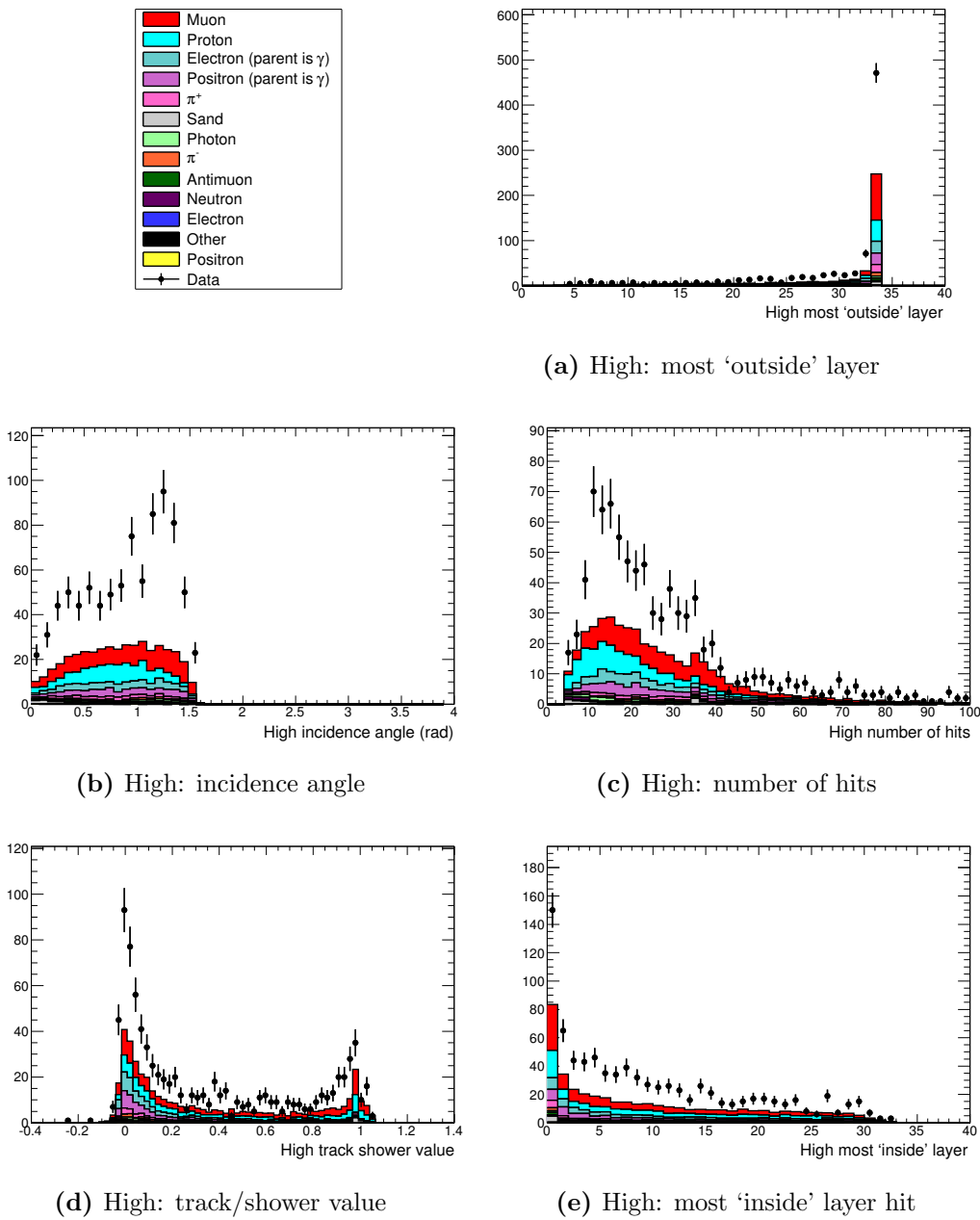


Figure A.8.: Data and MC distributions of ECAL variables used in TMVA for the high energy cluster in category one after pre-TMVA cuts. Plots are POT normalised. For label definitions see Table 6.8.

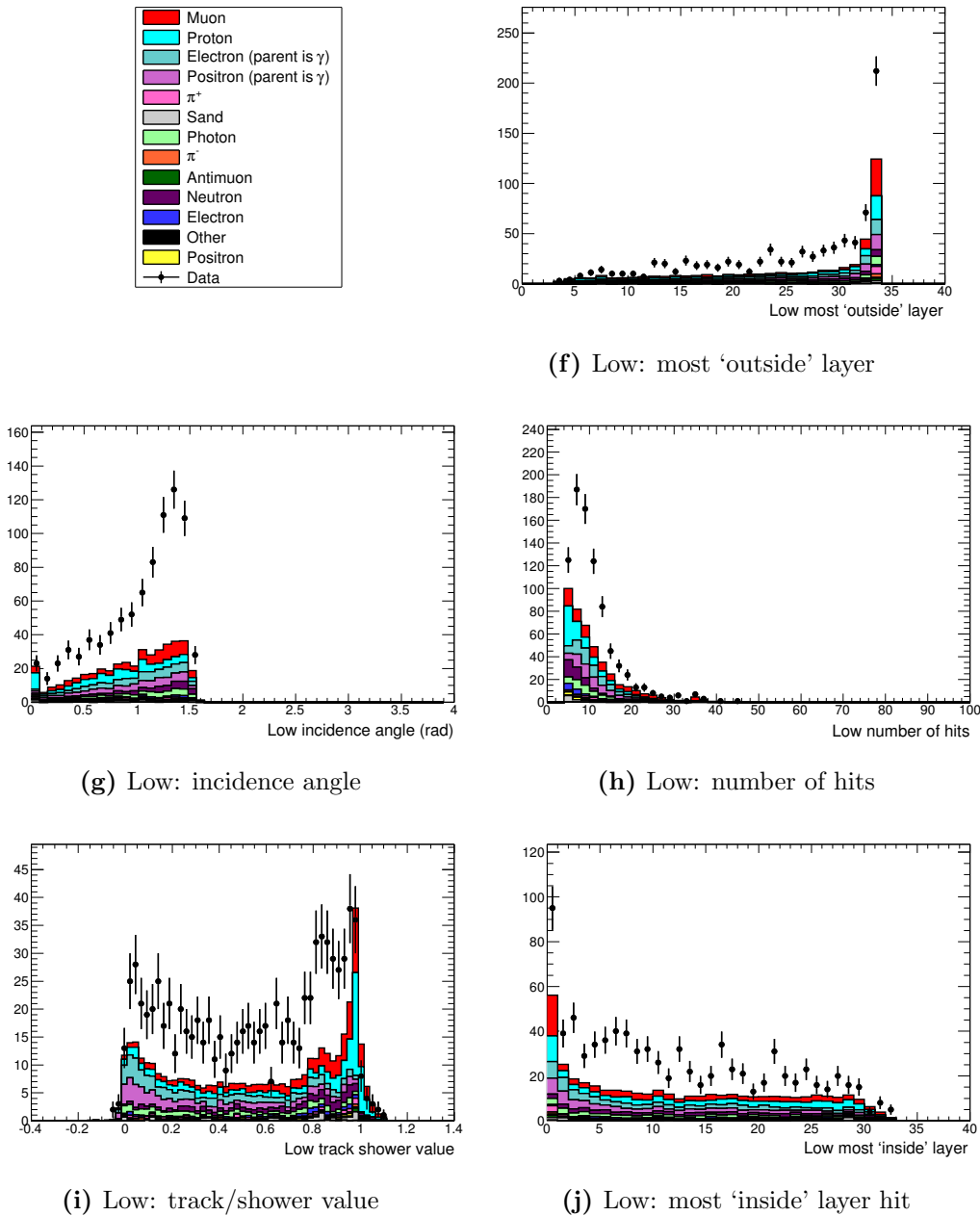
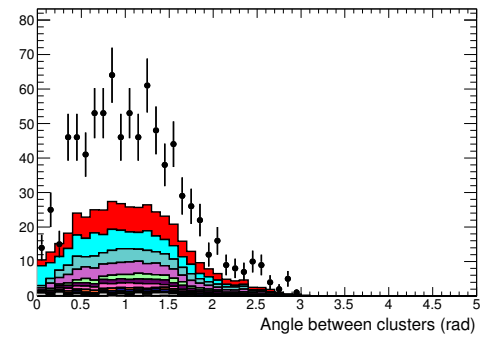
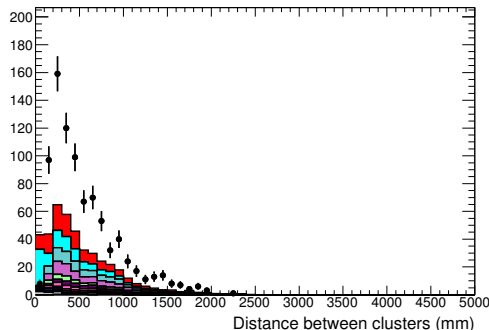


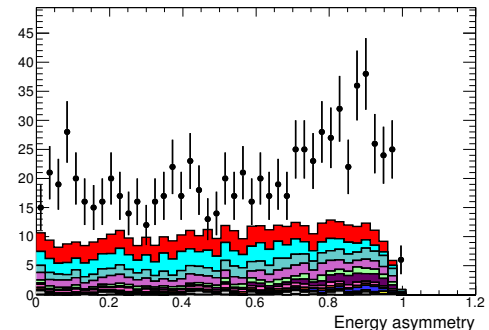
Figure A.8.: Data and MC distributions of ECAL variables used in TMVA for the low energy cluster in category one after pre-TMVA cuts. Plots are POT normalised. For label definitions see Table 6.8.



(k) Angle between clusters

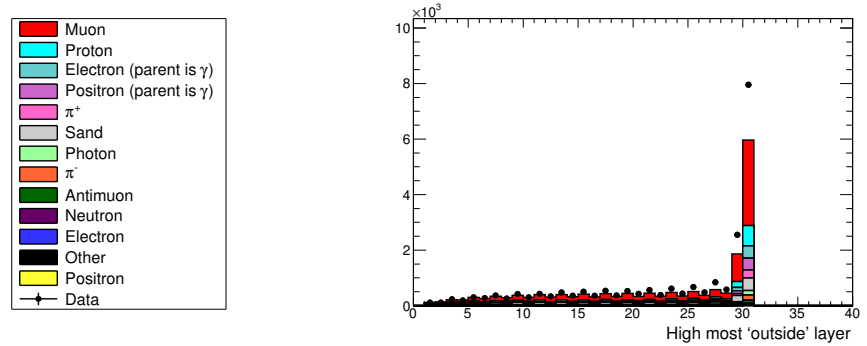


(l) Distance between clusters

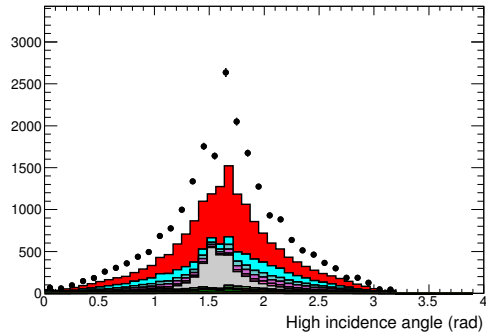


(m) Energy asymmetry

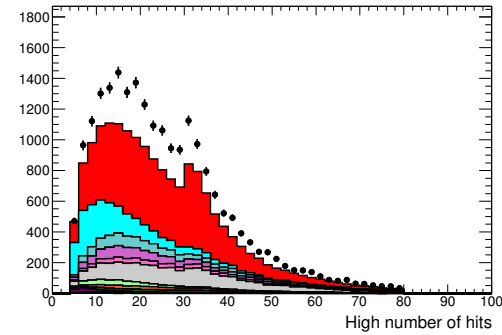
Figure A.8.: Data and MC distributions of ECAL variables used in TMVA for category one after pre-TMVA cuts. Plots are POT normalised. For label definitions see Table 6.8.



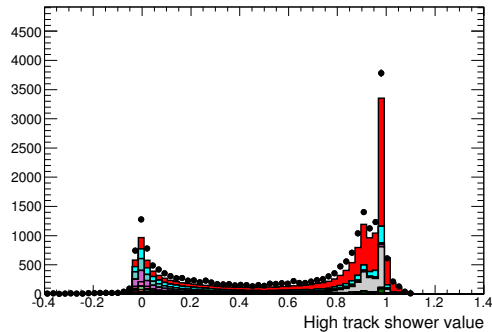
(a) High: most 'outside' layer



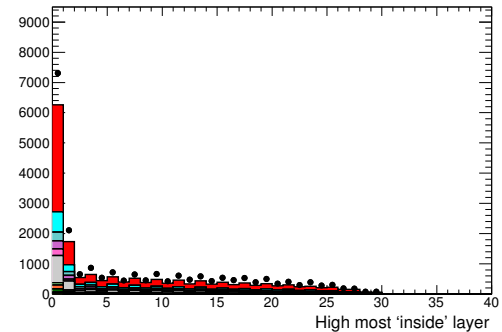
(b) High: incidence angle



(c) High: number of hits



(d) High: track/shower value



(e) High: most 'inside' layer hit

Figure A.9.: Data and MC distributions of ECAL variables used in TMVA for the high energy cluster in category two after pre-TMVA cuts. Plots are POT normalised. For label definitions see Table 6.8.

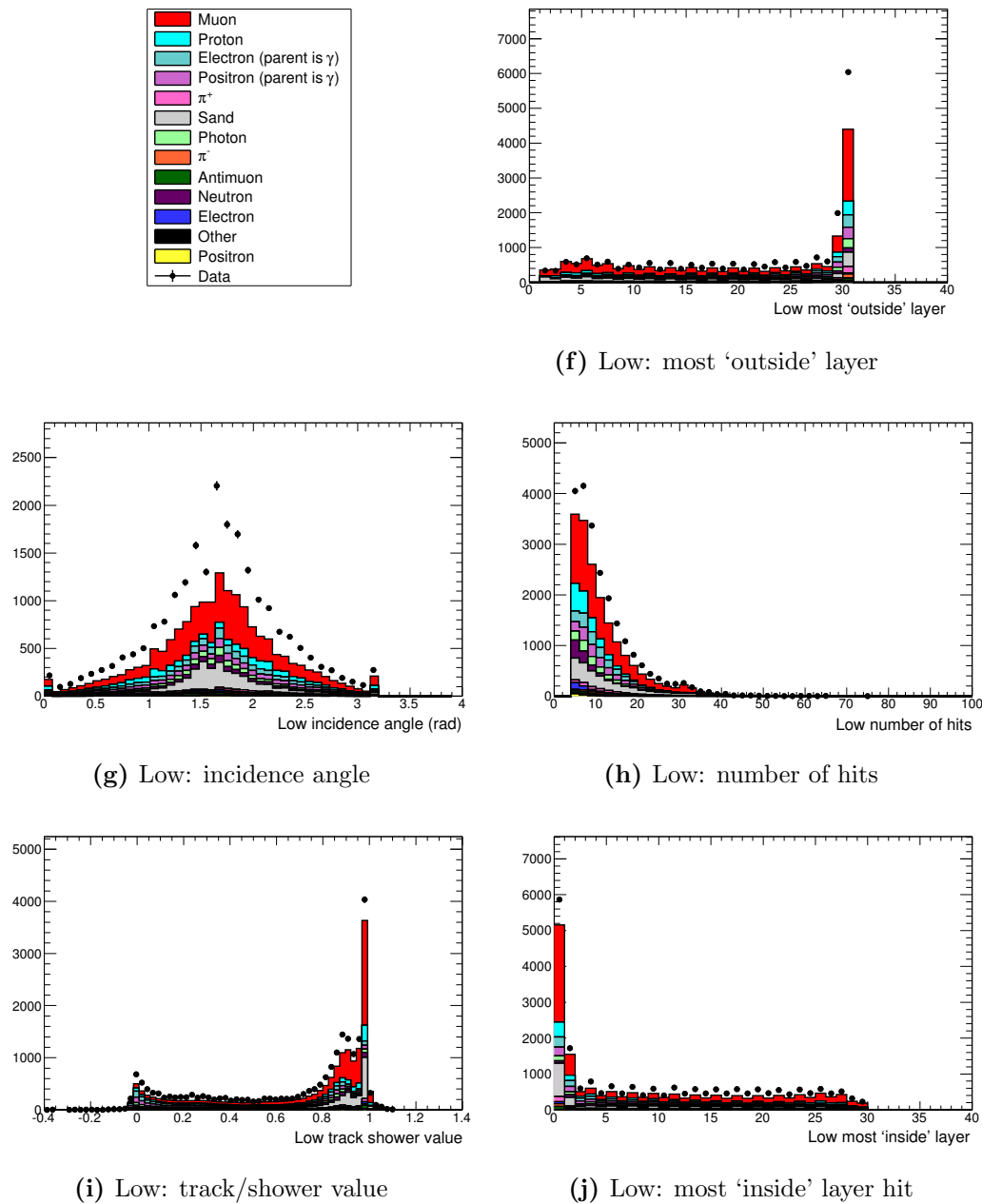
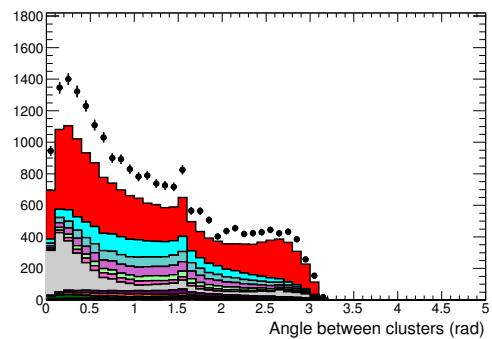
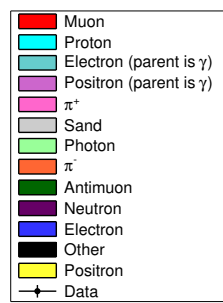
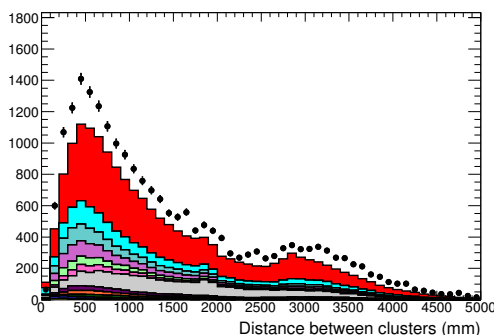


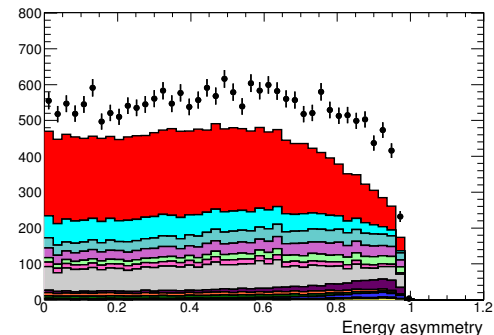
Figure A.9.: Data and MC distributions of ECAL variables used in TMVA for the low energy cluster in category two after pre-TMVA cuts. Plots are POT normalised. For label definitions see Table 6.8.



(k) Angle between clusters



(l) Distance between clusters



(m) Energy asymmetry

Figure A.9.: Data and MC distributions of ECAL variables used in TMVA for category two after pre-TMVA cuts. Plots are POT normalised. For label definitions see Table 6.8.

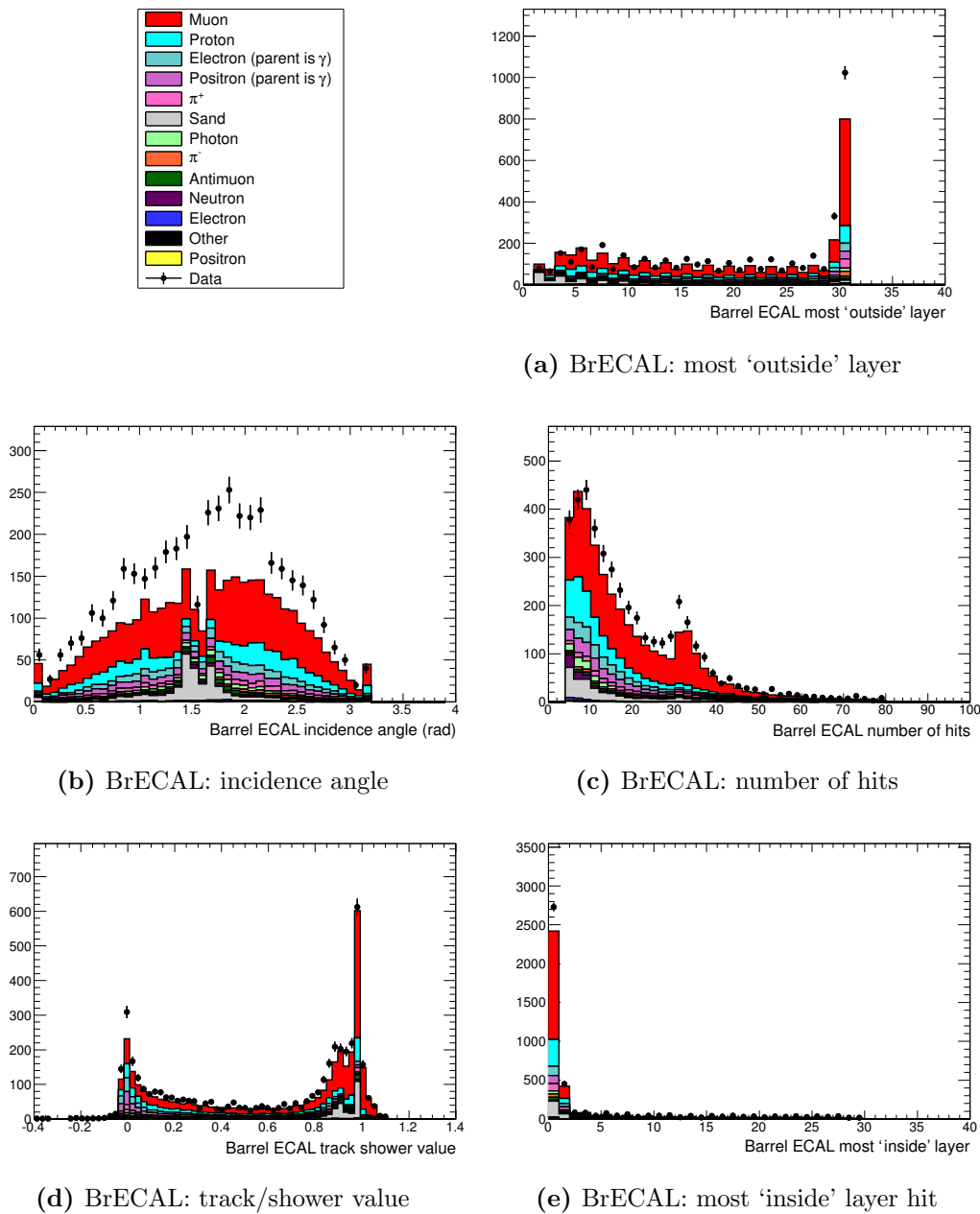


Figure A.10.: Data and MC distributions of ECAL variables used in TMVA for the BrECAL cluster in category three after pre-TMVA cuts. Plots are POT normalised. For label definitions see Table 6.8.

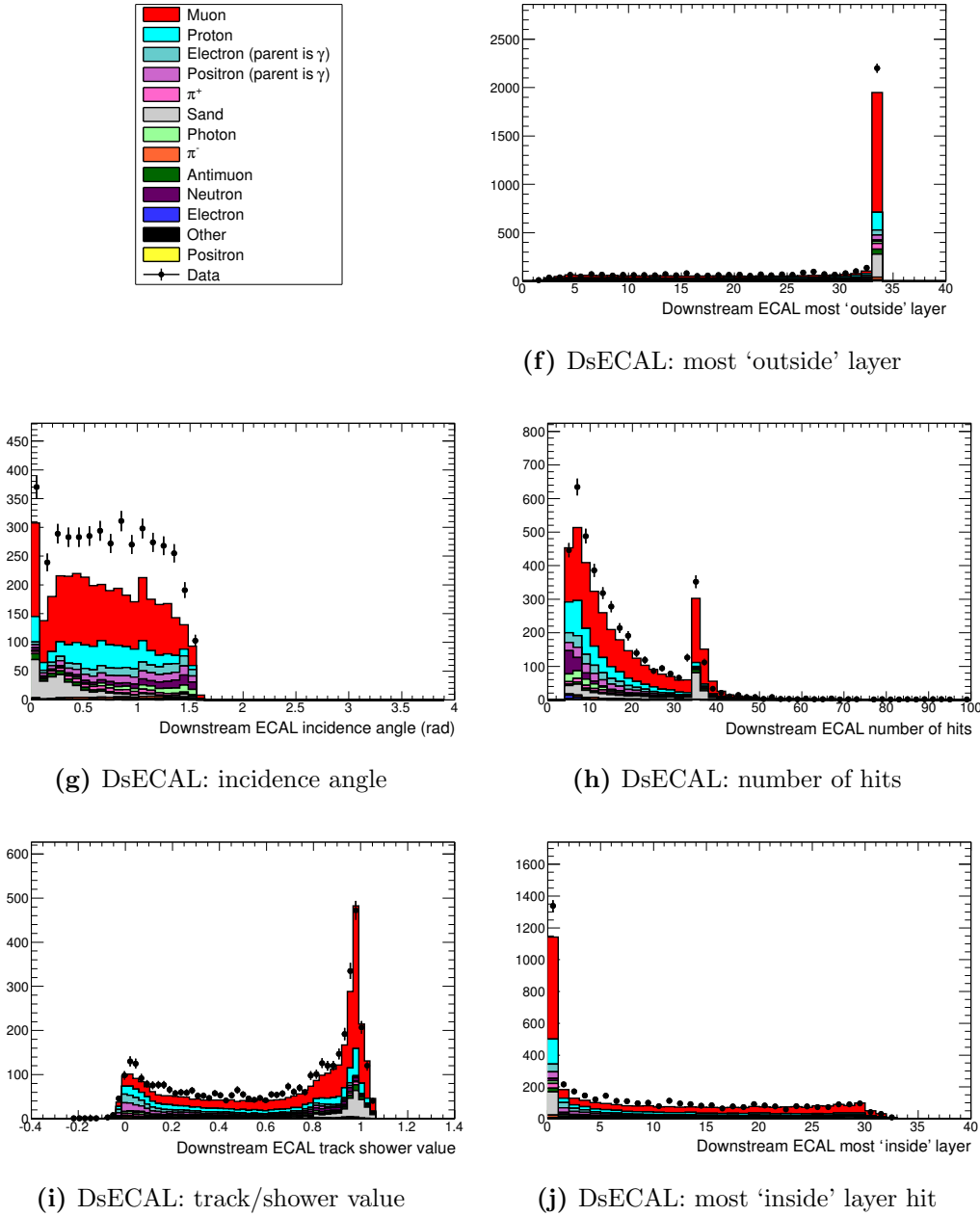
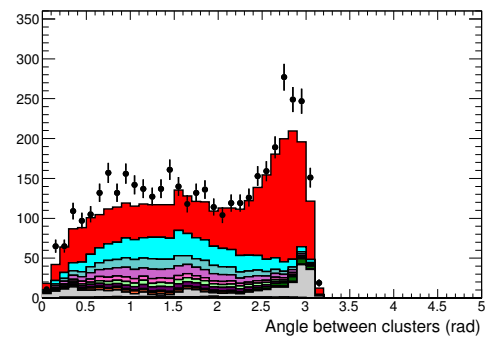
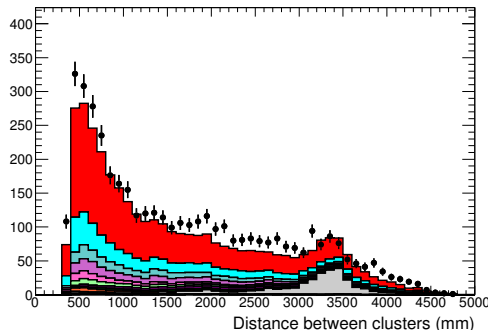


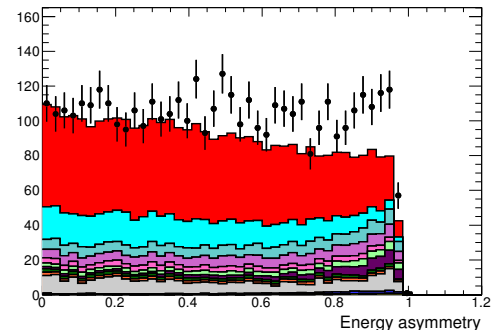
Figure A.10.: Data and MC distributions of ECAL variables used in TMVA for the DsECAL cluster in category three after pre-TMVA cuts. Plots are POT normalised. For label definitions see Table 6.8.



(k) Angle between clusters



(l) Distance between clusters



(m) Energy asymmetry

Figure A.10.: Data and MC distributions of ECAL variables used in TMVA for category three after pre-TMVA cuts. Plots are POT normalised. For label definitions see Table 6.8.

Type	Composition (%)
Signal	43
CC in ECAL	11
NC in FGD producing $1\pi^0 + X$	9
NC in TPC	8
CC in FGD producing $1\pi^0 + X$	7
NC in ECAL	5
CC in TPC	4
CC in the FGD (no π^0 produced)	3
CC in uninstrumented	2
Signal with different photon topology	1
Other	7

Table A.1.: Breakdown of backgrounds by interaction type for ECAL cluster position category one.

Type	Composition (%)
Signal	9
CC in ECAL	21
NC in ECAL	20
NC in TPC	9
CC in the SMRD	8
NC in FGD producing $1\pi^0 + X$	5
CC in uninstrumented	5
CC in TPC	3
CC in FGD producing $1\pi^0 + X$	3
CC in P0DECAL	3
NC in uninstrumented	3
NC in the P0D	2
NC in the SMRD	2
NC in P0DECAL	1
Signal with different photon topology	1
Sand interaction	2
Other	2

Table A.2.: Breakdown of backgrounds by interaction type for ECAL cluster position category two.

Type	Composition (%)
Signal	16
CC in ECAL	24
NC in ECAL	19
NC in TPC	8
NC in FGD producing $1\pi^0 + X$	5
CC in TPC	4
CC in the SMRD	4
NC in uninstrumented	3
CC in uninstrumented	3
Signal with different photon topology	3
CC in FGD producing $1\pi^0 + X$	2
NC in the SMRD	2
NC in the P0D	1
CC in the FGD (no π^0 produced)	1
Other	4
Sand interaction	<1

Table A.3.: Breakdown of backgrounds by interaction type for ECAL cluster position category three.

Appendix B.

Supplementary information for the analysis of systematic uncertainties

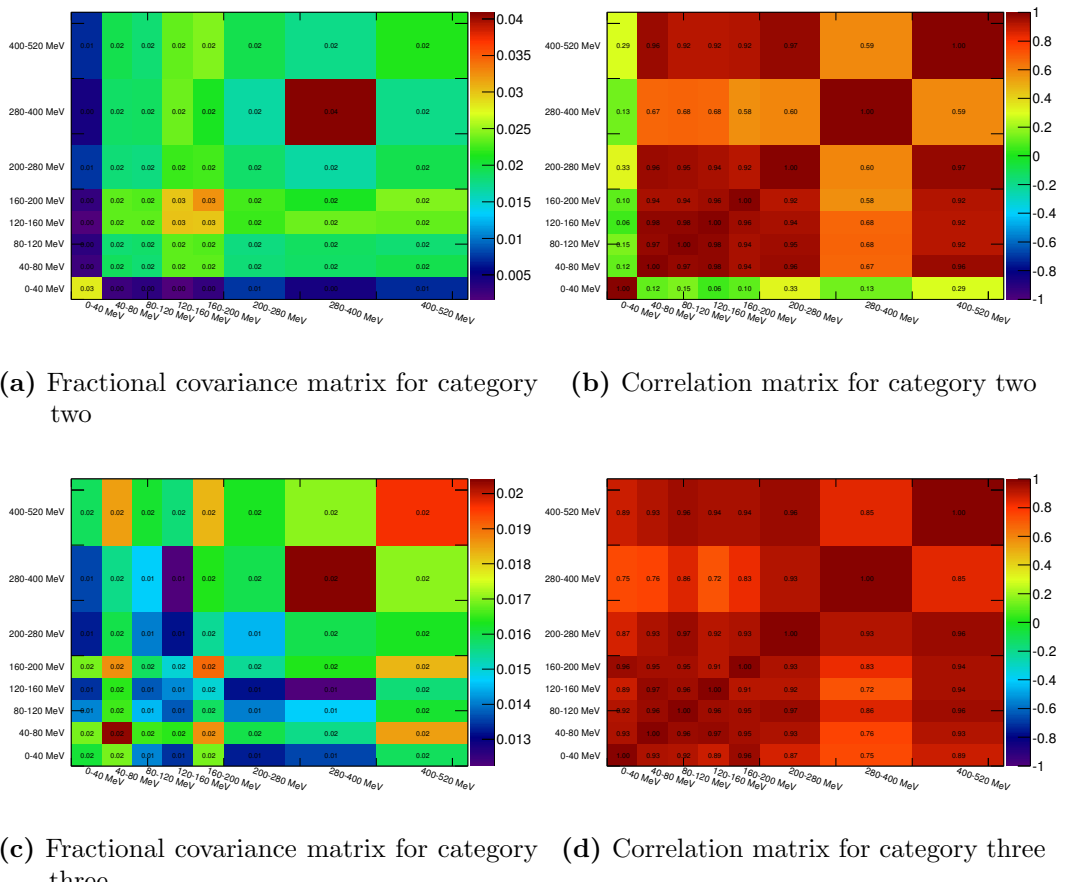
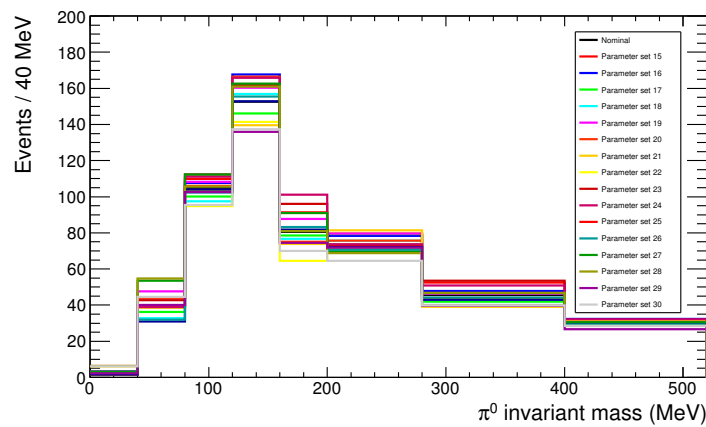
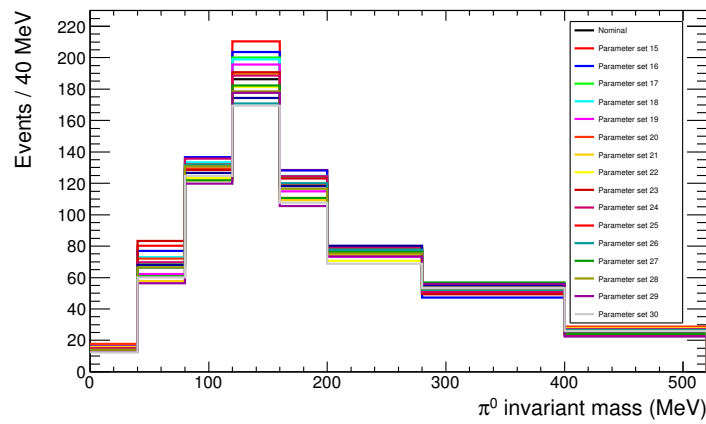


Figure B.1.: Fractional covariance and correlation matrices illustrating the effect of the cross-section model parameters on the π^0 invariant mass distribution for cluster position categories two and three.



(a) Category two



(b) Category three

Figure B.2.: The π^0 invariant mass distribution for ECAL cluster position categories two and three for all 16 throws of the FSI parameters and the nominal value.

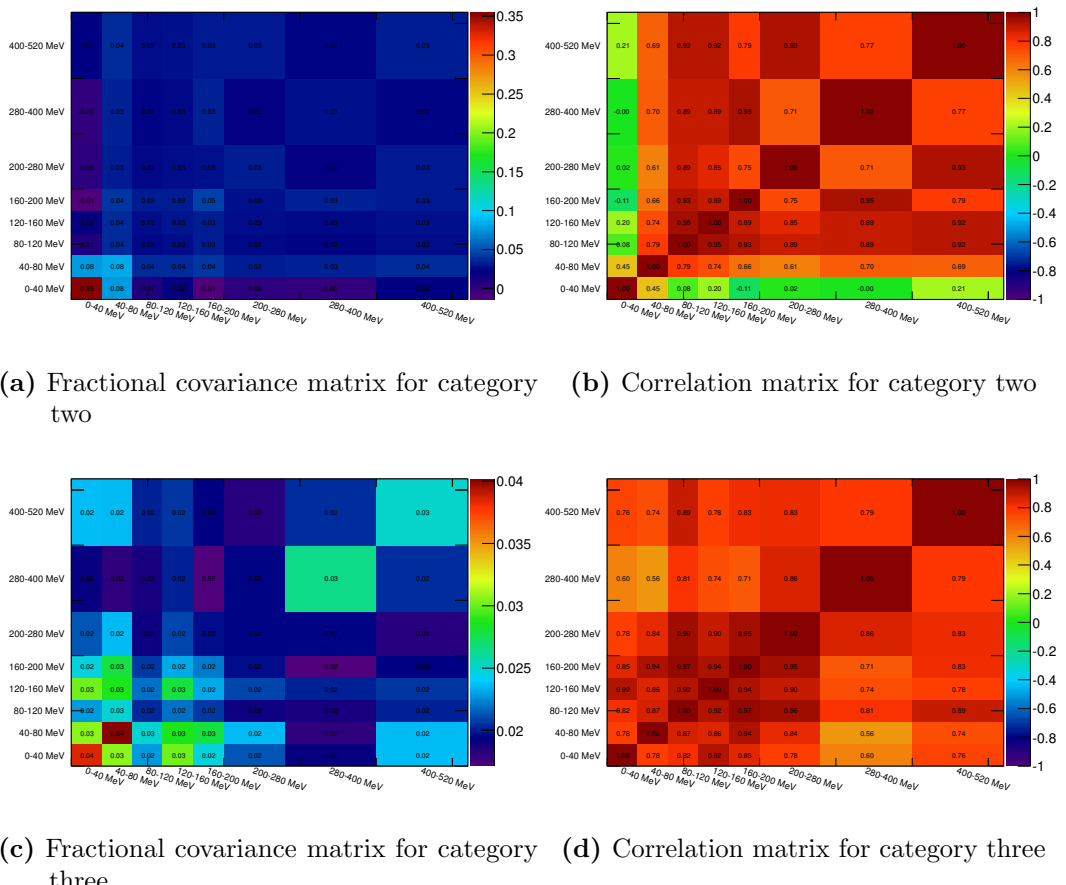


Figure B.3.: Fractional covariance and correlation matrices illustrating the effect of the cross-section FSI parameters on the π^0 invariant mass distribution for cluster position categories two and three.

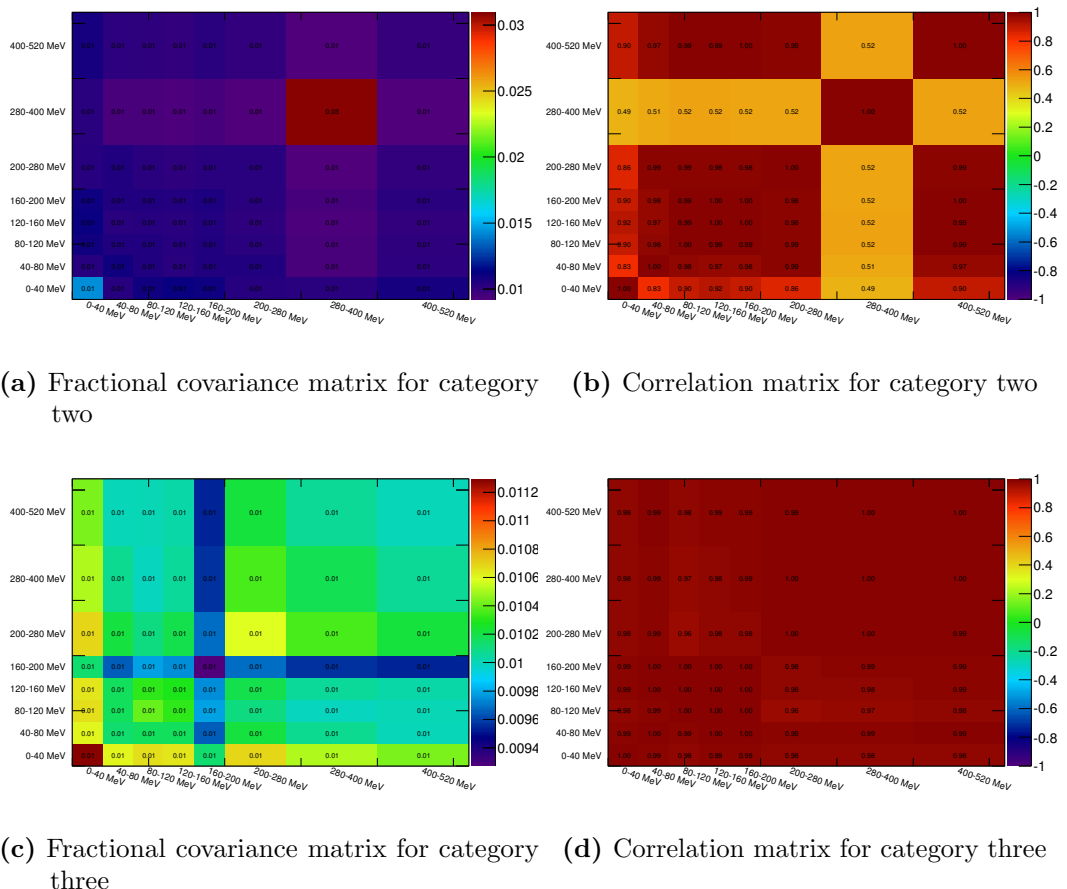


Figure B.4.: Fractional covariance and correlation matrices illustrating the effect of the neutrino flux uncertainty on the π^0 invariant mass distribution for cluster position categories two and three.

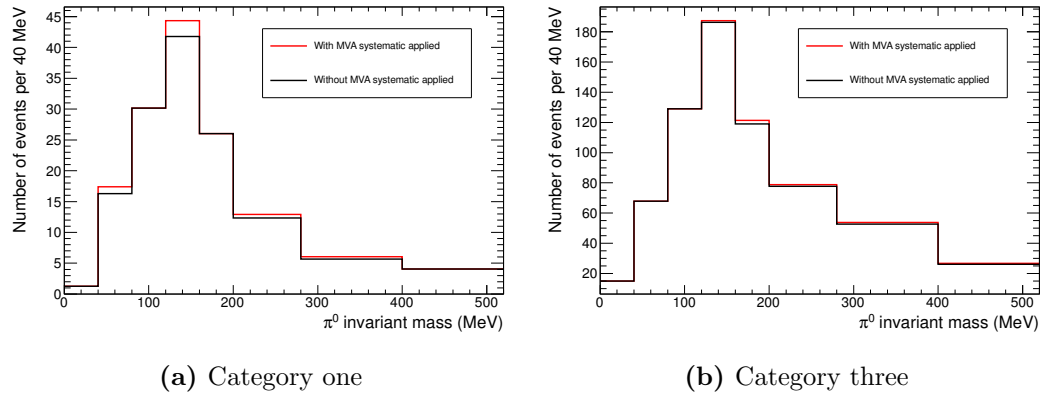


Figure B.5.: π^0 invariant mass with and without the TMVA shape systematic applied for ECAL cluster position categories one and three.

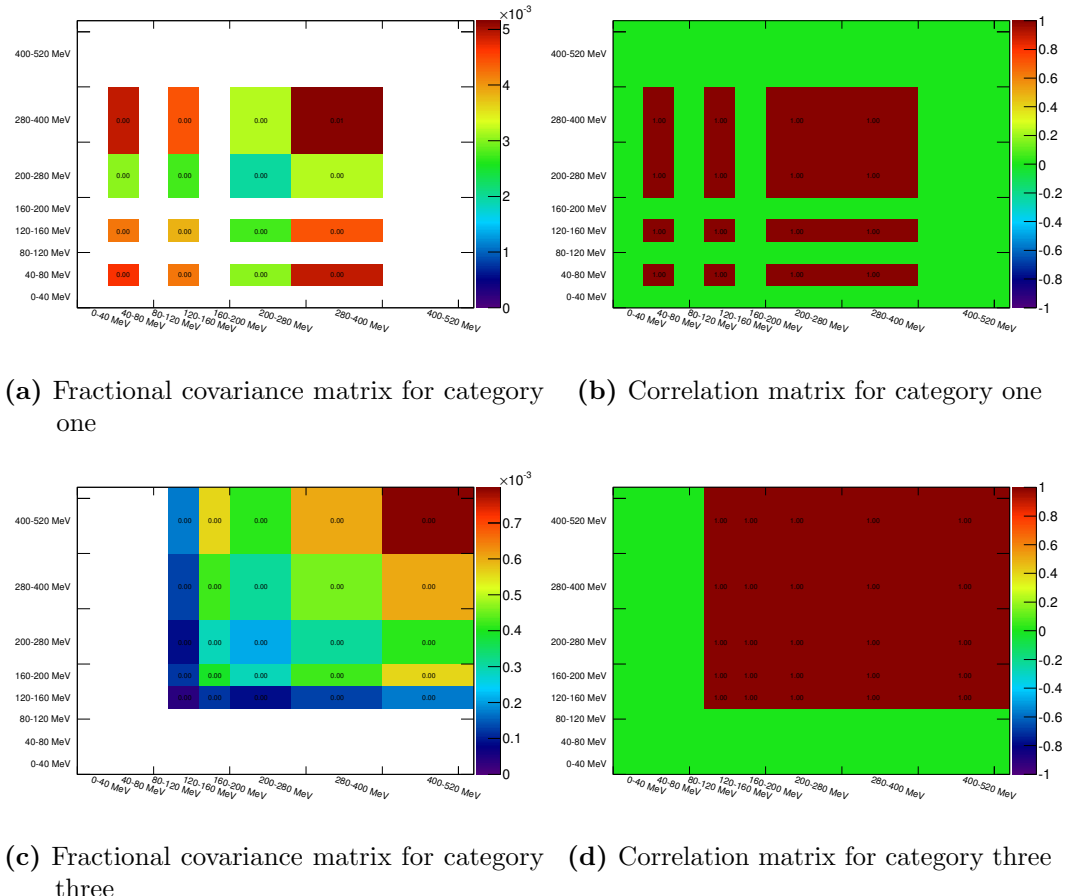


Figure B.6.: Fractional covariance and correlation matrices illustrating the effect of the discrepancy between data and MC on the final π^0 invariant mass distribution for cluster position categories one and three.